université PARIS-SACLAY

NNT : XXX

INSTITUT d'OPTIQUE GRADUATE SCHOOL ParisTech

Quantum simulation of spin models with assembled arrays of Rydberg atoms

Thèse de doctorat de l'Université Paris-Saclay
préparée à l'Institut d'Optique Graduate School

École doctorale n°572 Ondes et Matières (EDOM)
Spécialité de doctorat: Physique

Thèse présentée et soutenue à Palaiseau, le 10 décembre 2018, par

Sylvain de Léséleuc

Composition du Jury :

Jacqueline Bloch Directrice de recherche, CNRS – C2N	Présidente
Jean Dalibard Professeur, Collège de France	Rapporteur
Thierry Giarmarchi Professeur, Université de Genève	Rapporteur
Christian Groß Senior scientist, MPQ	Examinateur
Thierry Lahaye Chargé de recherche, CNRS – LCF	Directeur de thèse
Antoine Browaeys Directeur de recherche, CNRS – LCF	Invité

Thèse de doctorat

Contents

Chapter 1

Introduction

Walking around modern laboratories, the founders of quantum physics could observe the realization of their numerous *gedanken* experiments that they devised to assess the quality of their fascinating quantum mechanical theory of the microscopic world. Among the important milestones that marked the last decades, physicists built electro-magnetic traps where a single charged particle (an electron or an ion) can be maintained for days [Dehmelt, 1990; Paul, 1990], engineered a photon box where a microwave photon bounces back and forth for more than 40.000 km in a superconducting cavity [Haroche, 2013], or reached an exquisite level of control over neutral atoms cooled and trapped by lasers [Phillips, 1998; Ashkin *et al.*, 1986].

These quantum objects have the curious capacity to entangle, a fundamental concept from quantum physics with no classical counterpart, referring to the fact that the measurement on a quantum particle is strongly correlated to the one made by another observer on a second particle entangled with the first one. Entanglement has intriguing consequences, such as the non-locality of quantum physics, which was undeniably demonstrated, after more than 50 years of theoretical controversies, in experiments with two photons [Aspect, Grangier, and Roger, 1982; Aspect, 2015]. Entanglement is believed to be a resource for the speed-up of quantum computers, — based on qubits (elementary two-level systems) and entangling gates —, and in any case arises naturally in correlated many-body systems.

Quantum simulation, i.e, the capacity to use artificial quantum systems to study many-body problems, a concept introduced by Feynman, is another exciting prospect that recently became possible with state-of-the-art experimental apparatuses [Georgescu, Ashhab, and Nori, 2014]. A physical system realized in a laboratory is used to mimic and explore problems where quantum effects play a key role, as in high-energy physics, real world materials or even totally artificial models of mathematical physics. For the study of condensed-matter systems, a usual approach is to identify the relevant degrees of freedom and an effective Hamiltonian describing their evolution. For insulating magnetic materials, this gives spin Hamiltonians as the remaining degree of freedom is the magnetic moment of electrons localized at the sites of a crystalline ionic structure.

Spin models and quantum magnetism

In quantum physics, the different components of a spin $\mathbf{S} = (\hat{S}_x, \hat{S}_y, \hat{S}_z)$ are observables that do not commute, such that they cannot all be measured simultaneously and verify uncertainty relations. In the simplest case of a spin-1/2 particle, the observables take the form of Pauli matrices $(\hat{\sigma}_x, \hat{\sigma}_y, \hat{\sigma}_z)$ and the quantum state of a single spin expresses simply as $|S\rangle = \alpha\,|\uparrow\rangle_z + \beta\,|\downarrow\rangle_z$, with α (β) the probability amplitude to observe the spin (anti-)aligned with the measurement axis (here the z-axis). It is commonly represented on the Bloch sphere, as shown in Fig. 1.1(a). Since a spin possesses a magnetic moment, it couples to an external magnetic field $\mathbf{B}$ through the Hamiltonian $-\mu_B \frac{\hbar}{2}\hat{\sigma} \cdot \mathbf{B}$ (with μ_B the Bohr magneton). The torque applied by the magnetic field on the spin makes it precess, which lies at the heart of nuclear magnetic resonance (NMR) physics [Purcell, 1953; Bloch, 1953]. In materials, where relaxation processes are present, the spins tend to align along $\mathbf{B}$, thus forming a paramagnet [see Fig. 1.1(b)]. At high temperatures, thermal fluctuations destroy the magnetization as soon as the magnetic field is removed, but not at lower temperature, where magnetic order is stabilized by the interaction between spins.

There exist many physical processes, e.g., electron exchange (combining Coulomb repulsion and Pauli exclusion principle), that give rise to effective spin-spin couplings. The most studied ones are the fully isotropic Heisenberg Hamiltonian $H = \sum_{\langle i,j \rangle} J_{ij} \vec{\sigma}_i \cdot \vec{\sigma}_j$, the planar XY coupling $J(\sigma_i^x \sigma_j^x + \sigma_i^y \sigma_j^y)$ or the uni-axial $J\sigma_i^z \sigma_j^z$ one introduced by Ernst Ising [1925]. Despite the apparent simplicity of these Hamiltonians, they lead to a fascinating variety of collective phenomena referred to as quantum magnetism [Blundell, 2001]. For instance, with a negative coupling constant in the Ising model, the energy of the system is minimized when the spins are all aligned in a spontaneously chosen direction (either all up or all down), which explains the phase transition at the Curie temperature between a paramagnet and a ferromagnet, identified by the emergence of a spontaneous magnetization. Conversely, for $J > 0$ two coupled spins tend to point in opposite directions, giving rise to antiferromagnetic materials: for simple crystalline geometries, such as a square or cubic lattice, Louis Néel [1936] postulated a phase transition towards an ordered state of two intertwined sub-lattices with opposite orientations of the spins, shown in Fig. 1.1(c), explaining why no net magnetization could be observed despite experimental indications of magnetic ordering (e.g., via magnetic susceptibility measurements). The existence of this Néel state was later confirmed by neutron diffraction experiments [Shull, Strauser, and Wollan, 1951]. Interestingly, such ordered states cannot always be constructed, as in the triangular

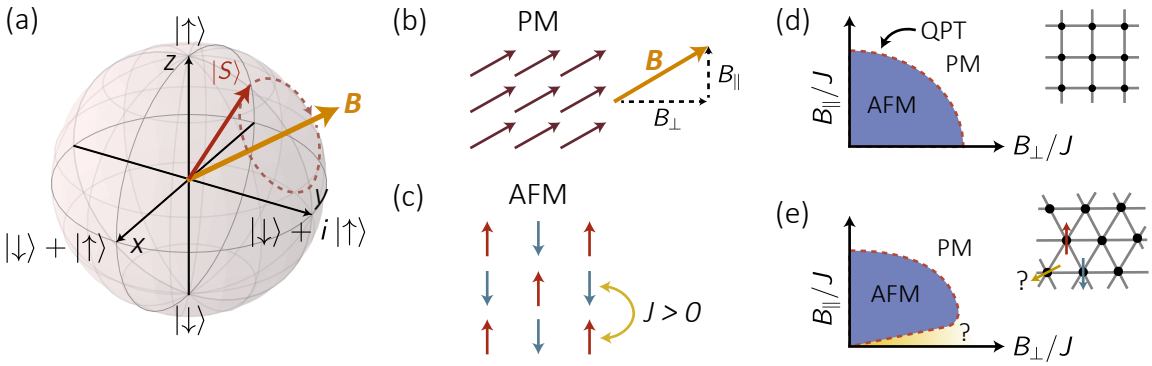

Figure 1.1: Spin-1/2 models. (a) Bloch sphere representation of a spin-1/2 (red arrow) precessing around a magnetic field $\mathbf{B}$ (orange arrow). (b) An ensemble of spins aligning along $\mathbf{B}$ forming a paramagnet (PM). (c) Anti-ferromagnetic Néel ground-state (AFM) of an Ising Hamiltonian with $J > 0$. (d) Phase diagram of the quantum Ising model at zero temperature showing a quantum phase transition (QPT) between a PM and AFM phase. $B_{\parallel}$ and $B_{\perp}$ are the magnetic field components parallel and transverse to the Ising-favored z-axis. (e) A triangular lattice frustrates the anti-ferromagnet constraints and an exotic phase is expected when interaction dominates.

or pyrochlore-like structures that prevent the antiferromagnetic constraint to be simultaneously satisfied on all links, an effect known as geometrical frustration. More exotic magnetic phases, like spin liquids, are expected to arise in these geometrically frustrated materials.

Spin Hamiltonians with arrays of Rydberg atoms

In real materials, it is often hard to study out-of-equilibrium physics or to obtain time- and spatially-resolved observable that would help identifying strong correlations between the spins. Quantum simulation is thus a promising approach to condensed-matter problems as effective spin materials can be extremely well engineered and isolated from their thermal environment with an easy access to any local observable. Exciting studies of spin models,— such as the propagation of correlations [Cheneau *et al.*, 2014; Richerme *et al.*, 2014; Jurcevic *et al.*, 2014], effective thermalization of zero-temperature interacting ensembles [Kaufman *et al.*, 2016], or many-body localization phenomena [Smith *et al.*, 2016; Choi *et al.*, 2016]—, have been reported using chains of ions [Blatt and Roos, 2012] ultracold gases in optical lattices [Gross and Bloch, 2017], and more recently with arrays of superconducting qubits [Roushan *et al.*, 2017; King, A. *et al.*, 2018].

Our group has shown, since 2014, the power of a Rydberg-atom quantum simulator for the implementation of large scale spin Hamiltonians. The sub-nanoscale crystalline structure of spin-1/2 particles of magnetic materials is mimicked by neutral alkali atoms trapped in holographic arrays of microscopic optical tweezers that can realize any two-dimensional geometry [Nogrette *et al.*, 2014]. These tweezers can be loaded with only a single atom, and not more, because of the so-called collisional blockade regime caused by strong, inelastic, light-assisted collisions between two atoms in the trap, discovered at the Institut d'Optique by Schlosser *et al.* [2001]. Despite a typical inter-atomic separation R of a few micrometers, effective spin-spin couplings between the atoms are made possible by exciting them to Rydberg states of high principal quantum number $n \geq 50$. In a classical picture, the valence electron orbits far away from the positively-charged nucleus to form a large electric dipole $\mathbf{d}$. The dipole-dipole interaction $\hat{H}_{dd} \sim \mathbf{d}_1 \cdot \mathbf{d}_2/(4\pi\epsilon_0 R^3)$ between two Rydberg atoms is then strongly enhanced compared to atoms in their electronic ground state, and can be used for quantum computing or the implementation of spin Hamiltonians (see the reviews of Saffman [2016] and Browaeys, Barredo, and Lahaye [2016]).

Historically, Jaksch *et al.* [2000] and Lukin *et al.* [2001] proposed to use the strong interaction between Rydberg atoms for the implementation of quantum gates through the 'Rydberg blockade effect'. Figure 1.2 illustrates this for an elementary setup of two atoms laser-driven from their electronic ground-state $|g\rangle$ to a Rydberg level $|r\rangle$ with a Rabi frequency Ω. The dipole-dipole interaction between two atoms in the same Rydberg state $|rr\rangle$ leads to a van der Waals shift $V = C_6/R^6$ of their energy. In the blockade regime, defined by $\hbar\Omega \ll V$, the doubly-excited state $|rr\rangle$ is sufficiently shifted away from the resonance to preclude the simultaneous excitation of the two atoms by a laser resonant on the $|g\rangle \leftrightarrow |r\rangle$ transition. Therefore, $|gg\rangle$ is only coupled to the entangled state $\frac{1}{\sqrt{2}}(|gr\rangle + |rg\rangle)$, where a single Rydberg excitation is symmetrically delocalized on the two atoms, with an enhanced coupling $\sqrt{2}\Omega$. These effects have been observed in experiments with exactly two atoms by Gaëtan *et al.* [2009] at the Institut d'Optique and by Urban *et al.* [2009] in the group of Prof. Mark Saffman, and soon led to the generation of entangled states [Wilk *et al.*, 2010] and the implementation of quantum gates [Isenhower *et al.*, 2010].

The Rydberg blockade effect can be readily extended to large systems of N atoms: When the blockade condition is verified for any pair of atoms, the excitation laser only couples $|G\rangle = |gg\ldots g\rangle$ to the entangled state $|W\rangle = \frac{1}{\sqrt{N}}\sum_i |g\ldots r_i \ldots g\rangle$ with a driving strength $\sqrt{N}\Omega$. This collective enhancement was measured for $N = 3$ by Barredo *et al.* [2014] and up to $N = 15$ by Labuhn *et al.* [2016] using optical tweezers

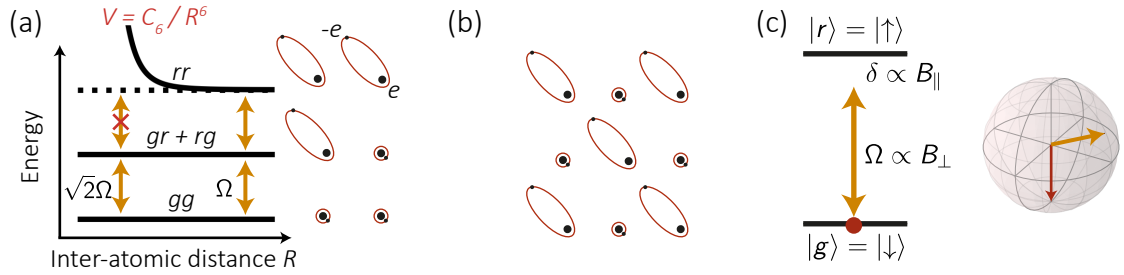

Figure 1.2: From Rydberg physics to Ising models (a) Two-atom blockade effect. With decreasing inter-atomic distance R, the doubly-excited state $|rr\rangle$ is shifted away due to the van der Waals energy correction $V = C_6/R^6$. When the driving strength Ω of the atomic $|g\rangle \leftrightarrow |r\rangle$ transition is much weaker than the interaction shift V, the two atoms cannot be excited simultaneously. The $|gg\rangle \leftrightarrow \frac{1}{\sqrt{2}}(|rg\rangle + |gr\rangle)$ transition is driven with a collective Rabi coupling $\sqrt{2}\Omega$. (b) The ordering of Rydberg excitations in an atomic array mimics an Ising anti-ferromagnet. (c) The laser driven ground-Rydberg two-level system implements a spin-1/2 particle in an external magnetic field $\mathbf{B}$.

arrays in our group, and with few hundred atoms in optical lattice experiments [Zeiher *et al.*, 2015]. In this fully blockaded limit, the dynamics of the system reduces to an oscillation between $|G\rangle$ and $|W\rangle$. One can also tune the interaction strength such that the blockade extends only to nearest neighbors and map the Rydberg atom problem into a quantum Ising spin model by considering the coherent laser drive as an external magnetic field $\mathbf{B}$ acting on the pseudo-spin states $|\downarrow\rangle = |g\rangle$ and $|\uparrow\rangle = |r\rangle$, and the van der Waals shift as an Ising coupling. Such implementations have been first reported on an optical lattice platform [Schauß *et al.*, 2012; Schauß *et al.*, 2015], and more recently using arrays of tweezers offering more flexibility in geometry [Labuhn *et al.*, 2016; Bernien *et al.*, 2017; Kim *et al.*, 2018].

A second feature of the dipole-dipole interaction allows implementing XY Hamiltonians: when encoding the spin-1/2 particle in two dipole-coupled Rydberg levels $|\uparrow\rangle = |r\rangle$ and $|\downarrow\rangle = |r'\rangle$, driven by a microwave field (playing again the role of an effective magnetic field), the dipole-dipole interaction is resonant and takes the form of an XY ('flip-flop') coupling $J(\sigma_1^x\sigma_2^x + \sigma_1^y\sigma_2^y)$. Although it seems to be only a slight extension of the Ising coupling, it leads to strikingly different properties, the main reason being that the Pauli matrices $\sigma^{x,y,z}$ do not commute. For two atoms, it leads to a spin-exchange oscillation between the two degenerate states $|\downarrow\uparrow\rangle$ and $|\uparrow\downarrow\rangle$, hybridized by the dipole-dipole coupling. It can also be seen as a spin-excitation hopping from one Rydberg atom to another, as observed by Barredo *et al.* [2015] with an elementary chain of three Rydberg atoms.

Despite successful proof-of-principle experiments with Rydberg atoms in tweezers, scaling the system size to more than a few atoms have been hindered, prior to 2016, by the stochastic loading of atoms in arrays of optical tweezers. When letting cold atoms fall into the microscopic tweezers, only half of them are loaded due to the collisional blockade. This is a weakness of the platform as it results in randomly filled atomic arrays. While the problem is absent in optical lattice experiments, which benefit from the transition from a superfluid phase to a Mott insulator state with a single atom per site [Greiner *et al.*, 2012], this comes at the expense of severe constraints on the geometries and low experimental cycling rate (≤ 0.1 Hz), as one has to start from a quantum degenerate gas.

Thesis outline

In this thesis, I present the improvements realized during the last three years of our quantum simulator of spin models and our recent studies of Ising and XY Hamiltonians. A first aspect is the preparation of perfectly ordered two- and three-dimensional atomic arrays of almost one hundred atoms allowed by the development of an atom-by-atom assembler. A second facet is the experimental simulation of an Ising spin model and the quantitative improvement of its ingredients: the coherent control of spins and the mapping of the van der Waals interaction to an Ising term. A third direction is the development of experimental tools for the preparation and manipulation of XY magnets, which enabled us to study the many-body topological phases of a Su-Shrieffer-Heeger (SSH) chain. This manuscript is thus arranged in three parts as follows.

Part I: Ordered 3D arrays of atoms

Chapter 2 starts with a general overview of the tweezers platform and then explains how arbitrary three-dimensional structures of traps are formed by holography. It continues with the implementation of tunable lenses enabling us to reconstruct 3D views of the trap and atomic arrays by taking successive images of different planes.

Chapter 3 describes the development of our atom-by-atom assembling machine, first the engineering of a moving tweezers to transfer an atom between two given traps, then combining many moves to re-order, atom-by-atom, half-filled 2D matrices of traps, which are finally repeated plane-by-plane to obtain ordered 3D arrays of atoms.

Part II: Ising models

Chapter 4 starts with an historical review of experimental and theoretical studies of laser-driven ground-Rydberg systems in van der Waals interaction, relating them to the phase diagram of a long-range Ising model where various ordered phases are stabilized by the effective spin-spin interaction. It describes quench experiments that probe the critical region between the paramagnetic and the ordered phases, and then gives a general classification of the latter. It finally focuses on the case where the long-range character of the interaction can be neglected and the system maps onto a perfect nearest-neighbor Ising model, and presents our attempt to create adiabatically the anti-ferromagnetic Néel state of the Ising model on a square lattice.

For both quench and adiabatic sweep experiments, we observe some deviations from a coherent model of spin-1/2 particles that requires a better understanding of our implementation of the two ingredients of the Ising model: the effective magnetic **B**-field by a coherent laser drive and the Ising coupling between two spins originating from the van der Waals interaction between two Rydberg atoms. The two following chapters enter into technical and physical details to understand and improve the fidelity of our Rydberg quantum simulator.

Chapter 5 describes the experimental techniques for the coherent manipulation of ground-Rydberg spin-1/2 particles, implementing an effective **B**-field. It presents the experiments we used to estimate independently the coupling strength of the excitation lasers, the detection errors of the atom internal state, and the various damping mechanisms that lead to a finite coherence time for the control of the two-level system. Future directions to improve these figures are given.

Chapter 6 presents how the dipole-dipole interaction between two atoms reduces to a simple van der Waals shift for two atoms in the same Rydberg level, which then maps onto an Ising term. It analyses how precisely a real atom with many ground and Rydberg levels can be restricted to a two-level system, while the dipole-dipole interaction tends to mix these levels. It allows us to find better experimental parameters to correct the discrepancies between experiment and theory observed earlier in Labuhn *et al.* [2016].

Part III: XY models

Chapter 7 presents a toolbox for the studies of XY magnets, from the preparation of all atoms in the Rydberg manifold with the STIRAP method, the global manipulation

of the spin-1/2 ensemble with microwave fields and the local addressing of a single spin with a focused laser beam. Elementary experiments with two atoms will then show our control of the dipole-dipole interaction strength, with precise measurements of its angular dependence and dynamical tuning with the addressing laser.

Chapter 8 presents our implementation of the SSH Hamiltonian, one of the most elementary models exhibiting two topologically distinct phases. After benchmarking our experiment on the known single-particle properties of the model, it explores the consequences of filling the model with many hard-core bosons. The study of interacting topological phases is currently a hot topic in condensed-matter physics and we will present conclusive signatures of a symmetry-protected topological phase of interacting particles.

Part I.

Ordered 3D arrays of atoms

Chapter 2

3D arrays of single atoms in optical tweezers

Contents

In this chapter, I will describe the trapping and imaging of many single atoms, each in an optical tweezers, forming 2D and 3D structures. I will start by an overview of the experimental setup in Section 2.1, recalling how we trap single atoms in an optical tweezers and how we perform experiments with them. I describe in Section 2.2 how we use holography to generate many copies of a trap with arbitrary 3D positioning and present an experimental characterization of the trap arrays using the atoms as an *in situ* probe. Finally, in Section 2.3, I explain how we image and reconstruct 3D views of the trap arrays and of the atomic fluorescence using electrically-tunable lenses to observe successively different planes. The results presented in this chapter (and the following one) led to two publications [Barredo *et al.*, 2016, 2018].

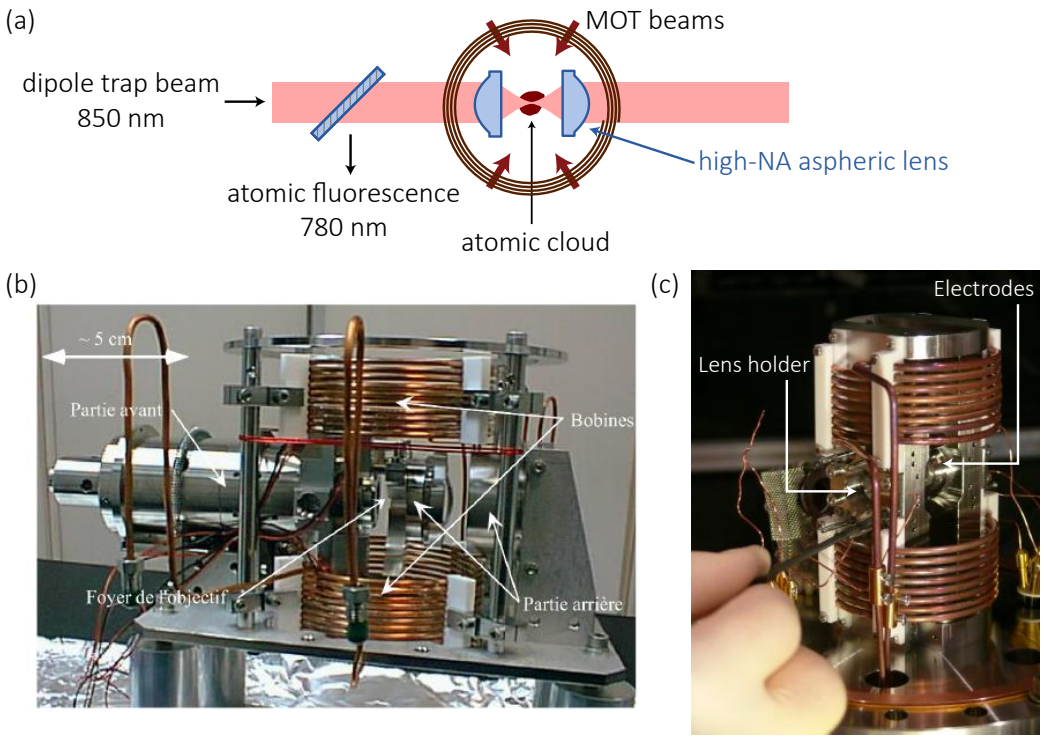

Figure 2.1: From MIGOU to CHADOQ. (a) Basic elements for single-atom trapping: A cloud of cold ^{87}Rb atoms is formed in a magneto-optical trap (MOT), where a dipole trap beam is strongly focused to a $\sim 1\,\mu$m-size by a high-NA optical system. (b) The massive nine-lens home-made microscope objective of MIGOU (image taken from [Schlosser, 2001]), which was operated till 2010. (c) The more compact CHADOQ setup with a pair of aspherical lenses and a set of 8 electrodes (hidden inside the holding structure) built by Béguin [2013] and coworkers. A pair of coils, visible in both images, is used to generate a gradient of magnetic field for the magneto-optical trap (in anti-Helmholtz configuration) or a vertical magnetic field to define the quantization axis (in Helmholtz configuration). Both systems are placed in a ultra-high vacuum chamber and combined with an atomic source (Zeeman slower), not shown here.

2.1 Overview of the experimental setup

Our group has a long history of single-atom control with optical tweezers. The basic principle, discovered here at the Institut d'Optique by Schlosser *et al.* [2001], is the so-called *collisional blockade* regime reached when loading atoms in microscopic dipole traps, also named optical tweezers. The experimental setup is schematically shown in Fig. 2.1: a magneto-optical trap (MOT) is formed by the intersection of six laser beams (only the four in the plane of the figure are represented) and a gradient of magnetic field generated by a pair of coils. The cloud of cold ^{87}Rb atoms trapped in

the MOT is used to load an optical tweezers. The latter is created by focusing a laser beam at 850 nm to a small waist of $\sim 1\,\mu$m with a high-numerical-aperture (NA) optical system.

Traditionally, large dipole traps ($\sim 10 - 100\,\mu$m) were used to manipulate atomic cloud made of a large number of atoms [Grimm, Weidemüller, and Ovchinnikov, 2000]: they combine (i) a conservative potential proportional to the intensity of the trapping beam and (ii) friction forces from the MOT beams, such that atoms are attracted and captured in the center of the trap. The illumination of the atoms by the MOT beams cause an additional effect: (iii) inelastic light-assisted collisions. When two atoms collide, we usually expect that they simply exchange some kinetic energy (elastic collisions), such that the atomic cloud is in a thermal equilibrium (it is important for evaporative cooling in ultra-cold quantum gas experiments). But, in presence of the MOT light, the two atoms will also experience inelastic collisions: absorbing a photon, they are excited to a short-lived bound state subjected to an attractive interatomic potential, then gain a large kinetic energy by getting closer together, and finally re-emit a photon at a larger wavelength. The gained kinetic energy of the two atoms is usually much higher than the trap depth and the two atoms are thus lost from the trap. This effect was initially considered as a nefast one, because it reduces the lifetime of dense atomic clouds.

It was then demonstrated by Schlosser *et al.* [2001] that this effect could be turned into an interesting tool to manipulate single atoms. Decreasing the trap size to a μm-scale enhances the light-assisted two-body loss rate such that it dominates over the loading rate of atoms from the MOT. In this now well-studied regime [Schlosser, Reymond, and Grangier, 2002; Fuhrmanek *et al.*, 2012], as soon as a second atom enters the trap, collisions with the first atom expel both of them, such that the number of trapped atoms alternates between 0 and 1, and never more. It thus gives us a stochastic single atom source with a probability $\eta = 50$ % to obtain one atom.

At the heart of this platform lies a high-NA objective lens focusing the trap laser beam down to a waist of $\sim 1\,\mu$m. The challenge is to combine the optical setup with the constraints of a cold atom experiment (ultra high vacuum, need for optical access) with Rydberg states (controlled electric environment). In our group, the choice has always been to use a large vacuum chamber and put the lens inside, rather than, e.g., using small glass cells and have the objective outside. In the first setup, MIGOU, the tweezers was focused with a home-made microscope objective of nine spherical lenses designed to obtain a diffraction-limited spot at both 780 and 850 nm wavelengths (for imaging and trapping) [Vigneron, 1998; Schlosser, 2001]. The setup

was then considerably simplified using a single commercial molded aspheric lens in the ASPHERIX setup [Sortais *et al.*, 2007; Fuhrmanek, 2011]. All the experimental work presented in this thesis has been performed on CHADOQ, the third generation experiment. It combines a custom asphere, an ITO (indium tin oxide) coating of its surface to prevent patch charges, and a set of eight electrodes in an octopole configuration to provide an active control of the electric field environment seen by the Rydberg atoms. The setup was built by Aline Vernier and Lucas Béguin [2013] and first used to perform experiments with pairs of atoms whose fluorescence was collected on avalanche photo-detectors (APDs). It was then improved by Daniel Barredo and Sylvain Ravets [2014] to add a third trap and a third APD, and latter scaled to $N \simeq 50$ atoms using holographic techniques to generate multiple traps in parallel [Nogrette *et al.*, 2014] and an EMCCD camera to detect and resolve the atomic fluorescence coming from each trap [Labuhn, 2016].

In this section, I first review the experimental setup dedicated to the atomic array preparation and imaging, which has greatly evolved in the last years with the inclusion of the atom assembler machine and the extension from 2D to 3D structures of traps. I then describe a typical experimental sequence and finally discuss the main characteristics of a single atom trapped in a tweezers.

2.1.1 The holographic optical tweezers platform

Figure 2.2 shows a simplified view of our experimental setup used to trap, image and assemble single atoms in arrays of optical tweezers. The part necessary to obtain a source of cold ^{87}Rb atoms — a diffusive oven, a Zeeman slower and a magneto-optical trap (MOT)— is described in great detail in the thesis of Lucas Béguin [2013] and is not discussed here. From the cloud of cold atoms, a single one is loaded in a microscopic optical tweezers formed at the focal point of a high NA (0.5) aspheric lens with an effective focal length $f = 10$ mm and a clear aperture diameter $D = 10$ mm. The trap laser, at $\lambda = 850$ nm, is chosen far red-detuned from the D_1 and D_2 lines of the ^{87}Rb atom to engineer an attractive potential with typical depth $U \simeq k_B \times 1$ mK (or $h \times 20$ MHz), much larger than the atomic temperature in the MOT ($T \approx 100\,\mu$K). The trapping beam is re-collimated by a second similar aspheric lens such that we can image the trap pattern onto the trap CCD camera.

We go from a single trap to a 3D structure of hundreds of them using holography: a phase mask is imprinted on the trapping beam with a spatial light modulator (SLM). Bergamini *et al.* [2004] first demonstrated the technique in our group for up to four

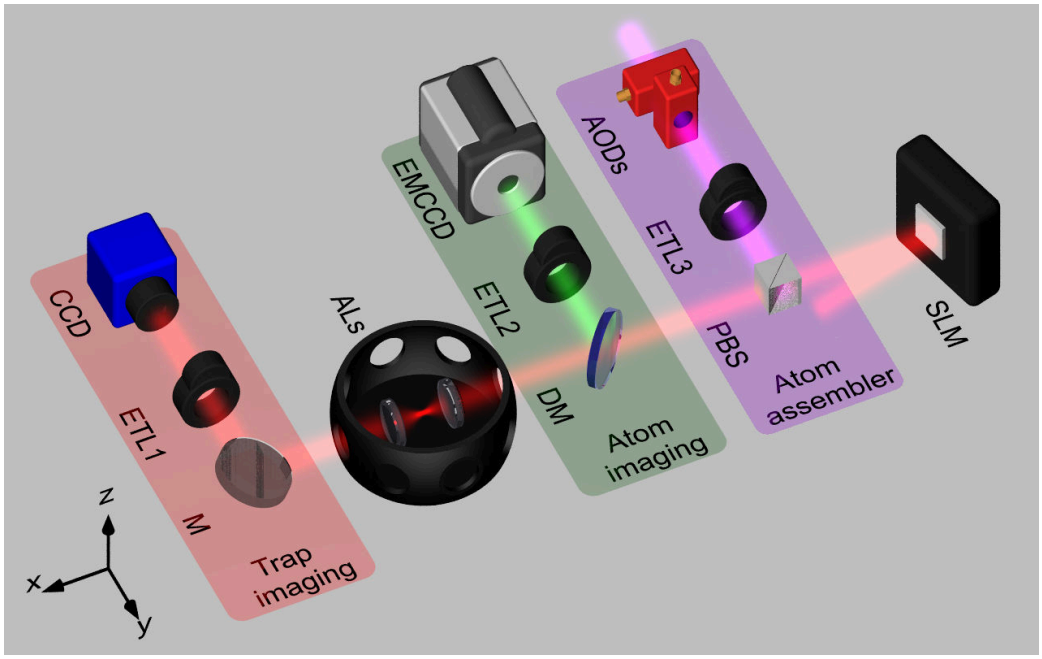

Figure 2.2: Experimental setup for creating ordered 3D structures of single atoms. The aspheric lenses (ALs) in the vacuum chamber focus a collimated beam to create an optical tweezers, which can load a single atom. The spatial light modulator (SLM) imprints a phase mask on the trapping beam duplicating a single tweezers in a 3D array of traps. The trap imaging setup gives an image of the trapping structure and the atom imaging system of the atomic fluorescence. The deflectors (AODs) in the atom assembler part create a moving tweezer used to assemble atom one by one in an ordered atomic pattern. Tunable lenses (ETL) allow to work on different planes of the 3D structures.

traps and Nogrette *et al.* [2014] improved it to generate a hundred of traps arranged arbitrarily in a plane. The technique is explained in the thesis of Henning Labuhn [2016] in the case of 2D arrays. However, we are not restricted to arrays of trap in the focal plane of the lens, as demonstrated on experiments with trapped colloidal particles [Leach *et al.*, 2004; Di Leonardo, Ianni, and Ruocco, 2007], and I explain the extension of our holograms to 3D in Section 2.2.

There are two imaging setups: one to diagnose the trap structure at 850 nm on a CCD camera using the re-collimated trapping beam and another one to observe the fluorescence photons emitted by the atoms at 780 nm, upon illumination by the cooling beams, on an electron-multiplying CCD camera (Andor iXon Ultra 897). We now use electrically-tunable lenses (ETLs) to image on-demand different 2D-cuts of the 3D structure onto the CCD chips, as described in Section 2.3. The trap imaging system is used to analyze the trap pattern and, e.g., measure the uniformity of the

trap intensities, which we feedback to the algorithm calculating the holograms. The atom imaging part allows us to detect the presence or absence of an atom in each trap.

The atom assembler machine, described in Chapter 3, was conceived to solve a long-standing issue of the optical tweezers platform: Due to the stochastic loading procedure based on the collisional blockade regime, there are only $\sim N/2$ atoms randomly positioned in an array of N traps. The atom sorting setup reorders the array by reshuffling atoms one by one with a moving tweezers (MT). The MT is computer-controlled with two crossed acousto-optical deflectors (AODs) allowing 2D movements (along y and z), extended to 3D by combining the AODs with a tunable lens.

2.1.2 A typical experimental cycle

I now describe a complete experimental run where the goal is to study a system of atoms excited to Rydberg states (what I will call a Rydberg experiment). In the following of this thesis, I will focus on the assembler part (Chapter 3) and all other chapters will be devoted to Rydberg experiments.

We first switch on the Zeeman slower and the MOT lasers to create a cloud of cold atoms loading the array of tweezers. The atomic fluorescence of each trap is continuously monitored and an experimental sequence is triggered as soon as enough atoms are present in the array. After switching off the Zeeman and the MOT beams to stop the loading, an initial fluorescence image is acquired by collecting the photons scattered by the atoms from the cooling beams during an exposure of 20 ms (see Appendix A). After the atom assembly, a second image is taken to confirm the successful preparation of the cold atom sample.

Then, we switch on a vertical magnetic field B_z, from a few Gauss up to 50 G depending on the experiment, to define the quantization axis and separate the different Zeeman sublevels. It is generated with the pair of coils located in vacuum, which is switched from the anti-Helmholtz configuration (to create a MOT) to the Helmholtz one in typically 5 ms. Three pairs of external coils, in Helmholtz configuration, are used to apply any offset of $\mathbf{B}$; their currents are also switched between two values: to position the MOT or to cancel B_x and B_y during a Rydberg experiment. Because they are located outside the vacuum chamber, we wait ~ 30 ms for the eddy currents to vanish ($1/e$ decay time of ~ 5 ms).

At that point, we can perform a variety of experiments involving Rydberg states. We first perform optical pumping (< 1 ms) to prepare all atoms in the same ground-state

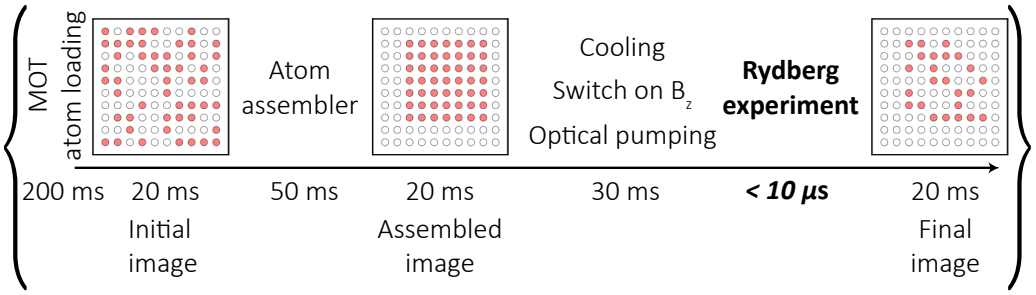

Figure 2.3: Experimental sequence. Three fluorescence images are taken: after the stochastic loading of atoms from the MOT, after the atom-by-atom assembly procedure and after the Rydberg experiment. A Rydberg excitation is observed as an atom loss. The experiment typically runs at a rate of 3 Hz, and can reach 10 Hz when we do not need ordered arrays and when atoms are recycled from one run to the other.

level. Then we switch off the tweezers to avoid perturbing the electronic levels and shine a set of excitation laser pulses to access the Rydberg states. The Rydberg experiment in itself is kept extremely short (less than $10\,\mu$s) compared to the full experimental cycle, as the atoms are in free flight and we are anyway limited by the typical lifetime of a Rydberg state ($\sim 100\,\mu$s). Finally, we switch back the traps and any atom left in the Rydberg manifold is repelled by the ponderomotive potential of the tweezers (see Section 5.2) and lost. We then read the state of the array with a third fluorescence image.

Fluorescence measurement During the imaging, the repumper beam is switched on and we observe all ground-state atoms, irrespective of the $F = 1$ and $F = 2$ hyperfine levels. For some experiments, we need a hyperfine-state sensitive measurement, which is achieved by first removing any atoms in the $F = 2$ level with a push-out beam tuned to the cycling transition $\left|5S_{1/2}, F = 2\right\rangle \leftrightarrow \left|5P_{3/2}, F = 3\right\rangle$ applied either during $4\,\mu$s if the atoms are in free flight or a few hundred of microseconds if they are trapped. In this thesis, we thus used only destructive measurements based on the loss of an atom depending on its internal degree of freedom (Rydberg state, hyperfine level...). However, we could also use a non-destructive method by performing the fluorescence measurement without the repumper beam [Fuhrmanek *et al.*, 2011; Gibbons *et al.*, 2011; Martinez-Dorantes *et al.*, 2017; Kwon *et al.*, 2017]. The interested reader will find more details about the process of converting a photon incoming on the EMCCD camera to a digital count sent to the computer, and the various noise sources currently limiting the exposure time to 20 ms, in Appendix A.

Repetition rate We repeat the full cycle many times to acquire enough data to decrease statistical errors or to scan some parameters. Indeed, the quantum projection noise, which is just the standard error on the mean (s.e.m.) of a probability p (the state population) estimated from N binary observations (the atom is in the state or not), is $\sigma_{\mathrm{QPN}} = \sqrt{p(1-p)/N}$ and reaches 5 % for $N = 100$ and 1 % for $N = 2500$ (for the worst-case $p = 0.5$). For some experiments, we can use many atoms in parallel and average the results over the entire array, but for others we have to keep a single atom (if they interact for example). It is thus crucial to have a high experimental repetition rate.

After loading the MOT, an experimental run takes typically 140 ms (3×20 ms for imaging, 50 ms for assembling, 30 ms for the settling time of magnetic fields), but it can be shorter (< 80 ms) if we do not need ordered arrays, e.g., when we work with independent atoms, or longer if we need to work with 3D structures, where the imaging and assembling has to be performed for each plane.

When all atoms are recaptured at the end of a run, they can be directly re-used in the next one, and the cycling rate can be as high as 10 Hz, which is quite fast for a cold neutral atom experiment. Much more often, we gain information about the atomic state through atom loss and we need to reload new atoms in the trap array. After improvement of the MOT parameters, we could decrease the loading time to ~ 200 ms, such that our typical repetition rate is around 3 Hz. It is really appreciable in day to day operation, as we can quickly perform all calibration experiments or achieve very low quantum projection noise. Aiming at even faster rate, we can replace the destructive state measurements by non-destructive ones to avoid the loading stage and there is still room for optimization of the assembler speed and exposure time.

2.1.3 A single atom in a tweezers

Here, I describe how we measure the main characteristics of a tweezers (trap depth and frequencies) and of a single atom (trapping lifetime, temperature).

Trap depth and trapping frequencies We usually describe the optical tweezers as a simple Gaussian beam, characterized by a waist w, a Rayleigh length $z_R = \pi w^2/\lambda$ and a trap depth U. Even in the absence of aberrations, this is already an approximation, as calculating the exact profile requires to take into account the diffraction of the input beam slightly clipped by the aspheric lens. The real trap shape lies between a Gaussian beam (no clipping) and an Airy profile (uniform illumination of the lens).

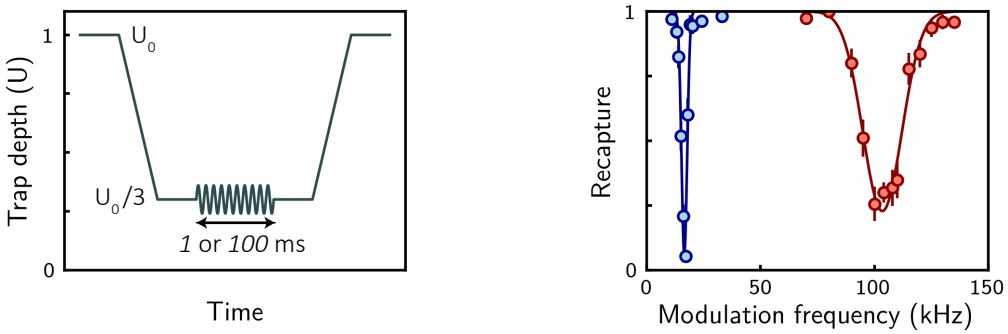

Figure 2.4: Parametric heating. We first lower adiabatically the trap depth to 1/3 of its initial 1 mK value and then modulate it by 15 % during 1 or 100 ms to excite, respectively, the radial (red) and axial (blue) resonances. The solid line is a fit used to extract the trapping frequencies: $2\omega_{\parallel} = 2\pi \times 16.5(1)$ kHz and $2\omega_{\perp} = 2\pi \times 103.5(5)$ kHz.

Anyway, as our atoms only explore the bottom of the tweezers, the relevant and experimentally accessible quantities are the trapping frequencies $\omega_{\parallel}$ and $\omega_{\perp}$ defining quadratic potentials $m\omega_i r_i^2/2$, where we distinguish the axial and radial directions. Assuming a Gaussian profile, we can extract effective parameters w and z_R from:

$$\omega_{\perp} = \sqrt{\frac{4U}{mw^2}} \quad \text{and} \quad \omega_{\parallel} = \sqrt{\frac{2U}{mz_R^2}}. \tag{2.1}$$

We measure the trapping frequencies by modulating the trap depth, looking for losses occurring at the parametric excitation resonance at $2\omega_{\parallel,\perp}$. The results are shown in Fig. 2.4(b) and we extract:

$$\omega_{\perp}/(2\pi) = 50.2(3)\,\text{kHz} \quad \text{and} \quad \omega_{\parallel}/(2\pi) = 8.3(1)\,\text{kHz}, \tag{2.2}$$

which combined with the tweezers depth $U/h = 5.5(1)$ MHz (measured by spectroscopy, see 2.2.3) and Eq (2.1) gives:

$$w = 1.01(2)\,\mu\text{m} \quad \text{and} \quad z_R = 4.31(8)\,\mu\text{m}. \tag{2.3}$$

The aspect ratio is slightly different than for a perfect Gaussian beam (z_R is larger than the theoretical $\pi w^2/\lambda = 3.6\,\mu$m), which could be explained by the real diffraction profile, as discussed previously, and aberrations.

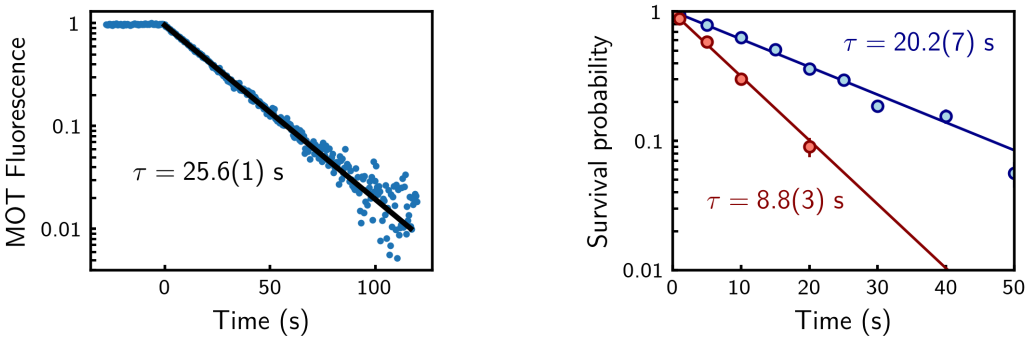

Figure 2.5: Atom lifetime. Background gas collisions limit the lifetime of atoms in a trap. (Left) MOT lifetime after switching off the Zeeman slower. (Right) Lifetime of a single atom in a tweezers when the cooling beams are off (blue) and on (red). The continuous cooling decreases the atom lifetime.

Atom lifetime For the small trapping depth (< 1 mK) achievable with neutral atoms and dipolar force, elastic collisions with the background gas (at 300 K) always expel the trapped particles. We first estimate the background-gas limited lifetime of atoms from the decay of fluorescence of the magneto-optical trap after switching off the Zeeman slower. Figure 2.5(a) shows a lifetime $\tau \simeq 25$ s, which is reasonable for this vacuum chamber with a limited bake-out temperature (constraint by the various elements placed inside). In a second experiment, we load a single atom in a tweezers, which we check with a first fluorescence image, and measure its survival probability after a variable time with a second image. There, we extract a lifetime of 20 s [Fig. 2.5(b), blue curve], similar to the one observed with the MOT. It varies from 5 to 20 s depending on the oven temperature (respectively 150° C and room temperature), as the atomic beam hit the atoms. Finally, in a third experiment (red curve), we let the cooling beams always on and observe a decreased lifetime ($\tau \simeq 8$ s), which is still not understood. It could be caused by the complicated interplay of the trapping potential and the cooling mechanisms leading to atomic trajectories out of the trap. In conclusion, the atom lifetime is typically 10 s, giving a reasonable $\simeq 1$ % probability to lose an atom during a 100 ms-long experiment. A solution to improve these numbers significantly would be to reach even lower background gas pressure by going for a cryogenic setup.

Atom temperature The energy distribution of a single atom trapped in a tweezers is given by its temperature T, which after loading from the MOT, is typically $\sim 50\,\mu$K. The kinetic energy is thus much larger than the energy spacing of the vibrational

levels ($\hbar\omega \simeq k_B \times 5\,\mu$K along the radial axis), such that the atom is far from the ground vibrational state of the trap and a classical description of the atomic external degrees of freedom (position $\mathbf{r}$ and velocity $\mathbf{v}$) is sufficient. Of importance for us, the atomic temperature T, together with the trapping frequency ω, give us the r.m.s. position and velocity uncertainties σ_r and σ_v of the atom in the tweezers:

$$\sigma_r = \sqrt{\frac{k_B T}{m\omega^2}} \quad \text{and} \quad \sigma_v = \sqrt{\frac{k_B T}{m}}, \tag{2.4}$$

with m the mass of ^{87}Rb and ω the trapping angular frequency. The position uncertainty is different along the strong (radial) and weak (axial) trapping axes.

We determine the atomic temperature (really the r.m.s. velocity) from a release and recapture experiment [Tuchendler *et al.*, 2008]: we switch off the optical tweezers, let the atom move away from the trap due to its velocity v during a variable time τ, and switch on the tweezers again. We compare how fast the recapture probability goes down with τ to a Monte-Carlo simulation of the classical dynamics of a particle at temperature T. For the simulation, the initial position and velocity are chosen according to normal distributions with widths $\sigma_{r,v}$, and we consider that an atom is lost if its kinetic energy is higher than the trap potential at the atom position after the time of flight. I show in Fig 2.6 a measurement together with the best fit simulation $T = 20\,\mu$K. For daily estimation of the atom temperature, we do not record the full curve, but only the recapture probability after a time of flight of $20\,\mu$s. Importantly, we observe that the recapture does not drop in the first $\sim 5\,\mu$s, meaning that we can perform a Rydberg experiment up to this duration without suffering from detection errors (see 5.2).

Prospects for further cooling The finite temperature of the atom thus limits the duration of a Rydberg experiment as they fly away from the optical tweezers and I discuss here how to increase the available experimental time by reaching lower temperature. After loading atoms from the MOT in the traps, or after a fluorescence image (the MOT beam parameters are the same for both), the atom temperature is $60\,\mu$K. We further cool the atom to $\sim 40\,\mu$K by increasing the detuning of the molasses to -8Γ (relatively to the transition frequency of a free atom). At this temperature, the average radial vibrational number is still $\bar{n}_\perp = k_B T/(\hbar\omega_\perp) \simeq 10$. Reaching the ground-state of the optical tweezers requires a more advanced technique than Doppler or sub-Doppler cooling: Raman sideband cooling. The technique was first employed for ions Monroe *et al.* [1995] where the much higher trapping frequencies (tens of MHz)

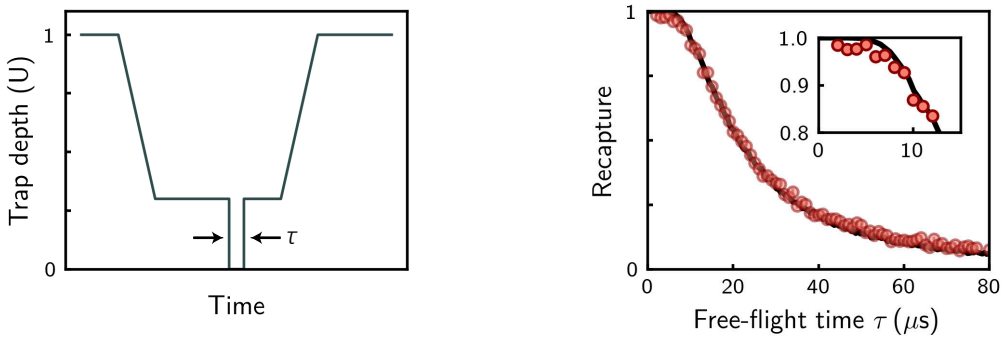

Figure 2.6: Time of flight. The atomic temperature is measured by releasing the atom during a time τ and observing the decrease in recapture. The data (red circles) are well reproduced by a classical simulation of the atom dynamics for $T = 20\,\mu$K.

facilitates its use compared to neutral atom dipole traps. Two groups simultaneously applied the technique to microscopic optical tweezers: Thompson *et al.* [2013b] obtained averaged occupation numbers $\bar{n}_\perp = 0.01$, $\bar{n}_\parallel = 8$ starting from an initial temperature of $50\,\mu$K, while Kaufman, Lester, and Regal [2012] reached a ground-state population of 90% ($\bar{n}_\perp = 0.02$, $\bar{n}_\parallel = 0.08$) starting from a lower temperature of $11\,\mu$K after a careful optimization of the polarization-gradient cooling (PGC). More recently, Yu *et al.* [2018] reported ground-state cooling of single Na atoms in a tweezers. The conclusion is twofold: (i) we should be able to reach lower temperature than now ($40\,\mu$K) with standard laser cooling (PGC), most likely by a better control of the cooling beam polarizations, and (ii) if necessary, ground-state cooling can be applied.

Position and velocity uncertainties As all the experiments presented in this thesis are performed on planar arrays of atoms, we are mainly interested in the radial position uncertainties $\sigma_{y,z}$, which affect the inter-atomic distance R in first order (but only in second order, $\propto \sigma_x^2/R$, for the axial one). At $T = 40\,\mu$K, the initial uncertainties are $\sigma_{y,z} = 0.1\,\mu$m ($\sigma_x = 0.7\,\mu$m) and $\sigma_v = 0.06$ m/s. During a Rydberg experiment, the traps are switched off and the position uncertainty increases due to the velocity of the atom, such that after $t \simeq 1.5\,\mu$s of free-flight the two contributions (σ_r and $\sigma_v t$) are equal. As our experiments typically last $\sim 5\,\mu$s, the r.m.s. velocity is the main source of uncertainties.

We can lower σ_v at the expense of σ_r by adiabatically lowering the trap depth U, which decreases the trapping frequencies $\omega \propto \sqrt{U}$. If the process is done adiabatically ($\dot{\omega} \ll \omega^2$), the population of each vibrational level is conserved: $\bar{n} = k_B T/(\hbar\omega)$ remains constant and the temperature is lowered proportionally to ω. Since the entropy is

conserved during the procedure (contrarily to laser cooling where spontaneously emitted photons take away entropy), the phase-space volume should remain constant. And indeed, while $\sigma_v \propto \sqrt{T}$ is decreased, $\sigma_r \propto \sqrt{T}/\omega$ increases and their product is unchanged. For too low final trap depth, the adiabaticity criterion becomes more difficult to fulfill and we start to lose atoms. Reducing U by a factor ~ 10, we obtain $T = 20\,\mu\mathrm{K}$ (see Fig. 2.6) and $\sigma_v = 0.04$ m/s.

2.2 3D arrays of traps

Scaling the number of traps from a single one to hundreds of them requires to parallelize their generation. In a first demonstration, Dumke *et al.* [2002] focused the trapping beam using an array of micro-lenses creating a 2D array of traps with large spacings of $100\,\mu$m, equal to the separation between the lenses. Our group proposed and demonstrated the use of a spatial light modulator (SLM), located in the Fourier plane of the aspheric lens, which imprints a phase pattern diffracting the beam and gives in the focal plane an intensity pattern related to the Fourier transform of the phase mask [Bergamini *et al.*, 2004]. This holographic technique gives great flexibility in the trap geometries, which can be changed, without any realignment of the optical system, by simply updating the SLM phase mask.

The technique has been improved to include the correction of aberrations and the equalization of the trap depths as described in Nogrette *et al.* [2014] and in the thesis of Henning Labuhn [2016]; a similar work has also been performed at Hamamatsu company [Matsumoto *et al.*, 2012]. The holograms are generated with the Gerchberg-Saxton (GS) algorithm [Gerchberg and Saxton, 1972], which uses Fourier transforms between the focal plane of the lens and its Fourier plane, where the SLM is located. This technique is very powerful as a large class of light patterns can be generated [Zupancic *et al.*, 2016]. Optical tweezers arrays, which are nothing more than an assembly of Gaussian spots, are only a very restricted set of light patterns. In this case, the formulation of the GS algorithm with Fourier transform is overkilled.

In this section, I will describe a simpler formalism based on the combination of elementary phase patterns [Di Leonardo, Ianni, and Ruocco, 2007], which allows the extension of our previous works to 3D. Then, I will present how to modify the GS algorithm to include a feedback measurement of the trap intensities. Finally, I will characterize the trap arrays using a single atom as an *in situ* probe.

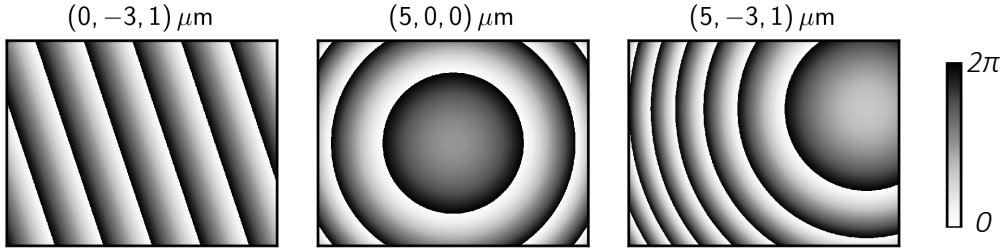

Figure 2.7: Elementary phase patterns. Simple holograms $\exp[i\Delta_m]$, see Eq. (2.5), creating a single trap at the position (x_m, y_m, z_m) .

2.2.1 Holograms for 3D arrays

I start by a quick review of the optical setup used for holography and refer a reader interested in extensive details to Labuhn [2016]. I will explain how an elementary phase pattern allows to displace a trap at an arbitrary position and then how to create a 3D assembly of traps by combining many such patterns.

Setup We shine our trap laser on a spatial light modulator (SLM, Hamamatsu X10468-02) imprinting a phase mask $\varphi_{\mathrm{SLM}}(y_s, z_s)$ where y_s, z_s are the coordinate system on the SLM plane. The SLM is constituted of 792×600 pixels, each of size $20 \times 20\,\mu\mathrm{m}^2$, giving a total area of $15.8 \times 12\,\mathrm{mm}^2$. The input beam is collimated with a diameter on the order of the SLM size, such that for simplicity we will consider a uniform illumination: the input light-field is described by the complex amplitude $A_0(y_s, z_s) = A_0$, and the output of the SLM by $A_0 e^{i\varphi}$. A relay telescope of magnification $M = -10/12$ images the SLM on the aspheric lens and rescales the SLM size to fit the lens diameter ($D = 10$ mm). If the beam size on the lens is too small, it effectively reduces the NA and increases the traps size; conversely if the beam is too big, the imaged SLM pixel size is unnecessarily large and it decreases the maximum extension of traps array. We will now see which phase pattern to imprint on the SLM to obtain the desired 3D trap structure around the focal plane of the lens.

A single trap Let us start with the elementary phase pattern $\Delta_m(y_s, z_s)$ creating a single trap at the position (x_m, y_m, z_m), where $(0, 0, 0)$ is the focal point of the lens and $\hat{x}$ the optical axis. If no phase pattern is imprinted on the input beam, a single trap is created at the focal point position. The trap can be displaced transversally (along $\hat{y}$ or $\hat{z}$) by tilting the wavefront of the beam, which is achieved by imprinting a linear phase increase along the displacement direction (a blazed grating). Similarly, the trap is

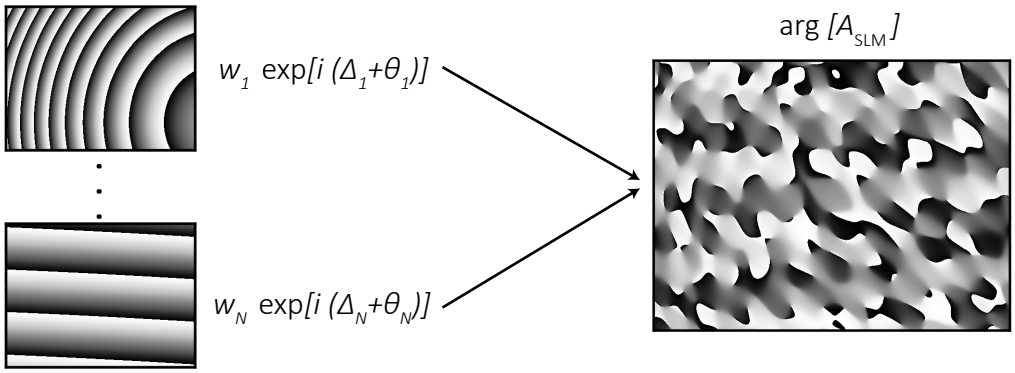

Figure 2.8: Hologram for N traps. N elementary phase patterns Δ_m are combined to give an interference pattern A_{SLM}, see Eq. (2.6), whose phase $\arg[A_{\mathrm{SLM}}]$ is the phase mask displayed on the SLM.

moved along the optical axis direction by changing the divergence of the beam and thus by imprinting a quadratic phase variation curving the wavefront (a Fresnel lens). The elementary phase patterns, shown in Fig. 2.7, are thus $\exp[i\Delta_m]$ with:

$$\Delta_m(y_s, z_s) = \frac{2\pi}{\lambda f}(y_m y_s + z_m z_s) + \frac{\pi x_m}{\lambda f^2}(y_s^2 + z_s^2). \tag{2.5}$$

Many traps To generate an assembly of N traps, we need to somehow combine the N elementary phase patterns $\{\Delta_m, 1 \leq m \leq N\}$ in a single phase mask φ_{SLM}. The solution appears when considering the following 'inverse' problem: what is the *interference* pattern formed on the SLM given by N point-like, coherent, light sources each located at (x_m, y_m, z_m) and emitting with a relative amplitude and phase $w_m e^{i\theta_m}$? The light propagates through the lens, acquires a propagation phase $\Delta_m(y_s, z_s)$ and interferes on the SLM where the complex amplitude of the light field is given by:

$$A_{SLM}(y_s, z_s) = \sum_m w_m e^{i[\Delta_m(y_s, z_s) + \theta_m]}. \tag{2.6}$$

To generate the trap array, we should imprint a phase and amplitude mask reproducing this interference pattern, which at first glance looks inaccessible to a phase-only SLM. However, a good attempt is to imprint only the phase mask:

$$\varphi(y_s, z_s) = \arg[A_{SLM}(y_s, z_s)], \tag{2.7}$$

calculated together with (2.5), (2.6) and a set $\{(w_m, \theta_m), 1 \leq m \leq N\}$, for which a good initial guess is to choose uniform $w_m = 1$ and random phases θ_m. Because we cannot display the amplitude part $|A_{\mathrm{SLM}}|$ of Eq. (2.6), the real amplitude and phase of each trap will differ from this initial choice.

Diffraction equation We denote by V_m the complex amplitude of the light field at the center of the m^{th} trap. It can be calculated from the phase mask φ and the elementary trap pattern Δ_m through the *diffraction* formula:

$$V_m = \iint e^{i[\varphi(y_s,z_s)-\Delta_m(y_s,z_s)]} \mathrm{d}y_s \mathrm{d}z_s, \tag{2.8}$$

where, in our numerical implementation, the double integral is replaced by a summation over all SLM pixels. In practice, we are not interested in the trap relative phases $\arg[V_m]$, but only in the trap intensities $I_m = |V_m|^2$, particularly in:

- the diffraction efficiency $e = \sum_m I_m$, as not all the light is diffracted to form the targeted traps, which increases the required laser power.

- the intensity inhomogeneity $\sigma_I = \sqrt{\langle (I - \bar{I})^2 \rangle}$, as some traps can be shallower than others, which affects their ability to trap atoms.

In the next section, I will explain how to find an optimized set of (w_m, θ_m) such that the hologram calculated with the simple equations (2.5-2.7) gives a high diffraction efficiency e and low intensity inhomogeneity σ_I.

Current method vs FFT I want to emphasize the difference in the way we calculate the hologram and the diffracted pattern as compared to our previous works [Nogrette *et al.*, 2014; Labuhn, 2016]. There, we were propagating the coherent light field between the SLM plane and the focal plane of the lens (or reversely) using Fast-Fourier Transform (FFT) operations, which are not necessary to generate arrays of Gaussian spots. Here, we replace the FFT calculations by the simpler equations (2.6) and (2.8), where the trap positions can run over the three dimensional space. I also find this approach more instructive as the hologram can be seen as the superposition of elementary phase masks with an optimized choice of their relative weights and phases.

2.2.2 Closed-loop feedback for intensity correction

I now discuss how we use the $2N$ degrees of freedom $\{(w_m, \theta_m), 1 \leq m \leq N\}$ to optimize the phase mask in regards of e and σ_I. It relies on an adaption of the Gerchberg-Saxton algorithm, which can be found in Di Leonardo, Ianni, and Ruocco [2007], that we further modified to add an external feedback by measuring the real trap intensities, instead of calculating them, resulting in an improved trap intensity uniformity σ_I [Nogrette *et al.*, 2014; Labuhn, 2016].

Concept The algorithm works as follows:

- initialization: calculate a phase mask φ^0 using equations (2.5-2.7), random trap phases θ_m^0 and uniform trap intensities w_m^0.
- repeat for each step $1 \leq k \leq N$:

  (i) calculate V_m^k with the diffraction formula (2.8) and φ^{k-1}.

  (ii) calculate a new hologram φ^k with the updated values:

$$\theta_m^k = \arg[V_m^k], \tag{2.9}$$

$$w_m^k = w_m^{k-1} \times \frac{\langle |V^k| \rangle_m}{|V_m^k|}. \tag{2.10}$$

In Eq. (2.10), the trap weight w_m^k is increased (decreased) for the next iteration if the calculated trap amplitude $|V_m^k|$ is lower (higher) than the average over all traps $\langle |V^k| \rangle_m$. In our closed loop implementation, we measure the trap intensities I_m^k at each iteration and replace the calculated trap amplitude $|V_m^k|$ by the measured one $\sqrt{I_m^k}$ in Eq. (2.10). The relative standard deviation $\sigma_I/\bar{I}$ of the trap intensities measured on the CCD camera, shown in Fig. 2.9(b), is reduced to $\sim 3\%$ after usually 10 iterations.

Implementation Our numerical implementation of the algorithm is written in Python. We operate on matrices of 792×600 entries representing the value of φ and Δ_m on each SLM pixel. The elementary phase patterns Δ_m are calculated once, when the user inputs the trap coordinates. Then two operations are time-consuming and are thus performed on a graphics card (GPU): (i) the *diffraction* equation (2.8) used to calculate V_m for each of the N traps, which requires to sum over the matrices φ and Δ_m, and (ii) the *interference* equation (2.6) used to obtain the SLM phase mask φ, which requires element-wise operations on the N matrices Δ_m. Both element-wise and

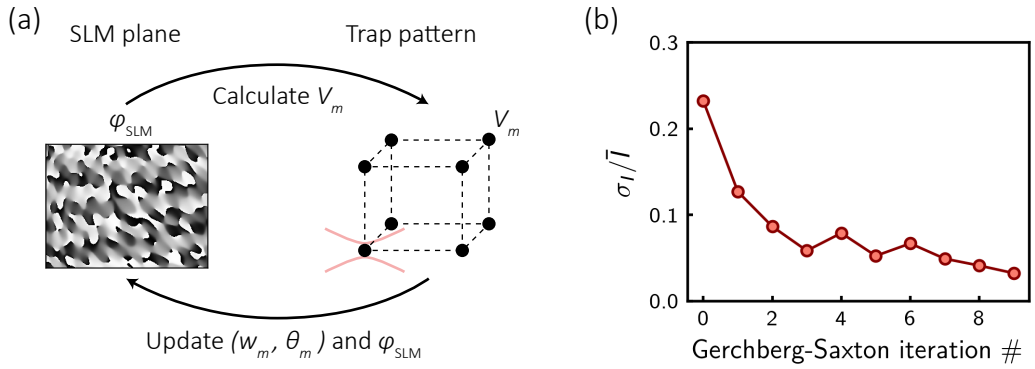

Figure 2.9: Gerchberg-Saxton algorithm. (a) Schematic of the weighted GS algorithm. We only calculate the amplitude of the light field V_m at the trap centers, and not over the entire 3D volume where it is a complicated interference of all the individual tweezers (light red). (b) Relative standard deviation σ_I/I of the trap intensities I measured on the camera. It decreases with the number of iterations down to $\sigma_I/I \simeq 3\,\%$.

reduction operations are performed on a GPU card (NVIDIA Quatro K2000) using the pyCuda wrappers [Klöckner *et al.*, 2012] giving access to Nvidia's CUDA parallel computation API. We obtained a seven times shorter calculation time by running the calculations on the GPU rather than on the CPU. The calculated phase pattern is projected on the SLM using the Python wrapper slmpy written by Popoff [2017]. We automatically acquire images of the trap pattern with a Python script making use of the pyicic wrapper for the Imaging Source trap CCD camera. The trap intensities are obtained by finding the brightest pixel in N pre-defined areas around the expected trap positions. For 3D structures, we take an image of each plane where a trap is focused.

2.2.3 In situ characterization of trap arrays

We have so far characterized the homogeneity of the trap arrays using the beam re-collimated by the second aspheric lens and imaged on a CCD camera. It means that any errors introduced by the imaging system (aberrations, fringes) cannot be distinguished from the real characteristics of the array. For example, internal reflections in the window of the CCD camera give rise to a $10\,\mu$m-period interference pattern with a contrast of $\sim 5\%$, which is imprinted on the trap array with our feedback procedure. We can measure and correct these fringes by scanning a single trap over the CCD camera. Nevertheless, we currently do not use this procedure and the real

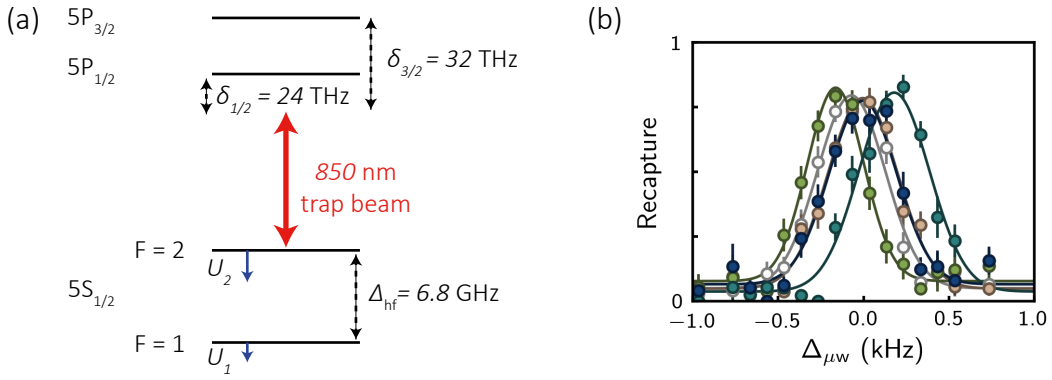

Figure 2.10: Differential light-shift (a) The AC Stark shifts U_1 and U_2 of the two hyperfine ground-state levels differ due to the increased detuning of the trapping beam from the $F = 1$ state. (b) Measurement of the differential light shift $U_2 - U_1$ by microwave spectroscopy of the hyperfine clock transition. We perform a π-pulse interrogation with a Rabi coupling $\Omega_{\mu w}/(2\pi) \simeq 300$ Hz and shows the resulting spectra for 4 traps. The line centers vary due to the inhomogeneity of trap depths.

trap depth inhomogeneity is thus probably higher than the one estimated from the camera. To avoid such potential bias of external diagnostics, it is better to characterize the traps using a single atom as an *in situ* probe. I discuss here measurements of the trap depths and trapping frequencies.

Microwave spectroscopy The dipole trap affects almost all electronic levels and there is a plethora of transitions that we can experimentally probe to measure an energy shift proportional to the trap depth: ground-Rydberg transitions, the D line ($5S - 5P$) or the microwave transition between the two hyperfine ground-state levels. The latter offers, by far, the largest quality factor allowing us to measure small inhomogeneities over the trap array. We prepare the atom in the $|5S_{1/2}, F = 2, m_F = 0\rangle$ state and drive the $\Delta m_F = 0$ clock transition to the $F = 1$ hyperfine level. The transition frequency is shifted because the 850 nm trap is not equally detuned from the two levels due to the hyperfine splitting $\Delta_{\rm hf} \simeq 6.8$ GHz, causing a differential light-shift ηU with:

$$\eta \simeq \Delta_{\rm hf} \frac{1/\delta_{1/2}^2 + 2/\delta_{3/2}^2}{1/\delta_{1/2} + 2/\delta_{3/2}} = 2.4 \times 10^{-4}, \tag{2.11}$$

where $\delta_{1/2} = 24$ THz and $\delta_{3/2} = 32$ THz are the 850 nm laser detuning from the D_1 and D_2 transitions. For a trap depth $U = 5$ MHz, we get $\eta U = 1.2$ kHz and aim at measuring variations of a few percents of this value over the trap array.

I show in Fig. 2.10(b) selected microwave spectra from an array of 9 traps where

we clearly see the inhomogeneity in line centers. Over the 9 traps, the deviation is $\sigma_\Delta = 87$ Hz, and together with the expected differential light-shift $\eta U = 1.2$ kHz, it gives a relative deviation $\sigma_\Delta/(\eta U) = 7.3\,\%$. As expected it is slightly larger than the one measured on the camera, but remains low enough not to cause any problems in trapping atoms. If in future experiments it becomes important to have trap depths equal at the percent level, we could improve the current homogeneity by correcting the camera fringes or using in situ measurement in the feedback procedure.

Trapping frequencies We also check the homogeneity of trap shapes, or equivalently of trapping frequencies, by performing parametric heating measurement, as in Fig. 2.4. Over a large 9×8 trap array, covering an area of $65 \times 65\,\mu\text{m}^2$, the relative standard deviation of trap frequencies is ~ 10 %. Because the trapping frequency depends on the trap depth, we expect the two to be partly correlated.

Limitations Finally, I discuss what kind of 3D structures we can create by holography. First, a natural concern when one thinks about 3D arrays of optical tweezers is that the light we have carefully structured in a given plane will propagate and give an unwanted blurred background in other planes. In practice, the Gaussian beams forming the tweezers diverges quickly, with a length scale given by the Rayleigh range $z_R \sim 5\,\mu$m set by the NA=0.5 of the aspheric lens, such that for well enough separated traps they only weakly interfere with each other. We can usually bring the trap as close as $\sim 3z_R$ axially and $\sim 3w$ transversally. Secondly, the maximum extent of the array is limited by (i) the field of view of the aspheric lens (coma and spherical aberrations will affect traps away from the focal point) and (ii) the SLM pixel size, which defines the maximum spatial frequency of the hologram (in the Fourier plane), and thus limits the largest spatial separation in the focal plane. In our case, the field of view is by far the limiting factor and we could create satisfying traps in a volume of $(100\,\mu\text{m})^3$. Further improvements in compactness and extent would rely on an objective lens with, respectively, a higher numerical aperture and a larger field of view.

2.3 3D imaging

In this section, I present the two imaging setups on which we rely to manipulate the atomic arrays:

- The trap imaging setup. The trap array and the moving tweezer beams (see next chapter), both at 850 nm, are imaged on the trap CCD camera. We use

this image during the creation of the hologram to feedback the trap intensities to the Gerchberg-Saxton algorithm. It is also used for the automatic alignment of the moving tweezers, such that it can grab and release atoms at the exact center of the traps. This imaging system is typically used once a day.

- The atomic fluorescence imaging setup. The fluorescence light emitted at 780 nm by the trapped atoms when illuminated with the cooling light is collected and refocused on an electron-multiplying CCD camera (EMCDD). It informs us on the presence or absence of an atom in each trap at different stages of an experiment.

These setups were first described by Labuhn [2016] and I focus here on the improvements made for the imaging of three-dimensional structures. First, I present how we integrate electrically tunable lenses in our imaging systems and then how we use them to obtain different 2D-cuts of the 3D structures of traps and atomic arrays.

2.3.1 Tunable lenses

Central to the two imaging systems are a pair of aspheric lenses designed to give diffraction-limited spots of $1.0\,\mu$m at 780 and 850 nm. This resolution goes together with a small depth of field, for the same reason that a Gaussian beam with a small waist w has a small Rayleigh range $z_r = \pi w^2/\lambda \sim 4\,\mu$m. It means that when imaging a 3D structure with interatomic separation of typically $10\,\mu$m, only one atomic plane will be focused on the CCD chip and give a clear signal while all other planes will be defocused and contribute to the background noise of the image.

Optotune lenses Similarly to a camera objective, we need a way to tune which plane is focused on the CCD chip and it should be fast, reproducible and computer-controlled. This is achieved by using electrically-tunable lenses (ETLs) from the company Optotune. These lenses, of typical aperture of 10 mm, contain an optical fluid in a flexible polymer membrane whose curvature is changed through a current-controlled electromagnetic actuator. A Python script is used for the serial communication with a USB driver (Lens Driver 4) generating the control current. The change in curvature, from concave to flat to convex, is characterized by the optical power D quoted in diopters: $D\,(\mathrm{dpt}) = 1/f$ and ranges from $D = -2$ dpt (divergent lens $f = -500$ mm) to $D = +3$ dpt (convergent lens $f = 333$ mm). Upon a change of the control current, D is updated with a rise time of ~ 5 ms and a settling time of ~ 20 ms during which

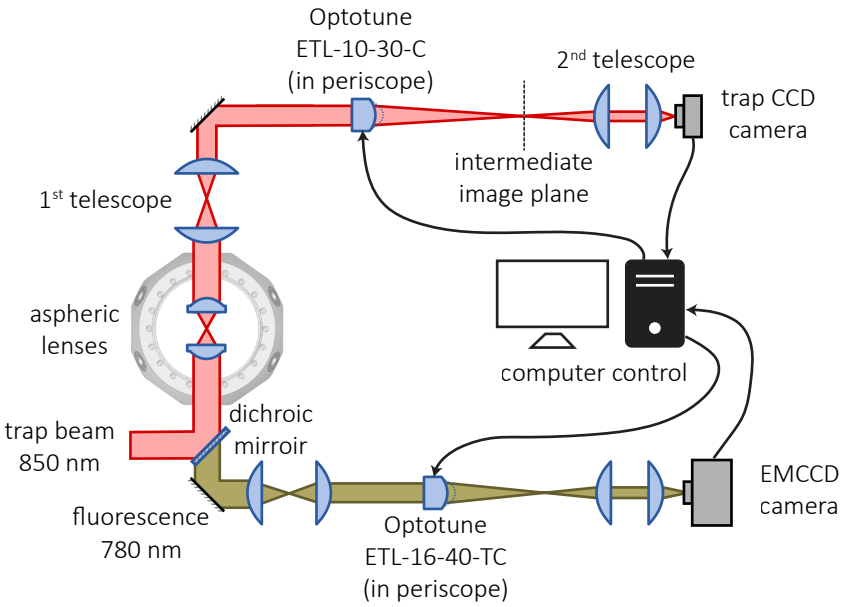

Figure 2.11: 3D imaging setups. The tunable lenses (or optotunes), controlled by computer, focus on-demand plane of the tweezers structure on the trap CCD camera (red beam) and of the atomic fluorescence on the EMCCD camera (brown beam).

Table 2.1.: Tunable lenses for the 3D imaging setups

optical setup	ETL model	Settle time (ms)	D (dpt)	aperture (mm)	1st telescope
trap imaging	ETL-10-30-C	15	-1.5 to +3.5	10	×0.5
atom imaging	ETL-16-40-TC	25	-2 to +3	16	×0.66

there are still small oscillations. We thus always wait for this time before taking an image. We ended up using two different ETL models (see Table 2.1) for the trap and atom imaging setups, as we wanted to compare their performances. To avoid beam clipping and aberrations, the ETLs need to be integrated in well designed optical setups, which I now describe.

Optical setup The imaging systems are shown in Fig. 2.11 and are basically the same for the trapping beam and the atomic fluorescence, except that we collect the latter propagating backwards compared to the trapping beam and they are separated using a dichroic mirror. The aspheric lens is first imaged on the tunable lens using a relay telescope decreasing the lens aperture by $M^{-1} \sim 0.5$. The latter results from a choice between small axial range (for large M, see 2.12) and aberrations induced by the ETL (for small M, as we would use only a large fraction of the imperfect

ETL aperture). The ETL are mounted horizontally inside periscopes to avoid coma aberrations, induced by the gravity deforming the lens. We then define a fictive intermediate image plane ~ 700 mm after the ETL, such that we obtain there an image of the focal plane of the asphere when $D = 1/0.7$ dpt. Finally, a second relay telescope rescales the image on the camera CCD chip to reach the required resolution: the fluorescence of one atom is concentrated on only a few pixels to improve the signal to noise ratio and we thus use a small fraction of the EMCCD chip, while the trap images cover the full CCD chip to optimize the alignment of the moving tweezers relatively to the traps.

The range of planes Δx, along the optical axis, which can be imaged on the cameras depends on the asphere focal length f, the first telescope magnification reducing the effective focal length by a factor M, and the ETL optical power range $\Delta D = 5$ dpt and is given by:

$$\Delta x = \Delta D \times f^2/M^2 \sim 100\,\mu\text{m}. \tag{2.12}$$

The expression is exact only if the optotune is conjugated with the asphere. Within this range, any plane can be focused on the camera by changing the optical power D, controlled from the computer. The stability of the ETL (how long does a given plane stays focused on the CCD) is limited by the sensitivity of the optical power to the temperature, which can vary due to the power consumption of the electromagnetic actuators (up to ~ 1 W). Nevertheless, we usually work with a fixed average dissipated power (as we fix the series of plane to be imaged), and after a few tens of minutes the lens has reached its equilibrium temperature and its stability is very good, comparable to the Rayleigh range over a day.

2.3.2 Trap patterns imaging

I now present some three dimensional views of increasingly complex trap structures: a single tweezers, multilayer arrays and arbitrary patterns. The tunable lens allows us to acquire series of stack images along the optical axis $\hat{x}$ with which we reconstruct the full 3D intensity distribution.

A single trap Let us start by imaging a single optical tweezers. Figure 2.12 shows 2D views of the trap at different x-positions along the optical axis (indicated in the top of each frame). The position is deduced from the ETL optical power and Eq. (2.12) with a ~ 10 % uncertainty. We observe that, as expected, the tweezers is not a Gaussian

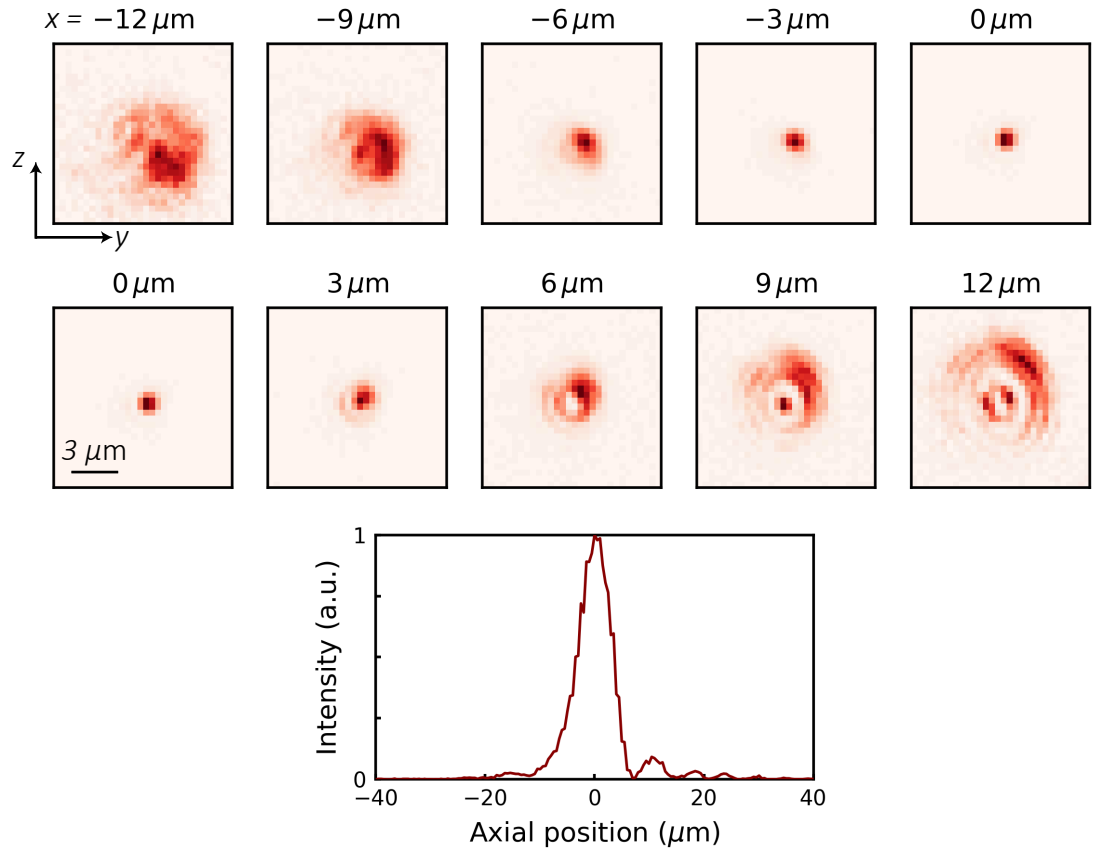

Figure 2.12: 3D views of a single trap. A single optical tweezers viewed at different positions away from the focal plane. The intensity is rescaled for each frame and is below 10 % after 5 μm. Bottom: on-axis intensity showing an Airy profile smoothened by spherical aberrations in one direction.

beam due to the diffraction on the aspherical lens. For example, we observe successive zeros of intensity along the optical axis ($y = z = 0$), as seen in the bottom plot. In the other direction, the zeros are smoothed away by the spherical aberrations. At this stage, it is difficult to know if they are already present in the focal plane, or induced by the imaging system.

Multilayer structures We now move to multi-plane structures made of two or three layers of traps. In Fig. 2.13(a), I show three layers of a triangular (or hexagonal) lattice used in the following chapter to assemble a pyrochlore structure. The layers are spaced by 25 μm, such that the tweezers focused in one layer are completely smeared out in other layers. In contrast, in Fig. 2.13(b), we have two square lattices at $\pm 2.5\,\mu$m. Because the lattices are shifted by half a lattice constant along y and z, the tweezers are well separated. It would not have been possible to overlap the two lattices at such

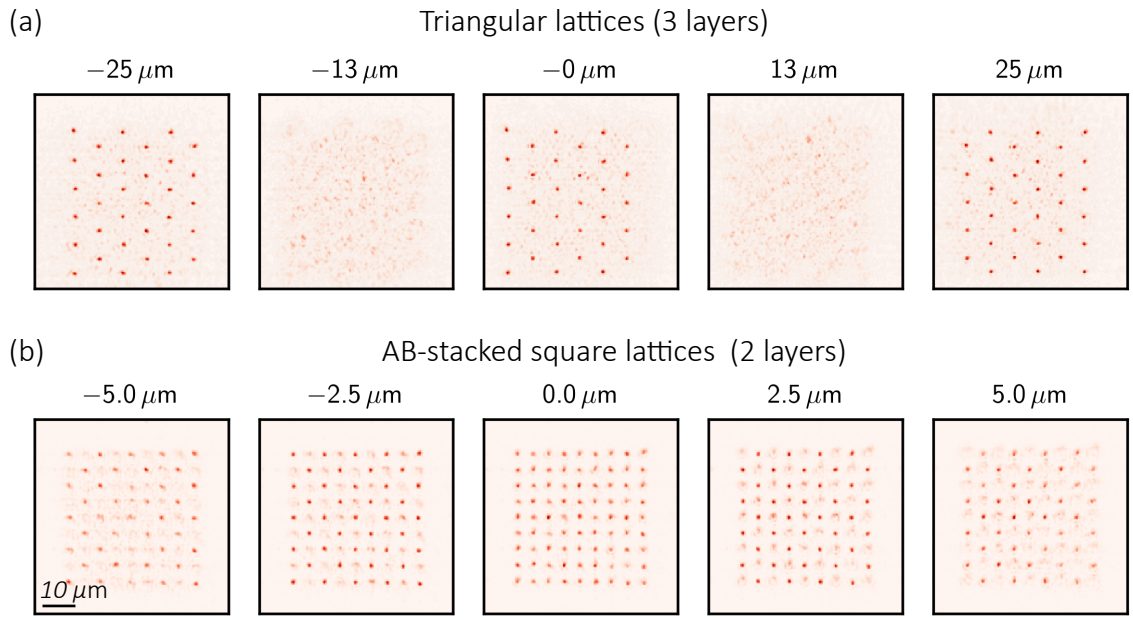

Figure 2.13: 3D view of a multilayer trap structure. Depending on the separation between 2D layers of traps, the tweezers focused on one plane are completely smeared out in the other layers (a) or only slightly defocused (b).

a close distance, comparable to the Rayleigh range of a trap, and we can distinguish the defocused tweezers of one layer in the other layer.

Arbitrary structures Finally, I show in Fig. 2.14 complex trap structures which cannot always be simply decomposed in a small number of layers. A 3D view is reconstructed using a maximum intensity projection method [Wallis *et al.*, 1989] from 200 x-images obtained with the trap CCD camera. For clarity, there is a minimum threshold under which we do not show the intensity. Except for the largest one (middle frame, 320 traps) for which we lack laser power to produce that many deep enough traps, we could load atoms in such structures and we will see in the following subsection similar images obtained from the atomic fluorescence.

2.3.3 Atomic fluorescence imaging

Single ^{87}Rb atoms are randomly loaded in the optical tweezers from the MOT and we collect the photons scattered by the atoms on the EMCCD camera. In Fig. 2.15, I show examples of 3D views reconstructed from series of 100 x-stack images covering

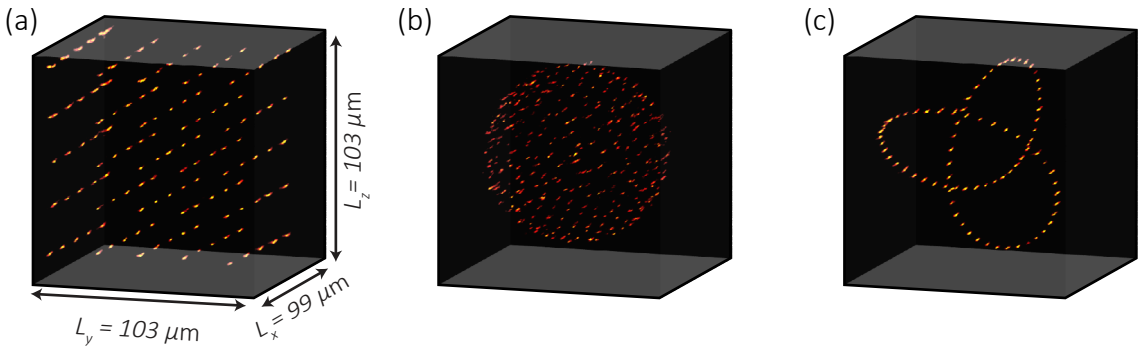

Figure 2.14: Arbitrary 3D trap patterns. Intensity reconstructions of exemplary 3D patterns obtained from a collection of x-stack images taken with the trap CCD camera. The regions of maximum intensity form (a) a $5 \times 5 \times 5$ cubic array, (b)a C_{320} fullerene-like structure, and (c) a trefoil knot. The dimensions of the images are $(\sim 100\,\mu\mathrm{m})^3$.

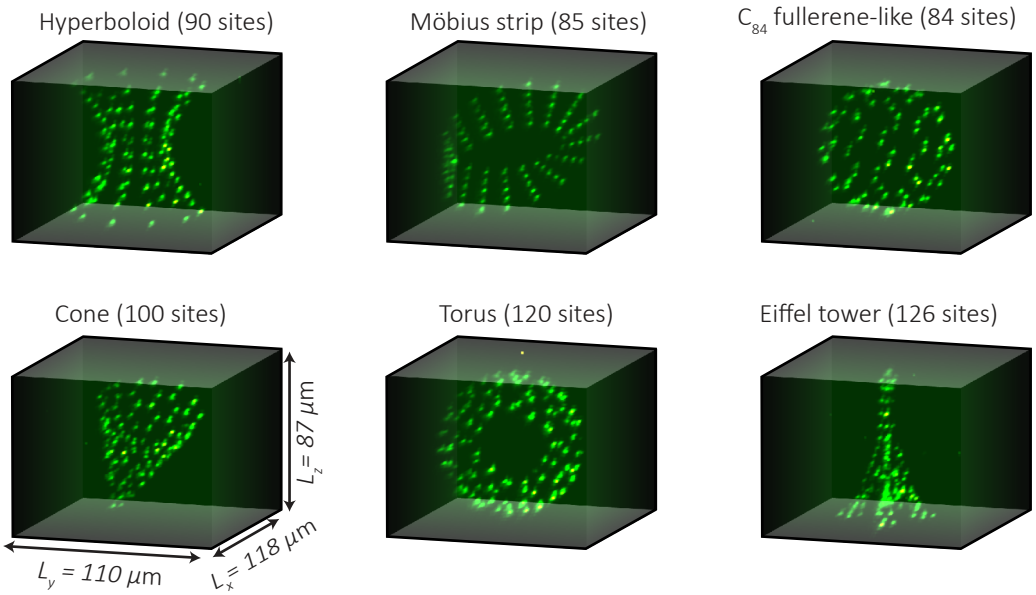

Figure 2.15: Single-atom fluorescence in 3D arrays. Maximum intensity projection reconstruction of the average fluorescence of single atoms stochastically loaded into exemplary arrays of traps. The x,y,z scan range of the fluorescence is indicated and is the same for all the 3D reconstructions. Reconstructing a 3D view takes a total exposure time of ~ 40 minutes as we aimed for a very high axial resolution and signal-to-noise ratio.

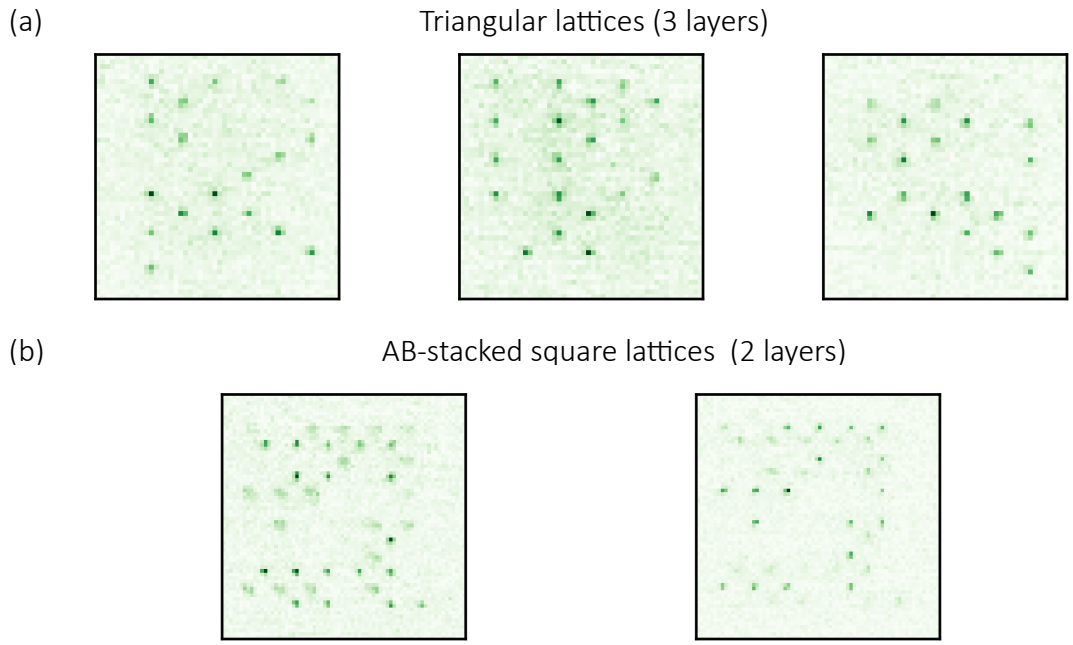

Figure 2.16: 3D view of a multilayer atomic structure. The layers are separated by 25 μm (a) or only 5 μm (b). In the latter case, we still distinguish the fluorescence coming from the other layer.

an axial range of $\sim 120\,\mu$m. For each image, we choose a long exposure time of ~ 15 s while operating the MOT to average the random loading and uncover the complete atomic structure. These reconstructed views demonstrate that we can create and image complicated 3D atomic structures, but takes too long to be used in a real experiment.

Single shot images We have seen in Section 2.1.2 that we take 3 images of the atomic structure (before assembly, after assembly, after Rydberg experiment). We need to minimize the total exposure time to keep reasonable experimental cycling time and low atom loss due to their finite lifetime. We achieve this by working with simplified 3D structures where all atoms lie in a few planes, limiting the number of images needed to reconstruct a 3D view. We also choose an optimal exposure time of 20 ms as described in Appendix A.

Figure 2.16 shows single-shot fluorescence images of atoms trapped in the multilayer structures of Fig. 2.13. The stochastic loading is responsible for the 50 % filling fraction. Similar 3D images were also reported by Nelson, Li, and Weiss [2007], there the focus of the imaging system was varied by displacing the objective lenses with a piezo-electric actuator.

2.4 Conclusion

In this chapter, we have seen how to create a *disordered* and *inert* atomic sample in one, two and three dimensions, the latter resulting from the improvement of the holographic technique and the use of electrically-tunable lenses that I presented in this chapter (see also [Barredo *et al.*, 2018]). We could trap up to ~ 60 atoms in arrays of 120 traps, this number being currently limited by the available trap laser power.

In the following chapter, I will describe how to re-arrange the atoms one by one in a well-ordered target structure. These ordered arrays will then be used in the second and third part of this thesis to implement spin models by exciting the atoms to Rydberg states, in which they strongly interact with each other. We will use the flexibility in geometry offered by the holographic technique to study these models on different patterns: 1D array with periodic boundary conditions [Labuhn *et al.*, 2016], 2D square and triangular patterns [Lienhard *et al.*, 2018] (see Chapter 4) and dimerized 1D chains (see Chapter 8). So far, we have not combined Rydberg excitations with large 3D arrays, as we lack power in the excitation lasers to illuminate them homogeneously.

Chapter 3

The atom-by-atom assembler

Contents

Despite the good scalability in trap numbers and flexibility in geometry offered by holographic optical tweezers, this has a serious drawback as only half of the tweezers are loaded with a single atom due to the collisional blockade [Schlosser *et al.*, 2001]. This filling fraction $\eta \simeq 50\%$ is a severe limit of the setup, and was so far avoided by studying few-atom systems or partially filled ones. Pushing the platform to its limit [Labuhn *et al.*, 2016; Marcuzzi *et al.*, 2017], we could obtain up to 9 atoms (in 9 traps) by continuously monitoring the trap occupancies and triggering the experiment only when all traps were loaded, at the expense of an extremely low cycling time (up to 2 minutes), increasing exponentially with the number of traps.

Several routes have been explored to increase the filling fraction by relying on physical processes such as Rydberg blockade [Ebert *et al.*, 2014] or tailored light-assisted collisions [Grünzweig *et al.*, 2010; Lester *et al.*, 2015]. These efforts resulted in a significant increase of the filling fraction, up to $\eta = 90\%$ for the latter technique, but still insufficient for preparing fully-filled arrays of tens of atoms, as the success probability $P_N = \eta^N$ is already down to 35% for $N = 10$ atoms.

Instead of relying on a physical process, we can rather engineer a feedback procedure: the initial positions of the randomly loaded atoms are recorded and the information is used to re-organize them to fill a sub-array of the initial structure. This concept dates back from more than ten years ago when Weiss *et al.* [2004] emitted the idea to re-order atoms using state-dependent translating lattices. Soon after, Dorner *et al.* [2005] proposed to implement quantum gates, through well controlled on-site collision between two atoms, by moving them between holographically generated tweezers with an independent fast moving head controlled by acousto-optic diffractors (AODs): exactly the technique we will use to order large atomic arrays. On the experimental side, two teams demonstrated, in the following year, single atom transport with an excellent efficiency. Miroshnychenko *et al.* [2006b] engineered a conveyor belt lattice and succeeded in rearranging 7 atoms in a 1D array with a single atom transport success rate of $\eta = 98\%$, while Beugnon *et al.* [2007] used a tip-tilt mirror to steer a moving tweezers in two dimensions while keeping the coherence of an atom in a superposition of electronic states. At this time, the holographic tweezers platform was not yet mature enough to combine it with single atom transport, but our recent progresses in engineering structures of up to 100 traps [Nogrette *et al.*, 2014] and a single-site addressing moveable tweezers [Labuhn *et al.*, 2014] allowed us to build an *atom assembler* machine, which I describe in this chapter.

An important preliminary question is: are these techniques of shuffling atoms scalable, at least up to hundred moves? We need to look at how fast we can displace an atom, which is set by the maximum acceleration for which the atom still follows a moving trap. A dimensional analysis gives $a_{\max} \sim w f_{\mathrm{rad}}^2 = 10^4\,\mathrm{m.s^{-2}}$, with a trap waist $w = 1\,\mu$m and a radial trapping oscillation frequency $f_{\mathrm{rad}} = 100$ kHz. By accelerating an atom during a time $\tau/2$ and decelerating it during another $\tau/2$, we can move an atom by $L = a\tau^2$. Even when choosing a very conservative acceleration $a = 10\,\mathrm{m.s^{-2}}$, three orders of magnitude smaller than the estimated limit, it still gives a displacement $L = 10\,\mu$m, typical of the inter-atomic distance in our experiments, in $\tau = 1$ ms. Hundred of atoms could then be moved in a reasonable time scale of ~ 100 ms, well below the lifetime of a single atom (~ 10 s), and we will see in this chapter how to engineer it.

The chapter is organized as follows: I present in Section 3.1 how we engineer a computer-controlled moving tweezers and use it to transfer a single atom between two traps. In Section 3.2, I describe how our home-made algorithm finds a set of individual moves re-arranging the atoms in an arbitrary 2D pattern, and discuss its performance and scalability. In Section 3.3, I explain how we serialize the 2D sorting to

many planes to create 3D atomic structures. Finally, in Section 3.4, I will compare our atom assembler to other techniques developed roughly at the same time [Kim *et al.*, 2016; Lee, Kim, and Ahn, 2016; Endres *et al.*, 2016; Kumar *et al.*, 2018]. The results discussed in this chapter have led to two publications [Barredo *et al.*, 2016, 2018].

3.1 Moving tweezers

Before this work, our group had already devised an independent *moveable* tweezers — albeit static during the experiment — to achieve single-site addressing [Labuhn, 2016]. With this tool, Labuhn *et al.* [2014] performed local rotations on a two-atom system and it was also used to prepare localized Rydberg excitations [Barredo *et al.*, 2015; Marcuzzi *et al.*, 2017]. While carrying on these experiments, we observed that the addressed atoms were ejected from their position when the moveable tweezers was not properly aligned. It made us realize that we could use this tweezers to transport an atom, and we upgraded the setup to build an automatic *moving* tweezers (MT). I first describe the MT optical and electronic setup and then detail how we align and displace the MT from trap to trap.

3.1.1 Optical and electronic setup

The current setup is shown in Fig. 3.1. It generates a single optical tweezers whose focus can be moved in three dimensions. Briefly, acousto-optical deflectors (AOD_y and AOD_z) handle the y (horizontal) and z (vertical) positions, while a tunable lens moves the tweezers along x, the optical axis. The computer controls the moving trap through an electronic setup based on Arduino boards and RF drivers.

Deflectors We use acousto-optical deflectors (AODs) instead of modulators (AOMs) for their larger deflection angle range $\Delta\theta$ (related to the velocity of the acoustic mode propagating in the material). AODs use the transverse (shear) mode propagating ~ 7 times slower than the longitudinal mode used for fast modulation. Our model is the DTSXY-400-850 from AA Opto Electronics, it is made of two crossed AODs (horizontal and vertical), each with a deflection range $\Delta\theta = 48$ mrad (for a bandwidth $\Delta\nu = 36$ MHz) and an aperture of $7.5 \times 7.5\,\mathrm{mm}^2$. The input beam is diffracted successively by the two AODs and the output is our moving tweezers. It is combined with the trapping beam coming from the SLM on a PBS (the moving tweezers and the

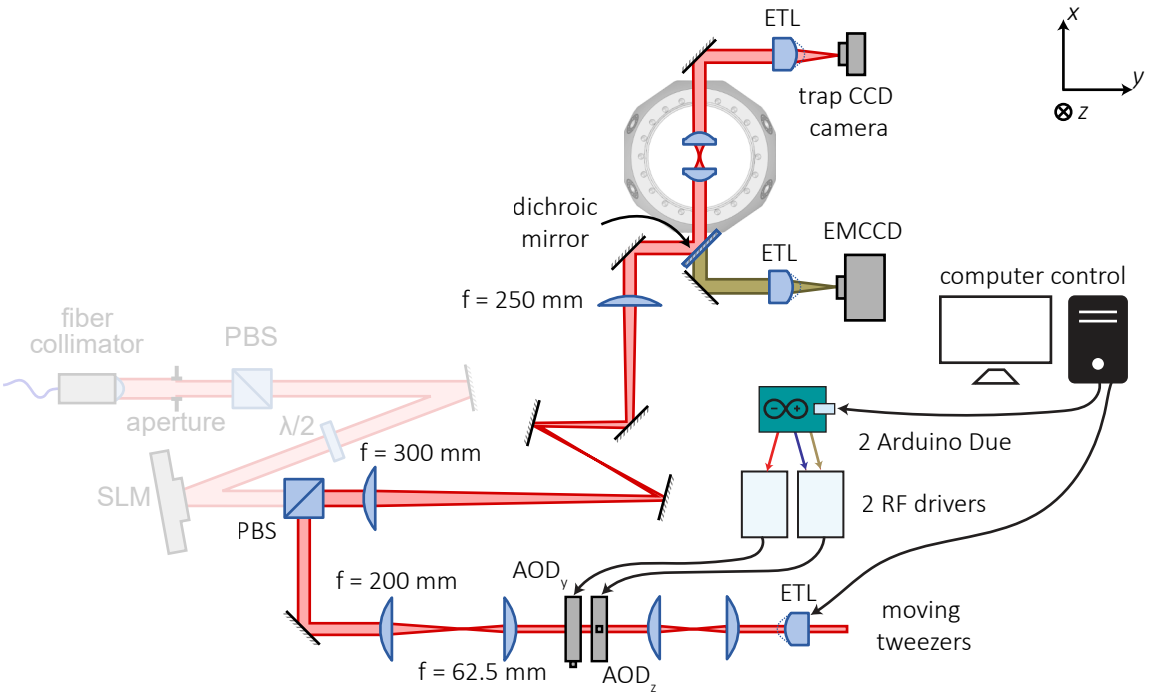

Figure 3.1: Setup of the moving tweezers. A 2d-AOD controls the moving tweezers position and intensity to grab the atom one by one and assemble the desired pattern from the disordered array.

fixed traps thus have orthogonal polarizations). Two telescopes (one being shared with the SLM beam) magnify the beam size by $M = 2.6$ and image the output pupil of the AODs on the aspheric lens. They act as relay lenses to avoid field aberrations and beam clipping on the asphere when changing the deflection angle. The resulting tweezers has a waist of $1.3\,\mu$m, measured *in situ* using a single atom and parametric heating. It is slightly bigger than the SLM traps, probably because of uncorrected aberrations. Given the focal length of the aspheric lens and the magnifying telescopes, the moving tweezers covers an area of $180 \times 180\,\mu\text{m}^2$ in the focal plane ($L_{y,z} = \Delta\theta \times f/M$).

Tunable lens Similarly to our 3D imaging system presented in Section 2.3, we use an Optotune electrically-tunable lens (model ETL-10-30-C, optical power range $\Delta D = 5$ dpt, clear aperture 10 mm) to change the convergence of the moving tweezers beam and thus the x-position of its focus. The ETL is placed before the deflectors, in a periscope to avoid gravity-induced aberrations, and a 1:1 relay telescope conjugates the ETL with the AODs. It keeps the beam size on the AODs independent of the wavefront curvature imprinted by the ETL. Given the three relay-telescope magnifications ($M = 2.6$), the tweezers focus covers a range $L_x = \Delta D \times (f/M)^2 = 70\,\mu$m. The computer

controls the ETL optical power through its USB driver via serial communication.

Electronic setup I now present the electronic setup designed to drive, from the computer, the horizontal and vertical deflectors. In short, we tune the radio-frequency (RF) signals fed to the AODs, whose diffraction angle (efficiency) is tuned by the RF frequency (power). The system, duplicated for the two AODs[1], is as follows. First, we use a Python script running on a computer to send, via USB serial communication, two 12-bits integers to an Arduino Due micro-controller board. They are then used by the board's digital-to-analog converters to create two voltage signals. These signals are sent to a home-built RF driver after amplification and filtered by a low-pass RC filter ($f_c = 5$ kHz). The latter rejects a 2 mV peak-to-peak noise at 540 kHz coming from the Arduino board. The driver generates a RF signal with frequency and amplitude controlled by the two voltages, with a response time of $10\,\mu$s, and the signal is finally fed to the AOD. We only need one AOD to control the moving tweezers intensity, so the vertical AOD is always used at maximum diffraction efficiency, and the horizontal one is varied. The system bandwidth is limited by the RC filter (which could be ~ 10 times faster) and ultimately by the RF driver response time. It is currently fast enough for the typical switching time and displacement speed of the tweezers, as described in the next subsection.

3.1.2 Moving a single atom

The elementary move of our atom assembler is shown in Fig. 3.2(a): the moving tweezers is aligned on a source trap containing a single atom and its power is gradually increased to capture the atom. It is then moved at a constant speed to an empty target trap where it releases the atom. The moves are performed only in two dimensions, meaning that the tunable lens stays at a constant optical power and only the deflectors are tuned. The 3D assembler works plane-by-plane and we just need to refocus the tweezers but we do not move the atoms in between planes, although full 3D assembly with moves between different planes could also be implemented in principle. I first describe how the MT position is calibrated relatively to the trap array and then our optimization of the transfer time.

[1] We use 2 Arduino Due boards, because we need three analog signals (horizontal and vertical position, intensity) and one board has only 2 available DAC outputs.

Automatic positioning For the computer, the MT position is set by two 12-bits integers (I will also call them MT-coordinates) and we thus need to know the coordinates of any holographically generated trap. Using the common imaging system for both SLM and MT beams, we can record the position of any tweezers (the fixed or the moving one). We first image the trap array and get the position, in terms of camera pixels, of each fixed tweezers. Then we scan the MT position for typically 7×7 values of the 12-bits integers and use an interpolating function to create a map from camera pixel to MT-coordinates. Using this map, and the recorded pixel-position of each trap, we can precisely set the MT on any of them to grab or release a single atom.

This calibration takes only a few minutes for the operator and stays accurate for days. To achieve this stability, special care has been taken to avoid temperature fluctuations of the AODs due to the dissipation of RF power. Instead of switching off the RF signals after the assembling procedure, which makes the average dissipated power dependent on the assembler workload, we let the RF signal at the nominal power and rather cut the moving tweezers with a mechanical shutter controlled from one Arduino board. In addition, we do not use the maximum diffraction efficiency of the deflectors, as we observed displacements, up to a few hundreds of nm, of the MT for too large RF powers.

Single-atom transfer To perform a move from a source trap to a target trap, the computer sends the initial and final MT-coordinates to the two Arduino boards. We have programmed the Arduinos to receive these coordinates and generate simple voltage waveforms controlling the MT depth and position [see Fig. 3.2(b)]. We first ramp up the moving beam intensity to reach a tweezers depth $U = 10$ mK, ten times as deep as a fixed trap, in a time $\tau = 300\,\mu$s. The MT having captured the atom, it then moves from one trap to another at a velocity $v = 10\,\mu\text{m.ms}^{-1}$, slow enough that the atom stays at the bottom of the MT. Finally, we release the atom from the MT in the target trap with the same $\tau = 300\,\mu$s. The DAC converter of the Due board generates a step-wise signal with a resolution of $4\,\mu$s, the signal is smoothed by the RC filter ($f_c = 5$ kHz) and the RF driver bandwidth (~ 100 kHz). It also limits the MT acceleration at the beginning and at the end of the moves.

We varied the moving tweezers depth U, switching time τ and speed v to find their experimental optimal values, as shown in Fig. 3.2(c-e). We could reach a probability of successful transfer of 99.3 %, limited by the probability of a collision with the background gas during the transport (atom lifetime of ~ 10 s). Despite choosing a very simple profile of the voltage ramps, we achieve a perfect transport of the atom

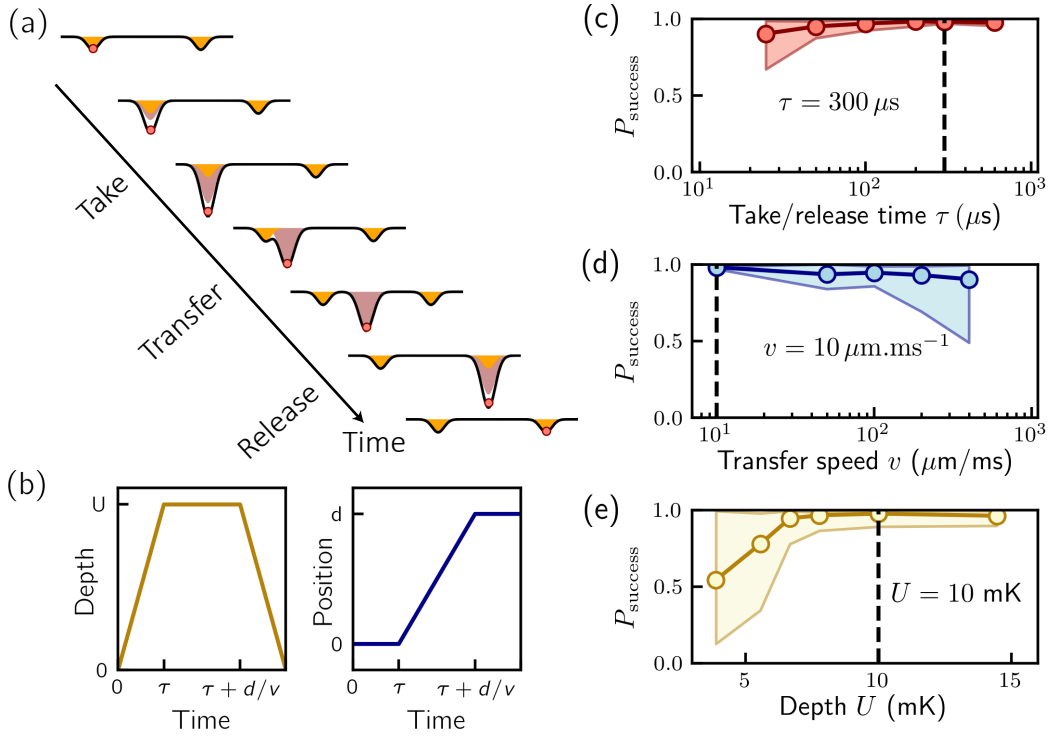

Figure 3.2: Moving a single atom. (a) Sketch of the moving tweezers grabbing an atom from one trap to release it in another one. (b) Temporal dependence of the moving tweezers depth and position. (c-e) Optimization of the transfer success through three parameters: the take/release time (c), the transfer speed (d) and the tweezers depth (e). The experiment is performed on 8 pairs of traps separated by 4 μm and the transfer success is measured on each one. The circles represent the average success rate. The efficiency is not the same on each pair of traps, and we also show the minimum and maximum efficiencies with the shaded areas. For the final parameters (dashed lines), the transfer is robust (small variations amongst the pairs) and reaches an efficiency of 99.3%.

in a short timescale of 1 ms. I expect that much faster displacements are possible, as discussed in the introduction of this chapter, and might be needed to assemble thousands of atoms with a single moving tweezers; improvements could come from an optimized ramp profile. Nevertheless, the current speed and transfer success rate are more than enough to now tackle the assembly of many tens of atoms.

3.2 2D assembler

We have seen in the previous section how to deterministically move a single atom between two traps. In this section, we will see how we combine many moves to

re-arrange an initially disordered 2D atomic arrays into a fully-filled sub-array of size N. The atom assembly procedure is shown in Fig. 3.3 and is as follows:

- We start from an array of $2N$ traps, which contains the target array as a subset, and load it from the magneto-optical trap. The loading of the array is monitored and we trigger the experiment as soon as at least N traps are filled with single atoms.

- The MOT is then switched off to stop the loading and a fluorescence image is acquired to record the initial positions of the atoms.

- After analysis of the image, an algorithm (see below) computes in real time a list of individual atom moves that can rearrange the initial configuration into the desired 2D pattern.

- This list is then sent to the Arduino microcontrollers via serial communication. The Arduino program converts it into a series of voltage sweeps performing sequentially all the single atom transfers, as explained previously. The two Arduino boards, controlling the vertical and horizontal AODs, are kept synchronized by triggering each other.

- Finally, after the rearrangement operation is completed, another fluorescence image is acquired to reveal the new positions of the atoms in the array and confirm the successful assembly.

From the moment the experiment is triggered, it takes ~ 100 ms to achieve the preparation of an array ready for a Rydberg experiment. We characterize the preparation efficiency using the filling fraction η of the target array or the probability $p_N \simeq \eta^N$ to obtain the fully-filled array. We typically reach a very high filling fraction $\eta = 98.5\,\%$, such that even for $N = 50$ atoms, a perfect array is obtained with a probability $p_N = 46\,\%$ at a 3 Hz rate. As we take a fluorescence image of the assembled structure before the Rydberg experiment, we can discard any experimental run with imperfect atomic arrays.

In the following, I explain our algorithm finding a set of moves ordering the array and then the performance and scalability of our 2D atom assembler.

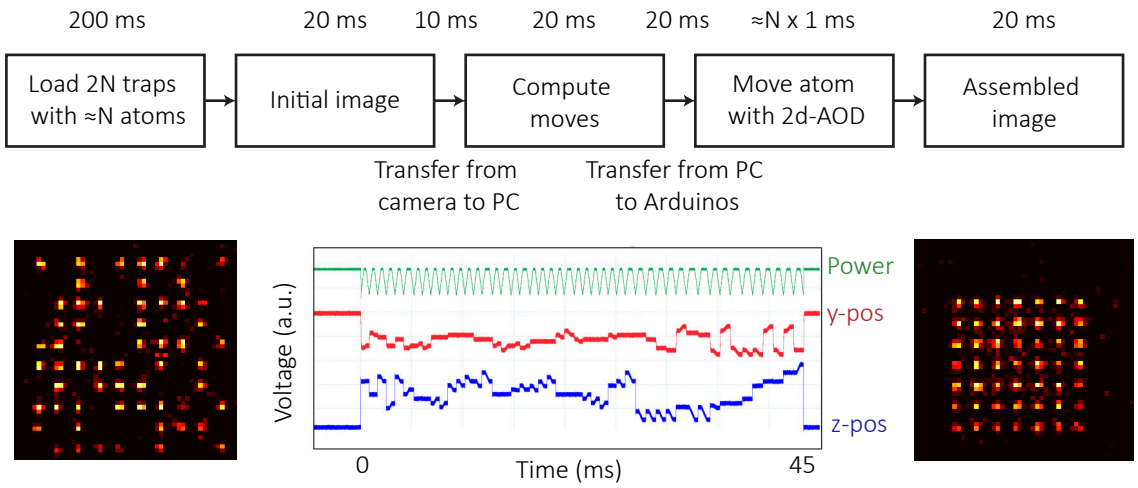

Figure 3.3: Array assembly step by step. The different steps of the assembler are shown together with their timings. The bottom images show an initially disordered 10×10 array reassembled on a fully filled 7×7 subset. The three traces are the voltages controlling the moving tweezers intensity, horizontal and vertical positions.

3.2.1 Sorting algorithm

We developed an algorithm that finds a set of individual moves which reorders the atomic pattern. We did not seek to make it optimal, in terms of assembly time for example, as it is a non-trivial task reminiscent of the traveling salesman problem and we work in a real-time experiment where we need to find a solution much faster than the atom lifetime. The algorithm works as follows:

- We first generate two lists, of size $\sim N$, representing the traps filled with an atom and the target traps.
- We then compute a list $\mathcal{L}$ of the N^2 distances between each pair of traps from the two lists and order them by increasing distance.
- $\mathcal{L}$ starts by pairs of traps at zero distance: a target trap is already filled with an atom and no action is necessary.
- $\mathcal{L}$ continues with nearest neighbor traps, and then with further and further distant pair of traps, and after checking that neither the source nor the target trap were previously encountered by the algorithm, we add them to a list of moves to perform.

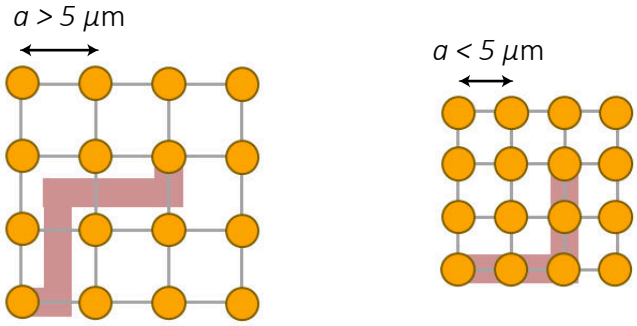

Figure 3.4: Two types of moves. If the nearest neighbor distance in the array is large enough (typically, $a > 5\,\mu$m), we move the tweezers directly from the source to the target, passing between adjacent atom rows ("type-1" moves). Otherwise, the atoms are moved along the lattice links ("type-2" moves).

- The algorithm ends when N pair of traps have been identified and the remaining unused atoms, if any, are discarded by moving them away from the trap array.

This algorithm is not optimal because it first selects the shortest moves, which can afterward force very long ones, instead of searching for a global solution. Nevertheless, it is fast (~ 1 ms) and versatile as it makes no assumption on the underlying array geometry.

Moving through a maze The problem is complicated by the fact that we cannot move the MT over or close to traps already containing an atom as it would expel them. We thus need a way to move the atom through the maze of other atoms. We first simplify the problem by working with trap patterns described by Bravais lattices, defined by two unit vectors u_1 and u_2 and lattice constants a and b. An exemplary square pattern is shown in Fig. 3.4. There are two situations: either the MT can move in between two rows or columns without expelling atoms located there, or the structure is too tight for the MT. Experimentally, we find that the lattice constant needs to be larger than $5\,\mu$m for the MT to go through.

In the first case, we simply perform 'type-1' moves by 'slaloming' between the traps. Each move, represented so far by the source and target trap indexes, are extended to a list of intermediate coordinates to guide the moving tweezers. If the array lattice constants are too small, we restrict the MT displacements to the grid defined by the Bravais lattice ('type-2' moves). We then need to ensure that no filled trap is on the way between the source S and target trap T. If an obstacle O (a filled trap) is present,

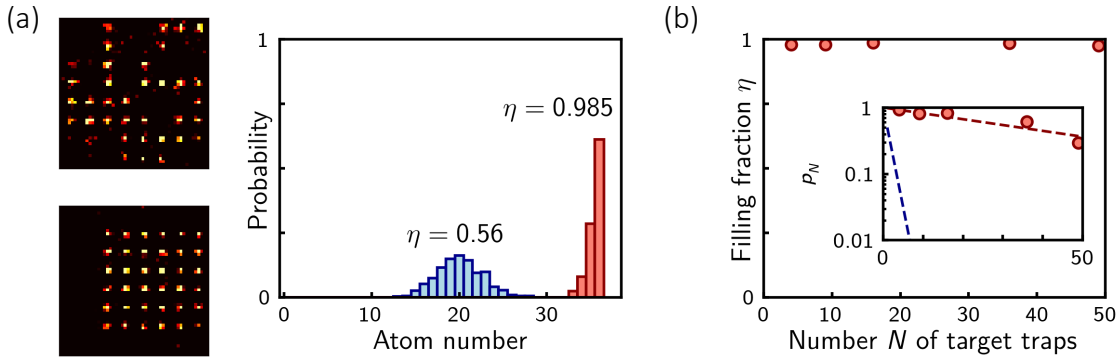

Figure 3.5: Performance. (a) Images of the initial and final configurations for a target 6×6 square array and distribution of the number of atoms in the target array before (blue) and after (red) sorting for 500 repetitions of the experiment. We measure a filling fraction $\eta = 98.5\,\%$, and defect-free arrays are obtained with a probability $p_N = 61$ %. (b) Evolution of η and p_N as a function of the number of traps N in the sorted array. The dashed blue line shows the result $p_N = 0.5^N$ corresponding to random loading and the red line shows the scaling 0.98^N.

we replace the move $S \to T$ by the two moves $O \to T$ and $S \to O$, in this order. In practice, we first run the sorting algorithm, ignoring that some moves will not be directly possible, and then run a procedure that eliminates all obstacles as just described. This way, we always find a solution even if the additional moves make it even less optimal. We will soon see two examples of target arrays, where our heuristic solution is almost optimal in one case, while it could be improved very significantly in the other.

3.2.2 Performance and scalability

We have seen the engineering details of the atom assembler and I now present its performance and scalability with the number of target traps N.

Performance Analyzing 500 repetitions of the experiment for a 6×6 square target array [Fig. 3.5(a)], we measure a filling fraction $\eta = 98.5$ %, limited by background gas collisions during the rearrangement. It is slightly worse than the success rate of a single move (99.3 %), also limited by the atom lifetime, because it takes longer to perform all the required moves. In Fig. 3.5(b), we see that η stays roughly constant for increasingly large target arrays, up to $N = 50$. We could not create more than 100 traps (so 50 atoms) due to limited laser power at the time we performed the experiment. It

demonstrates experimentally the scalability of the moving tweezers technique. These performances are better than initially presented in our 2016 paper [Barredo *et al.*, 2016], as in the meantime we improved the full procedure.

In the inset, I show the probability $p_N \simeq \eta^N$ to obtain a *defect-free* array of N atoms. Even if the assembler sometimes fails, we use the assembled image obtained before performing a Rydberg experiment to post-select runs with a perfect atomic sample. The probability p_N simply decreases the effective experimental cycling rate. Without the assembler (blue dashed line, $\eta = 0.5$), we could perform experiments up to $N = 9$ atoms, above which the cycling time was too slow; with the current performance of the assembler we would reach in principle the same cycling time for $N \simeq 300$ atoms!

Scalability Previously, I have shown the successful assembly of arrays of up to $N = 50$ atoms, I now discuss how the assembler would perform for even larger arrays, assuming that we had enough laser power to generate them. The figure of merit is again the filling fraction η of a target array of size N. As the success rate of an individual move does not depend on the number of traps, $1 - \eta$ is mainly set by the ratio of the assembling time over the finite atom lifetime (~ 10 s).

The assembling time first depends on the initial filling fraction of the lattice. In our case, it is 50 % and there is in average $N/2$ atoms to be re-arranged. When type-1 moves are possible, the assembling time directly scales as $N/2 \times 1$ ms, where 1 ms is the typical move duration. For type-2 moves, the scaling can be slightly worse, as some filled traps will be in the way of a move, thus requiring additional displacements. We numerically study the scaling in this case for two target geometries on the same square array: a 'checkerboard' pattern, where one every second trap is selected, and a 'compact' pattern. The results are shown in Fig. 3.6. While, in the first case, the scaling remains linear with only a small increase in the prefactor (0.5 to 0.85), it becomes worse for the compact geometry and increases as $N^{1.4}$. This can be understood qualitatively as follows: our naive algorithm first fills the perimeter of the target array, thus blocking the inner empty traps which cannot be filled with a direct transfer anymore. A significant fraction of the atoms needs to be moved several times. It illustrates the limit of our simple and versatile algorithm, which works for arbitrary target arrays on any Bravais lattice, but fails to obtain an optimal solution. For the specific case of a compact target array, a better solution is easily implemented and was already proposed by Weiss *et al.* [2004]: we first balance the number of atoms in each row and compact them.

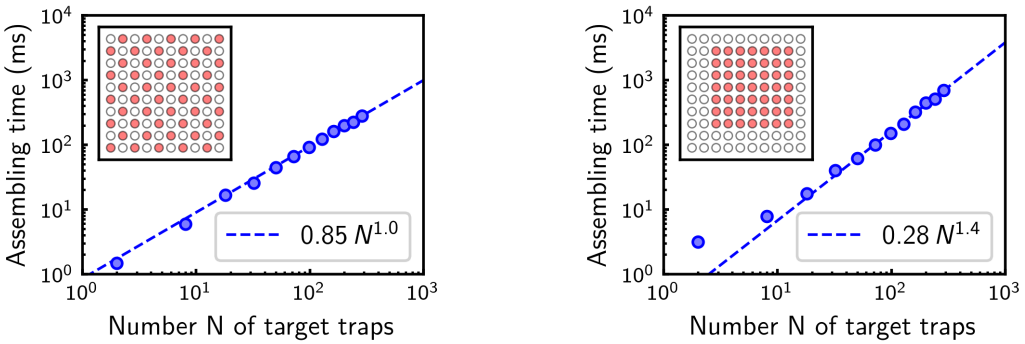

Figure 3.6: Scalability. Simulated assembling time using type-2 moves. (Left): For a "checkerboard" target in a square lattice, the assembly time scales linearly with N (dashed line). (B): For a "compact" target, it scales approximately as $N^{1.4}$.

Finally, we see from Fig. 3.6 that assembling $N = 100$ atoms is possible, while maintaining the assembling time below 0.1 s and thus the loss probability below 1 %. It could be improved by optimizing the displacement speed, by boosting the initial filling fraction using, e.g., tailored light-assisted collisions [Grünzweig *et al.*, 2010; Lester *et al.*, 2015], or by increasing the atom lifetime in a cryogenic setup. Concerning laser power, each trap currently requires 5 mW, which could be decreased by getting closer to the atomic resonance or achieving smaller waists of the tweezers.

Conclusion I end this section about the 2D atom assembler by showing, in Fig. 3.7, a gallery of 2D trap arrays with arbitrary, user-defined geometries relevant for quantum simulation (e.g., 1D chains, ladders, or lattices with square, triangular, honeycomb, or kagome structures). Neighboring traps are separated by distances $3 < a < 6\,\mu$m, for which interactions in the MHz range can be achieved by exciting the atoms to Rydberg states, as we will see in the next chapters. We also upgraded the assembler to move atoms along circular patterns (using concentric reservoir and target arrays) and devised a technique to inject multiple atoms in the same site (see also [Miroshnychenko *et al.*, 2006a; Serwane *et al.*, 2011]), but were lacking a measurement method circumventing the light-assisted inelastic losses to prove its success. In the next section, I will show how to extend the technique to the assembly of multilayer patterns. In practice, the assembler is very robust, with performance stable over the last year, and it requires only minor maintenance, i.e., checking the power and polarization of the MT beam. We have also seen that the calibration of the MT position was achieved in only a few minutes, once per day. All this makes the atom sorting machine a user-friendly and reliable tool to work with.

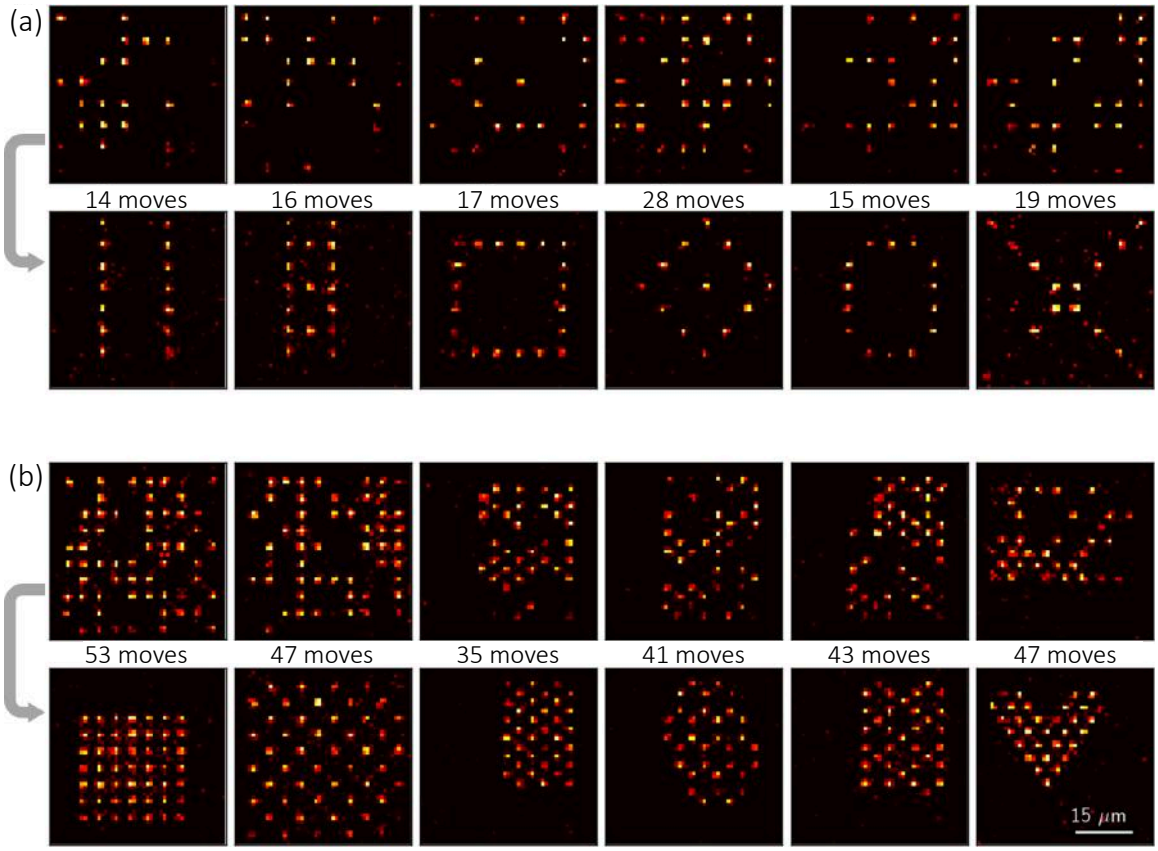

Figure 3.7: Gallery of assembled patterns. Arbitrary, user-defined 2D arrays (bottom images) are obtained from the initial, random configurations (top images). All images are single shots. (a) Type-1 moves were used; (b) type-2 moves were used. The number of elementary moves needed to achieve the sorting are indicated. The figure is adapted from Barredo *et al.* [2016].

3.3 3D assembler

We have introduced the possibility to focus the moving tweezers on different planes using a tunable lens (ETL). Combining it with the deflectors (AODs), we thus can realize arbitrary trajectories in three dimensions. Nevertheless, it would require to synchronize the ETL and the AODs, and a slightly more involved algorithm to avoid trajectories bringing the moving tweezers too close to other filled traps, noting that the axial extent of the tweezers is much longer than the radial one. As a first step to extend the assembler machine to arbitrary 3D patterns, we therefore restrict the problem to structures made of a few layers (up to 4), that we sequentially image and assemble independently. I first explore the minimum spacing between two layers such that the moving tweezers do not affect the second plane while we re-arrange the first

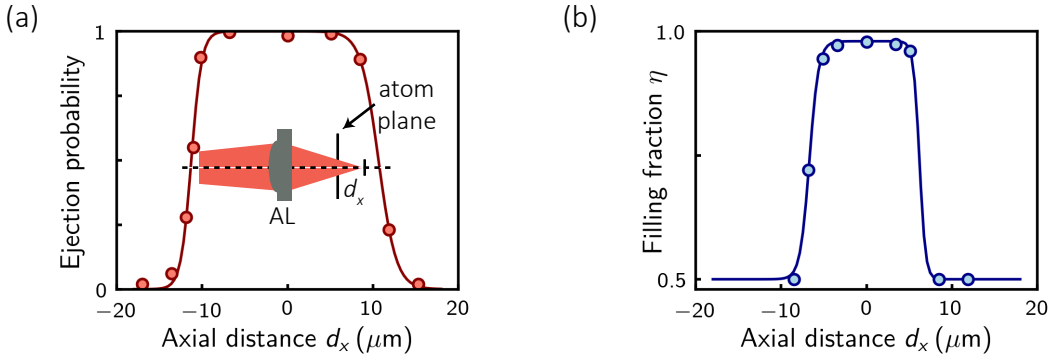

Figure 3.8: Tweezers axial range. Moving tweezers efficiency as a function of the axial distance between the MT focus and the plane where the atoms lie for an experiment where: (a) we remove all the atoms from a 46-trap array and (b) we assemble a 4×4 sub-array. The lines are guides to the eye.

one. Then, I will detail our procedure to prepare fully-loaded 3D arrays of up to 72 atoms.

3.3.1 Limit in compactness

We have seen in Section 2.3.2 that a single trap was quite elongated along the axial direction, with a typical extent given by the Rayleigh length $z_R \sim 5\,\mu$m. It is much longer than the radial resolution of a trap ($1\,\mu$m) and gives a stronger constraint to avoid getting too close to other traps.

We have explored, in two experiments, the range of axial distance d_x for which the MT still affects atoms. We use a simple planar structure of traps and set the moving tweezers focus at various axial positions d_x. First, having programmed the moving tweezers to remove all atoms, we observe that the probability to eject them remains high for $|d_x| < 15\,\mu$m [Fig. 3.8(a)]. Then, asking the computer to assemble a 4×4 sub-array, we see in Fig. 3.8(b) that the filling fraction remains optimal for a smaller range $|d_x| < 5\,\mu$m.

We understand these results in the following way: when the moving tweezers focus is too far from that of a fixed trap, the MT is still able to grab the atom for a large range as it is much deeper, but it cannot release the atom in the target trap. It gives us two constraints: (i) the MT focus has to coincide with the layer to better than $5\,\mu$m in the axial direction, which is easily achieved using our trap imaging system, and (ii) there should be no traps in a $\pm 15\,\mu$m range in front and behind the MT focus as it would eject atoms trapped there. We can still re-arrange two atomic arrays close

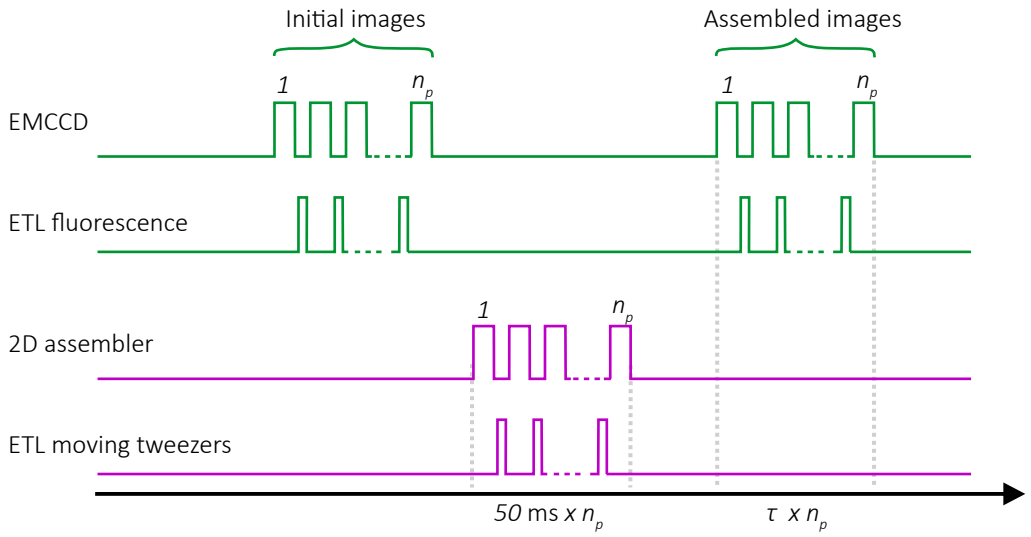

Figure 3.9: Plane by plane assembly. Time control sequence of the experiment. We start the experiment by recording, sequentially, an image for each target plane with an exposure time τ. The analysis of the resulting n_p images reveals the initial position of the atoms in the traps. The 2D atom assembler, in combination with a tunable lens, arranges the atoms plane by plane. Finally, a new set of sequential images is collected to capture the result of the 3D assembly.

to each other if their traps do not overlap. The limited compactness of 3D structures could be slightly improved by working with a higher NA aspheric lens, which would give a shorter axial extent of the moving tweezers.

3.3.2 Serial 2D assembly

I now explain the plane-by-plane assembly of 3D structures. We start by creating a 3D trap array which can be decomposed in several planes normal to x. In each plane we generate approximately twice the number of traps we need to load, such that we easily load enough atoms to assemble the target structure.

The sequence to create fully loaded patterns (see Fig. 3.9) starts by loading the MOT and monitoring the atoms entering and leaving the traps by sequentially taking a picture for each plane. We trigger the assembler as soon as there are, in each plane, enough atoms to fully assemble it. We then freeze the loading by dispersing the MOT cloud, and record the initial positions of the atoms by another series of x-stack images. Each plane is processed independently following the procedure described in the previous section, changing the x-position of the MT to go from one layer to another.

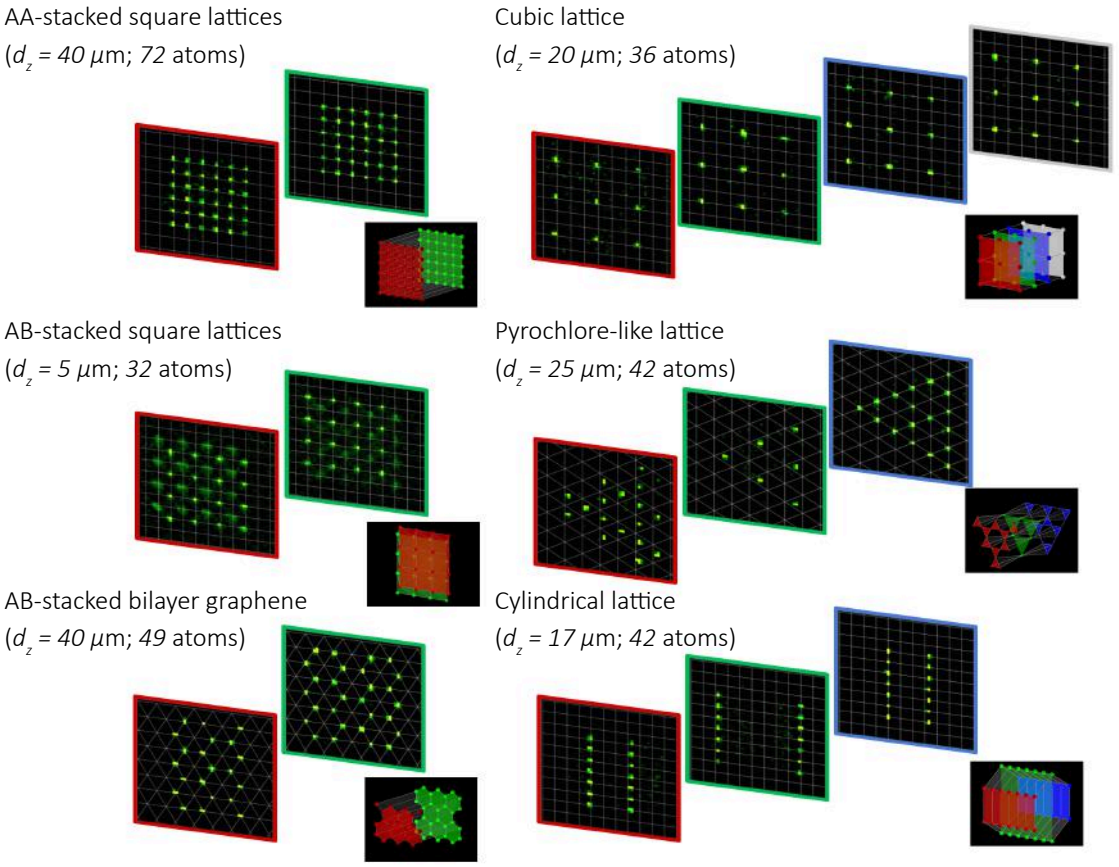

Figure 3.10: Gallery of assembled 3D patterns. Fully loaded arrays with various geometries in three dimensions. All images are single shots. The models of the 3D configurations are shown for clarity; the various colors of the frame around the images encode successive atomic planes.

Finally, we detect the final 3D configuration with another series of x-stack images.

Figure 3.10 shows a gallery of fully-loaded 3D atomic arrays with up to 72 atoms. The selected structures include simple cubic lattices, bilayers with a square or graphene-like [Castro Neto *et al.*, 2009] arrangements, lattices with inherent geometrical frustration such as pyrochlore [Bramwell and Gingras, 2001], or lattices with cylindrical symmetry, suitable, e.g., to study quantum Hall physics with neutral atoms [Lacki *et al.*, 2016]. The minimum interlayer separation we can achieve depends on the type of underlying geometry. This is illustrated with the AB-stacked square lattices with a layer separation $d_x = 5\,\mu$m. There, sites corresponding to the second layer are displaced by half the lattice spacing. Since traps belonging to neighboring layers do not have the same y-z coordinates, there is no limitation for the minimum interlayer distance that we can produce. In both images we can observe a defocused fluorescence

at inter-site positions due to atoms trapped in the neighboring layer.

Despite the additional complexity of working successively on different planes, our 3D assembler remains highly efficient: we reach filling fractions of typically 95 %. This measured efficiency is again limited by the lifetime of the atoms in the traps, and thus depends on the duration of the experimental sequence, which varies with the number of planes. In the images shown in Fig. 3.10, we used an exposure $\tau = 60$ ms, which could be decreased to 20 ms (see Appendix A) and the experiment takes ~ 700 ms for the largest structure made of $n_p = 4$ planes. The repetition rate of the experiment is then ~ 1 Hz, slightly smaller than the 3 Hz rate when we work in 2D.

3.4 Other approaches

Over the last two years, several other groups have demonstrated assemblies of atoms in one, two and three dimensions with techniques rather different than our. In this section, I give a brief overview of these other approaches and compare their respective advantages and limitations.

Reconfigurable 1D trap array Simultaneously to our publication of the 2D assembler machine [Barredo *et al.*, 2016], the group of Prof. Mikhail Lukin at Havard presented their own work on a reconfigurable linear chain of optical tweezers [Endres *et al.*, 2016] (see also the perspective article of Regal [2016]). Whereas we generate a static arrays of tweezers with a fixed hologram on a spatial light modulator, they create a 1D array of traps using an acousto-optical deflector (the same model that we used to engineer a single moving tweezers) fed with an RF signal composed of many (up to 100) different frequency components. Each tone diffracts the input beam to create an independent tweezers, and after optimizing the relative amplitude and phase of each frequency tone, they could obtain homogeneous 1D array of traps (see the Supplemental Material of Endres *et al.* [2016]). It is very similar to the Gerchberg-Saxton algorithm that we used to equalize the trap depths, and indeed one can view the deflector as a 1D SLM with a very fast response time.

After taking an image of the initially disordered array, they switch off the unoccupied traps and shift the occupied ones to form arbitrary 1D arrangements of atoms. The technique is very efficient and fast as all atoms are moved together in 3 ms, in contrast to our solution where we re-order the array atom by atom, each move taking 1 ms. Nevertheless, this solution is limited to 1D structures as using a second crossed AOD would not allow arbitrary 2D geometries and individual control of all traps, but rather

many copies of a 1D array. In future experiments, it might be possible to combine the flexibility of static arrays of holographic tweezers generated with a SLM and AODs creating multiple traps moving in parallel along a single line or column to re-arrange large atomic arrays faster.

Moving holograms The group led by Prof. Jaewook Ahn at KAIST in Korea have been working on an elegant approach of the problem by updating in real-time the hologram displayed on the SLM [Kim *et al.*, 2016; Lee, Kim, and Ahn, 2016]. They use the ability of SLMs to update the displayed hologram at a video rate of 60 Hz, thus dynamically changing the diffraction pattern. Usually, changing the SLM image leads to important flicker of the trap intensities causing severe atom losses. They overcome this problem using a special kind of hologram allowing flicker-free displacement of traps. Then, once the initial positions of the atoms are known, a set of 30 holograms are sequentially displayed on the SLM, reshuffling the atom in a target arrangement. The team first demonstrated an assembly of a 2×2 atomic array in 2D [Kim *et al.*, 2016] and then extented it to 3D movements (while keeping the initial and final structures planar) [Lee, Kim, and Ahn, 2016].

After these first demonstrations, limited in number of traps N by the decreasing diffraction efficiency of their holograms with N and the fact that they had to prepare in advance all the re-ordering videos[2], they improved their technique by using a modified version of the Gerchberg-Saxton algorithm for the computation of the holograms, whose efficiency remains constant with N, and by performing in real time the calculation on a graphic card. The team also reported a specific algorithm to find a good set of atomic trajectories avoiding collisions [Lee, Kim, and Ahn, 2017] and performed experiments on arrays of up to 20 atoms [Kim *et al.*, 2018]. The current limits of this approach are the slower re-arrangement of atoms, a video taking ~ 150 ms (due to the slow 60 Hz refresh rate of the SLM), and the necessity to repeat the procedure up to 9 times to achieve a 98 % filling fraction.

State-dependent optical lattices Finally, following the proposal of Weiss *et al.* [2004], two teams demonstrated state-dependent optical lattices re-ordering atoms: the group led by Prof. Dieter Meschede and Andrea Alberti reported on the arbitrary arrangement of 4 atoms in a short $0.43\,\mu$m-period 1D lattice [Robens *et al.*, 2017], while the group of Prof. David Weiss has shown 50 atoms arranged in two or three

[2]For $N = 9$ atoms, there are $2^9 = 512$ possibilities, each of them requires to save a 30-frame video with a 800×800 resolution (the SLM one), such that in total it takes 10 GB of memory, scaling exponentially with N.

layers of a large 4.9 μm-period 3D lattice [Kumar *et al.*, 2018].

The experimental procedure is similar for both cases and I detail it for the 3D sorting. The scheme relies on:

- individual-site addressing using two crossed dipole traps allowing to change the hyperfine level of a single ground-state atom with a microwave π-pulse [Wang *et al.*, 2015, 2016].
- spin-dependent translating lattices, where only atoms in one hyperfine level are shifted from one site to another.

After recording a set of images to obtain a 3D reconstruction of the lattice site occupancies [Nelson, Li, and Weiss, 2007], atoms to be moved are first transferred to the hyperfine state sensitive to the moving lattice, then shifted and finally pumped back in the original state. The operation is repeated until the target array is assembled. In addition, the atoms can be cooled to the ground-state of the lattice either with Raman sideband cooling or using projection sideband cooling [Li *et al.*, 2012], such that almost all the entropy can be removed from the lattice.

This technique allows to prepare quite compact 3D arrays of atoms using optical lattices instead of tweezers, at the expense of more restricted geometries than offered by holography. Another limit is the weaker efficiency of single atom moves, which requires to repeat the entire procedure up to 3 times to increase the filling fraction.

3.5 Conclusion

In this chapter, I presented the development of our atom assembler machine preparing quickly and efficiently fully-filled 3D atomic arrays of up to 72 atoms and counting. I first explained how a single moving tweezers, engineered with two deflectors and a tunable lens, could transfer an atom from one trap to another. Then, I have shown how to combine many such moves to re-order a 2D atomic array with an efficiency of 98.5 % per site, limited only by the finite lifetime of the atom. Finally, we scaled up the technique to the third dimension by repeated successively the 2D procedure on different layers of a 3D pattern.

The recent developments of atom sorting devices solved the long-standing issue of the stochastic loading of atoms in microscopic dipole traps. So far, only ultracold atoms in optical lattices could provide samples with high filling fraction using the quantum phase transition to a Mott insulator [Greiner *et al.*, 2012; Sherson *et al.*, 2010;

Bakr *et al.*, 2010]. The optical tweezers platform is now able to produce perfectly filled samples with more flexibility in geometries and at an experimental cycling rate higher by almost two orders of magnitude. In addition it can be adapted to any particles which can be trapped in optical tweezers but for which Bose or Fermi degeneracy have not yet been reached.

Finally, the atom assembler technique does not only open bright perspectives for experiments with Rydberg atoms as we will demonstrate in the two other parts of this thesis, but can also be applied to cold polar molecules [Yao *et al.*, 2012; Peter *et al.*, 2012], atoms coupled to a nanoscale cavity [Thompson *et al.*, 2013a], or used for metrology [Kómár *et al.*, 2016]. Combined with Raman sideband cooling [Kaufman, Lester, and Regal, 2012; Thompson *et al.*, 2013b; Yu *et al.*, 2018], it becomes a powerful tool to engineer entangling gates through collisions [Jaksch *et al.*, 1999; Kaufman *et al.*, 2012] or study cold chemistry by inserting two atoms in the same tweezers and building a molecule [Liu *et al.*, 2018].

Part II.

Ising magnets

Chapter 4

From van der Waals blockade to studies of Ising models

Contents

In the introductory chapter, we motivated the development of a quantum simulator based on Rydberg atoms by the study of many-body phenomena, and in particular of quantum magnetism. We are interested in realizing spin-1/2 Hamiltonians, where particles are fixed and only their spins play a role by interacting together and with an external magnetic **B**-field . One way to obtain such an Hamiltonian with cold atoms is to drive them, with lasers, from their electronic ground-state level $|g\rangle = |\downarrow\rangle$ to a Rydberg level $|r\rangle = |\uparrow\rangle$, where they experience strong van der Waals interactions. If the experiment is performed fast enough ($< 10\,\mu$s), the atomic motion ($< 1\,\mu$m) can be neglected, and the laser-driven frozen Rydberg gas is then well described by the following spin-1/2 Hamiltonian:

$$H = \frac{\hbar\Omega}{2}\sum_i \sigma_i^x - \hbar\delta\sum_i n_i + \sum_{i<j}\frac{C_6}{R_{ij}^6} n_i n_j. \tag{4.1}$$

where we use the Pauli operators $\sigma^{x,y,z}$ acting on the spin-1/2 particles and $n_i = (1+\sigma_i^z)/2$ is 1 for a Rydberg atom and 0 otherwise. The first term corresponds to the coherent drive with a Rabi frequency Ω of the $|g\rangle \leftrightarrow |r\rangle$ transition, the second to the laser detuning δ from the atomic transition. Their experimental implementation will be described in Chapter 5. The third term is the van der Waals shift $V = C_6/R^6$ given by the dipole-dipole interaction for two atoms, separated by a distance R, in the

same Rydberg state. The coefficient $C_6 \propto (n^\star)^{11}$ depends on the choice of Rydberg state $|r\rangle$ and increases dramatically with the principal quantum number $n^\star$.

Phase diagram: critical region and ordered states The connection between Eq. 4.1 and quantum magnetism is made explicit by considering the first two terms as playing the role of, respectively, the transverse and longitudinal components of an effective magnetic **B**-field, while the van der Waals interaction gives rise to an Ising coupling, with a long-range extent. A generic Ω-δ phase diagram resulting from this Hamiltonian is represented schematically in Fig. 4.1 for a repulsive interaction energy ($C_6 > 0$).

Along the $\Omega = 0$ line, the eigenstates are classical configurations where each atom is either in $|g\rangle$ or in $|r\rangle$. At negative detuning, the system energy is minimized when all the atoms are in $|g\rangle$, which we call a paramagnet. At positive detuning and for a non-interacting system ($C_6 = 0$), we have the opposite situation with all atoms in $|r\rangle$. The origin $\mathcal{O}$ is thus a critical point around which there is a jump of the Rydberg fraction $f_r = N_r/N$, where N_r is the number of atoms in $|r\rangle$ in a system of N particles. The interaction between Rydberg atoms then stabilizes ordered phases, where the number and position of Rydberg atoms result from the competition between the second and third term of the Hamiltonian. The Néel state, shown in Fig. 4.1, where nearest-neighbor Rydberg excitations are avoided, is one of the possible ordered states. In fact, the $1/R^6$ extent of the van der Waals interaction leads to a devil's staircase of classical ground states [Bak and Bruinsma, 1982]. For increasing laser drive $\Omega > 0$, the transverse field tends to destroy the order favored by the van der Waals term by creating and removing Rydberg excitations. At some point, the system undergoes a quantum phase transition (QPT) to a paramagnet.

Quench experiments A first experimental approach to the study of this phase diagram is to perform quenches of the transverse magnetic field. Starting with all atoms initially in $|g\rangle$, the excitation laser is suddenly switched on resonantly on the transition ($\delta = 0$), and we observe the subsequent dynamics of the system. First experiments of this kind were carried out on disordered cold atomic cloud [Tong *et al.*, 2004; Singer *et al.*, 2004; Vogt *et al.*, 2006; Heidemann *et al.*, 2007], where one can measure the final value of the Rydberg fraction f_r. It was reported than when driving high-$n^\star$ Rydberg states, van der Waals interactions prevent f_r from reaching unity, and the observed saturation depends strongly on the C_6 coefficient. Pictorially, this saturation can be explained by considering the Rydberg blockade effect 'preventing' two excitations to be located closer than a typical Rydberg blockade

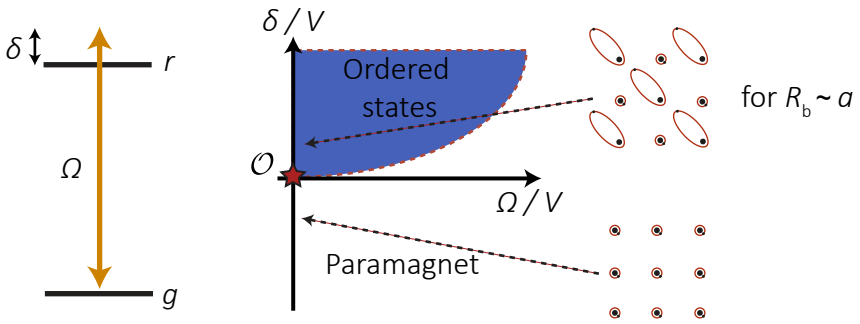

Figure 4.1: Phase diagram of laser-driven Rydberg ensembles. Left: a two-level atom is driven from the ground-state $|g\rangle$ to the Rydberg level $|r\rangle$. The coupling strength is Ω and the detuning from the transition is δ. Middle: Phase diagram in the $\Omega - \delta$ plane for a repulsive van der Waals shift between atoms ($C_6 > 0$). Above the critical point $\mathcal{O} = (0, 0)$, there is a crystalline phase where the position of the Rydberg excitations are strongly correlated to minimize the interaction energy. Outside this region, the laser drive dominates the interaction and the many-body ground-state is a paramagnet. In this chapter, we will explore the properties of the system close to the critical point $\mathcal{O}$. This figure is adapted from Weimer *et al.* [2008].

distance $R_\mathrm{b} = (C_6/\hbar\Omega)^{1/6}$, emerging naturally from Eq. 4.1. It corresponds to the interatomic distance at which the energy cost of having two Rydberg atoms is equal to the driving strength. Consequently, in a dense atomic cloud with many particles per Rydberg blockade volume, we expect:

$$f_r \simeq \frac{1}{\frac{4}{3}\pi R_\mathrm{b}^3 \rho} = \left(\frac{9}{16\pi^2}\frac{\hbar\Omega}{C_6\rho^2}\right)^{1/2} \tag{4.2}$$

where ρ is the atomic density. This naive estimate was refined by Weimer *et al.* [2008], which first pointed out that a quench experiment was probing the critical region $\delta = 0$ where a second order quantum phase transition separates the paramagnetic and ordered phase, and then used a mean-field theory to obtain the critical exponent $\nu = 2/5$ instead of $1/2$ in the above equation for a 3D cloud. The scaling law was confirmed experimentally by Löw *et al.* [2009].

In addition to a saturation of f_r, one expects many-body correlations between the position of the Rydberg excitations to arise from the quench dynamics [Robicheaux and Hernández, 2005], as we can only excite configurations where the Rydberg atoms are further away than R_b (all other configurations, violating the Rydberg blockade effect, being energetically decoupled). The observation of such correlations was made possible in an atomic cloud by using an ion imaging technique [Schwarzkopf *et al.*,

2013], in optical lattice experiments using a quantum gas microscope [Schauß *et al.*, 2012], and later using our optical tweezers platform [Labuhn *et al.*, 2016]. I will briefly review the latter experiment in this chapter. More recently, Kim *et al.* [2018] also presented a study of the thermalization dynamics following a quench in the Rydberg quantum simulator developed at KAIST, in Korea.

Adiabatic ground-state preparation Instead of quenching the system, which leads to a complex dynamics due to the beating of many excited states, one can also try to prepare adiabatically the ordered phases of the phase diagram [Pohl, Demler, and Lukin, 2010; Schachenmayer *et al.*, 2010; van Bijnen *et al.*, 2011]. Starting with the atomic system in a paramagnetic phase with no Rydberg excitation $|G\rangle = \prod |g\rangle$, a smooth evolution of the laser parameters $\{\Omega(t), \delta(t)\}$ brings the system in an ordered phase after crossing a quantum phase transition (QPT), provided there exists a gap between the ground state and the first excited ones.

This approach was first followed by Schauß *et al.* [2015] who reported the observation of many-body states with a few (2 to 4) Rydberg excitations with strongly correlated positions on a lattice containing ~ 100 atoms. The reason for such a small Rydberg fraction lies in the size of the Rydberg blockade distance, much larger than the interatomic separation ($R_\mathrm{b} \gg a$), fixed by the use of optical lattices. In this case, the ground-state properties depend on the system boundaries rather than on the underlying lattice geometry, which is smeared out by the large R_b.

With the development of Rydberg quantum simulators using optical tweezers with arbitrary spacings, it is now possible to explore the regime $R_\mathrm{b} \sim a$. During the course of this thesis, the group of Prof. Mickhail Lukin reported the preparation, on a one-dimensional chain, of ordered states with a large Rydberg fraction f_r from 1/4 to 1/2 by tunning R_b from $\sim 4\,a$ to a [Bernien *et al.*, 2017]. More recently, they studied the quantum phase transition between the paramagnetic state and these ordered phases [Keesling *et al.*, 2018]. In our group, we focused on the regime $R_\mathrm{b} \sim a$, that maps to a nearest-neighbor Ising model, where the atomic positions play a major role; for example in a triangular or kagome geometry it can lead to geometrical frustration. We attempted the adiabatic preparation of the anti-ferromagnetic ground state in a 1D chain, and a 2D square or triangular lattice [Lienhard *et al.*, 2018]. Finally, let us note the simultaneous work performed in the group of Prof. Waseem Bakr at Princeton University, where they demonstrated that it was possible to also reach the regime $R_\mathrm{b} \sim a$ in an optical lattice experiment by working with low-lying Rydberg states, so that R_b is small [Guardado-Sanchez *et al.*, 2018].

Outline In this chapter, I first briefly present, in Section 4.1, the results of our quench experiments already described in the thesis of Henning Labuhn [2016]. They motivated a detailed study of the mapping of the dipole-dipole interaction between Rydberg atoms to a simple van der Waals shift that will be presented in Chapter 6. In Section 4.2, I propose a general classification of recent experimental and theoretical studies of the different ordered phases emerging from Eq. 4.1, based on the Rydberg blockade distance. Finally, in Section 4.3, I present our attempt to prepare the antiferromagnetic ground state of the nearest-neighbor Ising model by adiabatic sweeps. I focus on experiments performed on a square lattice, and on how the preparation efficiency is yet limited by the coherence time in our experiment. This motivated a quantitative analysis of all dephasing mechanisms described in Chapter 5.

A more detailed analysis of the space- and time-dependent growth of correlations during the adiabatic preparation, for a wider range of geometries, will be given in the thesis of Vincent Lienhard. The experiments reviewed in this chapter have been published in Labuhn *et al.* [2016] and Lienhard *et al.* [2018].

4.1 Quench experiments

Our Rydberg experiment starts with an assembled atomic array all initialized in the electronic ground-state $|g\rangle$ by optical pumping, which is the paramagnetic phase described above. The excitation lasers, giving rise to a coherent coupling with a Rabi frequency Ω, are described in Chapter 5. A quench experiment consists in switching on suddenly the coherent drive for a variable time τ. Recall that the optical tweezers are off during a Rydberg experiment, and that they are switched back on at the end to recapture atoms in $|g\rangle$ and repel the ones in $|r\rangle$. Each experimental run ends with a fluorescence image from which we obtain the site-resolved measurement $n_i = 0$ (atom in $|g\rangle$ and recaptured) or 1 (atom in $|r\rangle$ and lost). We use this measurement to reconstruct the macroscopic Rydberg fraction $f_r = \sum\langle n_i\rangle/N$ and the density-density correlation map $C(i,j) = \langle n_i n_j\rangle - \langle n_i\rangle\langle n_j\rangle$. The latter can also be expressed in the form $g^{(2)}(i,j) = \langle n_i n_j\rangle/\langle n_i\rangle\langle n_j\rangle$, more popular in the quantum optics community. We will follow the evolution of these observables after a quench.

The experiments are performed on a system of typical size L and interatomic spacing a, and we can thus identify three main regimes:

- $R_\mathrm{b} \ll a$: the Rydberg blockade distance does not extend from one atom to the other. The atoms are thus independent and we have a collection of identical and

isolated two-level systems. The quench dynamics is a simple Rabi oscillation at a frequency Ω: the Rydberg fraction f_r oscillates between 0 and 1, and the pair-correlation function remains at the uncorrelated value $g^{(2)}(i,j) = 1$.

- $R_\mathrm{b} \gg L$: the Rydberg blockade volume encompasses the whole atomic ensemble. There can be only one Rydberg excitation, which is delocalized over all N atoms. The system thus restricts to only two states $|G\rangle = \prod_i |g_i\rangle$ and $|W\rangle = \frac{1}{\sqrt{N}} \sum_i |g \dots r_i \dots g\rangle$, coupled to each other with a collectively enhanced frequency $\sqrt{N}\Omega$. The quench dynamics is again a Rabi oscillation of this effective two-level system: f_r oscillates between 0 and $1/N$ and $g^{(2)}(i,j) = 0$.

- $a \lesssim R_\mathrm{b} \lesssim L$: the system cannot be restricted to an effective two-level problem. The quench projects the initial state $|G\rangle$ on a superposition of many eigenstates with different energies. The beating of incommensurate eigenfrequencies causes the oscillation of f_r to relax[1] towards a steady-state value between $1/N$ and 1 depending on the exact value of R_b, as discussed earlier. In the Rydberg blockade picture, we expect the correlation function to be close to a step function $g^{(2)}(|i-j| < R_\mathrm{b}/a) = 0$ and $g^{(2)}(|i-j| > R_\mathrm{b}/a) = 1$.

Experiment I now present one experiment performed in the third regime. Figure 4.2(a) shows the atomic array, a quasi one-dimensional chain, and the Rydberg blockade volume of radius $R_\mathrm{b} = 4.3\,a$ following the choice of Rydberg state $|r\rangle = \left|79D_{3/2}\right\rangle$ ($C_6/h \simeq -6 \times 10^3$ GHz.μm^6) and Rabi frequency $\Omega/(2\pi) = 1.0$ MHz. The oblong form of the blockade volume is due to the anisotropy of the van der Waals interaction for Rydberg $D_{3/2}$ states (see Chapter 6). The chain has periodic boundary conditions such that we roughly expect the average density to be uniform and the pair-correlation to depend only on $k = i - j$ (even if, strictly, the shape of the blockade volume breaks the translational invariance).

For increasing excitation time τ, we observe, in Fig. 4.2(b), an initial oscillation of f_r, which then reaches a steady-state value close to the naive estimate a/R_b. This is simply the adaptation of Eq. 4.2 to a one-dimensional system, where the blockade sphere is replaced by a 1D hard-rod. Alongside the oscillation of f_r, strong correlations between Rydberg atoms appear, as seen in Fig. 4.2(c). It roughly resembles the step function discussed above: at short-distance $k < R_\mathrm{b}/a$ there is a suppressed probability to find two Rydberg atoms, while at large distances $k \gg R_\mathrm{b}/a$ two atoms

[1] This 'thermalization' of a closed quantum system is a commonly encountered property of interacting ensembles [Deutsch, 1991].

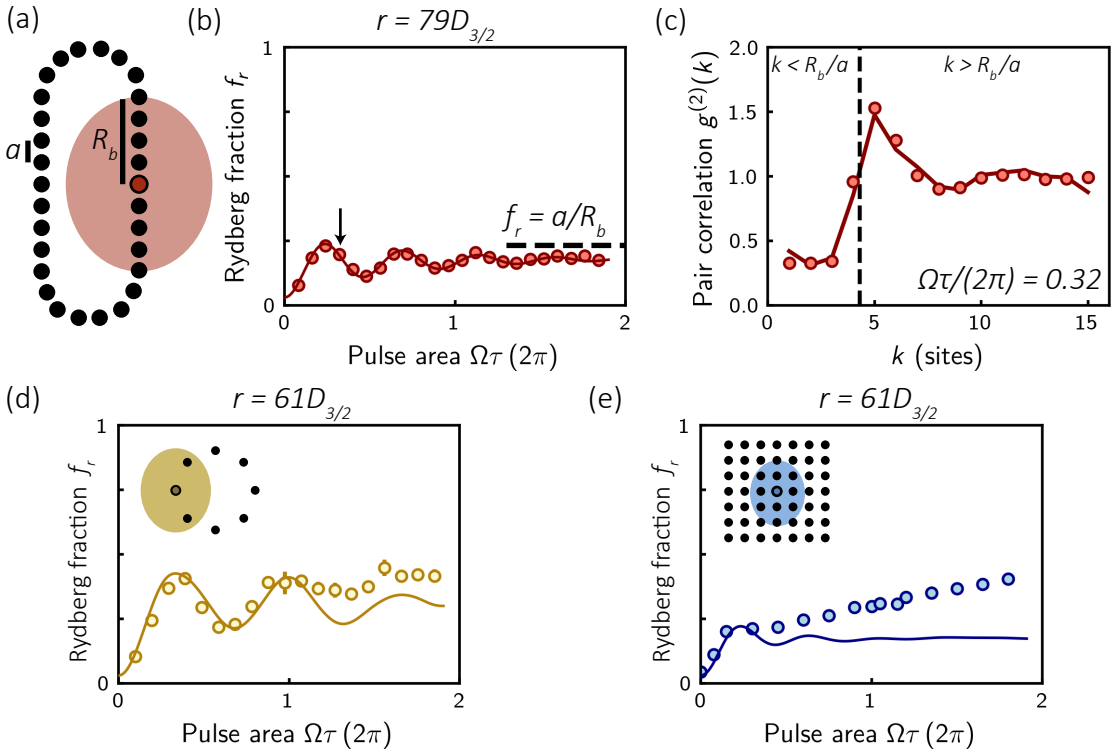

Figure 4.2: Dynamics following a quantum quench. (a) Quasi-1D chain with periodic boundary conditions. The Rydberg blockade radius is $R_\mathrm{b} = 4.3\,a$, with a the interatomic spacing. (b) Evolution of the Rydberg fraction f_r with the pulse area $\Omega\tau$. The dashed line indicates the maximal filling of the system with hard-rods of length R_b. The arrow indicates the time at which we calculate the pair correlation shown in (c). The blockade effect prevents the excitation of the second atom at a distance $k\,a < R_\mathrm{b}$. At larger separations, the correlator oscillates around the asymptotic value 1, corresponding to uncorrelated sites. (d,e) Quench dynamics using a different Rydberg state and geometry of the atomic array. Here, we observe a discrepancy between the experimental data and the prediction of the spin-1/2 model. We will search for the origin of the deviations in Chapter 6 and find better experimental parameters.

are uncorrelated. Interestingly, there is an enhanced probability to have two Rydberg atoms at $k \simeq R_\mathrm{b}/a$, also observed in Schauß *et al.* [2012]. This property can be explained using an hard-rod model [Ates and Lesanovsky, 2012; Petrosyan, Höning, and Fleischhauer, 2013].

The results presented in Fig. 4.2(b,c) are in very good agreement with ab-initio numerical simulations, without adjustable parameters and taking into account detection errors, carried out by Tommaso Macrì. However, for experiments performed on another set of geometry and Rydberg state $|r\rangle = \left|61D_{3/2}\right\rangle$, we observe a clear deviation with

the theory [see Fig. 4.2(d,e)]. The increased Rydberg fraction above the theoretical model indicates a failure of the Rydberg blockade effect and motivated a detailed analysis to explain and solve this problem that will be presented in Chapter 6.

4.2 Devil's staircase of ordered states

The phase diagram shown in Fig. 4.1 is only a rough description of the rich variety of ordered states that arise from the long-range Ising coupling of Eq. 4.1. I now give a more detailed description of these ordered phases, classifying them as a function of the size of the typical Rydberg blockade radius. I relate them to recent experimental and theoretical studies.

Let us start by noticing that the Hamiltonian (4.1), and so the phase diagram, are symmetric under the operation $|g\rangle \leftrightarrow |r\rangle$ and $\delta \leftrightarrow -\delta + \sum_{i<j} V_{ij}/N$. There is thus a second critical point $\mathcal{O}_2$ at $(\Omega, \delta) = (0, \sum_{i<j} V_{ij}/N)$ where the physics is the same as around $\mathcal{O}$, except that ground-state atoms are replaced by Rydberg excitations and vice-versa. Along the classical axis ($\Omega = 0$), the many-body ground-state Rydberg fraction rises from $f_r = 0$ at $\mathcal{O}$ to $f_r = 1$ at $\mathcal{O}_2$. In between the two critical points, there are many stable phases with a fixed number of Rydberg excitations whose positions are strongly correlated to minimize the interaction energy.

Because the van der Waals potential decreases quickly as $1/R^6$, the interaction is always dominated by the nearest-neighbor couplings. The largest crystalline phase in Fig. 4.3 is thus usually the one with a Rydberg fraction $f_r = 1/2$ with one excitation every other site: the Néel state (note that this is not true for frustrated geometries for example). Other phases, with $0 < f_r < 1/2$, are located very close to the critical point $\mathcal{O}$ where longer-ranged couplings play a role. It is possible to explore experimentally these small phases using the extreme tunability of a Rydberg quantum simulator, since the interaction strength $V \propto n^{11}/R^6$ can be varied by more than 6 orders of magnitude by choosing principal quantum numbers $n = 50 - 100$ and interatomic spacings $R = 3 - 10\,\mu$m (by changing the holographic array of tweezers[2]). In contrast, the laser drive Ω and detuning δ have stronger constraints and are typically on the order of 1 MHz: much higher coupling strengths Ω are not yet available in current experimental apparatus, while lower energy scales require longer experiments, that are precluded by the motion of the atoms, as long as Rydberg atoms are not trapped.

Tuning the van der Waals strength, at fixed δ and Ω, consists in zooming in and

[2]For optical lattice experiments, the spacing is much smaller and fixed to $a = \lambda/2 \sim 0.5\,\mu$m by the trap laser wavelength λ.

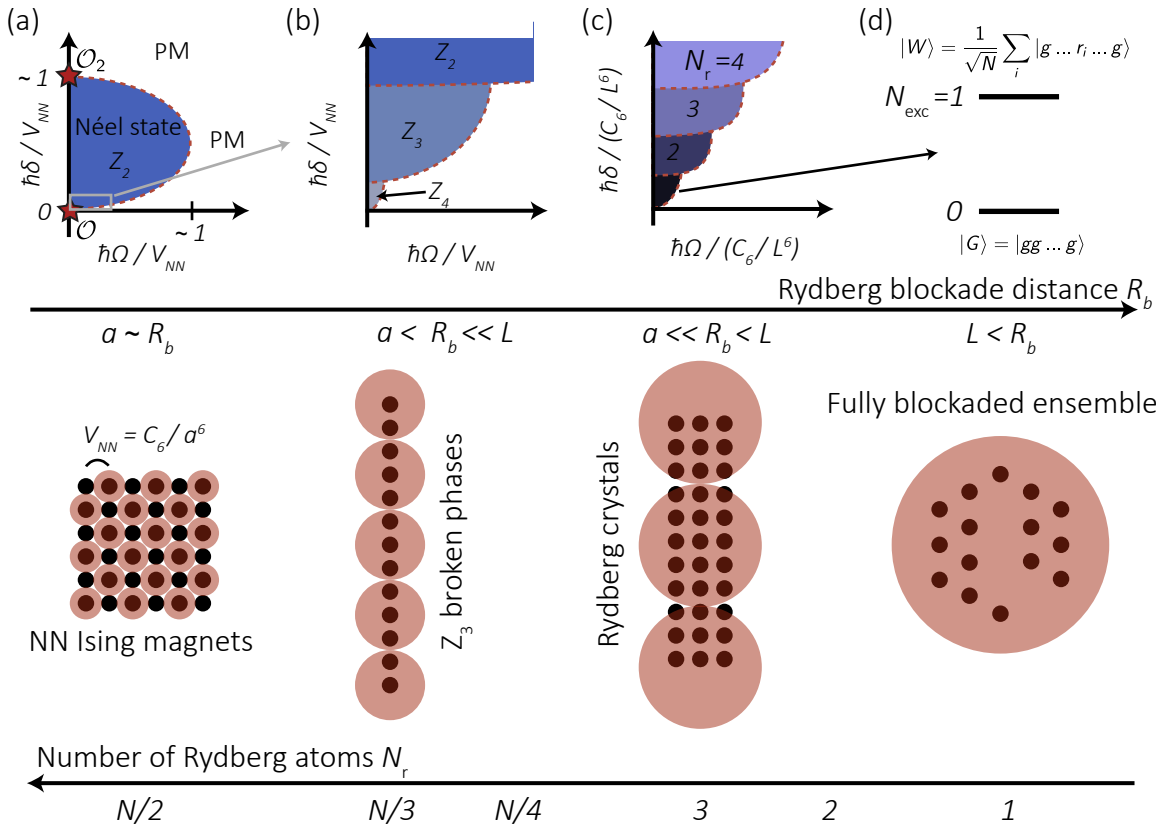

Figure 4.3: Tuning the Rydberg blockade volume. The top schemes represent the relevant area of the phase diagram, located closer and closer to the critical point $\mathcal{O}$, which can be studied by increasing the Rydberg blockade distance R_b. The bottom schemes illustrate a particular experimental realization: (a) nearest-neighbor Ising magnet implemented by Lienhard *et al.* [2018], (b) $\mathbb{Z}_3$ ordered state studied by Bernien *et al.* [2017], (c) crystal of three Rydberg excitations from Schauß *et al.* [2015] and (d) a fully blockaded system realized by Labuhn *et al.* [2016].

out of the critical point $\mathcal{O}$ and thus allows to observe extremely small features close to $\mathcal{O}$. In the following, I classify the different ordered states by using an effective Rydberg blockade distance $R_\mathrm{b} = \left[C_6/(h \times 1\,\mathrm{MHz})\right]^{1/6}$, going all the way from a regime of independent atoms ($R_\mathrm{b} \ll a$) to a fully blockaded system ($R_\mathrm{b} \gg L$).

Paramagnetic phase: $R_\mathrm{b} \ll a$. The interaction energy between two neighboring atoms is smaller than the laser drive Ω or detuning δ. The atoms are thus basically independent and act as free spin-1/2 particles under the influence of a magnetic field defined by $\mathbf{B} \propto (\Omega, 0, \delta)$: our system is a paramagnet (PM).

Nearest-neighbor interaction: $R_\mathrm{b} \sim a$. The interaction energy between neighboring sites $V_\mathrm{NN} = C_6/a^6$ is now sufficiently large for an interaction-dominated crystalline phase to be experimentally observable close to the critical point $\mathcal{O}$. The next-nearest neighbor term[3] $V_\mathrm{NNN} = V_\mathrm{NN}/64$ is usually neglected. In this approximation, Eq. 4.1 maps to the nearest-neighbor Ising model. The many-body ground state depends on the exact arrangement of lattice sites: For a simple atomic array geometry, as a 1D chain or a 2D square lattice, the many-body ground state is the Néel state, but this is not the case for a triangular lattice where geometrical frustration plays a role. Experiments performed in this regime have been reported by Bernien *et al.* [2017] and Keesling *et al.* [2018] (1D chain), Guardado-Sanchez *et al.* [2018] (2D square lattice) and Lienhard *et al.* [2018] (1D chain, 2D square and triangular lattices). I will present our results obtained on the 2D square lattice in the last section of this chapter. Figure 4.3(a) shows the phase diagram where the second critical point at $\delta = V$ is visible.

Z_n phases: $a < R_\mathrm{b} \ll L$. The Rydberg blockade radius now extends over a few lattice sites, but remains smaller than the system size. This regime has been studied in 1D by the Harvard team [Bernien *et al.*, 2017; Keesling *et al.*, 2018]. When R_b increases from $\sim a$ to $\sim 2a$, one has to consider the next-nearest neighbor interaction term V_NNN. The latter stabilizes, close to the critical point $\mathcal{O}$, a $\mathbb{Z}_3$ ordered state with one Rydberg excitation every 3 lattice sites. For increasing interaction strength, the long-range extent of the van der Waals interaction leads to a succession of $\mathbb{Z}_k$ phases with a Rydberg fraction $f_r = 1/k$, as shown by zooming close to $\mathcal{O}$ in Fig. 4.3(b). On an infinite-size system, there would be a never-ending succession of such phases, increasingly closer to the critical point. Weimer and Büchler [2010] performed a theoretical study of these phases for the particular case of a 1D chain. More generally, for larger Rydberg blockade volume, we expect the ground state to become less dependent on the exact lattice geometry.

Crystals with few Rydberg atoms: $a \ll R_\mathrm{b} < L$. In a finite-size system of N atoms, the sequence of $\mathbb{Z}_k$ phases is halted by the finite resolution of f_r, which can only change by step of $1/N$. For very large blockade distance, comparable to the system size L, there are crystalline phases hosting only a small number of Rydberg excitations N_r, as shown in Fig. 4.3(c). The relevant interaction energy is now $V_L = C_6/L^6$.

[3] Considering here a 1D chain. For a 2D square lattice, we would have $V_\mathrm{NNN} = V_\mathrm{NN}/8$ along the diagonal.

Closer to the critical point, there is a phase with a single Rydberg excitation (see next paragraph). The following phase is a crystal with two maximally separated Rydberg excitations: in a 1D chain they lie at the two extreme sites. It continues with crystals containing $N_r = 3, 4, \ldots$ Rydberg excitations. This regime has been studied by Schauß *et al.* [2015], who observed onsets of these crystalline states containing only a few Rydberg atoms. The difficulty of preparing adiabatically such states has been discussed by Petrosyan, Mølmer, and Fleischhauer [2016].

Fully blockaded systems : $L < R_\mathrm{b}$. Finally, the Rydberg blockade volume is larger than the size of the system, which is thus fully blockaded. We are left with only two accessible states: $|G\rangle$ and $|W\rangle$. While, from the point of view of many-body physics, the theoretical description of a fully blockaded ensemble is trivial, it lies at the basis of many proposed quantum devices [Jaksch *et al.*, 2000; Lukin *et al.*, 2001; Saffman and Walker, 2002; Müller *et al.*, 2009] and is a very active field of research (see the review of Saffman [2016]).

4.3 Nearest-neighbor Ising model

We are especially interested in the regime $R_\mathrm{b} \sim a$, where the Rydberg blockade radius extends only to nearest-neighbor sites. In this regime, the laser-driven Rydberg ensemble can be seen as realizing the nearest-neighbor Ising model and I thus reformulate Eq. (4.1) into:

$$H = \sum_i B_\perp \sigma_i^x + \sum_i (B_\parallel + B_\mathrm{loc}^i)\sigma_i^z + \sum_{i<j} J_{ij}\sigma_i^z\sigma_j^z. \tag{4.3}$$

First, the laser drive takes explicitly the form of an effective magnetic field $\mathbf{B} = B_\parallel \mathbf{e_z} + B_\perp \mathbf{e_x}$ with a transverse component $B_\perp = \hbar\Omega/2$ and a longitudinal part $B_\parallel = \hbar\delta/2$. Then, we use $n_i n_j = (1+\sigma_i^z)(1+\sigma_j^z)/4$ to decompose the van der Waals term in:

- a constant energy offset $\sum_{i<j} V_{ij}/4$ that is ignored.
- a local longitudinal magnetic field $B_\mathrm{loc}^i = \sum_{i<j} V_{ij}/2 = zV/2$ where z is the number of nearest neighbors.
- an Ising coupling $\sum_{i<j} J_{ij}\sigma_i^z\sigma_j^z$ with $J = V/4$.

When discussing the phase diagrams of infinite-size or periodic systems, the local field B_{loc} becomes position-independent and is absorbed in the global longitudinal field $B_{\parallel}$. Choosing a laser detuning compensating this local field, we obtain a zero total longitudinal field and, by symmetry of the Hamiltonian, the ground-state magnetization is $f_r = 1/2$. For bipartite lattices, such as a regular 1D chain or a 2D square array, the ground-state is the anti-ferromagnetic Néel state with one Rydberg excitation every other site. I now report our attempt to prepare adiabatically this state, which has been reported in Lienhard *et al.* [2018]. This work was done in collaboration with a team of theorists composed of Michael Schuler, Louis-Paul Henry and Prof. Andreas Laüchli.

4.3.1 Adiabatic sweeps to the Néel state

The experiment is performed by driving a 6×6 atomic array, shown in Fig. 4.4(a), to the Rydberg state $|r\rangle = \left|64D_{3/2}\right\rangle$ (this choice results from our study presented in Chapter 6 to avoid the problem observed in Fig. 4.2). From the calculated $C_6 = -875 \times 10^3$ GHz.μm^6 and a spacing[4] $a = 8.3\,\mu$m, we obtain a nearest-neighbor (NN) coupling strength $V_{\text{NN}}/h \simeq -2.7$ MHz (equivalently $R_{\text{b}} = 1.2\,a$). The next-nearest neighbor term $V_{\text{NNN}} = V_{\text{NN}}/8 \simeq h \times 0.3$ MHz is neglected and we describe our system using the NN Ising model.

The laser drive and detuning waveforms are shown in Fig. 4.4(b) and the trajectory in the phase diagram in (c). The results described in the following are obtained for an optimized sweep duration of $1\,\mu$s. We first observe, in Fig. 4.4(c), a quasi homogeneous density of excitations $n(i,j)$ over the atomic array, with a slight imbalance between edge and bulk sites due to the local field B_{loc}. The mean Rydberg fraction is 0.50(1) and there are in average $\bar{N}_{\text{exc}} = 18$ Rydberg excitations. Figure 4.4(d) shows the distribution of N_{exc} for ~ 300 realizations: it is significantly squeezed compared to a binomial distribution (which would be the case for independent atoms) but less than expected for a perfect Néel state even when taking into account detection errors (dashed red lines), indicating an imperfect adiabatic preparation.

I now discuss the pair-wise correlation map $C(k,l)$ defined by:

$$C(k,l) = \frac{1}{N_{k,l}} \sum_{i,j} \langle \sigma^z_{i+k,j+l} \sigma^z_{i,j} \rangle - \langle \sigma^z_{i+k,j+l} \rangle \langle \sigma^z_{i,j} \rangle, \tag{4.4}$$

where $N_{k,l}$ is the number of atom pairs separated by k sites horizontally and l sites

[4] The array is slightly squeezed along the horizontal direction to compensate the anisotropic interaction.

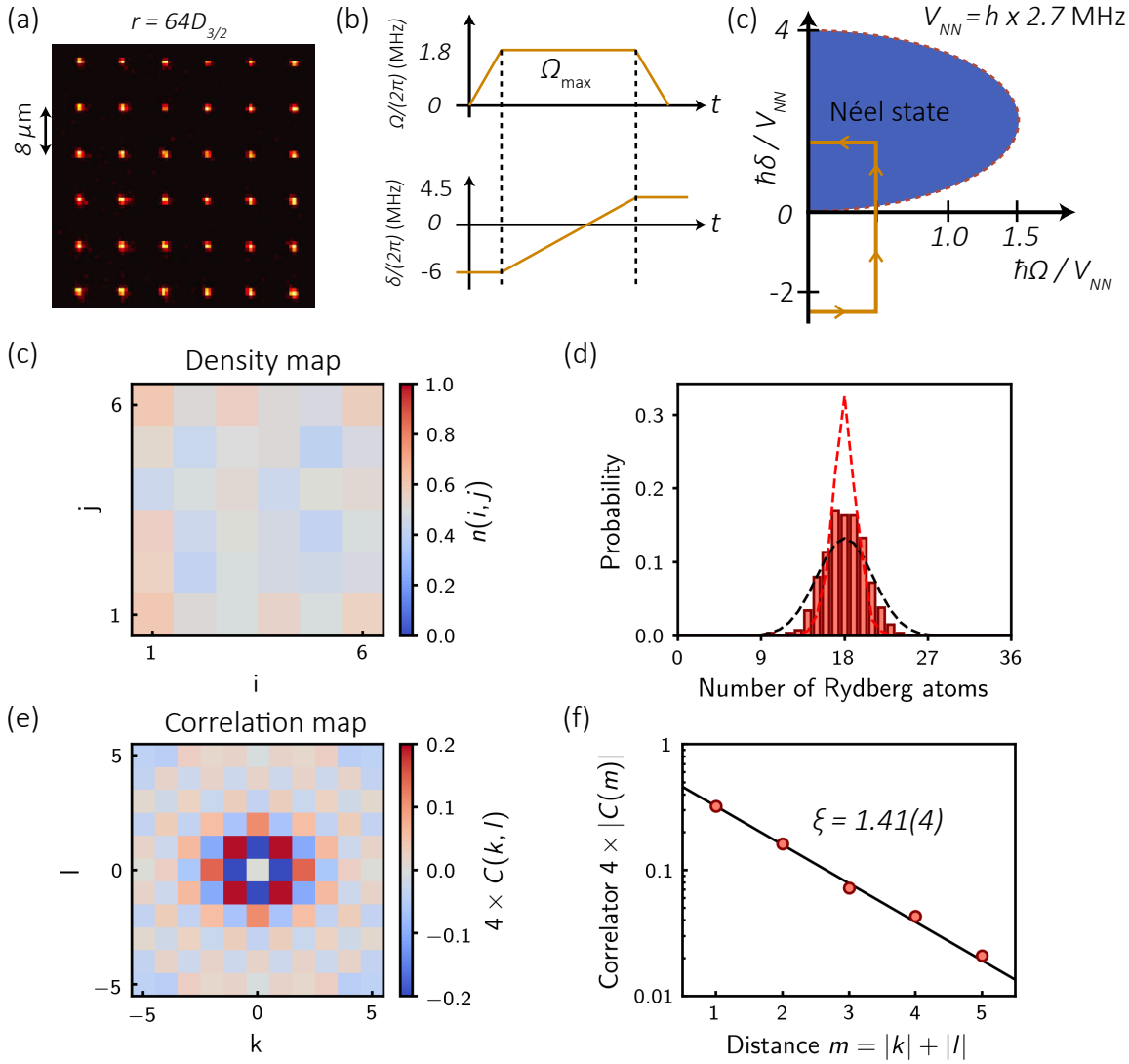

Figure 4.4: Creation of antiferromagnetic-like correlations with an adiabatic sweep. (a) 6×6 atomic array driven to the Rydberg state $|r\rangle = \left|64D_{3/2}, m_J = 3/2\right\rangle$ with time-dependent laser drive $\Omega(t)$ and detuning $\delta(t)$ shown in (b). Phase diagram and system trajectory (orange path) ending deep in the crystalline phase. (c) Quasi-homogeneous density map obtained at the end of the sweep. (d) Histogram of the number of Rydberg excitations for 264 experimental runs showing a squeezed distribution around $\bar{N}_{\mathrm{exc}} = 18 = N/2$. The dashed line is a binomial distribution that would be expected for independent atoms, the red line is the predicted histogram for the Néel state taking into account detection errors $(\varepsilon, \varepsilon') = (4, 4)$ %. (e) Measured correlation map $4 \times C(k, l)$ showing an antiferromagnetic pattern with a sign alternating as $(-1)^{|k|+|l|}$. For a perfect Néel state, the correlation would be saturated at ± 1. (f) Exponential decrease of the absolute value of the correlator with the distance $m = |k| + |l|$. The extracted correlation length is $\xi = 1.41(4)$.

vertically. Figure 4.4(e) shows clear antiferromagnetic correlations, which nevertheless remain much smaller than the expected $C_{k,l} = (-1)^{|k|+|l|}/4$ for the Néel state. In Fig. 4.4(f), I present the same data as a function of the distance $m = |k| + |l|$, where we observe an exponential decay with a fitted correlation length of $\xi = 1.41(4)$ sites.

4.3.2 Saturation of correlations by decoherence

An exact numerical simulation of the coherent evolution of our system during the sweep predicts much larger correlations, both in magnitude and in spatial extent, than obtained in the above experiment. We thus suspect some decoherence mechanisms to limit the efficiency of our adiabatic sweeps. This is further motivated by the fact that, already when performing a Rabi oscillation on a single atom (see next chapter), we observe a damping of the oscillation caused by some dephasing mechanisms. To comfort this analysis, our colleagues from the theory team proposed to use a simple model for the decoherence by introducing a phenomenological dephasing rate γ for the Rydberg state and solving a master equation for a 4×4 array (see Appendix C of Lienhard *et al.* [2018]). By fitting the model on an independently measured Rabi oscillation, we calibrated the dephasing rate to a value of $\gamma = 3\,\mu\text{s}^{-1}$.

We now compare the results of the numerical model including the dephasing rate and our experiments. To quantify the amount of correlation, we use the Néel factor:

$$S_{\text{Néel}} = 4 \times \sum_{(k,l)\neq(0,0)} (-1)^{|k|+|l|} C(k,l), \tag{4.5}$$

which should reach $S_{\text{Néel}} = N$ for a perfect preparation of the Néel state. Figure 4.5(a) shows the measured and calculated Néel factor at the end of a sweep for varying slopes of $\delta(t)$ and thus of different total sweep durations. For fast sweeps, $S_{\text{Néel}}$ is expected to be small, even for a coherent dynamics ($\gamma = 0$), due to the non-adiabatic evolution of the system, especially at the quantum phase transition ($\delta(t) \simeq 0$) where the gap between the many-body ground-state and the first excited state is smallest. For slower sweeps, the $\gamma = 0$ prediction rises much higher than the measured $S_{\text{Néel}}$, while the $\gamma = 3\,\mu\text{s}^{-1}$ calculation gives a much better agreement. In a second experiment, shown in Fig. 4.5(b), we choose the optimal duration of $1\,\mu$s indicated in panel (a), and record the time-resolved growth of correlations during the sweep. The measured values are again in good agreement with the numerical model.

From this study, we conclude that decoherence mechanisms, taken into account

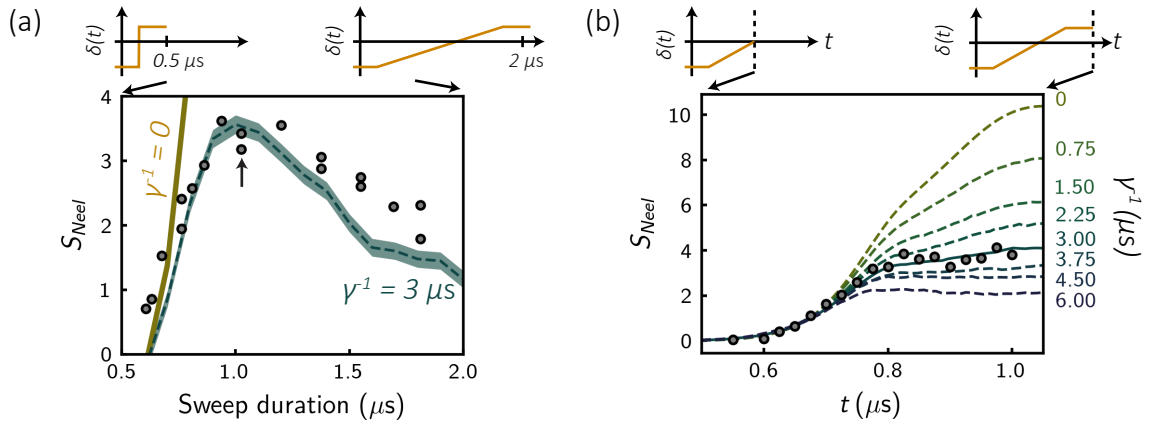

Figure 4.5: Influence of a dephasing rate on the adiabatic preparation. We compare the measured Néel factor $S_{\text{Néel}}$ to numerical simulations including a phenomenological dephasing rate γ affecting the Rydberg state. Using an independently measured Rabi oscillation, we estimate $\gamma = 3\,\mu\text{s}^{-1}$. (a) For a fast sweep, the ground-state preparation is limited by non-adiabatic evolution and the influence of the dephasing is negligible. For slower sweeps, the coherent evolution ($\gamma = 0$) gives a much larger $S_{\text{Néel}}$ that obtained experimentally (dark disks). Taking into account the finite dephasing rate gives numerical results closer to our observation. (b) Temporal evolution of $S_{\text{Néel}}$ during a sweep of $1\,\mu$s [indicated by the arrow in (a)]. The numerical results of the dephasing model are shown for various rates γ (dashed lines). The agreement is best for the independently obtained $\gamma = 3\,\mu\text{s}^{-1}$ (solid line). The numerical simulations have been performed by Michael Schüler.

here with a simplistic single-particle dephasing rate γ, limit the efficiency of the adiabatic sweeps. Similar limitations have also been reported by Guardado-Sanchez *et al.* [2018] and in early studies of ground-state preparation on an ion platform Islam *et al.* [2013]. Even if we obtained clear signatures of the underlying Néel ground-state, the properties of the final state depend mainly on the dephasing rate rather than on universal properties of the quantum phase transition. This motivated us to perform a detailed study of all possible dephasing mechanisms that is presented in Chapter 5, where I also describe how we plan to improve the current experimental setup to reach longer coherence times. This will allow future experiments studying the intriguing phase that arises at half-filling on a triangular lattice, where geometric frustration leads to a ground-state degeneracy.

Let us also note that for system of increasing number of particles, the gap between the ground state and the first excited ones closes at the QPT, which ultimately prevents an adiabatic evolution and leads to the creation of defects. The latter is in fact ubiquitous in physics: from magnetic domains with different spontaneously chosen

magnetization to the production of vortexes in Bose-Einstein condensates [Beugnon and Navon, 2017]. These defects are intrinsically connected to Lieb-Robinson bounds describing the propagation of correlations in the system [Lieb and Robinson, 1972], or to critical exponents of the QPT via the quantum Kibble-Zurek mechanism [Zurek, Dorner, and Zoller, 2005].

4.4 Conclusion

I have described the phase diagram of laser-driven Rydberg ensembles. I have first focused on the critical region $\delta = 0$ studied with quench experiments. I then detailed the different ordered phases that appear close to the critical point when increasing the Rydberg blockade distance. Finally, I presented our attempt to prepare the Néel ground-state with an adiabatic sweep, that led to the observation of antiferromagnetic-like correlations. A more detailed analysis of the temporal and spatial growth of correlations during the sweeps will be presented in the thesis of Vincent Lienhard.

In this chapter, I did not give any experimental details about how we implement the coherent laser drive, which mimics the **B**-field of the Ising model. This will be done in Chapter 5, where I also present a quantitative analysis of detection errors and of various dephasing mechanisms, which we showed limit the efficiency of our adiabatic preparation. I also did not explain the physical origin of the van der Waals interaction $V = C_6/R^6$ between two Rydberg atoms. This will be found in Chapter 6, together with a study and a solution to the Rydberg blockade failure observed in quench experiments [shown in Fig. 4.2(d,e)].

Chapter 5

Coherent ground-Rydberg Rabi oscillations

Contents

Our implementation and studies of the quantum Ising model rely on our ability to engineer an effective magnetic **B**-field for spin-1/2 particles encoded between a ground-state level $|g\rangle$ and a Rydberg state $|r\rangle$. This is achieved by coherently driving the $|g\rangle \leftrightarrow |r\rangle$ transition (see Fig. 5.1) using excitation lasers that lies at the heart of our studies. As described in the previous chapter, we can suddenly switching them on to perform quench experiments [Labuhn *et al.*, 2016], or rather vary slowly their intensity and frequency to obtain quasi-adiabatic sweeps crossing a quantum phase transition [Lienhard *et al.*, 2018]. Ideally, these experiments require a large range of coupling strength $\Omega/(2\pi) = 0.1 - 10$ MHz and to maintain the coherence between $|g\rangle$

and $|r\rangle$. In this chapter, we use a simple experiment, a Rabi oscillation, to check the level of control that we have on independent atoms, our objective being to observe fully contrasted, undamped, oscillations.

Background Coherent ground-Rydberg Rabi oscillations have been observed first in dilute gases [Deiglmayr *et al.*, 2006; Reetz-Lamour *et al.*, 2008], then on single atoms [Johnson *et al.*, 2008; Zuo *et al.*, 2009; Miroshnychenko *et al.*, 2010; Hankin *et al.*, 2014] and more recently in blockaded ensemble "superatoms" [Dudin *et al.*, 2012; Ebert *et al.*, 2015; Zeiher *et al.*, 2016; Labuhn *et al.*, 2016]. They are one of the crucial prerequisites for quantum information processing and the implementation of two-qubit gates [Saffman, 2016]. Despite intensive experimental efforts, fidelities of such gates have remained around ~ 80 % [Maller *et al.*, 2015; Jau *et al.*, 2016; Picken *et al.*, 2018], below their theoretically predicted intrinsic fidelities (> 99 %) [Zhang *et al.*, 2012; Xia, Zhang, and Saffman, 2013; Petrosyan *et al.*, 2017]. This remains much lower than on other experimental platforms such as trapped ions (99.9 %) [Monz *et al.*, 2011; Ballance *et al.*, 2016] or superconducting qubits (99 %) [Chow *et al.*, 2012; Barends *et al.*, 2014; Song *et al.*, 2017]. The reason is mostly imperfections in the coherent optical excitation to Rydberg states that I will describe in this Chapter. In addition to quantum information processing, we are interested here in using the coherent Rabi couplings for studies of Ising-like models [Schauß *et al.*, 2012; Schauß *et al.*, 2015; Labuhn *et al.*, 2016; Bernien *et al.*, 2017; Kim *et al.*, 2018; Lienhard *et al.*, 2018; Guardado-Sanchez *et al.*, 2018]. In the previous chapter, we identified the relatively short atomic coherence time as a limitation of the duration of quantum simulation.

Goal In all experiments reported until this year, one observes that the Rabi oscillations are quite damped and have a finite contrast. Figure 5.1 gives typical examples; similar behaviors were observed in other setups [Zhang *et al.*, 2010; Hankin *et al.*, 2014; Zeiher *et al.*, 2015; Bernien *et al.*, 2017; Kim *et al.*, 2018]. Typical $1/e$ damping times, for a 2 MHz Rabi frequency, are about $5\,\mu$s, much lower than the upper bound given by the lifetime of Rydberg states, in the $\sim 200\,\mu$s range. The purpose of this chapter is to understand *quantitatively* the origins of the damping, i.e., we want to replace the fits shown as solid curves by ab-initio numerical calculations. This analysis helps us to identify the limitations of our current setup and to plan its next generation. Let us also note the recent work performed by Levine *et al.* [2018] who reported a 97 %

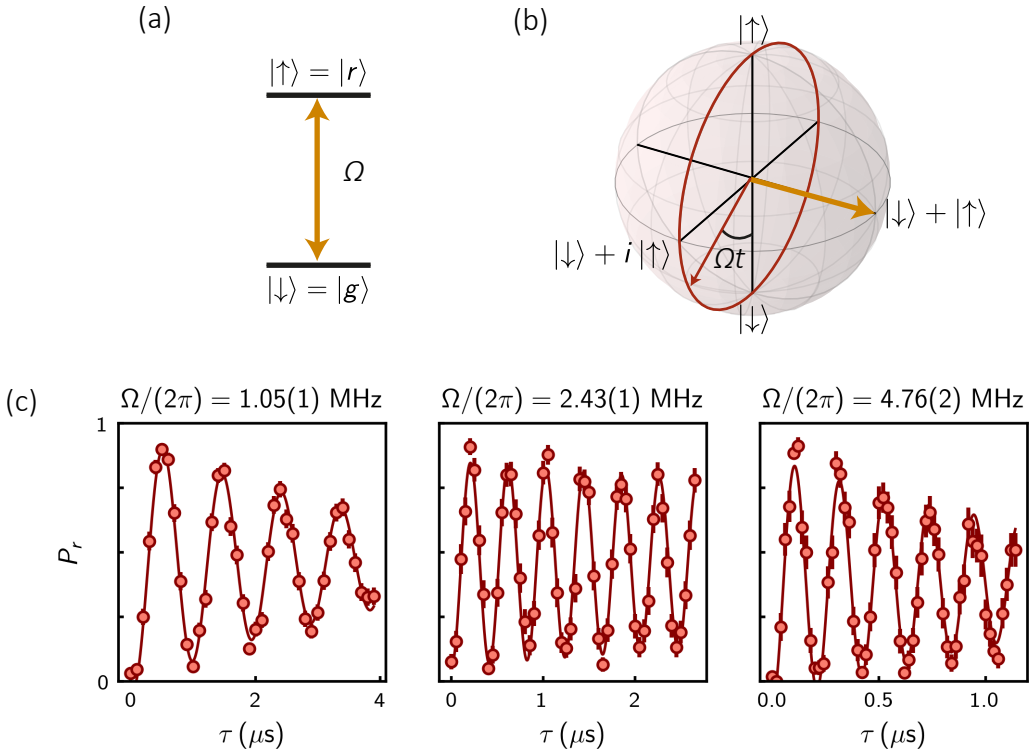

Figure 5.1: Rabi oscillations. (a) The spin-1/2 defined by a ground-state and a Rydberg level is driven resonantly by a laser field of coupling strength Ω. (b) Bloch sphere representation of a Rabi oscillation: the spin-1/2 (red arrow) rotates from pole to pole, at an angular frequency Ω, around the effective magnetic field pointing along the equatorial plane (for a resonant drive). (c) Experimental Rabi oscillations for different Ω. The solid lines are fits by a damped sine.

fidelity of preparation of an entangled[1] state between Rydberg atoms by solving much of the imperfections reported in this chapter.

This chapter is organized as follows: I first describe in Section 5.1 our two-photon excitation setup with which we drive the ground-Rydberg transition. Then, in Section 5.2, I show how to model and measure detection errors, decreasing the contrast of even a fully coherent Rabi oscillation. In Section 5.3, I model all the various effects that can explain the damping of Rabi oscillations. Finally, in Section 5.4, I combine all the effects in a comprehensive study and discuss their relative importance as a function of the Rabi frequency, and finally present how we plan to upgrade our optical setup to reach longer coherence times. The results presented in this chapter have been published in de Léséleuc *et al.* [2018a].

[1]Here the entanglement is not transfered back to the long-lived hyperfine ground-state levels.

5.1 Excitation scheme

The direct optical transition from the $5S_{1/2}$ ground-state $|g\rangle$ to a Rydberg state $|r\rangle$ is in the UV domain (297 nm). We avoid the need for a UV laser by using a two-photon excitation scheme *via* a low-lying excited state $|e\rangle$. Two possibilities are often considered for the latter: the $5P$ state (*regular* scheme) or the $6P$ state (*inverted* scheme) [Löw *et al.*, 2012]. For historical reasons, our group always used the $5P_{1/2}$ level, where the $|g\rangle \leftrightarrow |e\rangle$ transition is at 795 nm and the $|e\rangle \leftrightarrow |r\rangle$ one at ~ 475 nm. With this two-photon scheme, we can couple to Rydberg $S_{1/2}$ and $D_{3/2}$ states[2]. Two elements have to be considered when choosing which states to work with:

- The coupling strength. The electric dipole matrix element $\langle 5P|\,\hat{d}\,|r\rangle$ is almost twice as large for nD than for nS states. We will see in this Chapter that the damping of our Rabi oscillation is partly due to a too small coupling strength, indicating that D states should be preferred.

- The effect of the dipole-dipole Hamiltonian on two Rydberg atoms. As we will see in Chapter 6, the interaction between two $nS_{1/2}$ states is quite simple and ideal, all the opposite of $nD_{3/2}$ states. So far we have succeeded in proof of principle experiments with D states, but the wealth of phenomena occurring between two Rydberg D states might preclude a perfect mapping on a simple spin-1/2 model, as we will see in the next chapter.

The situation is complicated as we have to choose between a better coherent manipulation at the single atom level with $nD_{3/2}$ states and a better control of the two-atom interaction with $nS_{1/2}$ states. Our choice, at the beginning of this thesis, was to keep using the $nD_{3/2}$ levels as we would obtain longer coherence times, and to explore carefully the effect of interaction between $nD_{3/2}$ states (see Chapter 6).

We now discuss the choice of hyperfine and Zeeman sublevels to use, as shown in Fig. 5.2(a). The hyperfine structure of the $nD_{3/2}$ level [van Wijngaarden, Li, and Koh, 1993] is usually neglected as it is much smaller ($\sim$ kHz) than all other energy scales (Rabi coupling, Rydberg decay rate, Zeeman shift), here we keep it for consistency with the expression of the $5P_{1/2}$ and $5S_{1/2}$ states in the hyperfine basis and to clearly identify the π and $\sigma^{\pm}$ transitions. We work with the stretched Rydberg level $|r\rangle = |nD_3/2, F = 3, m_F = 3\rangle$[3] as: (i) the dipole-dipole interaction is simpler when the angular momentum is maximized ($m_F = F$) and (ii) the Clebsch-Gordan

[2] Coupling to $D_{5/2}$ states would be possible using the $5P_{3/2}$ intermediate level.
[3] $|r\rangle = |nD_{3/2}, m_J = 3/2\rangle$ in the fine basis.

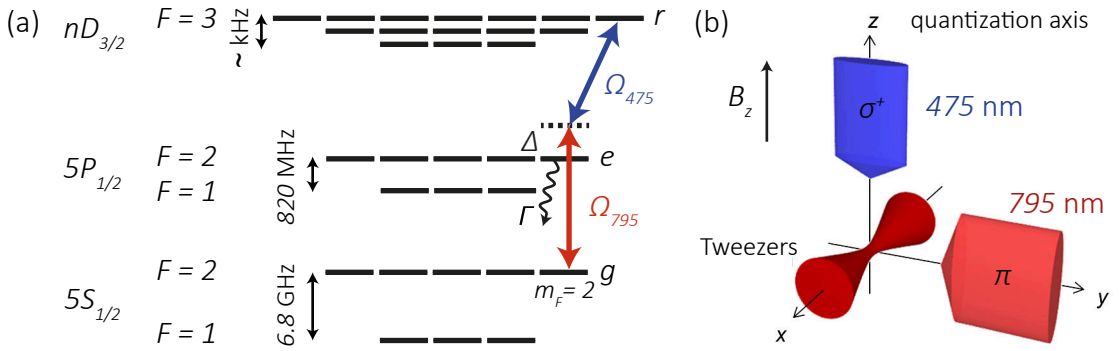

Figure 5.2: Regular excitation scheme. (a) Relevant levels involved to excite a ground-state atom $|g\rangle$ to a Rydberg state $|r\rangle$ with a two-photon transition via an intermediate state $|e\rangle$. (b) Excitation lasers: the blue and red beams have cross-sections with waists $(w_x, w_y) = (24 \times 40)\,\mu$m and $(w_x, w_z) = (100 \times 100)\,\mu$m, respectively. A vertical magnetic field B_z defines the quantization axis.

coefficient of the σ^+transition to $|e\rangle = \left|5P_{1/2}, F = 2, m_F = 2\right\rangle$ is maximal. Finally, we choose the ground-state level $|g\rangle = \left|5S_{1/2}, F = 2, m_F = 2\right\rangle$, into which the atom can easily be initialized by optical pumping.

Figure 5.2 shows the geometry of the 795 nm and 475 nm excitation lasers. The 475 nm laser is shone along the vertical quantization axis defined by a magnetic field B_z of a few Gauss and is σ^+-polarized, while the 795 nm beam is shone along the y-axis and is π-polarized. I denote by Ω_{795} and Ω_{475} the Rabi couplings, by Δ the single-photon detuning from the intermediate state and δ the two-photon detuning from the Rydberg state ($\delta = 0$ in the figure). The radiative decay rate from $|e\rangle$ is $\Gamma = 2\pi \times 5.75$ MHz. To obtain a coherent coupling between $|g\rangle$ and $|r\rangle$, despite the spontaneous emission from $|e\rangle$, we use a large detuning $\Delta/(2\pi) = 740\,\text{MHz} \gg \Omega_{475}, \Omega_{795}, \Gamma$, such that the intermediate state is almost not populated. As a result the system is well described by the two-level Hamiltonian:

$$H = \frac{\hbar\Omega_{\text{eff}}}{2}\left(|r\rangle\langle g| + |g\rangle\langle r|\right) + \hbar\delta_{\text{eff}}|r\rangle\langle r|, \tag{5.1}$$

where Ω_{eff} is the effective two-photon Rabi frequency:

$$\Omega_{\text{eff}} = \frac{\Omega_{795}\Omega_{475}}{2\Delta}, \tag{5.2}$$

and δ_{eff}, the effective detuning, which takes into account the AC-Stark shift caused by the excitation laser:

$$\delta_{\text{eff}} = \delta + \frac{\Omega_{795}^2 - \Omega_{475}^2}{4\Delta} \tag{5.3}$$

In the following, we will simply write them Ω and δ. In practice, we work with the 475 nm laser at maximum power and vary Ω by tuning Ω_{795}.

Experimental sequence We observe a Rabi oscillation between $|g\rangle$ and $|r\rangle$ (see Fig. 5.1) using the following experimental sequence: After preparing the atom in $|g\rangle$ by optical pumping[4], we switch off the tweezers and illuminate the atom with the Rydberg excitation lasers for a time τ up to a few microseconds, and finally switch on the tweezers again. The tweezers are off during the Rydberg experiment to avoid the strong light-shift they would apply on $|g\rangle$, which would not be the same from trap to trap (see Section 2.2.3) and would also depend on the exact position of the atom in the tweezers (changing from shot-to-shot due to its non-zero temperature). The measurement of the ground-state and Rydberg populations (P_g and P_r) are detailed in Section 5.2. Briefly, we rely on the recapture of an atom in $|g\rangle$, while a Rydberg atom is repelled by the tweezers due to the ponderomotive potential and is lost. The presence or absence of the atom after the Rydberg experiment is observed with a fluorescence image. We repeat the sequence at least 100 times to obtain a good estimate of the populations. In the following two subsections, I give more details about the 795 nm and 475 nm setup and especially the achievable Rabi couplings Ω_{795} and Ω_{475}.

5.1.1 795 nm excitation laser

The 795 nm light source is a Toptica DL 100 diode with an output power of ~ 100 mW. A small fraction of the output is directed to a high finesse ULE (ultra-low expansion) cavity for active stabilization of the laser frequency using the Pound-Drever-Hall technique. The cavity has a finesse of $\mathcal{F} \simeq 20000$ and a free spectral range FSR = 1.5 GHz (linewidth $\nu_{\text{cav}} = \text{FSR}/\mathcal{F} = 75$ kHz); more details are given in the thesis of Sylvain Ravets [2014]. The PDH technique requires frequency sidebands generated by a resonant fiberized EOM (electro-optic modulator) placed in the path going to the cavity. The rest of the laser output goes through:

- an AOM (acousto-optic modulator) in a double pass configuration, with which we can dynamically tune the laser power and thus the Rabi coupling $\Omega_{795}(t)$ and the laser frequency (over a ~ 50 MHz range) with a response time of less than

[4] We checked independently, by performing microwave transitions between the ground-state hyperfine levels, that the pumping efficiency was higher than 99 %. In the following we will suppose that it is perfect.

100 ns. It is used to performing adiabatic sweeps (see Section 4.3.2) or STIRAP excitation (see Section 7.1.1).

- an EOM (LINOS free-space) with a rise time of ~ 10 ns, used to quickly switch on and off the beam and generate square pulses for Rabi oscillations or quench experiments.

- a polarization maintaining fiber bringing the light close to the experimental chamber where we can obtain up to 10 mW of laser power.

Thanks to the large dipole matrix element between the ground-state and the first excited level, we reach up to a few ~ 100 MHz of Rabi frequency at full power even for a beam with a waist as large as $\sim 100\,\mu$m. The beam is aligned on the atomic array by maximizing the heating-induced loss of atoms from the tweezers when shining the laser on resonance on the $5S$-$5P$ transition. The Rabi frequency Ω_{795} is estimated by measuring the light-shift $\Omega_{795}^2/4\Delta$, applied on the ground-state level, by spectroscopy of the Rydberg line.

5.1.2 475 nm excitation laser

The 475 nm light source is a Toptica TA-SHG laser: an ECDL (extended-cavity diode laser) emits a 950 nm beam, a small fraction of it is sent to the ULE cavity to stabilize the laser frequency, while the rest is amplified by a tapered amplifier and injected in a resonant SHG (second harmonic generation) cavity. The output can reach up to 650 mW at 475 nm. The diode current is modulated at ~ 20 MHz to generate frequency sidebands for the Pound-Drever-Hall (PDH) lock of the SHG cavity (and also the ULE one). This is different than for the 795 nm setup where we modulated only the light going to the ULE cavity and not to the atoms. We thus take care to use a modulation as small as necessary to still lock the two cavities to avoid the frequency sidebands to drive the atomic transition and perturb the Rabi oscillation.

The dipole matrix element between $|e\rangle$ and $|r\rangle$ is much weaker than with $|g\rangle$ and much more laser intensity is thus required to achieve similar Rabi frequency. To make the best use of the available laser power, we decided to avoid coupling the light to a fiber and rather place the laser source close to the experimental chamber. The beam first goes through an AOM, for temporal shaping of $\Omega_{475}(t)$, and is then focused on the atomic plane. We use the natural ellipticity of the beam at the laser output to create a sheet-like shape with a reduced waist along the optical axis ($w_x = 24\,\mu$m)

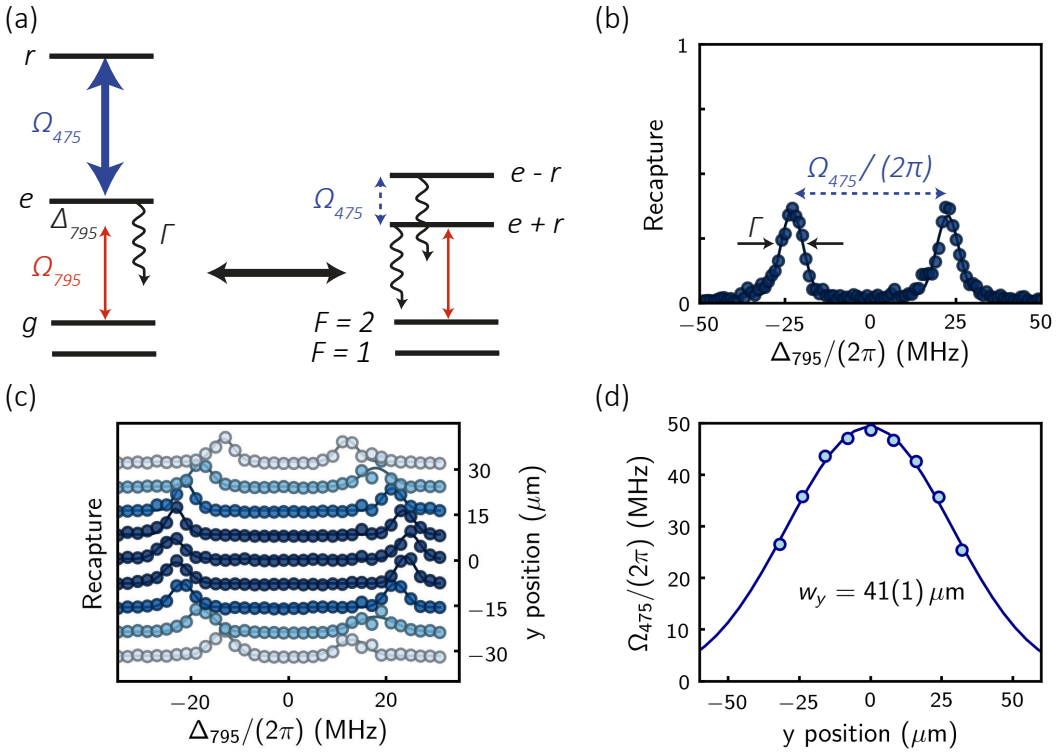

Figure 5.3: Autler-Townes splitting. (a) Scheme of the Autler-Townes effect. (b) We extract Ω_{475} from the splitting between the two resonances, observed when scanning the 795 nm laser detuning. (c) Stack of Autler-Townes spectra obtained for atoms at different positions in the excitation beam. (d) The Rabi coupling has a spatial dependence $\Omega_{475}(y) = \Omega_0 \exp(-y^2/w_y^2)$ with a fitted waist $w_y = 41(1)\,\mu$m.

compared to $w_y = 40\,\mu$m. This is well adapted for planar atomic arrays, but not for three-dimensional structures. Along the z-axis the ~ 5 mm Rayleigh range is much larger than the typical extent of atomic arrays.

Due to the small waist of the 475 nm laser and the fact that the beam propagates more than two meters from the laser source, we have to check its alignment on a daily basis. We engineered a semi-automatic method: a computer-controlled mirror mount steers the beam along x and y and the beam is aligned by maximizing the ionization-induced loss of atoms when shining together the 780 nm (MOT cooling beams) and the 475 nm lasers.

Autler-Townes splitting We measure the Rabi coupling Ω_{475} using the Autler-Townes effect, as sketched in Fig. 5.3(a). When strongly driving on resonance the $|e\rangle \leftrightarrow |r\rangle$ transition ($\Omega_{475} \gg \Omega_{795}$), the $|g\rangle \leftrightarrow |e\rangle$ line splits in two, corresponding to the symmetric and anti-symmetric superpositions $|e\rangle \pm |r\rangle$ at an energy $\pm\hbar\Omega_{475}/2$

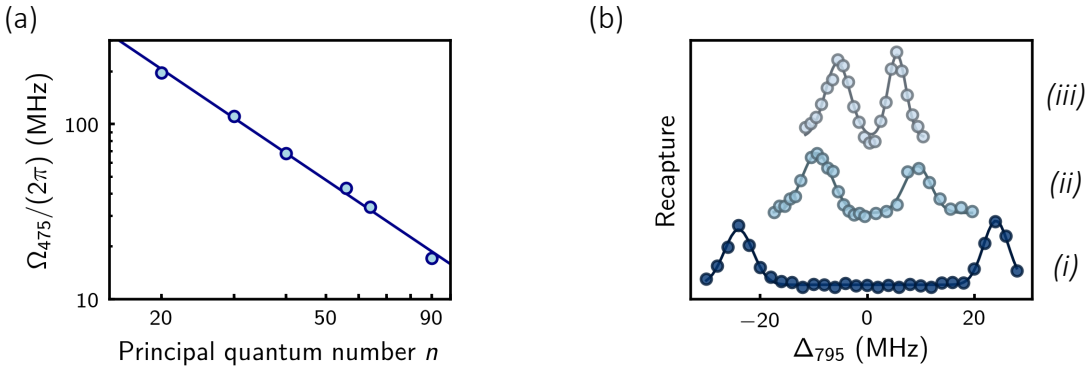

Figure 5.4: Dependence with Rydberg states. (a) Ω_{475} measured on different $|e\rangle \leftrightarrow |r\rangle = \left|nD_{3/2}, 3/2\right\rangle$ transitions, illustrating the $n^{-3/2}$ scaling with the principal quantum number n. Disks: experimental data. Solid line: power-law fit. (b) Autler-Townes spectra on different $|e\rangle \leftrightarrow |r\rangle = \left|60S_{1/2}\right\rangle$ and $|r\rangle = \left|60D_{3/2}\right\rangle$ transitions (see text).

in the rotating frame. After preparing the atom in $|g\rangle$, we record an Autler-Townes spectrum by scanning the detuning Δ_{795} of the weak 795 nm probe ($\Omega_{795} \leq \Gamma$). When the latter excites the atom to the short-lived $|e\rangle \pm |r\rangle$ states, it decays back to the $F = 1$ or $F = 2$ ground states. We remove atoms in $F = 2$ with a push-out beam and observe only atoms depumped in $F = 1$ in the fluorescence image. Figure 5.3(b) shows the resulting Autler-Townes spectrum from which we extract $\Omega_{475}/(2\pi) = 45.6(1)$ MHz.

Since the 475 nm beam is focused on the atomic array, Ω_{475} depends on the atom position along the y axis. Figure. 5.3(c) shows nine spectra obtained for different y-position of the atom, mapping the intensity profile of the excitation laser and giving a beam waist $w_y = 41(1)\,\mu$m. These results were obtained for $|r\rangle = \left|65D_{3/2}\right\rangle$ and ~ 400 mW of laser power on the atoms. For most of the experiments presented in this part (Rabi oscillations, simulation of Ising models), we had a weaker coupling ~ 30 MHz, as they were performed before improving the 475 nm optical setup.

Dependence with the principal quantum number The Rabi coupling to the Rydberg state scales, for a fixed laser intensity, as $\Omega_{475} \propto n^{-3/2}$ with n the principal quantum number. In Fig. 5.4(a), I show on a log-log scale the measurement of Ω_{475} for $n = 20 - 90$. To cover this range, the frequency of the 475 nm laser was changed by 11 THz and the power varied by $\sim 25\,\%$. Each measurement was rescaled by $\sqrt{P_{475}/170\text{ mW}}$, around the averaged power at the time of this experiment. The experimental data are well fitted by $\Omega_{475}/(2\pi) = 35(1)\,\text{MHz} \times (n/60)^{-1.59(5)}$, in good agreement with the expected scaling.

S states vs D states I use Autler-Townes spectra to illustrate the reduced coupling to $nS_{1/2}$ states and the importance to choose the right intermediate level $|e\rangle$. Figure 5.4 shows the achievable Rabi coupling for the same laser power (~ 400 mW) on three transitions:

- (i) $\left|5P_{1/2}, F = 2, m_F = 2\right\rangle \leftrightarrow \left|60D_{3/2}, m_J = 3/2\right\rangle$: $\Omega_{475}/(2\pi) = 48.1(1)$ MHz.
- (ii) $\left|5P_{1/2}, F = 1, m_F = 1\right\rangle \leftrightarrow \left|60S_{1/2}, m_J = 1/2\right\rangle$: $\Omega_{475}/(2\pi) = 18.8(2)$ MHz.
- (iii) $\left|5P_{1/2}, F = 2, m_F = 1\right\rangle \leftrightarrow \left|60S_{1/2}, m_J = 1/2\right\rangle$: $\Omega_{475}/(2\pi) = 11.1(2)$ MHz.

Clearly the coupling is reduced for S states. Then, for the same Rydberg state, Ω_{475} is maximal for a stretched transition: the measured ratio of Rabi frequencies between (ii) and (iii) is 1.69(3), close to the expected $\sqrt{3} \sim 1.73$ from the ratio of Clebsch-Gordan coefficients [Steck].

5.2 Detection errors

In this section, I detail how we obtain the population of the ground and Rydberg states by the recapture of the atoms after the experiment. It relies on the repulsion of an atom in $|r\rangle$ by the tweezers. The method is extremely simple as we only need to switch on the tweezers at the end of the Rydberg experiment, but is affected by small detection errors of two types:

- *false positive* errors, with a probability $\varepsilon = P(r|g)$ to incorrectly infer that a ground-state atom was in $|r\rangle$ because it was lost, e.g. due to background-gas collisions. We discuss this in Section 5.2.1.
- *false negative* errors, with an error rate $\varepsilon' = P(g|r)$, caused by the decay of $|r\rangle$ (radiative lifetime of $\sim 200\,\mu$s) to a ground-state level before it is too far away from the trapping region to be recaptured (see Section 5.2.2).

We denote by $\tilde{P}_g$ and $\tilde{P}_r$ the real population of the states $|g\rangle$ and $|r\rangle$, and by P_g and P_r the measured population altered by the nonzero values of $(\varepsilon, \varepsilon')$:

$$P_g = (1-\varepsilon)\left[\tilde{P}_g + \varepsilon'\tilde{P}_r\right], \tag{5.4}$$

$$P_r = \varepsilon\tilde{P}_g + (1-\varepsilon'+\varepsilon\varepsilon')\tilde{P}_r. \tag{5.5}$$

It implies that, even if the real population $\tilde{P}_r$ undergoes a perfect Rabi oscillation $\tilde{P}_r(t) = \sin^2(\Omega\tau/2)$, the measured one $P_r(t)$ has a finite contrast. Figure 5.5 illustrates

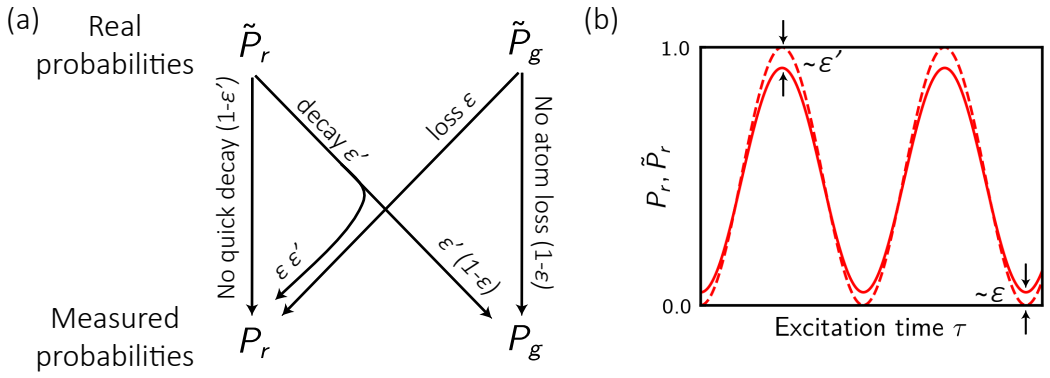

Figure 5.5: Effect of detection errors. (a) Probability tree connecting the real $(\tilde{P}_g, \tilde{P}_r)$ and measured (P_g, P_r) ground and Rydberg population. In addition to the first order processes (ground-state atom loss and Rydberg atom recapture due to its quick decay), it is also possible to loose a Rydberg atom having decayed with a small probability $\varepsilon\varepsilon'$. (b) Small but finite values of $(\varepsilon, \varepsilon')$ reduce the contrast of the measured probability P_r (solid line) assuming a perfect Rabi oscillation $\tilde{P}_r$ (dashed line). The second order terms $\varepsilon\varepsilon'$ can be neglected.

the effect to lowest order in $(\varepsilon, \varepsilon')$. In principle, one can invert the above equations [Shen and Duan, 2012], e.g., using a maximum likelihood procedure, to correct these errors and recover the real populations, even for many qubits [Bernien *et al.*, 2017]. In our publications we rather include these errors on the calculated populations when comparing with experimental data.

5.2.1 False positives

The various sources of atom loss during an experiment[5] are:

- Collisions with the background gas. Given the vacuum-limited lifetime of ~ 10 s and the 30 ms delay between the two images taken before and after the experiment, we estimate an error rate of 0.3 %.

- Loss due to the MOT cooling beam. The atom lifetime is reduced to 8 s in presence of the cooling beam; for fluorescence images of 20 ms this results in an error rate of 0.3 %.

- Release of the atom during the experiment. The recapture depends on how long

[5] Strictly speaking, we should distinguish a loss occuring before a Rydberg experiment (preparation error) and after it (detection error).

we open the traps. For typical atom temperature $T = 30\,\mu$K and release time $6\,\mu$s, the loss probability is estimated to be 1 % (see Section 2.1.3).

Adding all three contributions, we estimate a false positive rate $\varepsilon < 2\,\%$, in good agreement with typically measured values.

5.2.2 False negatives

Here, I first explain the origin of the ponderomotive potential and experimentally show its repulsive effect on a Rydberg atom. I then combine it with the calculated lifetime of Rydberg states in a quantitative model giving ε' and describe a measurement method.

Ponderomotive potential The potential experienced by an atom in an electromagnetic field oscillating at an angular frequency ω takes the form $U(\mathbf{r}) = -\frac{1}{4}\alpha_i(\omega)|E(\mathbf{r})|^2$, where α is the polarizability of the atom depending on both the internal electronic state $|i\rangle$ and the trap laser frequency $\omega/(2\pi) = 352$ THz.

- For the Rydberg state $|r\rangle$, α_r is obtained by considering that the valence electron, being in average very far away from the nucleus, is a free charged particle. In this case, the ponderomotive effect gives $\alpha_r = -e^2/m\omega^2$, which always repel the particle from the bright region.

- For the ground-state $|g\rangle$, the polarizability α_g is calculated by taking into account the strong D_1 and D_2 transitions to the first excited levels $5P_{1/2}$ and $5P_{32/}$, giving $\alpha_g = e^2/m(\omega_0^2 - \omega^2)$, where $\omega_0/(2\pi) = 382$ THz is the average frequency of the two resonances.

For our wavelength (850 nm), the ratio of polarizabilities $\beta = \alpha_r/\alpha_g$ is:

$$\beta = -(\omega_0^2 - \omega^2)/\omega^2 \simeq -0.17. \tag{5.6}$$

For an increased detuning of the trap laser from the $5P$ states, and at constant laser power, the ponderomotive repulsion of Rydberg states increases relatively to the trapping potential: it is 7 % at 810 nm, 85 % at 1064 nm. ε' thus depends on the trap wavelength and its depth.

Repulsion of Rydberg atoms I illustrate the repulsion of Rydberg atoms by the tweezers with a modified release and recapture experiment:

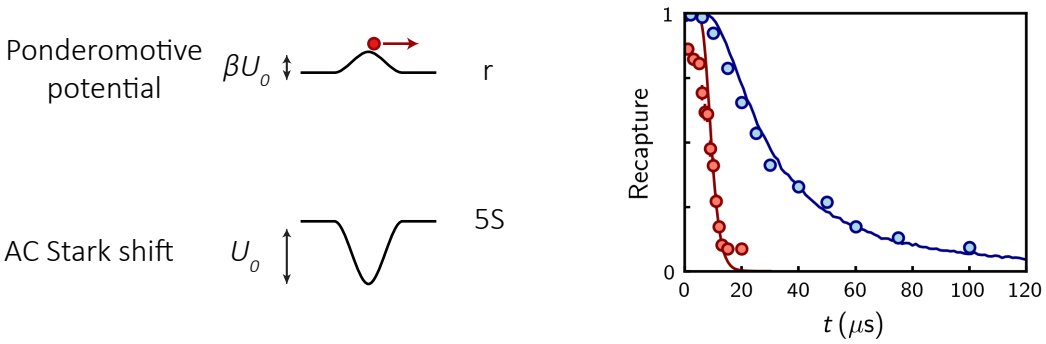

Figure 5.6: Ponderomotive potential. Recapture probability $p_{\mathrm{recap}}(t)$ including anti-trapping by the optical tweezers (red) and neglecting the anti-trapping (blue). For the simulations, we use $T = 20\ \mu$K, $U_0 = 1$ mK, and $\beta = -0.17$. The reduced contrast of the red data with respect to the simulation is due to the finite efficiency of Rydberg (de-)excitation.

1. We excite the atom to $|r\rangle$ with a Rabi π-pulse of efficiency ~ 90 %,
2. We switch on the tweezers and let the Rydberg atom evolve during a time t in the repulsive ponderomotive potential $\beta U(\mathbf{r})$,
3. We de-excite the atom from $|r\rangle$ to $|g\rangle$ with a second π-pulse and measure the recapture probability in the attractive potential $U(\mathbf{r})$.

Figure 5.6 shows the recapture for the usual release and recapture experiment where the atom is in free-flight (blue points) and the modified one where the atom is subjected to the repulsive potential (red points). We observe the faster escape of the atom in the second case. The solid lines are Monte-Carlo simulation for a classical particle with a temperature $T = 20\,\mu$K and are in excellent agreement with our experimental observations. The effect is well captured by a characteristic time during which a Rydberg atom stays in the trapping region:

$$t_{\mathrm{recap}} = \int p_{\mathrm{recap}}(t)\,\mathrm{d}t \simeq 10\,\mu\mathrm{s}, \tag{5.7}$$

where p_{recap} is the red curve shown in Fig. 5.6. t_{recap} is almost independent of the atom temperature ($6\,\mu$s at $100\,\mu$K, $13\,\mu$s at $5\,\mu$K) since it is dominated by the ponderomotive repulsion. The latter thus plays an important role in our detection scheme.

Model for ε' A detection error occurs when the Rydberg atom decays back to the $5S_{1/2}$ ground-state levels, while it is still in the trapping region of the tweezers, as

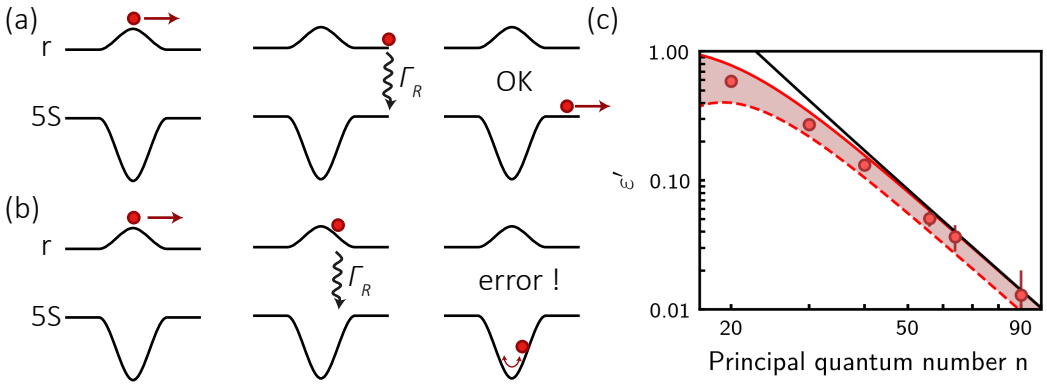

Figure 5.7: False negative. (a) The detection relies on the expulsion of a Rydberg atom far enough from the trap before it decays back to the ground-state. (b) With a probability ε', the Rydberg atom decays too quickly and is recaptured. (c) Detection error rate ε' as a function of n. As the Rydberg decay rate Γ_R, ε' scales as n^{-3}. Red disks: measurement. Various lines: ab-initio models (see text).

sketched in Fig. 5.7(a,b). The error rate is then given by:

$$\varepsilon' = \int_0^\infty p_{\text{recap}}(t)\, \dot{p}_g(t)\, \mathrm{d}t. \tag{5.8}$$

where p_{recap} was defined above and $\dot{p}_g(t) = \Gamma_R \exp(-t\Gamma_R)$ is the time derivative of the ground-state population for an atom initially in $|r\rangle$ and decaying by spontaneous emission (via low-lying excited states) with a rate Γ_R[6]. The radiative decay rate scales with the principal quantum number as n^{-3} [Gallagher, 1994; Beterov *et al.*, 2009]. The error rate thus depends on the principal quantum number. For the state $60D_{3/2}$, the radiative lifetime is $\Gamma_R^{-1} \simeq 210\,\mu$s and is much longer than the recapture time $t_{\text{recap}} \simeq 10\,\mu$s. In this limit, the error rate is simply given by:

$$\varepsilon' \simeq t_{\text{recap}} \Gamma_R. \tag{5.9}$$

I show in Fig. 5.7(c) the result of the exact formula (5.8) as a red solid line and of the approximation (5.9) in black. The two are in excellent agreement for $n > 50$.

Measurement of ε' I now explain how we directly measure the real Rydberg population $\tilde{P}_r$ and the error rate ε' by combining two measurements. After performing a Rabi π-pulse of efficiency $\tilde{P}_r$, we measure either:

[6] At finite temperature black-body radiation increases the depopulation rate of $|r\rangle$, but by transferring population to neighboring long-lived Rydberg states, and thus it hardly affects the rate at which $|g\rangle$ gets populated.

- the Rydberg population $P_r \approx (1-\varepsilon')\tilde{P}_r$ with the regular detection method.

- the proportion of Rydberg atoms being recaptured $\varepsilon'\tilde{P}_r$, by removing all atoms that remained in $|g\rangle$ just after the Rydberg excitation. We neglect the small terms of order $\varepsilon\varepsilon'\tilde{P}_r$ and $\varepsilon\tilde{P}_g$.

The latter is achieved by shining a push-out beam ($F = 2 \leftrightarrow F' = 3$), together with a repumper beam ($F = 1 \leftrightarrow F' = 2$), during $4\,\mu$s removing with an efficiency of 99.6 % any ground-state atoms. If an atom is observed in the final fluorescence image, it has necessarily decayed back from $|r\rangle$ and been recaptured. The measured ε', obtained for Rydberg states ranging from $n = 20$ to 90, are shown as red disks in Fig. 5.7(c). The values are in good agreement with the expected n^{-3}-scaling and our numerical models. The measured values are slightly affected by the $4\,\mu$s push-out time that also removes atoms which have decayed during this interval. We can simply estimate a lower bound to the measured ε' by calculating the integral of Eq. (5.8) starting not at $t = 0$ (upper bound, red solid line) but at $t = 4\,\mu$s (lower bound, red dashed line).

In our experiments, we typically use Rydberg states with principal quantum number $n > 50$, and therefore the false negative rate is limited to $\varepsilon' < 0.05$. This error becomes more severe with tweezers schemes also trapping Rydberg states as proposed by Zhang, Robicheaux, and Saffman [2011]. To improve this detection method, one could consider, e.g, ionizing the Rydberg atoms by applying a strong electric field [Löw *et al.*, 2012].

5.3 Damping of Rabi oscillations

I now turn to effects that lead to a decreasing amplitude of the Rabi oscillation when the excitation time τ increases. We do not distinguish between effects causing the damping when we average many experiments (due to dephasing between different runs) or the one already affecting a single shot Rabi oscillation. The main sources of decoherence are: the Doppler effect, the spontaneous emission from $|e\rangle$, and the phase noise of the excitation lasers. I describe models for each imperfection and compare their predictions to experiments where the magnitude of a specific deleterious effect is increased on purpose.

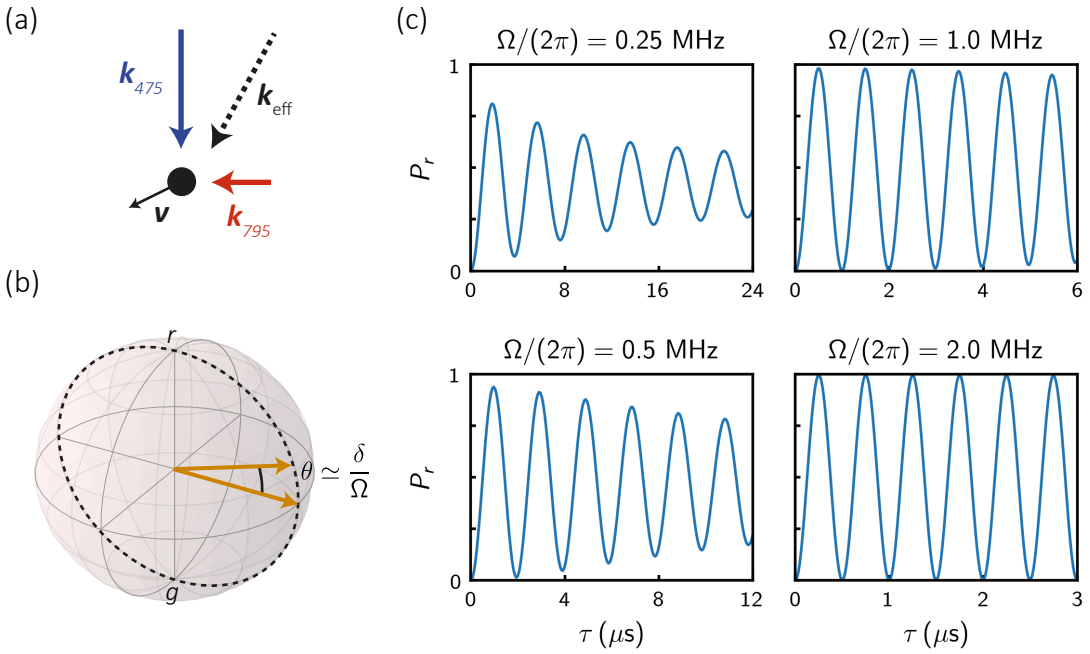

Figure 5.8: Doppler effect. (a) The atom temperature ($T = 30\,\mu$K) gives a shot-to-shot variation of the atom velocity v. Through the Doppler effect, this translates in a detuning δ of the excitation lasers varying for each experiment. (b) In the Bloch sphere picture, the effective magnetic field points away from the equator with an angle given by the ratio of detuning δ over the driving strength Ω. (c) Simulated Rabi oscillations at various $\Omega/(2\pi)$.

5.3.1 Doppler effect

A first contribution to damping is the Doppler effect: for each experimental run, the atom has a different velocity v related to its temperature T, which, through the Doppler effect, translates into a spread of two-photon detuning δ. In the Bloch sphere picture, it is equivalent to a shot-to-shot fluctuation of the longitudinal magnetic field $B_z \propto \delta$. If the spread in detuning is comparable to the Rabi frequency Ω, it gives rise to a strong damping of the Rabi oscillation.

In our setup, for exciting Rydberg $D_{3/2}$ states, the two excitation lasers with wavevectors $\mathbf{k}_{795}$ and $\mathbf{k}_{475}$ are orthogonal to each other, resulting in an effective wavevector of magnitude $k_{\text{eff}} \simeq 1.5 \times 10^7$ m^{-1}. A temperature $T = 30\ \mu$K corresponds to a one-dimensional r.m.s. velocity spread $\Delta v = \sqrt{k_B T/m} \simeq 0.05\,$m/s and the two-photon detuning is thus a random variable with a centered Gaussian probability distribution of standard deviation $k_{\text{eff}}\Delta v \sim 2\pi \times 120$ kHz. Figure 5.8 shows the calculated influence of the Doppler effect for various Rabi frequencies $\Omega/(2\pi)$: below 1 MHz there is a strong damping, while from 1 MHz up the effect is hardly noticeable.

A first route to diminish the Doppler effect is to use counter-propagating beams, instead of orthogonal ones, which will decrease the effective wavevector k_{eff}. Nevertheless, we chose to have excitation beams with polarization coupling only the stretched Zeeman sublevels of the ground, intermediate and Rydberg states. This constraint precludes the use of counter-propagating beams for the specific Rydberg state $\left|nD_{3/2}, m_J = 3/2\right\rangle$, but it is possible with $\left|nS_{1/2}\right\rangle$ [Bernien *et al.*, 2017; Kim *et al.*, 2018] and $\left|nD_{5/2}\right\rangle$ states [Maller *et al.*, 2015]. If we exclude more technically demanding ways to substantially decrease the Doppler effect, e.g., by using three-photon excitation [Ryabtsev *et al.*, 2011] or reducing the temperature by cooling the atom to the tweezers ground-state [Kaufman, Lester, and Regal, 2012; Thompson *et al.*, 2013b], the above results indicate that one should use high Rabi frequencies.

5.3.2 Spontaneous emission from the intermediate state

The coherent two-photon coupling from the ground-state $|g\rangle$ to the Rydberg level $|r\rangle$ relies on the adiabatic elimination of the short-lived excited state $|e\rangle$ for $\Delta \gg \Omega_{475}, \Omega_{795}$ (we usually work with $\Delta/(2\pi) = 740$ MHz). Nevertheless, the spontaneous emission is not strictly suppressed but reduced to an effective lifetime τ reading:

$$\frac{1}{\tau} = \Gamma \times \frac{\Omega_{795}^2 + \Omega_{475}^2}{4\Delta^2} \tag{5.10}$$

with $\Gamma = 2\pi \times 5.75$ MHz the radiative decay rate of $|e\rangle$. We can define a quality factor $Q = 2\pi \times \Omega\,\tau$, which is the number of oscillations performed at a Rabi frequency $\Omega = \Omega_{795}\Omega_{475}/(2\Delta)$ during the time τ. Q is maximal for equal drives $\Omega_{795} = \Omega_{475}$, but the Rabi coupling is then limited by the 475 nm coupling strength. Larger Rabi frequencies Ω are achieved by increasing the 795 nm power, at the expense of a smaller Q. For example:

- for the optimal $\Omega_{795} = \Omega_{475} = 2\pi \times 35$ MHz, we calculate $\tau = 25\,\mu$s and $\Omega/(2\pi) = 0.8$ MHz, giving $Q = 20$.
- for the larger $\Omega_{795}/(2\pi) = 210$ MHz, we find $\tau = 1.3\,\mu$s and $\Omega/(2\pi) = 5.0$ MHz, giving $Q = 6.3$.

The Q-factor gives a good estimate of the influence of spontaneous emission, but it neglects the different decay channels from $|e\rangle$ to the various $5S_{1/2}$ levels: there is a probability 1/3 to go back to $|g\rangle$ and a probability 2/3 to go to 'spectator' states $|g'\rangle$ not coupled by the excitation lasers. In addition to the loss of atomic coherence,

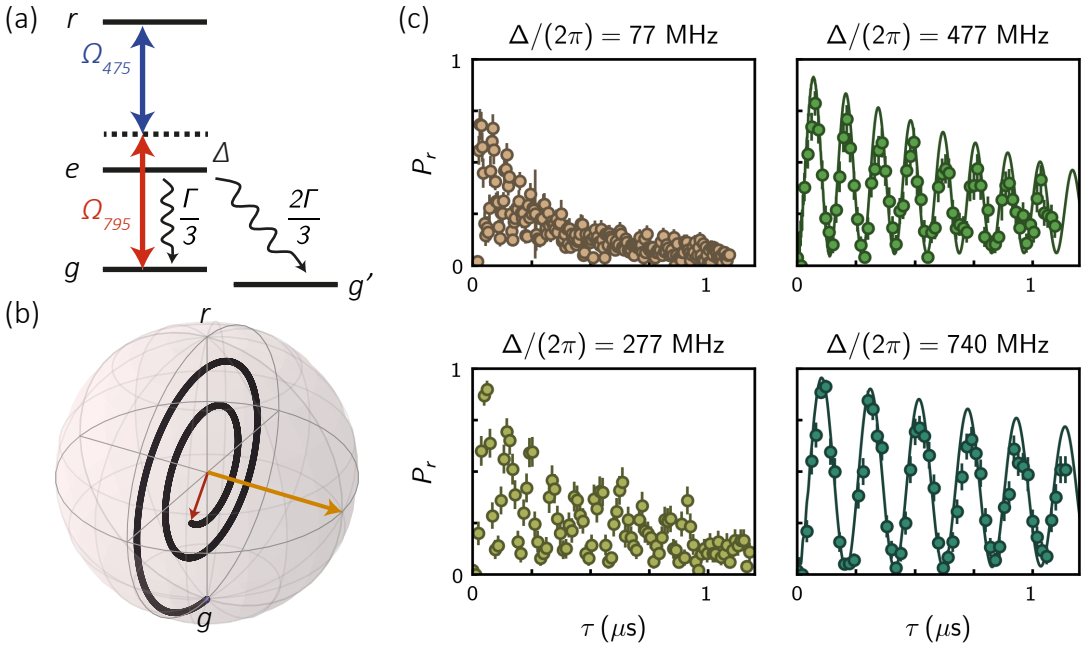

Figure 5.9: Spontaneous emission. (a) The intermediate state $|e\rangle$ decays back to the initial ground-state level $|g\rangle$ or to other spectator states $|g'\rangle$ with a rate $\Gamma/3$ and $2\Gamma/3$. (b) In the Bloch sphere picture, the loss of atomic coherence and the escape of population out of $\{|g\rangle, |r\rangle\}$ due to the depumping to $|g'\rangle$ is represented by a decaying amplitude of the state vector (red arrow). (c) Measured Rabi oscillations for different intermediate detuning Δ with $\Omega_{475}/(2\pi) = 35$ MHz and $\Omega_{795}/(2\pi) = 210$ MHz. The results of the optical Bloch equation, using the independently measured parameters, are shown as a solid line for the two largest detuning Δ.

spontaneous emission also depumps the atom to $|g'\rangle$. I illustrate this effect in Fig. 5.9 with a set of experiments performed with various intermediate detuning Δ and fixed couplings $\Omega_{475}/(2\pi) = 35$ MHz and $\Omega_{795}/(2\pi) = 210$ MHz. The latter was chosen particularly large to enhance the role of spontaneous emission. We clearly observe a stronger damping when Δ is reduced and a characteristic asymmetry: the successive maxima of P_r become significantly smaller, while the minima remain close to zero due to the depumping to the dark states $|g'\rangle$, which are not differentiated from $|g\rangle$ in our fluorescence measurement.

We now try to numerically reproduce the effect of spontaneous emission. As done already in Miroshnychenko *et al.* [2010], we use a 4-level model of the atom ($|g\rangle$, $|g'\rangle$, $|e\rangle$ and $|r\rangle$) and solve the optical Bloch equations (OBEs) for the density matrix ρ:

$$\frac{\mathrm{d}\rho}{\mathrm{d}t} = \frac{1}{i\hbar}[H, \rho] + \mathcal{L}[\rho] \tag{5.11}$$

where the Hamiltonian reads, in the rotating wave approximation:

$$\begin{aligned} H/\hbar &= \frac{\Omega_{795}}{2}\left(|g\rangle\langle e| + |e\rangle\langle g|\right) + \frac{\Omega_{475}}{2}\left(|e\rangle\langle r| + |r\rangle\langle e|\right) \\ &\quad -\Delta\,|e\rangle\langle e| - \delta\,|r\rangle\langle r|\,. \end{aligned} \tag{5.12}$$

with the two-photon detuning $\delta = -\left(\Omega_{795}^2 - \Omega_{475}^2\right)/(4\Delta)$ adjusted to compensate for the light-shifts. The dissipator has the Lindblad form:

$$\mathcal{L}[\rho] = \sum_{i=g,g'} \frac{\Gamma_i}{2}\big(2\,|i\rangle\langle e|\,\rho\,|e\rangle\langle i| - |e\rangle\langle e|\,\rho - \rho\,|e\rangle\langle e|\,\big), \tag{5.13}$$

with $\Gamma_g = \Gamma/3$ and $\Gamma_{g'} = 2\Gamma/3$. Here, decay of $|r\rangle$ is neglected. The probability to be in the Rydberg state is $P_r = \rho_{rr}$ and is shown as a solid line in Fig. 5.9 for the two largest detunings and are in very good agreement (without adjustable parameters) with the experimental data. We note that the problem of spontaneous emission is avoided when using a direct single-photon excitation scheme [Hankin *et al.*, 2014] or reduced by a factor ~ 4 when choosing the intermediate $6P$ state with a natural linewidth of 1.3 MHz [Levine *et al.*, 2018].

5.3.3 Laser phase noise

So far we have considered that the excitation lasers were purely monochromatic with perfectly stable laser phases $\phi_{795}(t)$ and $\phi_{475}(t)$. In fact, the phases of the two lasers fluctuate in time such that the effective two-photon Rabi coupling is given by:

$$\Omega(t) = |\Omega|e^{i\phi(t)} \quad \text{with} \quad \phi(t) = \phi_{795}(t) + \phi_{475}(t) \tag{5.14}$$

In the Bloch sphere representation, see Fig. 5.10, the azimuthal angle ϕ of the effective magnetic field fluctuates in time around the equator (for a resonant drive $\delta = 0$). It thus affects the trajectory of the state vector and leads to damping of a Rabi oscillation when averaged over many realizations of the noise. Let us first consider a purely sinusoidal phase modulation $\phi(t) = A\sin(2\pi f t)$, where f is the Fourier frequency and $A \ll 1$ is the small modulation amplitude. The effect of this time-varying phase on the Rabi oscillation depends on both f and Ω:

- $2\pi f \ll \Omega$: the axis of rotation moves very slowly compared to the angular frequency of the state vector. The latter always stays on the great circle generated by the instantaneous axis, or stated otherwise, the atomic coherence

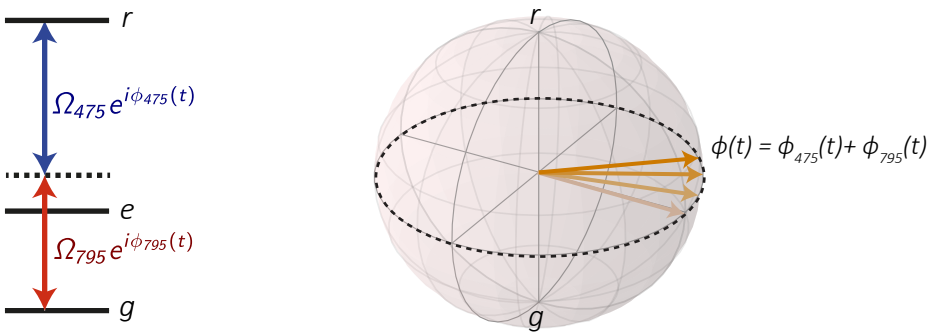

Figure 5.10: Laser phase noise on the Bloch sphere. Left: time varying phases of the excitation lasers. Right: Bloch sphere representation where the azimuthal angle of the rotation axis (effective magnetic field) is the total phase ϕ of the two excitation lasers.

follows adiabatically the laser phases.

- $2\pi f \gg \Omega$: the atom do not respond to the very fast variations of the laser phases and the state vector simply rotates around the averaged rotation axis.
- $2\pi f \sim \Omega$: the modulation affects maximally the Rabi oscillation.

The interesting quantity is thus the power spectral density of phase noise $S_\phi(f)$, or the related spectral density of *frequency* noise $S_\nu(f) = f^2 S_\phi(f)$ [Riehle, 2004], and particularly their components close to the Rabi frequency, typically around $f = 1$ MHz.

I now give three remarks. Firstly, the laser linewidth is often used to estimate the influence of phase noise. I emphasize that this quantity is not very relevant for us as it does not give any information about the spectral distribution of noise. Secondly, our situation is drastically different than in another area where phase noise is an important issue: optical clocks [Ludlow *et al.*, 2015]. There, interrogation of the clock transition is performed with a very weak Rabi coupling around 1 Hz, such that low frequency phase noise is critical. The technical developments engineered in this field, as in Zhang *et al.* [2017], are thus not necessarily relevant. Thirdly, the frequency stabilization of the lasers relies on an active feedback loop using the Pound-Drever-Hall (PDH) error signal from the ultra-stable cavity. The technique is very efficient to reject low-frequency noise outside the bandwidth of the loop (typically ~ 1 MHz), but the latter is too limited to decrease the high-frequency contribution important for our fast Rabi oscillations.

In the following I explain how we estimate $S_\nu(f)$ and then include it in a numerical model to reproduce the damping. In a third paragraph, I make a short digression to discuss which quantity (S_ν, or S_ϕ, or ...) is directly proportional to the damping.

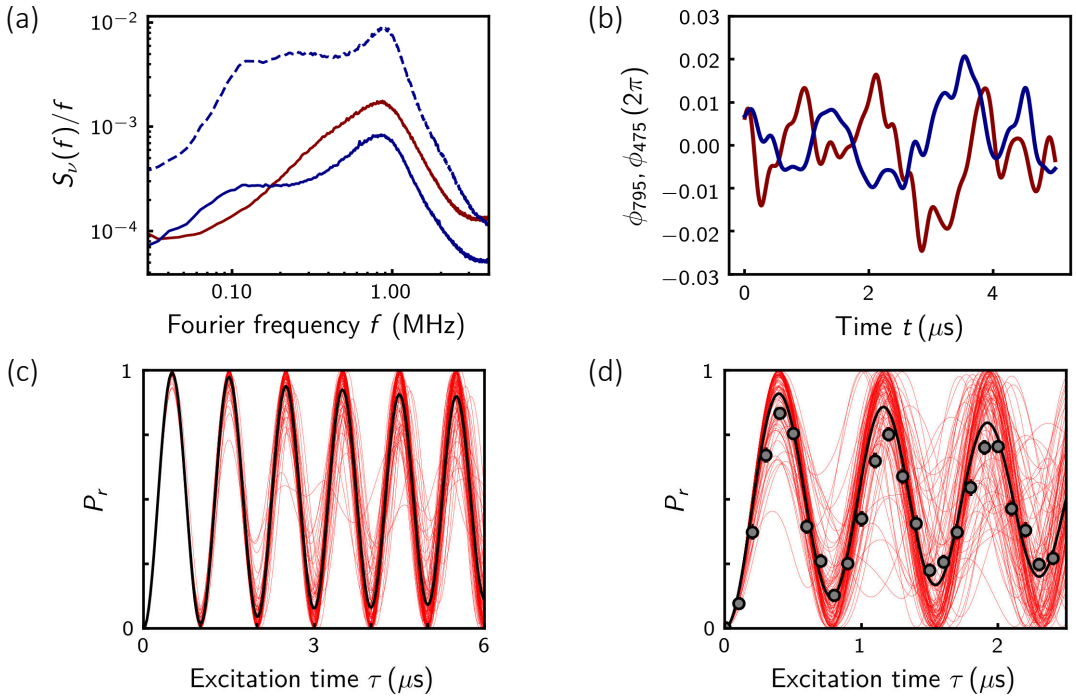

Figure 5.11: Spectral noise density and simulations. (a) Estimated spectral density $S_\nu(f)/f$ of the frequency noise of the 795 nm (red) and 950 nm laser (blue). Solid (dashed) lines: usual (enhanced) noise. (b) Calculated random processes $\phi_i(t)$. (c) Many simulated Rabi oscillations (thin lines), each for a given realization of $\phi_i(t)$, are averaged (thick black line). (d) With intentional extra noise in the 950 nm laser, the damping is increased, and the simulation compares well with the experimental data (dark disks).

Finally, I present possible improvements of the current setup to solve the issue of laser phase noise and the recent progress in the Harvard group [Levine *et al.*, 2018].

Spectral density of frequency noise Measuring the spectral density of noise directly is not an easy task, but we obtain a reasonable estimate of $S_\nu(f)$ for f above acoustic frequencies, where the cavity noise is negligible, by analyzing the in-loop PDH error signal with an RF spectrum analyzer. The *voltage* noise spectral density $S_V(f)$ allows to retrieve $S_\nu(f)$, knowing the slope K of the PDH error signal and taking into account the storage time of light in the cavity, or equivalently its linewidth $\nu_{\text{cav}} = 75$ kHz, causing a roll-off of the cavity response (see, e.g., Tarallo [2009], page 17):

$$S_V(f) = S_\nu(f) \times \frac{K}{1 + 4(f/\nu_{\text{cav}})^2}. \tag{5.15}$$

Figure 5.11(a) shows the estimated $S_{\nu_i}(f)/f$ (I explain latter why I rescale it by f) for the 950 and 795 nm lasers[7] measured when operating the experiment. We observe a broad maximum of noise around 1 MHz, due to the limited feedback loop bandwidth.

Numerical simulation In order to assess quantitatively the influence of laser phase noise, rather than calculating analytically a sensitivity function (see, e.g., Martin [2013]), we solve the Schrödinger equation of a two-level system driven by the time-dependent Rabi coupling given in Eq. (5.14), each time for a different realization of the random processes $\phi_{795}(t)$ and $\phi_{475}(t) = 2\phi_{950}(t)$[8]. The latter are drawn according to the measured $S_\phi(f)$ (see e.g. Cladé [2004], page 65):

$$\phi(t) = \sum_f A\cos(2\pi f t)df \quad \text{with} \quad A = 2\sqrt{S_\phi(f)}. \tag{5.16}$$

Examples are shown in Fig. 5.11(b). We then average the results of the simulation over typically 500 realizations of the phase noise. In Fig. 5.11(c), I show all individual Rabi oscillations (thin red lines) and their average (solid black line) for our typical spectral noise density and a Rabi frequency of 1 MHz. We observe a slow damping of the oscillation and can extract a Q-factor of ~ 24, similar to the best-case spontaneous emission (see previous Section). To experimentally isolate the effect of phase noise and compare it to our numerical simulation, we increase the spectral noise density of the 475 nm laser, now shown as a dashed line in Fig. 5.11(a). In these conditions, the experimental Rabi oscillation damping is increased and is in good agreement with the numerical simulation, as seen in Fig. 5.11(d).

Different types of noise I now justify why the quantity $S_\nu(f)/f$ is shown in Fig. 5.11 and not $S_\nu(f)$ or $S_\phi(f) = S_\nu(f)/f^2$. We already understand that the damping of a Rabi oscillation, quantified by its Q-factor, depends only on the spectral density of noise at a Fourier frequency f around the Rabi frequency $\Omega/(2\pi)$. Going a step further, I repeat the previously described numerical simulations by varying the Rabi frequency Ω, and the type of frequency noise $S_\upsilon(f) = Kf^\alpha$, $\alpha \in \{0, 1, 2\}$ (respectively known as white frequency, flicker phase and white phase noise [Riehle, 2004]). For each parameters, the averaged Rabi oscillation is fitted by a damped sine and we extract a

[7] We use the 950 nm beam for frequency stabilization and not the frequency-doubled 475 nm one.
[8] We consider that the frequency components of 950 nm laser phase are within the bandwidth of the SHG cavity used for frequency doubling.

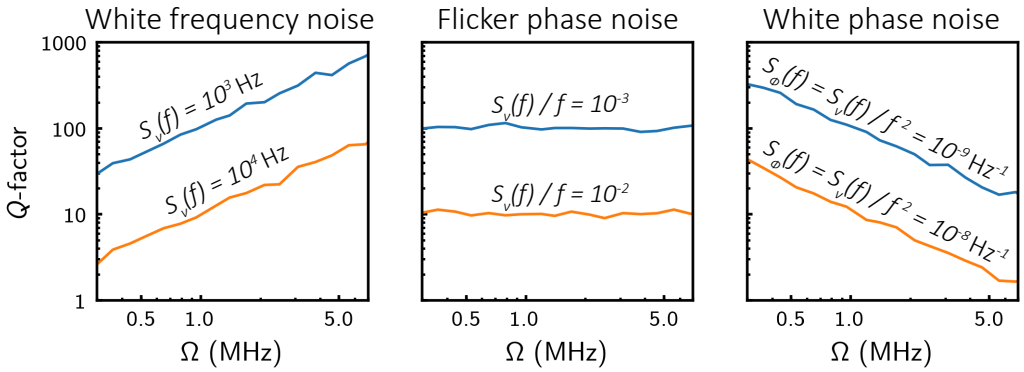

Figure 5.12: Various type of noises. Q-factor of a Rabi oscillation at frequency Ω for elementary types of noise $S_\nu(f) = Kf^\alpha$ with $\alpha = 0, 1, 2$ (left to right). Orange (blue) curves: $S_\nu(1\,\mathrm{MHz}) = 10^4$ Hz (10^3 Hz).

Q-factor which is shown in Fig. 5.12. We observe the simple empirical relation:

$$Q(\Omega = 2\pi f) \simeq 0.1 \times \left(\frac{S_\nu(f)}{f}\right)^{-1} \tag{5.17}$$

In conclusion, I show $S_\nu(f)/f$ in Fig. 5.11 because we can then directly read the expected damping as a function of the Rabi frequency.

Solution Finally, I discuss the possible solutions to increase the deleterious effect of phase noise. A first step is to optimize the PID controller settings, while observing on a spectrum analyzer the spectral density of voltage noise from the PDH signal, to avoid adding too much noise in the MHz range. Then, we took care to work with minimal current modulation fed to the 950 nm diode, as it gives rise to frequency modulation and noise of the laser beam sent to the atom.

Finally, it is possible to use the ULE cavity not only as an active frequency discriminator but also as a passive low-pass filter with a transfer function:

$$S_\nu^{\mathrm{filt.}}(f) = \frac{S_\nu(f)}{1 + 4(f/\nu_{\mathrm{cav}})^2} \tag{5.18}$$

with a frequency cut-off given by its linewidth ν_{cav} (full width at half-maximum). The light transmitted by the cavity exhibits a decreased noise at high Fourier frequencies, where the active feedback loop is inefficient, and can be used to inject another laser diode, which then benefits from its spectral purity. This technique was first reported by Hald and Ruseva [2005] and has been recently implemented[9] in the Harvard group

[9] See Nazarova *et al.* [2008] and Akerman *et al.* [2015] for earlier implementations in other areas.

leading to a significant increase in coherence time from 7 to 27 μs for a 2 MHz Rabi oscillation [Levine *et al.*, 2018]. The fourfold increase in Q-factor (from 14 to 54) indicates at least a similar reduction of $S_\nu(f)$ according to Eq. (5.17). In fact, it is much larger (~ 65) as seen by inserting their reported $\nu_{\text{cav}} = 500$ kHz in Eq. (5.18), and the remaining damping probably comes from other sources.

5.3.4 Other possible effects

Several other effects can in principle contribute to damping and dephasing of the Rabi oscillations. First, the Rydberg states have a finite lifetime due to spontaneous emission leading to decay to low-lying excited states and to black-body radiation transferring the atom to close-by Rydberg states [Beterov *et al.*, 2009]. We have solved the OBEs with and without including the finite lifetime of Rydberg states $n > 50$ and observed no significant differences on our experimental timescale of a few microseconds for the single-atom Rabi oscillation. Thus, so far, this finite lifetime is not a limitation in our setup, but should become the ultimate limit in coherence time once all previously described sources will be eliminated.

Then, due to the random thermal motion of the atom in the optical tweezers, it explores the intensity profile of the excitation beams and experiences different Rabi frequencies and light-shifts from shot to shot. Along the x-direction, where the 475 nm excitation laser beam waist of 24 μm is minimal and the Gaussian distribution width of the atom position is maximal ($\sigma_x \approx 1\,\mu$m), the relative standard variation of Rabi frequencies are only 2.5×10^{-3}. We have checked that for our experimental parameters, this effect should be negligible unless the excitation beams are strongly misaligned. Another dephasing mechanism is the shot-to-shot variation in the pulse areas of the excitation beams. We have estimated the relative fluctuations of the intensity of the pulses to be below 0.2% rms, which does not lead to any measurable dephasing over our experimental timescales.

Finally, stray transverse electric fields leading to mixing between different Zeeman sublevels of the targeted Rydberg state could lead to a degradation of the Rabi oscillation, as $|g\rangle$ would be coupled to several Rydberg states with different coupling strengths. However, using the set of eight electrodes under vacuum, we zero out the electric field to better than $|E| < 5\,$mV/cm by performing Stark spectroscopy on high-n Rydberg states (typically $n \sim 100$). For such low values of E, the expected effect of stray fields is negligible.

5.4 Prospects for improvements

In this section, I first combine all the effects previously described, explaining the different behaviors presented in Fig. 5.1. Using these numerical results, I describe how we plan to improve the current excitation laser setup.

5.4.1 Damping: a combination of all effects

Having developed a quantitative modeling of each of the experimentally relevant imperfections listed above, we can now include them all in a global simulation. All parameters (Rabi couplings Ω_{795}, Ω_{475}, detuning Δ, detection errors $(\varepsilon, \varepsilon')$, atomic temperature T, laser phase noises S_ν) are given their independently measured values. We draw fluctuating parameters according to their respective distributions, integrate the OBEs with these parameters, and then average over typically 500 realizations. Figure 5.13(a) shows a comparison between an experimental Rabi oscillation (for $\Omega/(2\pi) = 4.8$ MHz, disks) and a parameter-free simulation (solid line) including all effects detailed in the previous Section. Let us note the difference with Fig. 5.1 presented at the beginning of this chapter, where the Rabi oscillation was reproduced by a fitting function, in contrast to the present ab-initio calculations.

Figure 5.13(b) shows how the different effects depend on the Rabi frequency Ω. The simulations are performed for a fixed $\Omega_{475}/(2\pi) = 35$ MHz and a varying Ω_{795}. To characterize the asymmetric damping of the Rabi oscillation, I use, instead of a Q-factor, the oscillation amplitude during the fifth half-period [indicated in Fig. 5.13(a)]. We observe that the damping is minimized for $\Omega/(2\pi) \approx 2$ MHz and that:

- the Doppler effect (dash-dotted line) is the dominant source of damping for $\Omega/(2\pi) < 0.7$ MHz,
- the spontaneous emission (dashed line) is minimized at $\Omega/(2\pi) = 0.8$ MHz (when $\Omega_{475} = \Omega_{795}$) and becomes dominant at large coupling strength.
- the phase noise influence (dotted line) peaks at $\Omega/(2\pi) = 1$ MHz, but remains currently at the same level that the two other sources.

Analyzing a selection of Rabi oscillations performed over the course of this thesis (red disks), we obtain a good agreement with these predictions, except around 1 MHz.

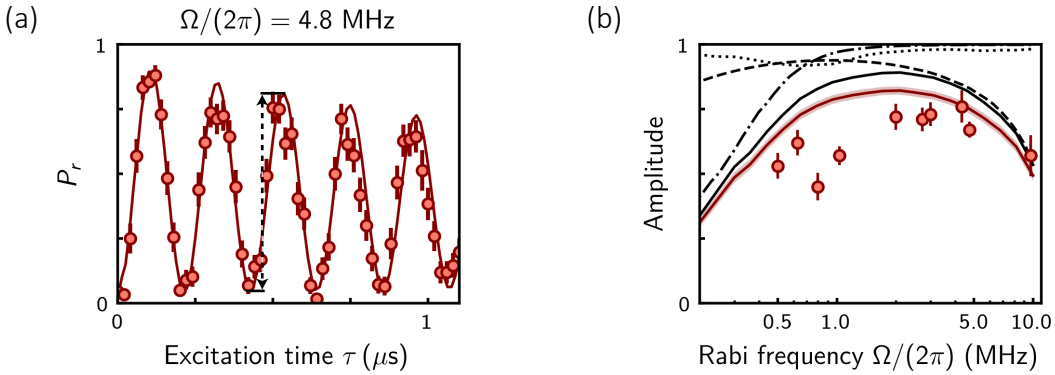

Figure 5.13: Combining all effects. (a) Experimental Rabi oscillation and a parameter-free simulation. The arrow indicates the amplitude on the 5th half-period used as an indicator characterizing the asymmetric damping. (b) Influence of the Rabi frequency Ω on the damping. The curves show simulations for Doppler effect (dash-dotted line), spontaneous emission (dashed line), laser phase noise (dotted line), combining all of them (solid black line) and adding the detection errors (solid red line). The shading on the latter curve corresponds to s.e.m. of the Monte-Carlo simulation for 600 runs. The red disks are experimental results.

5.4.2 Future improvements

For each damping source, we have already detailed possible solutions to improve the coherence time of the Rabi oscillation. Here, I present the route that we should follow in the future. Firstly, we will be interested in Rydberg S states: despite the reduced dipole matrix element compared to D states, we will see in the next chapter that the interaction between two Rydberg S levels is preferable. Another immediate advantage is the reduced Doppler effect as we could use counter-propagating lasers.

Secondly, we will use the *inverted* excitation scheme, changing the intermediate state from the $5P$ to the $6P$ level. The spontaneous emission will be reduced as the radiative decay from the $6P$ state is only 1.3 MHz (5.75 MHz for $5P$). Then, the $|e\rangle \leftrightarrow |r\rangle$ transition is now at a wavelength of 1013 nm, for which high-power laser sources (Ytterbium-doped fiber amplifiers, up to 10 W) are now available allowing large couplings to Rydberg states. Meanwhile, the $|g\rangle \leftrightarrow |e\rangle$ transition is shifted to 420 nm, where we could use a similar laser source than at 475 nm and obtain a few 100 mW of laser power, large enough for strong Rabi coupling to the intermediate state. This solution is the one implemented in the Harvard group and reported in Bernien *et al.* [2017]. Thirdly, the phase noise contribution to decoherence can be suppressed using the ULE cavity as a passive filter and injecting its output in a slave diode [Levine

et al., 2018].

Concerning detection errors, the false positive rate ε (collision with background gas) could be suppressed by working, e.g., in a cryogenic environment, which would have the additional benefit of suppressing the BBR decay of Rydberg atoms. False negative (ε') could be avoided by quickly ionizing Rydberg atoms [Löw *et al.*, 2012] or by mapping $|g\rangle$ and $|r\rangle$ to the two hyperfine ground-state levels [Wilk *et al.*, 2010]. Let us note that detection errors are not as detrimental as decoherence since they do not affect the unitary evolution of the quantum system.

5.5 Conclusion

In this chapter, we have studied how the coherent coupling between a ground-state and a Rydberg level of a single atom could be affected in many ways by physical and technical limitations. We developed models for each detection error and dephasing sources obtaining good quantitative agreements with experimental observations. The conclusion, from our study and the recent results obtained by Levine *et al.* [2018], is to upgrade the optical setups to reach longer atomic coherence times between the ground and Rydberg level.

The latter is especially important for the quantum simulation of Ising models where a spin-1/2 is encoded between $|g\rangle$ and $|r\rangle$, which is the focus of this second part of the thesis. Finally, let us remark that the coherence time between $|g\rangle$ and $|r\rangle$ does not always matter. For example, in the third part of this thesis, we will implement XY quantum magnets for which the spin-1/2 is encoded between two Rydberg states and we only use the excitation lasers to prepare the atoms in $|r\rangle$ quickly and efficiently. If this is accomplished with a Rabi π-pulse, we are back to the problem of minimizing the decoherence of Rabi oscillations during the first half-period. But, other schemes can be used, such as STIRAP (see Section 7.1.1) and I will demonstrate excellent excitation to Rydberg S and D states (with an efficiency > 95 %), even with the current excitation scheme.

Chapter 6

Implementing the Ising coupling using the van der Waals interaction between $nD_{3/2}$ states

Contents

In Chapter 4, we stated that a quantum Ising model could be implemented by driving an ensemble of atoms from their ground state $|g\rangle$ to a single Rydberg level $|r\rangle$ from the Rydberg manifold. Crucially, the mapping requires that all other Rydberg states $|r'\rangle$ are decoupled from the dynamics. Already in a two-atom system, shown in Fig. 6.1, the dipole-dipole interaction $\hat{H}_{dd}$ challenges this simplification as it couples the pair-state $|rr\rangle$ to many others $|r'r''\rangle$. Nonetheless, the spin-1/2 approximation is restored in the van der Waals regime, where the mixing with other pair-states is negligible, such that they can all be ignored. The interaction only amounts to a simple van der Waals energy cost $V = C_6/R^6$ of having two Rydberg atoms separated by a distance R; and can be considered either as an Ising coupling, or giving rise to a

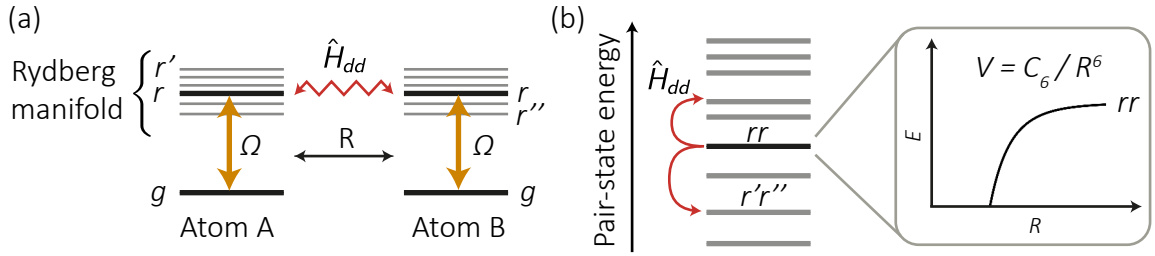

Figure 6.1: The van der Waals interaction. (a) A ground-state level $|g\rangle$ and a specific state $|r\rangle$ from the Rydberg manifold defines a spin-1/2 driven with a coupling strength Ω by the excitation lasers. Two atoms, separated by a distance R, interact through the dipole-dipole Hamiltonian. (b) $\hat{H}_{dd}$ couples $|rr\rangle$ to other pair-states $|r'r''\rangle$. In the van der Waals regime, the state $|rr\rangle$ is largely detuned from any $|r'r''\rangle$, such that it does not mix with them but its energy is modified by a van der Waals shift $V = C_6/R^6$.

Rydberg blockade volume of size $R_b = (C_6/\hbar\Omega)^{1/6}$, inside which only a single Rydberg excitation can be created.

Motivation The validity of the Rydberg blockade picture has been disputed in many theoretical works predicting its failure due to various competing processes, occuring already in two-atom system, — molecular resonances [Derevianko *et al.*, 2015], Zeeman degeneracy [Walker and Saffman, 2005, 2008], or in presence of a magnetic field, competition with the Zeeman effect [Vermersch, Glaetzle, and Zoller, 2015]—, or when a third atom is considered [Pohl and Berman, 2009; Cano and Fortágh, 2012]. Motivated by these studies, Barredo *et al.* [2014] performed experiments on a system of three atoms all within a blockade volume, and concluded positively on the efficiency of the Rydberg blockade mechanism.

Going a step further than this fully blockaded regime, we then studied a situation, reported in Section 4.1, where the blockade volume extends only over a fraction of large 2D arrays [Labuhn *et al.*, 2016]. Figure 6.2(a) shows the evolution of the Rydberg fraction f_r (the proportion of atoms excited to Rydberg states) as a function of the excitation lasers pulse area $\Omega\tau$, for different geometries and choice of Rydberg states. Comparing the experimental data with a numerical simulation of the spin-1/2 model (solid lines), we obtain an excellent agreement for the quasi-linear chain of 30 traps (left), but observe clear deviations for the ring of 8 atoms and on the 7×7 square array. These deviations imply that our interacting Rydberg atoms do not map perfectly on simple spin-1/2 particles. As the Rydberg fraction increases above the prediction of the model, it indicates a failure of the Rydberg blockade.

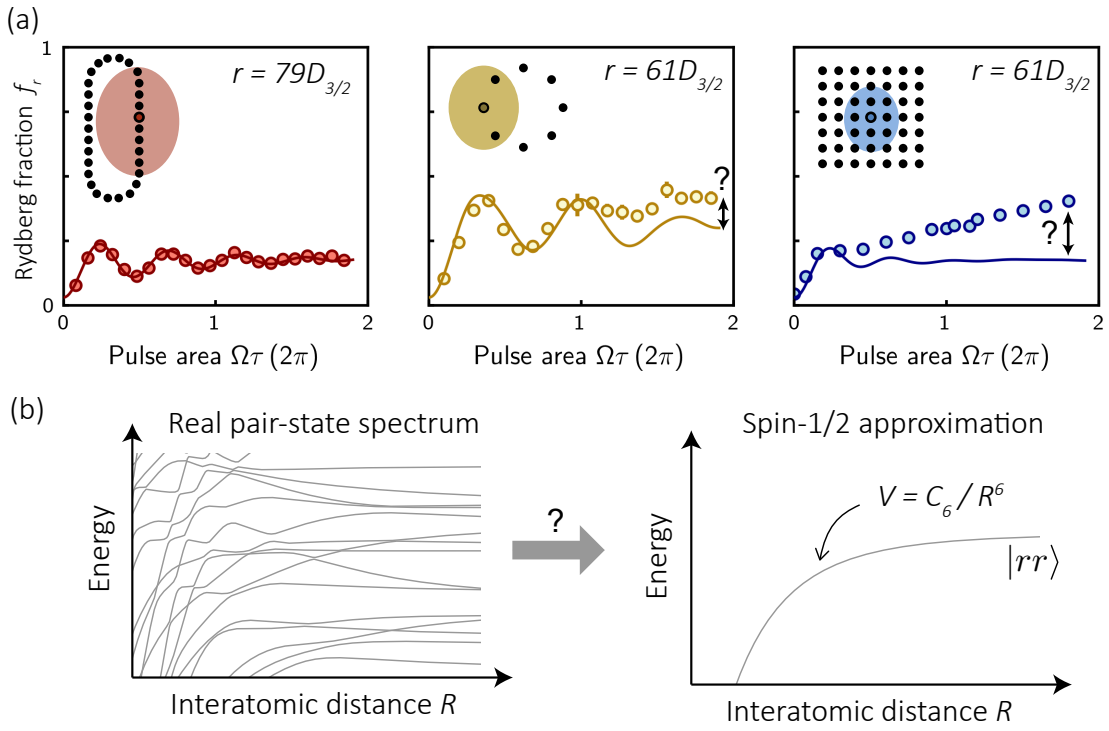

Figure 6.2: Failure of spin-1/2 mapping. (a) Experiments reported in Labuhn *et al.* [2016]: the excitation lasers are switched on with a strength Ω for a variable time τ, the fraction f_r of Rydberg excitations is shown as a function of the pulse area $\Omega\tau$. Each inset shows the atomic array and the extent of the Rydberg blockade volume. In two cases, the data deviate from numerical simulations of a spin-1/2 model (solid lines). (b) We will show that the deviations originate from the approximation of the real pair-state spectrum (left panel, worst-case scenario) by a single potential curve (right panel).

Following these observations, we collaborated with Prof. Hans-Peter Büchler and Sebastian Weber from the University of Stuttgart to find the origin of this failure. They have recently developed the open-source *pairinteraction* software [Weber *et al.*, 2017] (see also the one by Šibalić *et al.* [2016] from the University of Durham), which can calculate the eigenstates of $\hat{H}_{dd}$ by full diagonalization, while taking into account external magnetic and electric fields. Figure 6.2(b) shows an example of pair-state potentials calculated with the *pairinteraction* software in a particularly complicated scenario, which we will encounter in this chapter. The mapping of Rydberg atoms to spin-1/2 particles requires that this can be replaced by a single potential curve [Fig. 6.2(b), right panel]. By considering only a two-atom system, they pointed out that the failure could be caused by a too high magnetic field $B_z = +6.9$ G, applied to perform optical pumping into the initial state $|g\rangle$ and to lift the Zeeman degeneracy of

the Rydberg manifold, and chosen at this value for historical reasons. Thereupon, we decreased B_z to 3.5 G, repeated the experiments, and observed a much better agreement, as we will see at the end of this chapter.

Goal I will describe the origin of the Rydberg blockade failure by going through more and more subtle modifications of the pair-state atomic structure caused by the dipole-dipole Hamiltonian and external fields. This will make this chapter quite technical. We will see that Rydberg nD states are particularly affected, and I remind the reader that our original motivation to use these states is the larger driving strength achievable with our excitation scheme (see Chapter 5).

This chapter is organized as follows. First, in Section 6.1, I remind how the dipole-dipole coupling of two atoms in the same Rydberg state ideally gives rise to a simple van der Waals shift, and show spectroscopic measurement of the latter. In Section 6.2, I study the validity of the van der Waals approximation and the spin-1/2 mapping in a quite simple configuration where two atoms are aligned with the quantization axis and external fields are neglected. I will focus on two states, a $nS_{1/2}$ state and the $58D_{3/2}$ state, illustrating two very different situations. In Section 6.3, we will consider the general case with non-zero external fields and an angle between the atomic pair and the quantization axis. Using the *pairinteraction* software to perform numerical calculations, we will investigate extensively the pair-state spectrum of the $61D_{3/2}$ state for which we observed the failure of the spin-1/2 approximation in Fig. 6.2. Finally, in Section 6.4, having identified the origin of these deviations, we will demonstrate a much better agreement of the dynamics of the many-body system with the spin-1/2 model. Parts of the material presented in this chapter have been published in de Léséleuc *et al.* [2018b].

6.1 Introduction to van der Waals interaction

I start by briefly presenting the structure of the Rydberg manifold of states of a single atom. Figure 6.3(a) shows the different Rydberg series around the principal quantum number $n = 60$ and how the levels are interleaved due to the difference in quantum defects[1] δ. The fine-structure splitting is ~ 0.5 GHz between the $nP_{1/2}$ and $nP_{3/2}$, and ~ 0.05 GHz between the $nD_{3/2}$ and $nD_{5/2}$ states. Being sub-MHz, we neglect it

[1] They are currently known with a precision of 10^{-6} from measurements performed in the group of Prof. Thomas F. Gallagher [Li *et al.*, 2003; Han *et al.*, 2006], which is important for the precise estimate of the energy defects ΔE.

for the $nF_{5/2}$ and $nF_{7/2}$ states. The hyperfine splitting is also ignored as it is below 300 kHz for $S_{1/2}$ states [Li *et al.*, 2003] and sub-kHz for $D_{3/2}$ states [van Wijngaarden, Li, and Koh, 1993]. We thus express all Rydberg states in the fine basis $|nL_J, m_J\rangle$ where the magnetic quantum number m_J is the projection of the angular momentum $\hat{J}$ on the quantization axis. Recall that the excitation lasers are polarized to couple only to the stretched state ($m_J = J$). I now present the effect on a single atom of external magnetic $\mathbf{B}$ and electric $\mathbf{E}$ fields.

Zeeman effect $\hat{H}_{\mathrm{Z}}$ splits the Zeeman manifold, shifting the m_J level by $\Delta E_{\mathrm{Z}} = g\mu_B m_J B$, where the g-factor depends on the Rydberg series (we neglect diamagnetic terms here). We usually apply a moderate vertical magnetic field $B_z \simeq 3 - 8$ G, for which $\Delta E_{\mathrm{Z}} \leq 20$ MHz remains smaller than the fine-structure splitting of D states. Transverse magnetic fields (B_x, B_y) are canceled, to avoid mixing the different Zeeman sublevels, by performing microwave spectroscopy between the two hyperfine ground-state.

Stark effect $\hat{H}_{\mathrm{Stark}}$ creates a quadratic Stark shift $\frac{1}{2}\alpha E^2$, where α is the static polarizability (scaling as n^7 and depending also on the Rydberg series) and mixes Rydberg states of different angular momentum L, which induces a permanent electric dipole. The electric field $\mathbf{E}$ thus strongly affects the dipole-dipole interaction and we try to minimize it. Using the extreme sensitivity of large ($n = 100$) Rydberg state to $\mathbf{E}$, we measure and cancel $\mathbf{E}$ to better than 5 mV/cm over a region of $30 \times 30\,\mu\mathrm{m}^2$ using our set of eight electrodes. In this chapter, we will sometimes apply a weak vertical electric field $E_z = 20$ mV/cm to observe its effect on the interaction between a pair of atoms.

6.1.1 Dipole-dipole interaction

Considering now two Rydberg atoms (A and B), we construct the set of *unperturbed* pair-states $|r'_A r''_B\rangle$. The goal of this section is to show how the pair-state $|rr\rangle$, describing two atoms in the *same* Rydberg state[2], is modified by the dipole-dipole interaction:

$$\hat{H}_{dd} = \frac{1}{4\pi\epsilon_0} \frac{\mathbf{d}_A \cdot \mathbf{d}_B - 3(\mathbf{d}_A \cdot \mathbf{n})(\mathbf{d}_B \cdot \mathbf{n})}{R^3}, \tag{6.1}$$

[2]In the third part of this thesis, we will consider two atoms in *different* Rydberg states.

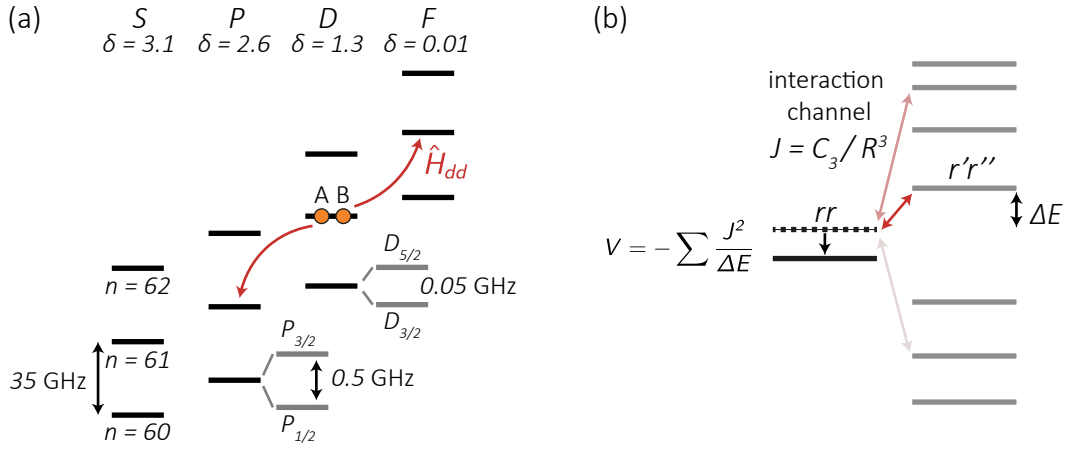

Figure 6.3: Single- and two-atom spectra. (a) S, P, D and F Rydberg series for $n = 60 - 62$, and their quantum defects δ. The fine-structure splittings for P and D states are indicated (not to scale), we neglect the sub-MHz splitting between the $F_{5/2}$ and $F_{7/2}$ states. The Zeeman sublevels are not shown for simplicity. (b) Two atoms in the same Rydberg state $|rr\rangle$ are coupled by $\hat{H}_{dd}$ to many other pair-states $|r'r''\rangle$. The red arrows in (a) shows one of the interaction channel with $|rr\rangle = |nD, nD\rangle$ and $|r'r''\rangle = |nP, nF\rangle$. The detuning between two pair-states is denoted ΔE and the coupling strength J. The contribution of all interaction channels leads to the van der Waals shift V.

where $\mathbf{d}$ is the dipole operator, R the interatomic distance, and $\mathbf{n}$ is a unit vector along the internuclear axis. We denote by θ the angle made by $\mathbf{n}$ with the quantization axis, and refer to it as the *interaction angle*. We can reformulate Eq. (6.1) by expressing $\mathbf{d}$ in terms of its components d^-, d^0 and d^+ on the spherical basis, which respectively decreases, conserves and increases by one unit the magnetic quantum number m_J:

$$\begin{aligned}\hat{H}_{dd} = \frac{1}{4\pi\epsilon_0 R^3}\Big[&\frac{1-3\cos^2\theta}{2}\left(d_A^+ d_B^- + d_A^- d_B^+ + 2d_A^0 d_B^0\right)\\ &+\frac{3}{\sqrt{2}}\sin\theta\cos\theta\left(d_A^+ d_B^0 + d_A^- d_B^0 + d_A^0 d_B^+ + d_A^0 d_B^+\right)\\ &+\frac{3}{2}\sin^2\theta\left(d_A^+ d_B^+ + d_A^- d_B^-\right)\Big]\end{aligned} \tag{6.2}$$

The first group of term conserves the total magnetic number of two atoms $M = m_A + m_B$, the second changes it by $\Delta M = \pm 1$ and the third by $\Delta M = \pm 2$.

We will take into account the action of $\hat{H}_{dd}$ on the pair-state spectrum in three steps of increasing complexity: (i) in Section 6.1.2, we will ignore the details of the various couplings between pair-states and simply state the results of the second-order perturbation theory; (ii) in Section 6.2, we will investigate 'manually' the various

couplings to check the validity of the second-order approximation in the simpler case $\theta = 0$; (iii) in Section 6.3, motivated by the experimental results of Fig. 6.2, we will focus on the specific $61D_{3/2}$ Rydberg state and include all effects, a non-zero interaction angle and external fields, using numerical calculations.

6.1.2 The van der Waals regime

The two-atom Hamiltonian $\hat{H}_{dd}$ couples $|rr\rangle$ to many pair-states $|r'r''\rangle$ as sketched in Fig. 6.3(b). Each $|rr\rangle \leftrightarrow |r'r''\rangle$ coupling defines an interaction channel, characterized by an energy (or Förster) defect $\Delta E = E_{r'r''} - E_{rr}$ and a coupling strength $J = \langle r'r''| \hat{H}_{dd} |rr\rangle = C_3/R^3$. In the limit $J \ll \Delta E$, for all channels, we can apply second-order perturbation theory resulting in a simple shift of the pair-state energy by:

$$V = -\sum_i \frac{J_i^2}{\Delta E_i} = \frac{C_6}{R^6} \quad \text{with} \quad C_6 = -\sum_i \frac{C_{3_i}^2}{\Delta E_i} \tag{6.3}$$

where the sum runs over all interaction channels. In this so-called van der Waals regime of the dipole-dipole interaction, the mixing of $|rr\rangle$ with other pair-states is negligible. In practice, only a few interaction channels significantly contribute to V and it is very instructive to identify them, as done by Reinhard *et al.* [2007] and Walker and Saffman [2008]. It allows us to understand the origin of the van der Waals shift, obtain a good estimate of V and find the limiting cases where the second-order approximation fails. We will perform this identification in Section 6.2 for two extreme cases: the very simple $nS_{1/2}$ states and the *Förster resonance* occurring for the $58D_{3/2}$ state as a specific pair-state is almost degenerate ($\Delta E \ll J$) with $|rr\rangle$.

Scaling laws Beforehand, let us discuss the dependence of the interaction strength with the principal quantum number n. The C_3 and C_6 coefficients scale as:

$$C_3 \propto n^4 \quad \text{and} \quad C_6 = -\sum_i \frac{C_3^2}{\Delta E} \propto n^{11}, \tag{6.4}$$

since C_3 is proportional to the product of two electric dipole moments, each scaling as n^2, and the energy mismatch of an interaction channel usually decreases as $\Delta E \propto n^{-3}$. We can compare this scaling law with calculations of the C_6 coefficients for all $|rr\rangle$ pair-states[3] of the S, P and D Rydberg series using the *pairinteraction* software.

[3] We choose the stretched pair-states with maximal total quantum number M for the calculations.

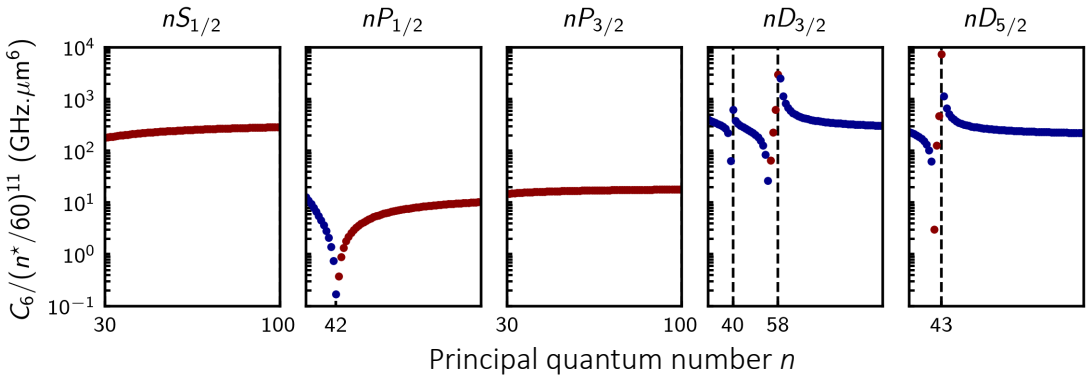

Figure 6.4: Scaling of the C_6 coefficient. Calculated C_6 for the five important Rydberg series, rescaled by the expected n^{11}-dependence with the principal quantum number n. Red: positive, blue: negative C_6. Dashed line: position of the Förster resonances. We choose $n = 60$ as a reference for the energy scale.

Figure 6.4 shows the rescaled $C_6/(n^\star/60)^{11}$, which should remain constant according to Eq. (6.4). We use the effective quantum number $n^\star = n - \delta$ corrected for the quantum defect of each Rydberg series. The scaling law is remarkably valid over the full range $n = 30 - 100$ for $S_{1/2}$ and $P_{3/2}$ states, with a few exceptions for $P_{1/2}$, $D_{3/2}$ and $D_{5/2}$ states. For $42P_{1/2}$, the van der Waals shift almost vanishes as the various interaction channels compensate each others. On the contrary, the interaction strength is strongly enhanced at $n = 40, 58$ for $D_{3/2}$ and $n = 43$ for $D_{5/2}$, due to a Förster resonance. Whereas C_6 is increased at the resonance, it can change sign or strongly decrease around the resonance, as the Förster defect ΔE goes from positive to negative and possibly compensates the van der Waals contribution of all other channels. Finally, let us note that, while the interaction strength of a nP states is more than one order of magnitude smaller than for a nS and nD states, it suffices to choose a slightly larger n to obtain the same van der Waals shift due to the strong n^{11} scaling.

6.1.3 Measuring the van der Waals shift

The first experimental demonstrating an interaction shift between two isolated Rydberg atoms was the observation of the Rydberg blockade effect [Urban *et al.*, 2009; Gaëtan *et al.*, 2009]. Driving the atoms from the ground-state $|g\rangle$ to a Rydberg state $|r\rangle$ with a coupling strength Ω, the probability P_{rr} to excite the two atoms is suppressed for a large interaction shift $V \gg \hbar\Omega$. Going a step further, Béguin *et al.* [2013] measured the van der Waals shift by using an intermediate regime where $\hbar\Omega \approx V$ and fitted the

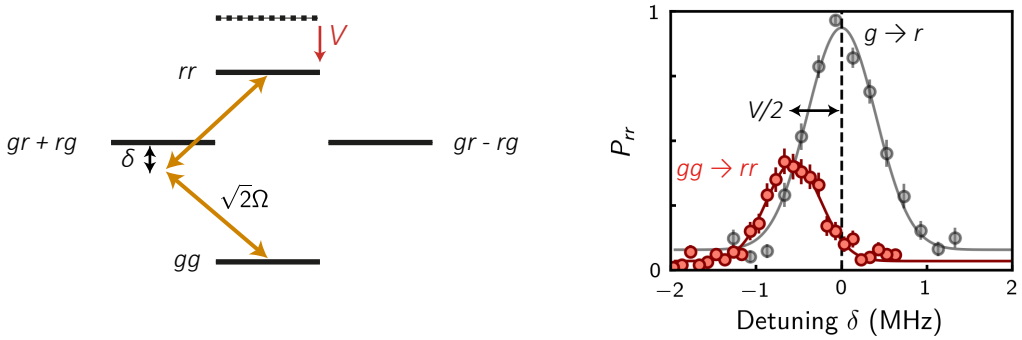

Figure 6.5: Measurement of van der Waals shift. The excitation of two Rydberg atoms is restored when the detuning δ of the excitation lasers matches half the van der Waals shift. Comparing the two-atom resonance (red curve) to the single-atom one (dark), we obtain $V/h = -1.22(2)$ MHz.

evolution of P_{rr} to numerical simulations. Here, I describe a spectroscopy method of measuring the interaction energy by probing the $|gg\rangle \leftrightarrow |rr\rangle$ transition.

Figure 6.5 shows how the excitation of $|rr\rangle$ is restored by a four-photon process[4] for a laser detuning $\delta = V/2$ from the single atom $|g\rangle \leftrightarrow |r\rangle$ transition. The experiments was performed with the Rydberg state $\left|61D_{3/2}, m_J = 3/2\right\rangle$ for two atoms aligned with the quantization axis and separated by $R = 9\,\mu$m. Comparing the resonances observed with one and two atoms, we directly extract the van der Waals shift $V/h = -1.22(2)$ MHz, which can be compared to $V_{\text{th}}/h = -1.44$ MHz obtained from the calculated $C_6 = -769$ GHz.μm^6. As we trust the theory, it indicates a systematic error in the calibration of the interparticle distance, which I now discuss.

Distance calibration Over the course of this thesis, we noticed that the calculated interaction energies were always larger than the measured ones, not only for van der Waals shift as here, but also for the resonant dipole-dipole interaction discussed later in Chapter 7. Because of the R^{-6} (or R^{-3} in the second case) scaling of the interaction strength, it is crucial to precisely estimate the separation between two optical tweezers. The latter was calibrated by optical ways [Béguin, 2013] but can be affected by systematic uncertainties in the focal length of the asphere. In fact, we can reverse the problem and use the dipole-dipole interaction as a way to precisely calibrate the inter-atomic distance. It leads to 4.5 % larger distances than from the optical calibration.

[4] $|g\rangle \leftrightarrow |r\rangle$ being itself a two-photon process, see Section 5.1

6.2 Two simple cases with pure dipole-dipole interaction

We have considered, in the previous section, that the dipole-dipole Hamiltonian $\hat{H}_{dd}$ could be taken into account using second-order perturbation theory. Nevertheless, this approximation is valid only when, for each interaction channel, the coupling strength J remains much smaller than the energy difference ΔE between the pair-states. In this section, we check this condition by identifying the various interaction channels in the simple case $\theta = 0$, where $\hat{H}_{dd}$ conserves the total magnetic quantum number ΔM. I will focus on $nS_{1/2}$ and $nD_{3/2}$ states since they are the only two accessible with our excitation scheme.

6.2.1 $nS_{1/2}$: ideal van der Waals regime

We have seen in Fig. 6.4 that the C_6 coefficients of the $nS_{1/2}$ series were, to a very good approximation, following the n^{11}-scaling law over the full range $n = 30 - 100$. We thus expect the situation to be roughly independent of n and we focus here on the pair-state $|rr\rangle = \left|60S_{1/2}, 60S_{1/2}\right\rangle$. The only available interaction channels are of the form:

$$\left|60S_{1/2}, 60S_{1/2}\right\rangle \leftrightarrow |n'P_i, n''P_j\rangle\,, \tag{6.5}$$

where $i, j = 1/2, 3/2$ indicates the fine-structure of the P level, (n', n'') runs over the full Rydberg manifold and we do not write the Zeeman sublevels for clarity. Only the contribution $C_3^2/\Delta E$ of a few channel will be significant, as C_3 drastically decreases with the difference in principal quantum numbers (due to the smaller dipole matrix elements), while the energy mismatch ΔE increases:

- **Energy mismatch.** From Fig. 6.3(a), we identify that a nS state lies roughly halfway between the $(n-1)P$ and nP levels (because $\delta_S - \delta_P \sim 0.5$), such that the closest pair-state are of the form $|(60+k)P, (59-k)P\rangle$. The calculated energy defect ΔE is -1.7 GHz[5] for $k = 0$, -5.5 GHz for $k = 1$, -13 GHz for $k = 2$... It turns out that these pair-states all lie below $|nS, nS\rangle$, such that the van der Waals shift will be positive (repulsive interaction), and coupling to $|60P, 59P\rangle$ will likely be the dominant interaction channel.

- **Coupling strength.** It is largest for the $|60P, 59P\rangle$ state (~ 4 GHz.μm^3),

[5] Or more precisely, taking into account the fine-structure splitting of the P states (0.46 GHz at $n = 60$): -2.2 GHz, -1.7 GHz, -1.7 GHz and -1.2 GHz for the four combinations $|nP_i, (n-1)P_j\rangle$.

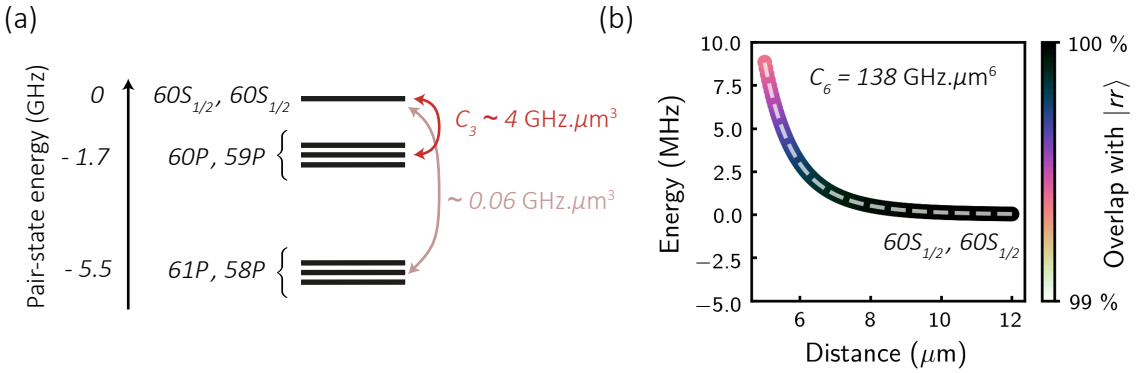

Figure 6.6: $nS_{1/2}$ states: van der Waals regime. (a) Closest pair-states to $|rr\rangle = |60S_{1/2}, 60S_{1/2}\rangle$ and their C_3 coupling. (b) Numerical calculations from the *pairinteraction* software. The thick colored curve represents the eigenstate energy and its overlap with $|rr\rangle$, which remains > 99.5 % for $R > 5\,\mu$m. The dashed curve shows the C_6/R^6 van der Waals scaling.

while it is already down to 0.06 GHz.μm^3 for $|61P, 58P\rangle$.

These two results are shown graphically in Fig. 6.6(a). They indicate that the closest pair-states $|60P, 59P\rangle$ are, in excellent approximation, the only ones contributing to the van der Waals shift, the contribution of the second set being weaker by a factor 10^4. Let us now precisely count the number of channels. Because of the fine-structure of the P levels, there are 4 $|60P_i, 59P_j\rangle$ and 4 $|59P_i, 60P_j\rangle$ states. We also need to take into account the Zeeman sub-structure, noting that we only couple to $M = 1$ states: there are only 1 in the $|P_{1/2}, P_{1/2}\rangle$ manifold ($|m_J = 1/2, m_J = 1/2\rangle$), 2 in $|P_{1/2}, P_{3/2}\rangle$ and 3 in $|P_{3/2}, P_{3/2}\rangle$ giving a total of 16 channels. Finally, we can estimate $C_6 \approx 16\, C_3^2/\Delta E = 150$ GHz.μm^6 in quite good agreement[6] with a more precise numerical estimate shown in Fig. 6.6(b) using the *pairinteraction* calculator.

We can now check that the second-order approximation is valid. For example, at a distance of $5\,\mu$m, the coupling strength on a single channel $J \simeq 32$ MHz remains much smaller than the detuning $\Delta E \simeq 1.7$ GHz. Numerically, we find that the overlap of the unperturbed pair-state $|rr\rangle$ with the real eigenstate is larger than 99.5 %. The remarkably simple situation explored here, with only a few interaction channel well separated from $|rr\rangle$, is general for $nS_{1/2}$ states, which are thus particularly well suited for the implementation of spin-1/2 Ising models. We will see in the next section that it remains true even for a non-zero interaction angle. As we already stated, the

[6] The small discrepancy is because we ignored the variation of C_3 over the different Zeeman pair-states (due to the Clebsch-Gordon coefficients) and the variation of ΔE due to the fine-structure splitting.

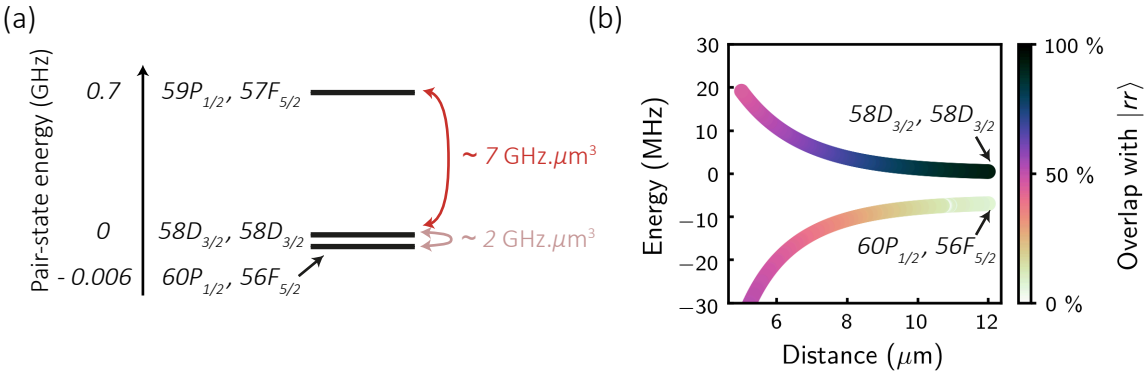

Figure 6.7: $58D_{3/2}$ states: quasi-resonant regime. (a) The coupling strength to $|59P_{1/2}, 57F_{5/2}\rangle$ is larger than to $|60P_{1/2}, 56F_{5/2}\rangle$, but the latter is almost resonant with $|rr\rangle = |58D_{3/2}, 58D_{3/2}\rangle$ and thus dominates the interaction. (b) Numerical calculation showing the strong mixing of the two quasi-resonant channels. The interaction energy varies between $\sim \sqrt{2}C_3/R^3$ at short distances and $\sim C_6/R^6$ with $C_6 = 2C_3^2/\Delta E$ at large distances.

only reason why we do not use $nS_{1/2}$ states is the weaker laser coupling Ω from the ground-state (see Section 5.1).

6.2.2 $58D_{3/2}$: A Förster resonance

We now repeat the same procedure for Rydberg $D_{3/2}$ states. As we observed in Fig. 6.4 a strong enhancement of the C_6 coefficient around $n = 58$, we will focus on this specific case. The dipole-dipole interaction couples $|rr\rangle = |58D_{3/2}, 58D_{3/2}\rangle$ to pair-states of the form:

$$|n'P_i, n''P_j\rangle\,, \quad |n'P_i, n''F_{5/2}\rangle\,, \quad \text{and} \quad |n'F_{5/2}, n''F_{5/2}\rangle \tag{6.6}$$

with $i, j = 1/2, 3/2$. Of the three[7], the second one will have the smaller energy difference as a nD states lies almost halfway of a nP and a nF level, and the most important pair-sates are thus $|(58+k)P_{1/2}, (58-k)F_{5/2}\rangle$. The energy defect Δ is -4.5 GHz for $k = 3$, only -6 MHz (!) for $k = 2$, 0.7 GHz for $k = 1$, and 2.5 GHz for $k = 0$. Let us note the incredibly small detuning of the $|pf\rangle = |60P_{1/2}, 56F_{5/2}\rangle$ pair-state. This accidental quasi-degeneracy is called a Förster resonance. Figure 6.7(a) shows the two closest pair-states and their respective coupling to $|rr\rangle$. At a distance of $5\,\mu$m, the coupling on the Förster channel, $J \simeq 20$ MHz is much larger than ΔE, such

[7]For the first and third channels, the energy defect are larger than 10 GHz at $n = 58$, as seen in Walker and Saffman [2008].

that the eigenstates become:

$$\approx \frac{1}{\sqrt{2}}\big(\,|rr\rangle \pm |pf\rangle_s\,\big) \quad \text{at} \quad E \simeq \pm\frac{\sqrt{2}C_3}{R^3} \tag{6.7}$$

where we introduced the notation $|pf\rangle_s$ for the symmetric state[8] $\frac{1}{\sqrt{2}}(|pf\rangle + |fp\rangle)$ and the $\sqrt{2}$ enhancement of the coupling strength comes from this symmetrization. At larger distances, the mixing between the two states decreases and we recover the van der Waals regime, as seen in the shading of the two potential curves in Fig. 6.7(b). Carefully looking at the two potential curves of Fig. 6.7(b), one can notice a slight asymmetry between the upper and lower branches: this comes from the negative van der Waals shift caused by the interaction with the far-detuned $\left|59P_{1/2}, 57F_{5/2}\right\rangle$ level.

Förster resonance and spin-1/2 mapping Even if the interaction does not take the form of a van der Waals shift, it remains quite simple (there are two well identified pair-states) and useful for experiments as the interaction energy is much larger than in the regular van der Waals regime. In fact, the Förster resonance was used in the first works of the group to achieve very efficient Rydberg blockade [Gaëtan *et al.*, 2009; Wilk *et al.*, 2010]. In addition, $|rr\rangle$ and $|pf\rangle_s$ can be tuned precisely to resonance with an electric field using the different static polarizability of P, D and F states, allowing a dynamical control of the interaction [Ravets *et al.*, 2014].

Amongst the $|r\rangle = \left|nD_{3/2}\right\rangle$ Rydberg states, we have studied the specific $n = 58$ case where the Förster defect ΔE between $|rr\rangle$ and $\left|(n+2)P_{1/2}, (n-2)F_{5/2}\right\rangle$ is only -6 MHz. The situation is almost identical at $n = 59$ where $\Delta E = +9$ MHz. For $56 \leq n \leq 63$, $\Delta E < 50$ MHz still leads to non-negligible mixing between $|rr\rangle$ and $|pf\rangle_s$ for interacting atoms. Can it explain the deviations from the spin-1/2 model observed in Labuhn *et al.* [2016], and shown in Fig. 6.2, for experiments performed with $\left|61D_{3/2}\right\rangle$ states? We can think of two cases depending on the interatomic distance:

- For a pair of atoms far from each other, $J \ll \Delta E$, and we are still in the van der Waals regime. The mixing is negligible, we can safely remove $|pf\rangle$ from the Hilbert space and the mapping to a spin-1/2 model is valid.

- For a pair of atoms close to each other, $J \gg \Delta E$, and the two states strongly mix. But in addition, the pair-states are strongly detuned from the laser resonance ($J \gg \Omega$), such that they are not coupled to by the excitation lasers and $|pf\rangle$ will not be populated. Again, the mapping is valid.

[8] The anti-symmetric state $|pf\rangle - |fp\rangle$ does not couple to $|rr\rangle$.

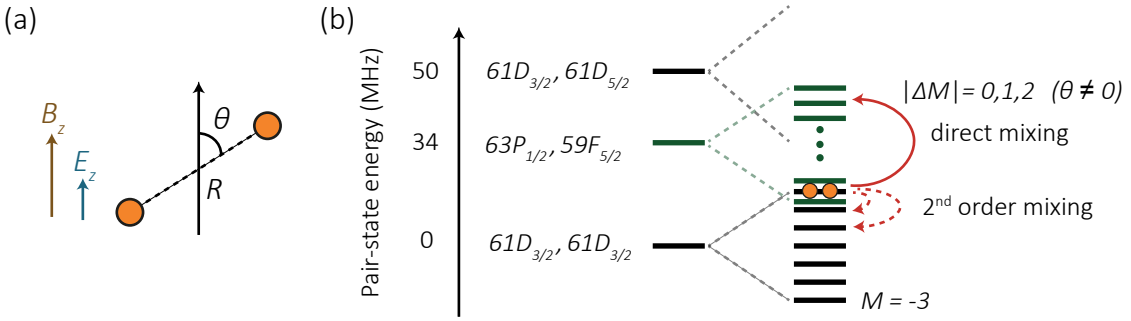

Figure 6.8: The situation in Labuhn et al. [2016]. (a) We consider a vertical magnetic (B_z) and electric (E_z) external field, and a non-zero interaction angle θ between the pair of atoms and the vertical quantization axis. (b) Focus on the pair-state spectrum around $|rr\rangle = |61D_{3/2}, 61D_{3/2}\rangle$. The $M = -3, \ldots, 3$ Zeeman sublevels are split by B_z. For $B_z \simeq 4$ G, the manifolds from $|rr\rangle$ and $|63P_{1/2}, 59F_{5/2}\rangle$ start to overlap. The direct and second-order mixing are described in the text.

Following these arguments, the mixing caused by the Förster channel is compatible with a spin-1/2 model, as long as the Förster defect ΔE is much larger than the excitation lasers strength Ω and detuning δ. Nevertheless, we did not yet consider (i) the non-zero interaction angle θ, (ii) the magnetic field B_z and (iii) the possibility of a small electric field E_z.

6.3 General case: non-zero external fields and interaction angle

In this section, we investigate the more general case where $(\theta, B_z, E_z) \neq 0$. We will now use the open-source *pairinteraction* software [Weber *et al.*, 2017] as it becomes difficult to track manually all the various interaction channels. I start by recalling that the Zeeman manifold of $|61D_{3/2}, 61D_{3/2}\rangle$ is composed of 16 sublevels denoted as[9]:

$$|61D_{3/2}, m_J; 61D_{3/2}, m'_J\rangle \equiv |M = m_J + m'_J\rangle \quad \text{with} \quad m_J, m'_J = \pm 1/2, \pm 3/2. \quad (6.8)$$

For $\theta = 0$, the $|rr\rangle = |M = 3\rangle$ level (the only one coupled to by the polarized excitation lasers) does not mix with other ones as $\hat{H}_{dd}$ conserves M. The situation is now different as $|\Delta M| = 0, 1, 2$ couplings are allowed as $\theta \neq 0$. In addition, we will have to consider the splitting of the Zeeman manifold by B_z. Figure 6.8 schematically shows the various pair-states and how they couple to each other:

[9] Strictly, we should denote them as $|M, \alpha\rangle$, where α takes into account the pair-state degeneracy for $|M| \neq 3$. I ignore it to simplify the notations.

- At $n = 61$, the Förster channel $|pf\rangle = \left|63P_{1/2}, 59F_{5/2}\right\rangle$ is only detuned by ~ 35 MHz, leading to significant 'direct' mixing between $|rr\rangle$ and $|pf\rangle$ as described in the previous section. While we now couple to the $M = 1, 2$, and 3 sublevels of $|pf\rangle$ (see also Ravets *et al.* [2015]), we still rule out this mixing as an explanation for the failure of the spin-1/2 approximation.

- Interaction channels of the form $|M = 3\rangle \rightarrow |r'r''\rangle \rightarrow |M' \neq 3\rangle$ leads to a 'second-order' mixing of the Zeeman manifold. We investigate this in Section 6.3.1.

- The Zeeman manifolds of $|rr\rangle$ and $|r'r''\rangle$ overlap for $B_z > 4$ G, we will see in Section 6.3.2 that this gives rise to an extreme sensitivity of the pair-state spectrum to even small electric fields.

- Finally, we will systematically explore in Section 6.3.3 the parameters space spanned by (θ, B_z, E_z), and also vary the choice of principal quantum number n, to find conditions under which the mapping to a spin-1/2 system holds.

6.3.1 Mixing of the Zeeman manifold

In Section 6.1, the dipole-dipole interaction was restricted to channels of the form $|M = 3\rangle \rightarrow |r'r''\rangle \rightarrow |M = 3\rangle$, as the total magnetic quantum number M was conserved. As we now consider pair of atoms at an angle with the quantization axis, channels of the form $|M = 3\rangle \rightarrow |r'r''\rangle \rightarrow |M'\rangle$ are allowed. As it involves two dipole-dipole couplings, each changing the magnetic quantum number by up to $|\Delta M| = 2$, the range of final state is $M' = -1, ..., 3$. For $B_z = 0$ G, all Zeeman sublevels are degenerate and $\hat{H}_{dd}$ should be taken into account using the theory of degenerate second-order perturbation. The van der Waals interaction is then described by a matrix $\mathcal{V}$. Expressed in the Zeeman basis, its off-diagonal coefficients correspond to the coupling strength between two different Zeeman sublevels. For $B_z \neq 0$, there is a competition between these 2^{nd} order mixing terms and the Zeeman splittings, as the different M sublevels are not degenerate anymore. We explore this situation using the *pairinteraction* software to calculate the pair-state potentials for a generic[10] interaction angle $\theta = 78°$ and different B_z. The results are shown in Fig. 6.9:

- For $B_z = 0$ G, the degeneracy of the Zeeman manifold leads to a complete mixing of all $|M\rangle$ states by the dipole-dipole interaction. One eigenstate experiences a

[10] All $\Delta M = 0, \pm 1$ and ± 2 couplings are allowed according to Eq. (6.2).

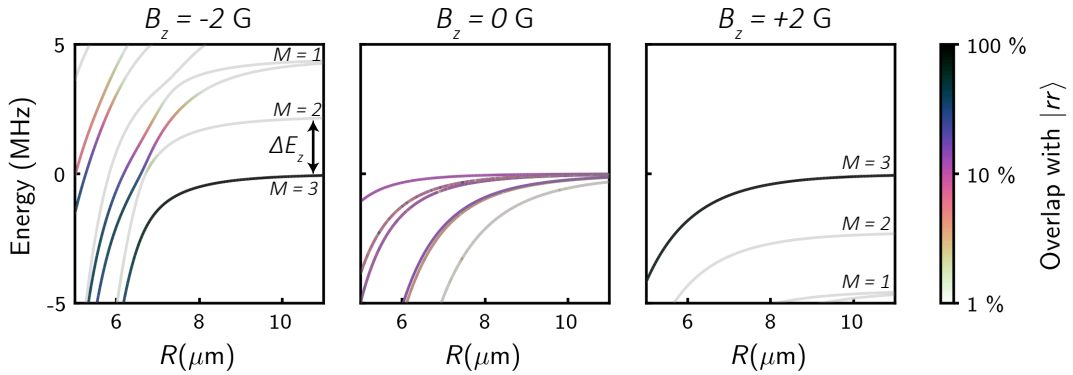

Figure 6.9: Second-order mixing of the Zeeman manifold. Pair-state potentials of the $|61D_{3/2}, 61D_{3/2}\rangle$ Zeeman manifold composed of 16 pair-states initially ordered, at large distances, by their total magnetic quantum number M. The zero is fixed to the energy of $|rr\rangle = |M = 3\rangle$ at $R = \infty$. The color encodes the overlap with $|rr\rangle$ and thus the coupling to the excitation lasers. We do not distinguish all 16 potential curves as some remain degenerate and the Zeeman manifold extent is larger than the energy axis. For $B_z = -2$ G and 0 G, we observe a clear mixing between the different pair-states, absent for $B_z = 2$ G.

weak van der Waals shift, preventing efficient Rydberg blockade as recognized by Walker and Saffman [2008].

- For $B_z = -2$ G, the Zeeman splitting ΔE_z prevents the mixing as long as $V \ll \Delta E_z$. For decreasing R, the $|M < 3\rangle$ pair-states 'fall back' on $|M = 3\rangle$ as they usually experience a stronger van der Waals shift. It leads to (i) a strong mixing and (ii) failure of the Rydberg blockade at *magic* distances where a coupled eigenstate crosses zero-energy [Vermersch, Glaetzle, and Zoller, 2015].
- For $B_z = +2$ G, the situation remains ideal: we do not observe any mixing between the pair-states for the range of distances and energies considered here.

Experimental confirmation I illustrate the effects discussed above with Rydberg spectroscopy experiments performed on a two-atom system: The excitation lasers detuning δ from the single-atom transition is varied and we measure the probability P_{rr} to excite the two atoms. Figure 6.10 shows the results for three different magnetic fields B_z. For $B_z < 0$ (left and middle panels), we observe two peaks corresponding to two eigenstates connected at $R = \infty$ to the $M = 3$ and $M = 2$ unperturbed pair-states. The second is coupled to by the excitation lasers because of the 2^{nd} order mixing with $|M = 3\rangle$. Notably, at $B_z = -1.9$ G, this pair-state is at zero-energy (in

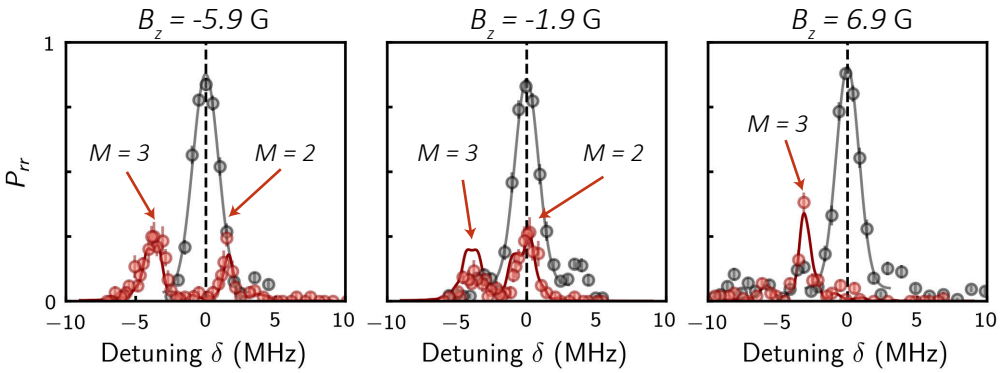

Figure 6.10: Experimental observation of 2^{nd} order mixing. Excitation spectra for two atoms at $R = 6.5\,\mu$m and $\theta = 23°$ for $B_z = -5.9$ G, -1.9 G and 6.9 G. Peaks in P_{rr} indicates the position of the different Rydberg pair-states coupled to by the excitation lasers. In the absence of second-order mixing of the Zeeman manifold, only $|rr\rangle = |M = 3\rangle$ would be observed. For $B_z < 0$, we clearly see a second peak corresponding to $|M = 2\rangle$. The black points are single-atom reference spectra. The red solid curves are ab-initio calculations performed by Sebastian Weber.

the rotating frame) realizing the situation envisioned by Vermersch, Glaetzle, and Zoller [2015] of a Rydberg blockade failure at a specific 'magic' distance. These results are in very good agreement with simulations without any adjustable parameters (red solid lines).

For $B_z = +6.9$ G (right panel) only one peak is observed: there is a single eigenstate coupled to by the excitation lasers confirming what was predicted from Fig. 6.9. We conclude that for a positive magnetic field, the mapping to a spin-1/2 model remains correct even for a non-zero interaction angle. Let us note that this second-order mixing is specific to P and D states, but does not affect Rydberg S states, as already remarked by Vermersch, Glaetzle, and Zoller [2015]. For $S_{1/2}$ states, the off-diagonal coefficients of $\mathcal{V}$ are smaller by two orders of magnitude than the diagonal ones causing a simple shift, whereas they are of the same order of magnitude for P and D states.

6.3.2 Sensitivity to electric fields

We now investigate the combined effect of an electric field E_z and of a magnetic field $B_z > 4$ G, large enough to mix the $\left|61D_{3/2}, 61D_{3/2}\right\rangle$ and $\left|63P_{1/2}, 59F_{5/2}\right\rangle$ Zeeman manifolds. Figure 6.11 shows that the pair-state potentials are drastically modified by a small electric field, $E_z = 20$ mV/cm, when $B_z = 6.9$ G. I emphasize that, at the

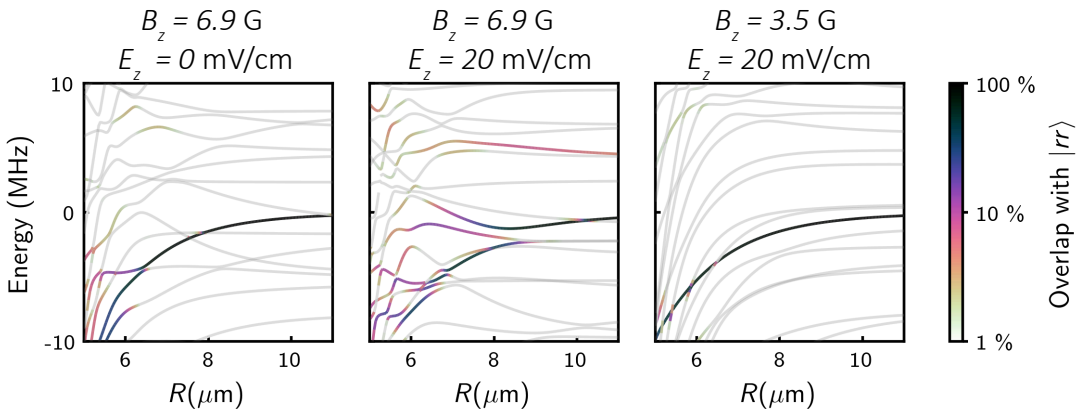

Figure 6.11: Sensitivity to E_z. Pair-state potentials for different settings of B_z and E_z. In contrast to Fig. 6.9, the additional potential curves originate from the $|63P_{1/2}, 59F_{5/2}\rangle$ manifold. For $B_z = +6.9$ G, a weak $E_z = 20$ mV/cm leads to a strong mixing, while the effect is absent at $B_z = +3.5$ G. The interaction angle is $\theta = 78°$.

single-atom level, such a weak electric field has almost no effect (the Stark shift is only ~ 0.1 MHz), but the high density of pair-states, due to the overlap of the Zeeman manifolds, makes the pair-states very sensitive to E_z. The effect indeed disappears for a weaker $B_z = 3.5$ G as the manifolds are more separated.

I now turn to the experimental test of the above analysis by performing two-atom blockade experiments with four different settings of the external fields: the magnetic field is either 3.5 or 6.9 G, and the electric field either zero or 20 mV/cm. The two atoms are a distance $R = 6.5\,\mu$m and form an angle $\theta = 78°$ with the quantization axis. We can estimate an interaction energy $V/h \sim 10$ MHz from the C_6 coefficient of the van der Waals regime, such that for a driving strength $\Omega/(2\pi) = 1.2$ MHz we expect an efficient Rydberg blockade and a strong suppression of the probability P_{rr} to obtain two Rydberg excitations. The evolution of P_{rr} with the excitation time is displayed in Fig. 6.12. As excepted from our previous numerical calculations of the pair-state potentials, we observe a strong suppression of P_{rr} for all settings, except for $B = 6.9$ G and $E = 20$ mV/cm.

To compare with the theory, we simulate the dynamics of the two-atom system solving the Schrödinger equation and calculate the probability to excite the two atoms. We assume two different models to describe the interacting system: in the first one (solid line), we use the full interaction spectrum and include around 800 pair-states within 2 GHz from the resonance. In the second model (dashed line), we make the spin-1/2 approximation where we only keep a single potential curve (the one with the largest overlap with $|rr\rangle$). The numerical simulations were performed by Sebastian

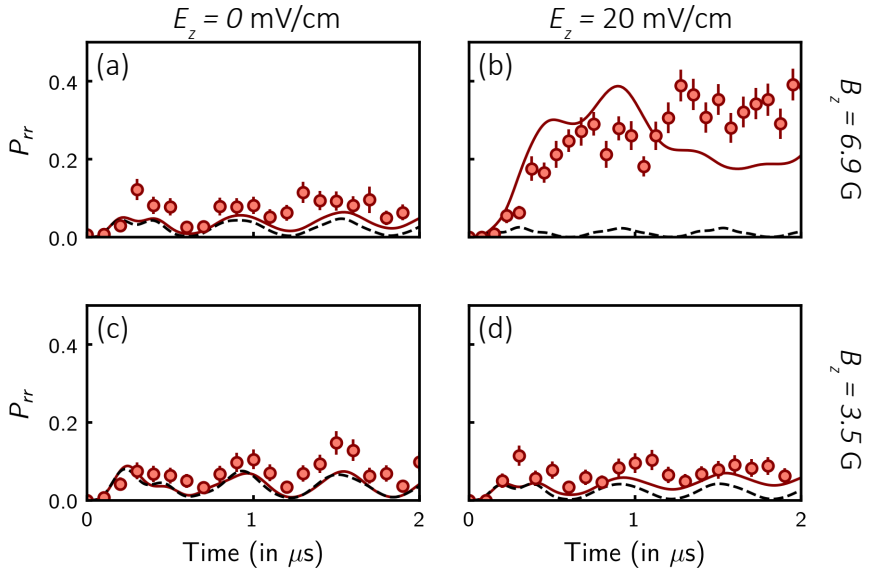

Figure 6.12: Observation of exaggerated E_z-sensitivity. Probability P_{rr} to excite the two atoms as a function of the time. For $B = 6.9$ G (a-b), increasing E_z from 0 to 20 mV/cm breaks the Rydberg blockade. At $B = 3.5$ G (c-d), an efficient blockade is maintained, even in the presence of the electric field. The solid lines result from a simulation taking into account the full interaction spectrum. The dashed lines are obtained by modeling the atoms as spin-1/2 particles with a single interaction potential for $|rr\rangle$. The interatomic distance is $R = 6.5\,\mu$m and the angle $\theta = 78°$. The simulations have been performed by Sebastian Weber.

Weber. The agreement between the experimental data and the ab-initio calculation is quite satisfactory.

6.3.3 Systematic search

We now investigate systematically how the choice of $nD_{3/2}$ states, interaction angle θ and the value E_z and B_z of the external fields affect the accuracy of the mapping on a spin-1/2 model. Similarly to the previous section, we use the double excitation probability P_{rr} during a Rydberg blockade experiment as a marker for the failing of the spin-1/2 approximation, and thus search a range of parameters for which P_{rr} remains small. The results are shown in Fig. 6.13:

- For any n and θ, we observe a breaking of the Rydberg blockade for negative B_z as explained in Section 6.3.1, except at $n = 55 - 57$ where the van der Waals shift becomes negative and the failure thus occurs for $B_z > 0$.

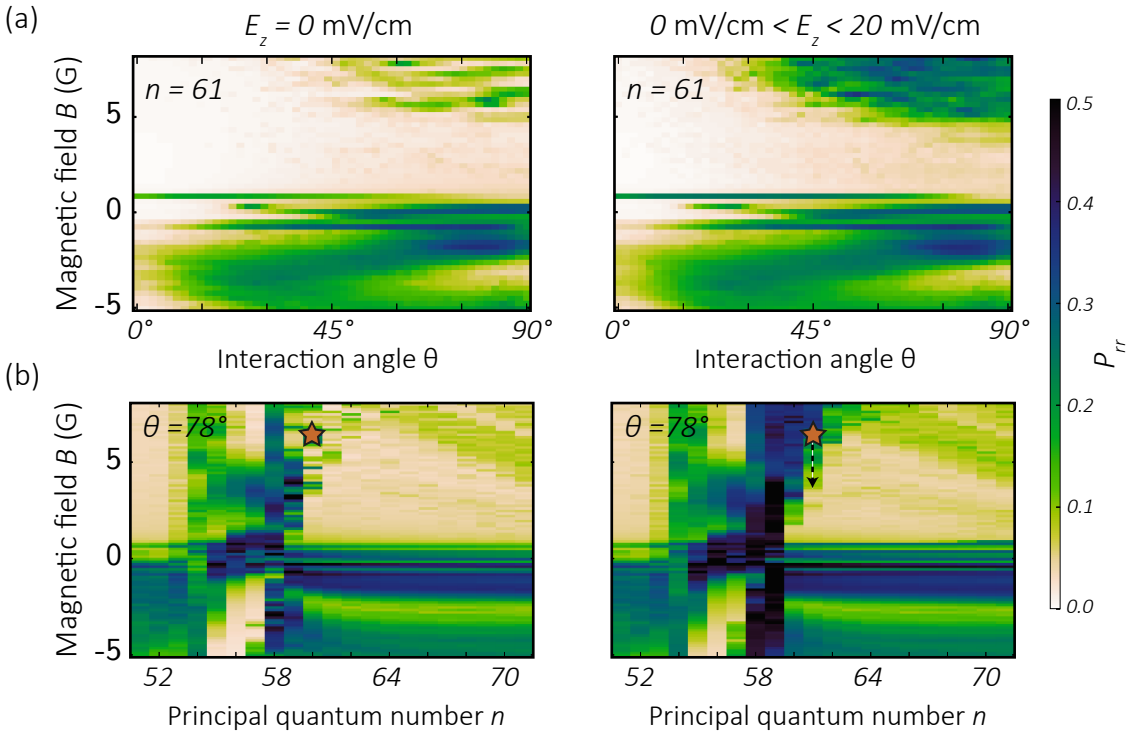

Figure 6.13: Parameters scan. Influence of n, θ, B_z, E_z on the mapping onto a spin-1/2 system: the latter fails when P_{rr} is non-zero. The interatomic distance is fixed at $R = 6.5\,\mu$m in (a) and adjusted to maintain a constant interaction shift in (b). The electric field is $E = 0$ in the left panels and chosen between 0 and 20 mVcm such that P_{rr} is maximized in the right panels. The orange star marks the experimental parameters used in Labuhn *et al.* [2016] where deviations from a spin-1/2 model were observed. The calculations have been performed by Sebastian Weber.

- For too large a B_z, we observe the strong sensitivity to an electric field, described in Section 6.3.2. From Fig. 6.13(b), we confirm that this effect is caused by the close-by Förster resonance at $n = 58, 59$. It is impossible to map a two-atom system onto a spin-1/2 model at the resonance due to the strong mixing, and it requires a fine tuning of B_z for $n = 60 - 64$ as the Förster channel remains only weakly detuned.

Effective C_6 coefficients. In the optimal regime where the Rydberg blockade and the spin-1/2 approximation is valid, for example at $B_z = 3.5$ G according to Fig. 6.13, we check if we can describe the energy of $|rr\rangle$ by a van der Waals potential with an angular dependence $C_6(\theta)/R^6$. Figure 6.14(a) shows the energy dependence as a function of R for $\theta = 78°$ together with a $1/R^6$ fit. We observe, that for $R \gtrsim 8\,\mu$m, the

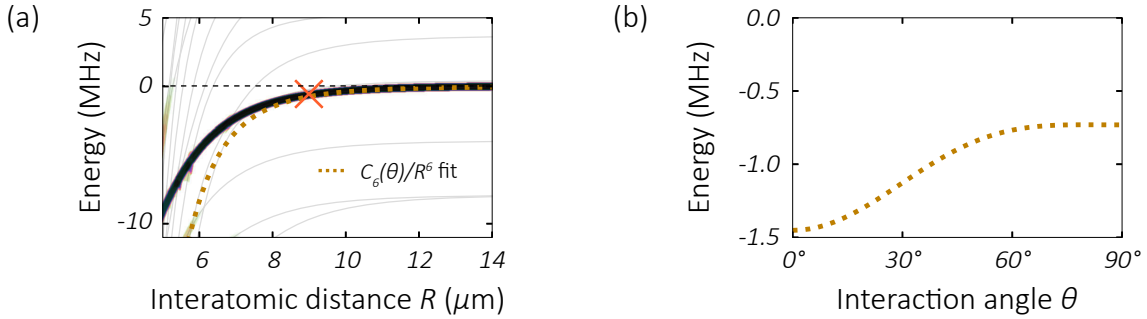

Figure 6.14: Approximation of the interaction by an anisotropic van der Waals potential $C_6(\theta)/R^6$. (a) Comparison of the exact interaction energy (solid line) with the asymptotic determination of the van der Waals potential (dashed line) for a fixed angle $\theta = 78°$ and $B = 3.5$ G. (b) Angular dependence of $C_6(\theta)/R^6$ at $R = 9\,\mu$m marked by the cross on (a).

van der Waals description is an excellent approximation. Figure 6.14(b) shows the angular dependence of the coefficient $C_6(\theta)$. We have thus extended the anisotropic effective potential approach of Barredo *et al.* [2014] and Vermersch, Glaetzle, and Zoller [2015] beyond the strong blockade regime. Consequently, we represent the Rydberg blockade volume not by a sphere but by an ellipsoid.

6.4 Conclusion

Now that we have identified parameters allowing to map our two-atom system onto a spin-1/2 model, we check experimentally that this can be extended to many-body problems. We thus revisit the experiments reported in Fig. 6.2, but with a weaker $B_z = 3.5$ G (6.9 G previously). We illuminate the atoms with the excitation lasers and measure the evolution of the fraction f_R of atoms in Rydberg states. Figure 6.15 shows the results for two atomic arrays together with predictions of the spin-1/2 model (solid line). For the 8-atom ring, we can obtain an exact numerical solution, while for the 7×7 array, the Hilbert space is too large. Sebastian Weber thus used the fact that two neighboring atoms cannot be excited due to the Rydberg blockade to truncate the Hilbert space from 2^{49} to $\sim 2^{30}$ states and checked, with systems of up to 25 atoms, that the truncation gives the same results as an exact calculation. In both experiments, we experimentally find a much better agreement with the simulation than at the beginning of this chapter, despite the wealth of phenomena affecting Rydberg $D_{3/2}$ states.

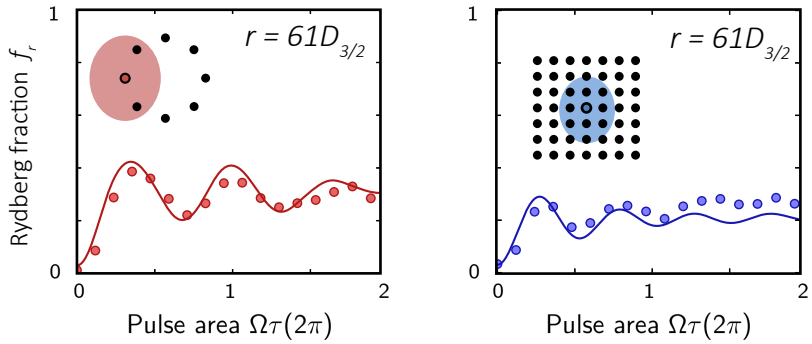

Figure 6.15: Success of spin-1/2 approximation. Same experiment as in Fig. 6.2 but with $B_z = +3.5$ G instead of 6.9 G. The points shows the evolution of the Rydberg fraction f_{R} with the pulse area $\Omega\tau$. Left: 8-atom ring with a nearest neighbor spacing of $6.5\,\mu$m. The shaded ellipse illustrates the range of the anisotropic blockaded region $U > \hbar\Omega$. Right: Square lattice of 7×7 traps (lattice spacing $6.1\,\mu$m), the blockade extends over nearest and next-nearest neighbors. The solid curve is a simulation of a spin-1/2 model. The agreement is much better than in Fig. 6.2.

Conclusion We have explored the mapping on spin-1/2 models of interacting multilevel Rydberg atoms by taking into account the underlying details of the atomic structure in the presence of electric and magnetic fields. The latter has been made possible thanks to the recent development of open-source numerical solvers for the dipole-dipole interaction [Šibalić *et al.*, 2016; Weber *et al.*, 2017]. We found experimental conditions under which the Rydberg atoms can be simply viewed as spin-1/2 particles. Using two-atom systems, and then larger one of up to 49 particles, we confirmed these theoretical findings and demonstrated a much better agreement with a spin-1/2 model than in Labuhn *et al.* [2016]. The insights brought by the numerical solver could also help improving the control of interactions in Rydberg dressing experiments using $nP_{3/2}$ states [Jau *et al.*, 2016], as well as for Rydberg slow light polaritons with nD states [Tresp *et al.*, 2015]. We will use the *pairinteraction* solver again in the third part of this thesis to explore the interaction of two atoms in different Rydberg states and the mapping to a spin-exchange Hamiltonian. In the future, our goal is to move towards Rydberg S levels, where the two most deleterious effects described in this chapter, Förster resonance and Zeeman structure mixing, are absent. It requires improving the excitation laser setups as described in the previous chapter.

Part III.

XY magnets

Chapter 7

Controlling Rydberg atoms interacting via a resonant dipolar coupling

Contents

Despite their similar forms, the Ising coupling ($J\sigma_i^z\sigma_j^z$) and XY coupling ($J[\sigma_i^x\sigma_j^x + \sigma_i^y\sigma_j^y]$) have very distinct properties. One of the striking difference is that a spin excitation $|\downarrow \ldots \downarrow\uparrow\downarrow \ldots \downarrow\rangle$ is a stationary eigenstate of the Ising model, while it delocalizes on an XY magnet, as can be seen by rewriting the coupling as a spin-exchange term $J(\sigma_i^+\sigma_j^- + \sigma_i^-\sigma_j^+)$. A spin excitation can then be considered as a particle hopping from site to site of the lattice, with the condition that two particles cannot be on the same lattice site (they can be considered as hard-core bosons). Remarkably, any

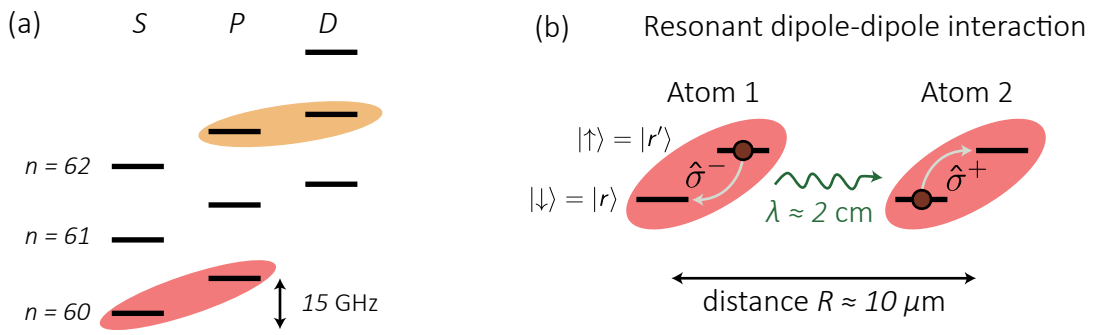

Figure 7.1: XY coupling with Rydberg atoms. (a) Energy levels of the Rydberg S, P and D series for principal quantum number $n = 60 - 62$. Our excitation scheme allows the preparation of Rydberg S or D levels, which are both dipole-coupled to any nP states. The colored areas show two possible set of pseudo-spin levels, which we have used for our experiments. The typical transition frequency is ~ 15 GHz. (b) The dipole-dipole interaction resonantly couples two spin-1/2 particles, which amounts to a spin-exchange coupling $(\sigma_1^+\sigma_2^- + \text{h.c.})$ where a spin excitation on atom 1 is coherently transfer to atom 2.

one-dimensional XY model with only nearest-neighbor couplings maps to an exactly solvable free fermion problem via the Jordan-Wigner transformation [Giamarchi, 2003]. In any other situation (long-range couplings or higher dimensions), the mapping is much more complex [Galitski, 2010] and finding the ground-state of XY magnets is an active field of research [Varney *et al.*, 2011].

Stimulated by the perspectives of studying an XY magnet in quantum simulators, there have been proposals to realize an XY coupling between effective spin-1/2 particles encoded in ions [Deng, Porras, and Cirac, 2005], superconducting qubits [Dalmonte *et al.*, 2015] or polar molecules [Bohn, Rey, and Ye, 2017]. Another system where an XY coupling arises is an ensemble of Rydberg atoms in resonant dipole-dipole interaction. We start by considering only two dipole-coupled Rydberg levels $|r\rangle$ and $|r'\rangle$ of opposite parity, as indicated in Fig. 7.1(a), with a transition frequency in the microwave domain ($\nu_0 \sim 15$ GHz, $\lambda \sim 2$ cm). Two Rydberg atoms in the pair-state $|r'r\rangle$ are resonantly coupled to $|rr'\rangle$ by the dipole-dipole interaction: pictorially, a virtual microwave photon emitted by atom 1 going from $|r'\rangle$ to $|r\rangle$ is absorbed by atom 2 which is then excited from $|r\rangle$ to $|r'\rangle$ [see Fig. 7.1(b)]. The resonant dipolar interaction takes the form, in our spin-1/2 picture, of the XY coupling $J(\sigma_1^+\sigma_2^- + \text{h.c.})$ with $J = C_3(\theta)/R^3$ depending on the chosen Rydberg orbitals and their orientation compared to the interatomic axis.

Although the dipolar exchange process is a coherent phenomenon, all experiments performed on cold atomic gases,— from the original works in the group of Prof. Pierre

Pillet [Mourachko *et al.*, 1998] and Prof. Thomas Gallagher [Anderson, Veale, and Gallagher, 1998] to more recent realizations [van Ditzhuijzen *et al.*, 2008; Günter *et al.*, 2013; Bettelli *et al.*, 2013; Maxwell *et al.*, 2013] —, resulted in the observation of incoherent transfer due to the random positions of the Rydberg atoms. Only with the development of the tweezers technique, Barredo *et al.* [2015] could observe in our group a coherent exchange oscillation directly between two Rydberg atoms, measure the $1/R^3$ dependence of $J(R,\theta)$, and realize an elementary XY magnet of three atoms. Since then, we have engineered our atom-by-atom assembler and can now contemplate the realization of larger systems. This will be detailed in the next chapter, and I present here newly developed tools for the manipulation of Rydberg atoms: efficient initialization of all atoms in the Rydberg manifold, fast read-out of the pseudospin-state populations, robust global spin-flips by microwaves sweeps, optical addressing, injection of a spin excitation, and dynamical control of the interaction.

This chapter is structured as follows. In Section 7.1, I describe the STIRAP (STImulated Raman Adiabatic Passage) technique allowing us to transfer robustly all atoms of a large atomic array in the same Rydberg state $|r\rangle$, which initializes the XY magnet. After the experiment, the state of each Rydberg atom is read by depumping $|r\rangle$ to the electronic ground-state while $|r'\rangle$ is unaffected. In Section 7.2, I focus on the manipulation of spin-1/2 particles. The microwave field driving the $|r\rangle \leftrightarrow |r'\rangle$ transition plays again the role of a global magnetic field for the spins. I also present a local addressing tool, based on a focused laser beam, allowing to split (by the Autler-Townes effect), or shift (by an AC-Stark shift), the microwave transition. In Section 7.3, we will measure the dipole-dipole interaction between two Rydberg atoms and observe the characteristic angular dependence of a dipolar coupling. Finally, in Section 7.4, I will show how to tune the interaction between two atoms from the resonant to van der Waals regime by detuning the two pair-states $|rr'\rangle$ and $|r'r\rangle$ using the addressing beam. This will allow us to freeze the dipolar exchange process and create an entangled subradiant state of two atoms. Part of the material presented in this chapter have been published [de Léséleuc *et al.*, 2017].

7.1 Efficient excitation to Rydberg states and readout

In the previous chapters, we have performed experiments starting simply with all atoms in the ground-state level $|g\rangle = \left|5S_{1/2}, F = 2, m_F = 2\right\rangle$, in which they were prepared by optical pumping. After the Rydberg experiment, we took a fluorescence image and attributed the loss of an atom to its excitation to the Rydberg state (see Chapter 5).

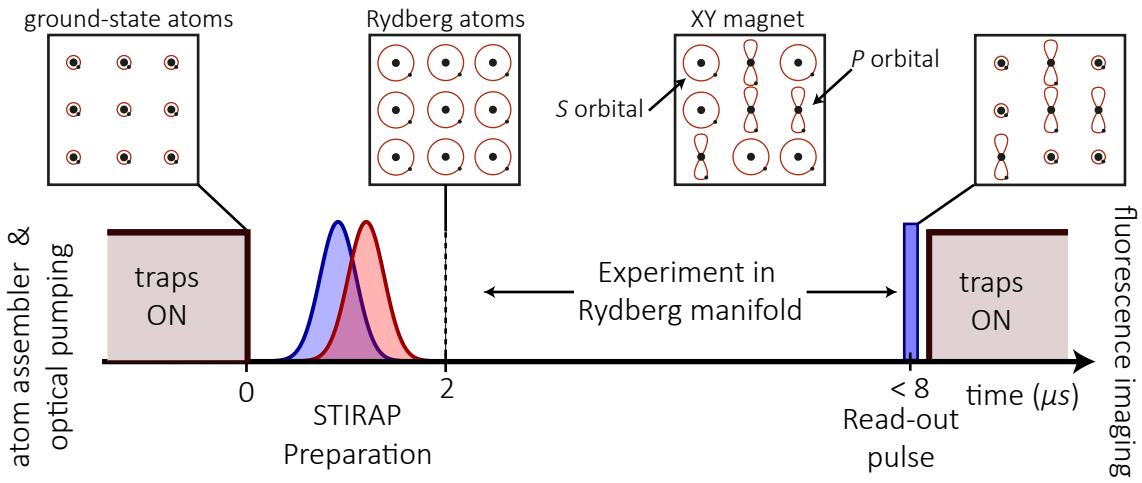

Figure 7.2: Typical experimental sequence. An array of atoms is prepared using the atom-by-atom assembler technique and is optically pumped into a well-defined ground-state level. A two-color STIRAP pulse excites all atoms in the same Rydberg state $|r\rangle$, here an S orbital. The Rydberg atoms are coupled by a microwave field to another level $|r'\rangle$, here a P orbital, which implements an XY magnet. At the end of the experiment, all atoms in $|r\rangle$ are depumped by a short read-out pulse to the electronic ground-state where they are recaptured in the tweezers, while atoms in $|r'\rangle$ are unaffected and subsequently lost. The state of the atomic array is read by a final fluorescence image. The traps are switched off during the entire Rydberg experiment as they repel excited atoms. The sequence duration is limited to $\sim 8\,\mu$s by the escape of the free-flying atoms away from the tweezers.

Studies of XY magnetism require a slightly more involved preparation and read-out, since the experiment is now performed entirely in the Rydberg manifold. A typical experimental sequence is shown in Fig. 7.2. After switching off the traps, atoms are transferred from the ground state $|g\rangle = |5S_{1/2}, F = 2, m_F = 2\rangle$ to a Rydberg level $|r\rangle$ (either a $nS_{1/2}$ or $nD_{3/2}$ orbital) with a two-photon pulse. To do so, a first possibility is to use a Rabi π-pulse, but it is affected by the damping of Rabi oscillations, as discussed in the Chapter 5, and additionally the finite sizes of the excitation lasers preclude an homogeneous pulse area over a large atomic array. We thus implemented the more robust and efficient STIRAP technique described thereafter in Section 7.1.1.

Following the preparation, which takes up to $\sim 2\,\mu$s (the exact timing depends on the choice of Rydberg states), we realize our experiment in the Rydberg manifold. It ends by a read-out pulse transferring only atoms in $|r\rangle$ back to the ground-state where they are recaptured by the tweezers. Atoms in $|r'\rangle$ are left in the Rydberg manifold, repelled by the tweezers and lost. For the de-excitation, we opted for an incoherent depumping by coupling resonantly $|r\rangle$ to the short-lived $5P_{1/2}$ level from which it

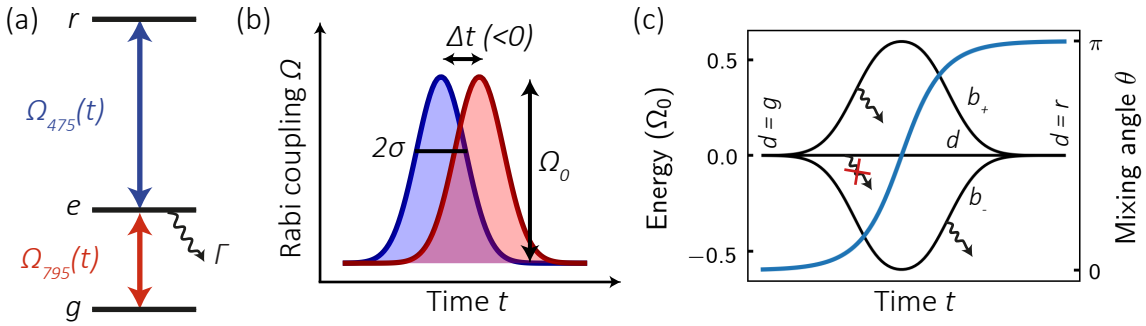

Figure 7.3: The STIRAP scheme. (a) Three-level system $\{|g\rangle, |e\rangle, |r\rangle\}$ resonantly driven by the 795 nm and 475 nm excitation lasers. (b) The time-dependent Rabi couplings $\Omega_{795}(t)$ (red) and $\Omega_{475}(t)$ (blue) are shaped as Gaussian pulses with temporal width σ and delay Δt. The 'counter-intuitive' sequence $\Delta t < 0$ is shown, with the 475 nm pulse arriving first. (c) Evolution during the pulses of the three eigenstates $|b^+\rangle, |b^-\rangle, |d\rangle$ (black). Only the dark-state $|d\rangle$ does not have any contribution from $|e\rangle$ and is thus not affected by spontaneous emission. The mixing angle θ (blue curve) indicates the composition of $|d\rangle$ and evolves smoothly from $\theta = 0$ ($|d\rangle = |g\rangle$) to $\theta = \pi$ ($|d\rangle = |r\rangle$).

decays to the ground state, as will be discussed in Section 7.1.2.

7.1.1 STIRAP excitation

The STIRAP technique, standing for STImulated Rapid Adiabatic Passage, was introduced in the nineties for the manipulation of three-level systems composed of two-long lived states, $|g\rangle$ and $|r\rangle$, and a short-lived one $|e\rangle$. Figure 7.3(a) shows such a system in a ladder configuration, with the two transitions $|g\rangle \leftrightarrow |e\rangle$ and $|e\rangle \leftrightarrow |r\rangle$ driven by lasers. The STIRAP exploits a beautiful property of three-level systems, namely the existence of a 'dark-state' free from the spontaneous emission of $|e\rangle$. The technique, recently reviewed by Vitanov *et al.* [2017], has found a myriad of applications in different fields of physics, and has notably been used for Rydberg excitation of atomic clouds [Cubel *et al.*, 2005; Deiglmayr *et al.*, 2006], and of a single ion [Higgins *et al.*, 2017]. Below, I present the main theoretical concepts.

Principle We consider time-dependent resonant drives $\Omega_{795}(t)$ and $\Omega_{475}(t)$ of the two transitions. The three atomic levels $|g\rangle$, $|e\rangle$ and $|r\rangle$ are mixed (or dressed) by the laser drives to form three instantaneous eigenstates $|b_+\rangle$, $|b_-\rangle$ and $|d\rangle$ with respective

energy $\pm\frac{\hbar}{2}\sqrt{\Omega_{795}^2+\Omega_{475}^2}$ and 0. The zero-energy dark-state $|d\rangle$ reads:

$$|d\rangle = \cos\theta(t)|g\rangle - \sin\theta(t)|r\rangle \tag{7.1}$$

$$\theta(t) = \arctan\left[\Omega_{475}(t)/\Omega_{795}(t)\right] \tag{7.2}$$

where the mixing angle θ depends on the ratio of the two Rabi couplings. Remarkably, there is no contribution of $|e\rangle$ in $|d\rangle$, which is thus unaffected by radiative decay. An atom initially in $|g\rangle$ can be perfectly transferred to $|r\rangle$ by varying θ from 0 to π slowly enough for the system to remain in the instantaneous eigenstate $|d\rangle$. The adiabaticity condition takes the form:

$$\dot{\theta}(t) \ll \sqrt{\Omega_{475}^2(t)+\Omega_{795}^2(t)}. \tag{7.3}$$

The variation rate of mixing angle $\dot{\theta}$ has to remain much smaller than the energy difference between the dark state and the two other eigenstates. This criterion is respected using a 'counter-intuitive' sequence of pulses, sketched in Fig. 7.3(b), where the 475 nm pulse arrives before the 795 nm one. For a good choice of pulse parameters (discussed later), θ varies significantly only when the energy splitting is maximal. The advantage of the STIRAP over a Rabi π-pulse is that, while the latter requires the pulse area to match exactly π, the former works as long as the pulse area is large enough, which is thus more robust to variations of the coupling strengths over large atomic arrays, but also to day-to-day fluctuations of lasers power and beams pointing.

Implementation Most of the technical details about the excitation lasers have already been described in Section 5.1. We have first worked on the Rydberg excitation of $nD_{3/2}$ states, which benefits from higher coupling strength, but our studies presented in Chapter 6 motivated us to also prepare $nS_{1/2}$ levels. To maximize the coupling to $\left|nD_{3/2}, m_J = 3/2\right\rangle$, we use the intermediate level $\left|5P_{1/2}, F = 2, m_F = 2\right\rangle$, while for $\left|nS_{1/2}, m_J = 1/2\right\rangle$, we choose $\left|5P_{1/2}, F = 1, m_F = 1\right\rangle$. The lasers intensities are dynamically tuned with acousto-optic modulators[1] to obtain:

$$\Omega_{475/795}(t) = \Omega_0 \exp\left[-\frac{(t \mp \Delta t/2)^2}{2\sigma^2}\right], \tag{7.4}$$

with a Gaussian pulse width σ, a maximal coupling strength Ω_0 and a delay Δt between the two pulses. The peak Rabi coupling is chosen equal for the two transitions

[1] We use an arbitrary waveform generator to create a 30 MHz signal with an envelope given by Eq. (7.4), which is then mixed with a 80 MHz local oscillator, amplified and fed to the AOMs.

by working with the 475 nm laser at full power and adjusting the power of the 795 nm beam. The highest coupling strength that we can achieve is $\Omega_0/(2\pi) \simeq 50$ MHz for $60D_{3/2}$ state and ~ 25 MHz for $60S_{1/2}$.

Optimization The pulse widths σ and the delay Δt are experimentally optimized to obtain the best transfer efficiency from $|g\rangle$ to $|r\rangle$. Figure 7.4(a) shows how the efficiency depends on σ and Δt for $\Omega_0/(2\pi) = 50$ MHz. First, we observe the clear signature of the STIRAP, as the efficiency drops as soon as the pulses are sent in the wrong ('intuitive') order. Then we see that for larger pulses, there is a wide range of pulse delays for which the efficiency remains constant. It is again typical of the STIRAP, which only requires a smooth evolution of the couplings. In practice, we are interested in performing the transfer as fast as possible and our experimentally optimized parameters are:

- for $60S_{1/2}$ with $\Omega_0/(2\pi) = 25$ MHz: $\sigma = 360$ ns and $\Delta t = 400$ ns,
- for $60D_{3/2}$ with $\Omega_0/(2\pi) = 50$ MHz: $\sigma = 120$ ns and $\Delta t = 100$ ns.

We can check that the pulse parameters meet the adiabaticity criterion of Eq. 7.3 by a factor 20 for the transfer to $60S_{1/2}$ state. For this state, the total STIRAP sequence takes $\sim 2\,\mu$s, after which we can start an experiment in the Rydberg manifold.

In addition to the pulse parameters, we can also tune the detuning Δ from the intermediate $5P_{1/2}$ state, while maintaining the two-photon resonance condition on the $|g\rangle \leftrightarrow |r\rangle$ transition. Experimentally, we obtained better transfer efficiencies when working with a finite single-photon detuning $\Delta/(2\pi) = \pm 20$ MHz rather than with both beams at resonance $\Delta = 0$. While this result is not expected in theory, a reasonable explanation could be that incomplete extinctions of the beams (causing a slow depumping from the initial and final states), and imperfect polarizations (coupling to other Zeeman sublevels) are made less critical by working with a small detuning.

Effect of the van der Waals interaction So far, we only described the STIRAP technique for the excitation of a single atom; we are however interested in preparing an *array* of Rydberg atoms: how does the van der Waals interaction affect the process? On the theoretical level, there have been a lot of proposals combining the STIRAP technique and Rydberg blockade to perform robust entangling gates [Møller, Madsen, and Mølmer, 2008; Beterov *et al.*, 2011, 2013; Petrosyan, Rao, and Mølmer, 2015], but no experimental realization yet. Here we rather want to overcome the Rydberg blockade, which might be possible up to a certain van der Waals interaction strength.

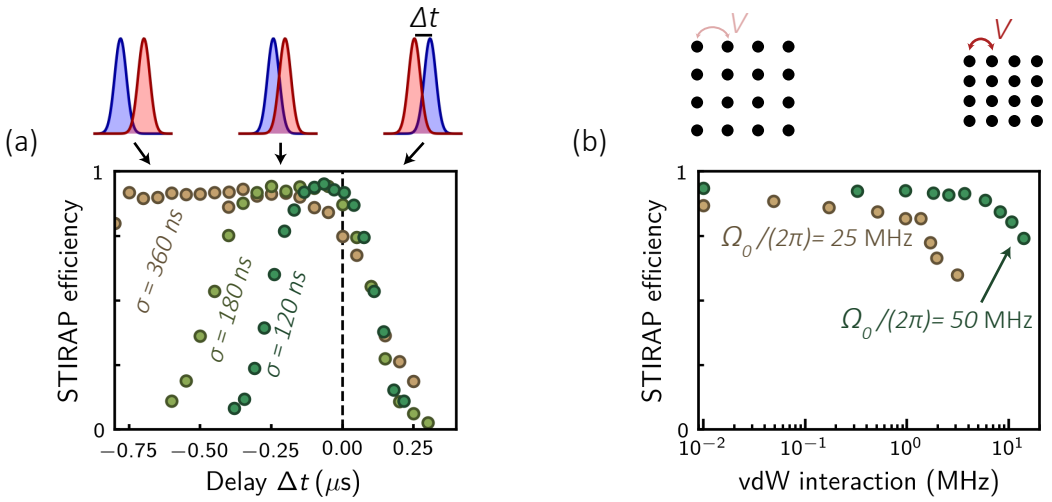

Figure 7.4: STIRAP optimization. (a) Preparation efficiency for various pulse widths σ and delays Δt, for the maximum achievable coupling $\Omega_0/(2\pi) = 50$ MHz. The transfer is optimal for a 'counter-intuitive' sequence of pulses with negative delays $\Delta t < 0$, a signature of the STIRAP technique. For wider pulses (brown curves), the transfer is insensitive to the precise timings of the pulses. (b) In an array of atoms, the van der Waals interaction competes with the STIRAP preparation, which starts to fail for van der Waals shifts higher than 3 MHz.

We experimentally probe this limit by measuring the STIRAP efficiency on 4×4 arrays of atoms with various inter-atomic separations. The efficiencies are shown in Fig. 7.4(b) as a function of the calculated interaction strength V between two Rydberg atoms. For $\Omega_0/(2\pi) = 50$ MHz, it remains remarkably good up to $V \simeq 3$ MHz, while it degrades sooner ($V \simeq 1$ MHz) for the weaker 25 MHz coupling. In the following experiments of this thesis, the van der Waals shift will always be smaller than 0.1 MHz and does not perturb the STIRAP preparation. In the future (see Outlook), we might perform experiments where both van der Waals and dipolar exchange interactions are of similar strength: the results shown here demonstrate that we would still be able to prepare an array of Rydberg atoms using STIRAP.

Effect of the beam inhomogeneity I show here how the finite size of the 475 nm excitation lasers affects the preparation of large Rydberg atomic arrays. In our current optical setup, the 475 nm beam is focused on the atomic arrays with waists along the x and y-axis of $w_x = 25\,\mu$m and $w_y = 40\,\mu$m (Fig. 7.5). We will consider the excitation of planar arrays located at $x = 0$, such that only the spatial dependence $\Omega_{475}(y) = \Omega_0 \exp(-y^2/w_y^2)$ plays a role. Figure 7.5 shows the excitation efficiency as a

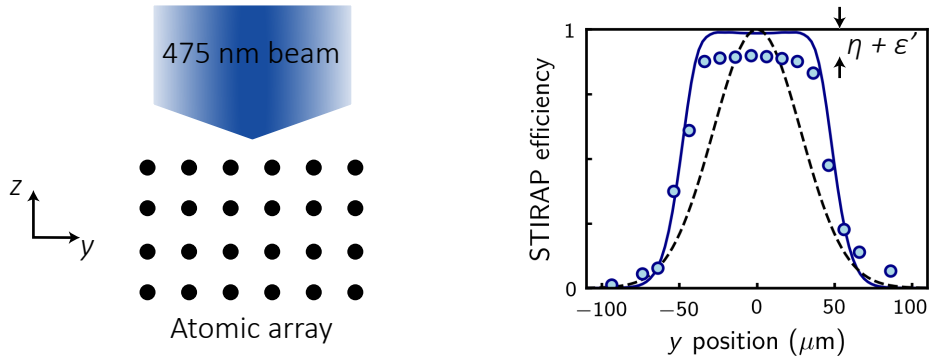

Figure 7.5: STIRAP efficiency. (Left) Inhomogeneous illumination of a large planar atomic array by the 475 nm excitation beam with a waist of $40\,\mu$m in the y direction. The 795 nm beam (not shown) is much larger and can be considered as homogeneous. (Right) STIRAP excitation efficiency as a function of the y position: experimental data (circles) and numerical simulation (blue line). For comparison, the dark dashed line shows the spatial dependence of the Rabi coupling. The deviation from unit efficiency decomposes in detection errors ε' and STIRAP errors η.

function of the y position for experiments performed with $\Omega_0/(2\pi) = 25$ MHz. We observe that the STIRAP pulses remain highly efficient over $\sim 60\,\mu$m. The spatial dependence of the experimental data (circles) is well reproduced by a numerical simulation of the optical Bloch equations using the independently measured parameters (beam waist and Rabi coupling) of the spatial and time-dependent Rabi drives. We also remark that the simulation predicts a perfect transfer in the center.

Transfer efficiency The STIRAP efficiency measured in the previous figures are $P_r = 90(1)$ % in Fig. 7.5 for the excitation of Rydberg S states and $P_r = 93(1)$ % [Fig. 7.4(a)] for D states. A first explanation for these imperfect efficiencies comes from detection errors, that we have discussed in Section 5.2.2. There is a probability ε' that a Rydberg atom is erroneously detected as a ground-state atom. The radiative lifetime of Rydberg $60D$ ($60S$) state is 209 μs (260 μs), from which we calculate an error rate $\varepsilon' = 4.8$ % (3.9 %) and retrieve[2] the real Rydberg population $\tilde{P}_r \simeq P_r/(1-\varepsilon') = 97(1)$ % (94 % for S states). The last few percents are STIRAP errors η, which could be explained by laser phase noise. From the better results with D, rather than S states, we believe that larger Rabi couplings Ω_0 is one of the key to reach higher excitation efficiency and would also allow a quicker preparation. In the future, we intend to obtain this stronger coupling by opting for the 'inverted' scheme discussed in Section 5.4.2.

[2]Neglecting the other detection error ϵ, which affect the measured value only by $\varepsilon\varepsilon'$ and $\varepsilon(1 - P_r)$.

Conclusion We have demonstrated the preparation of large arrays of Rydberg atoms with an efficiency of $(1-\eta) \sim 95$ % using two-photon resonant STIRAP pulses lasting less than $2\,\mu$s. It leaves us with enough time for studies of XY magnetism compared to the $\sim 10\,\mu$s experimental time window with atoms released from their tweezers. On the pratical side, the STIRAP technique is a very robust tool with a constant efficiency along the days, with η small enough to perform experiments without being too much affected by missing Rydberg atoms.

7.1.2 Fast read-out technique

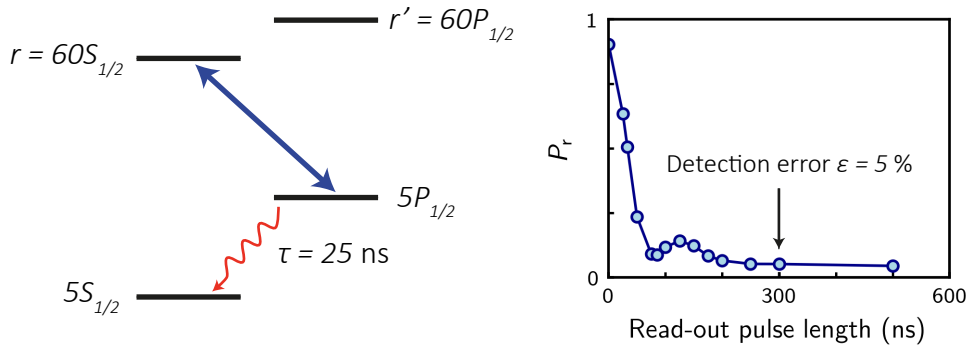

Figure 7.6: Read-out pulse. Left: The 475 nm beam is shone on resonance between a single Rydberg state $|r\rangle$ and the short-lived ($\tau = 25$ ns) intermediate $5P_{1/2}$ level. Right: The strong spontaneous emission leads to an extremely fast damping of the $|e\rangle \leftrightarrow |r\rangle$ Rabi oscillation, as the atom decays to the ground-state. In our experiments, we shine the read-out pulse during 300 ns, 6 times as long as the fitted decay time constant. There remains a $\epsilon = 5$ % probability not to recapture the atom, which will be considered as an atom in $|r'\rangle$ and thus causes a detection error.

After preparing the atoms in a Rydberg state $|r\rangle$ and performing an experiment in the Rydberg manifold between $|r\rangle$ and another Rydberg level $|r'\rangle$, we want to measure the population of the two states. This is achieved using a read-out pulse, where atoms in $|r\rangle$ is de-excited to the ground-state $|g\rangle$, where it is then recaptured by the tweezers and observed by fluorescence imaging. This projective measurement needs to be quick compared to the dynamics driven by the dipole-dipole interaction.

We achieve a fast de-excitation by shining the 475 nm laser beam on resonance with the $|r\rangle \leftrightarrow |e\rangle$ transition. We then benefit from the short lifetime (25 ns) of $|e\rangle$ to quickly bring the atom to the ground state. In Fig. 7.2, we observe that the probability

to remain in $|r\rangle$ decreases quickly with the read-out pulse length. The small oscillatory behavior at ~ 100 ns comes from a strongly damped Rabi oscillation between the Rydberg and intermediate levels. The depumping laser is derived from the same source as the 475 nm excitation beam used in the STIRAP sequence, but goes through an independent AOM to tune its frequency precisely to the resonance while the excitation beam is detuned by $\Delta/(2\pi) \simeq 20$ MHz. The read-out beam is quickly switched on and off (~ 10 ns) with an EOM. A high extinction ratio of the latter is critical to avoid depumping the Rydberg atoms during the experimental sequence and is re-optimized daily.

Detection errors We fix the read-out pulse length to 300 ns, for which we measure a recapture probability of 95 % that does not increase for longer pulses. This gives us a detection error $\epsilon = 5$ %, as we are going to attribute the loss events to an atom in $|r'\rangle$, whereas it was truly in $|r\rangle$. Most of these errors are caused by background-gas collisions and by the displacement of the atom away from the capture region of the tweezers, as already described in Section 5.2. Here, ϵ is slightly higher than what it is predicted from the previously mentioned error sources (~ 3 %), as we also need to consider stimulated transfer to other Rydberg levels by the 300 K black-body radiation: for a principal quantum number $n = 60$, for which we have performed this experiment, the depopulation rate is $\Gamma_{\mathrm{BBR}} \simeq 1/(150\,\mu\mathrm{s})$, which integrated during the $\sim 3\,\mu$s that we spent in the Rydberg manifold gives an error rate of 2 %.

7.2 Manipulation of an array of Rydberg atoms

I now turn to the control of spin-1/2 particles defined by two dipole-coupled Rydberg levels. With our two-photon excitation scheme, we can prepare Rydberg $nS_{1/2}$ and $nD_{3/2}$ states and both have a direct microwave transition to Rydberg P orbitals. During this thesis, we performed experiments with two different sets of pseudo-spin states:

- $|\downarrow\rangle = \left|60S_{1/2}, 1/2\right\rangle$, $|\uparrow\rangle = \left|60P_{1/2}, -1/2\right\rangle$ with a 16.7 GHz transition frequency,
- $|\downarrow\rangle = \left|61D_{3/2}, 3/2\right\rangle$, $|\uparrow\rangle = \left|62P_{1/2}, 1/2\right\rangle$ with a 9.5 GHz transition frequency.

Initially, all atoms are prepared in $|\downarrow\rangle$ by the STIRAP pulses. In this section, I first present how to drive the spin-1/2 particles with microwave radiations and then demonstrate the control of the transition frequency with an addressing beam.

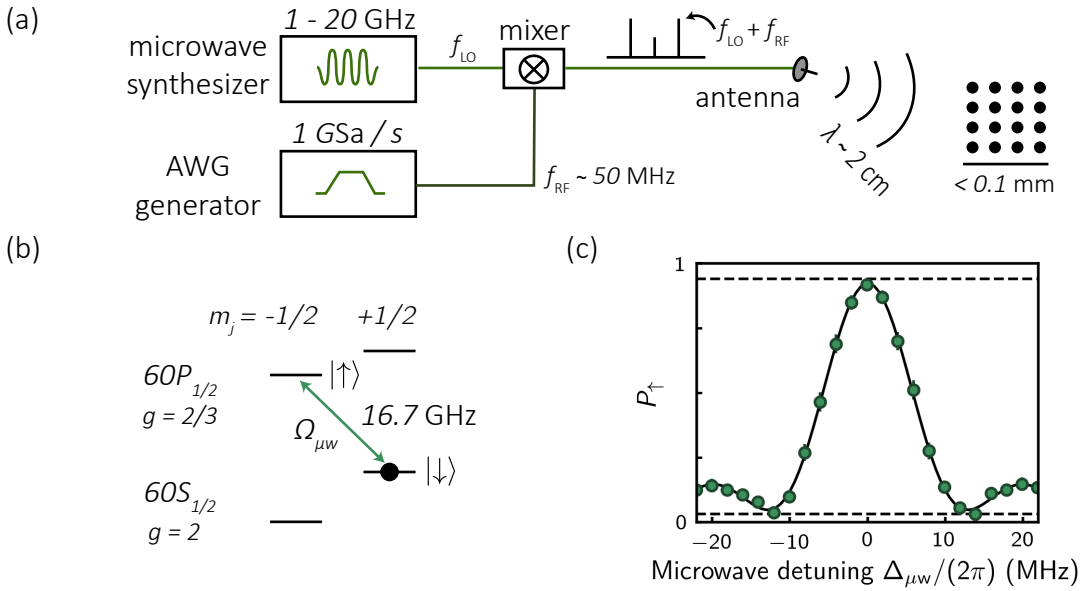

Figure 7.7: Rydberg-Rydberg microwave transition. (a) Microwave experimental setup (described in the text). (b) A possible spin-1/2 system using the Rydberg $60S_{1/2}$ and $60P_{1/2}$ states. The green line indicates the microwave transition between the two chosen pseudo-spin states $|\uparrow\rangle$ and $|\downarrow\rangle$. The solid disk indicates the level in which atoms are prepared after the STIRAP sequence. The Zeeman manifolds are split by a magnetic field. (c) Microwave spectrum of the $|\downarrow\rangle \leftrightarrow |\uparrow\rangle$ transition with $\Omega_{\mu w}/(2\pi) = 7.4$ MHz.

7.2.1 Global rotations with a microwave field

Here, I show how to manipulate spin-1/2 particles, independent or in interaction, using microwave pulses driving the transition between the two Rydberg orbitals. Due to the extremely large electric dipole matrix element between $|\downarrow\rangle$ and $|\uparrow\rangle$, the two-level system is efficiently driven even with weak microwave intensities. I start by describing the experimental setup shown in Fig. 7.7(a): first, a microwave synthesizer outputs a 13 dBm local oscillator (LO) of frequency f_{LO} up to 20 GHz, a mixer then combines it with an RF signal $A(t)\cos[2\pi f_{\mathrm{RF}} t + \phi(t)]$ with $f_{\mathrm{RF}} \sim 50$ MHz and programmable time-dependent amplitude and instantaneous phase generated by an arbitrary waveform generator. At the output of the mixer, we get two main sidebands at $f_{\mathrm{LO}} \pm f_{\mathrm{RF}}$ around the LO signal attenuated by ~ -30 dB. Then, f_{RF} is chosen sufficiently large such that only the upper sideband drives the atom.

The microwave pulse is then radiated by a simple dipole antenna placed outside the vacuum chamber. The field polarization is not controlled due to the presence of the metallic lens holder (spaced by ~ 1.5 cm) strongly affecting the propagation of the

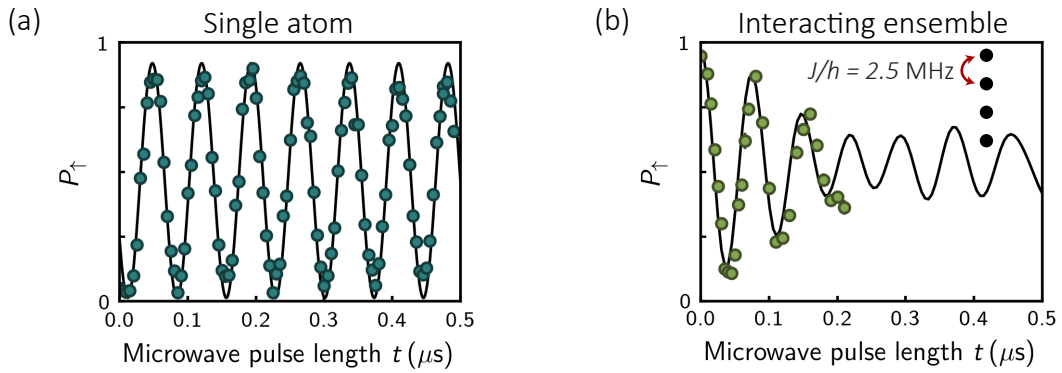

Figure 7.8: Highly coherent microwave Rabi oscillations (a) Rabi oscillation on a single atom. There is no observable damping on the 6 first periods shown here. The solid line is a fit used to extract the microwave Rabi frequency $\Omega_{\mu w}/(2\pi) = 13.4(1)$ MHz. The finite contrast is only caused by preparation and detection errors. (b) Same experimental sequence but on a chain of four Rydberg atoms coupled by the dipole-dipole interaction. The relaxation of the oscillations is induced by the spin-spin couplings. The solid line is a result of an ab-initio calculation using the Rabi coupling obtained in (a).

microwave radiation ($\lambda \sim 2$ cm). We thus rely on the splitting of the Zeeman manifold by an applied magnetic field B_z to energetically isolate a single transition between two Zeeman sublevels. For the atomic levels shown in Fig 7.7(b), and a magnetic field $B_z = 50$ G, the σ^- transition between $|\downarrow\rangle$ and $|\uparrow\rangle$ is separated by 45 MHz from the closest π transition between $|\downarrow\rangle$ and $\left|60P_{1/2}, 1/2\right\rangle$. Finally, Fig. 7.7(c) shows a microwave spectrum of the two-level resonance $|\downarrow\rangle \leftrightarrow |\uparrow\rangle$ with a Rabi frequency $\Omega_{\mu w}/(2\pi) = 7.4$ MHz.

Rabi oscillations I then demonstrate the high level of coherence obtained on a single atom driven with microwaves. Figure 7.8(a) shows a Rabi oscillation between $|\downarrow\rangle$ and $|\uparrow\rangle$ that is strikingly better than any optically-driven ground-Rydberg Rabi oscillations obtained in our experiments (see Chapter 5). Firstly, there is no observable damping, which is explained by the fact that the microwave transition is not affected by Doppler effect, spontaneous emission or phase noise of the driving field. The finite contrast of the spin-flip rotation is only caused by the preparation and detection errors. Secondly, we can reach high Rabi coupling, here $\Omega_{\mu w}/(2\pi) = 13.4(1)$ MHz, which is here limited on purpose to avoid coupling to the other Zeeman sublevels. Using the full available microwave power, we could reach driving strengths of many tens of MHz.

With this tool, we can already perform a simple experiment demonstrating the presence of dipolar interactions between Rydberg atoms. We repeat the same Rabi

oscillation experiment as above, but now with a small chain of four Rydberg atoms. The pair-wise dipolar coupling constant is calculated to be $J/h = 2.5$ MHz and will compete with the Rabi drive $\Omega_{\mu w}/(2\pi) = 13.4$ MHz. Consequently, the Rabi oscillation shown in Fig. 7.8(b) is strongly damped, not by decoherence but by the interaction-induced dephasing of each spin relatively to the microwave field. Similar experiments, but in a cold atomic gas, have been reported by Orioli *et al.* [2018].

Microwave sweeps Using the arbitrary waveform generator, we can generate time-dependent microwave Rabi couplings $\Omega_{\mu w}(t)$ and detunings $\Delta_{\mu w}(t)$. Recall that, in our mapping to spin-1/2 particles, they are equivalent to transverse $B_\perp$ and longitudinal $B_\parallel$ magnetic fields, respectively. In the previous paragraph, we have observed the precession of a spin around a fixed transverse magnetic field ($B_\parallel = 0$, $B_\perp(t) = B$), resulting in many Rabi spin-flips. Another approach to perform a spin-flip is to use a microwave sweep to adiabatically rotate the spin from $|\downarrow\rangle$ to $|\uparrow\rangle$, as illustrated on the Bloch sphere in Fig. 7.9(a). An adequate microwave profile is shown in Fig. 7.9(b): the detuning is swept in $0.3\,\mu$s from -15 MHz to $+15$ MHz around the resonance, while the Rabi coupling is momentarily increased up to $\Omega_{\mu w}/(2\pi) \simeq 10$ MHz. As a first step, we apply this sweep on a single atom initially in $|\downarrow\rangle$ and record the temporal evolution of $P_\uparrow$ by interrupting the sweep at different times. The experimental data are shown in Fig. 7.9(d) and are in excellent agreement with a numerical simulation of the two-level system dynamics taking into account the independently measured preparation and detection errors. A microwave sweep is as efficient as a Rabi π-pulse, though much slower: $0.3\,\mu$s instead of $0.05\,\mu$s for $\Omega_{\mu w}/(2\pi) = 10$ MHz.

The advantage of microwave sweeps appears clearly when considering an ensemble of interacting Rydberg atoms. Starting from a many-body state with all spins pointing down, we want to prepare them all in $|\uparrow\rangle$. We have seen in the previous paragraph that strong dipole-dipole interactions between Rydberg atoms led to dephasing between the spins during a Rabi oscillation, which prevented an efficient global spin-flip. The effect of interactions is mitigated by using a large effective magnetic field $|\mathbf{B}(t)| \gg J$. In this case, the ensemble of spins is always in a paramagnetic state with only a change in orientation of the magnetization during the sweep, which is illustrated in Fig. 7.9(c) and demonstrated experimentally in Fig. 7.9(e). At the end of the sweep, all atoms are in $|\uparrow\rangle$, and the evolution of the population $P_\uparrow$ averaged on the four spins is again in very good agreement with an ab-initio calculation taking into account the independently measured preparation and detection errors $(\eta, \epsilon, \epsilon') = (0.05, 0.04, 0.05)$ %. The measured spin-flip efficiency is consistent with the perfect transfer predicted numerically.

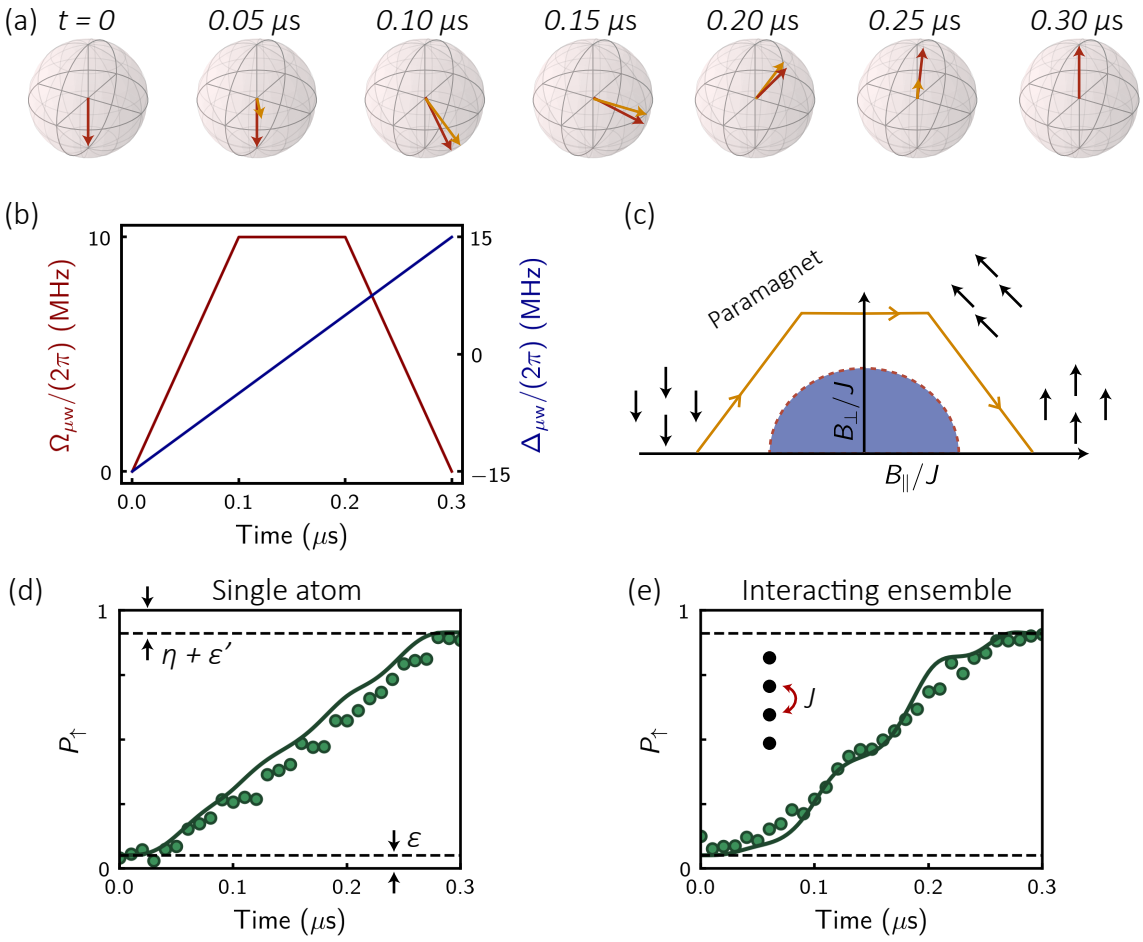

Figure 7.9: Spin-flips with microwave sweeps. (a) Snapshots of the spin-1/2 state (red arrow) and effective magnetic field (orange) on the Bloch sphere during an adiabatic evolution of the microwave Rabi coupling $\Omega_{\mu\mathrm{w}}(t)$ and detuning $\Delta_{\mu\mathrm{w}}(t)$ shown in (b). (c) Phase diagram of the ground-state of an ensemble of interacting spins in the parameter space spanned by the rescaled transverse $B_\perp/J$ and longitudinal $B_\parallel/J$ magnetic fields, with J the typical dipole-dipole coupling. For sufficiently large B-field, the ensemble is always a paramagnet and the orientation of the spins follows the magnetic field. The gap between the ground state and the first excited states closes only when $B/J \lesssim 1$: the system goes through a quantum phase transition (red dashed line) and the new ground state depends on the exact geometry of the atomic array. The microwave sweep is represented by the orange profile and remains deep in the paramagnetic phase. (d,e) Temporal evolution during the sweep of the probability $P_\uparrow$ for an experiment performed on a single atom (d) or a chain of 4 interacting spins (e). The solid line is the result of an ab-initio calculation taking into account independently measured preparation and detection errors (dashed lines).

7.2.2 Local addressing with a focused laser beam

The previous section has shown that microwave manipulation is a very powerful tool, but it has a disadvantage: we cannot manipulate a *single* Rydberg atom in an atomic array. For our studies of spin Hamiltonians, we ideally need a technique to manipulate single spins, while leaving others unaffected. We achieve this by focusing, on a single atom, an addressing beam tuned close to the 1006 nm transition between the Rydberg state $|\downarrow\rangle$ (S or D orbitals) and the low-lying $6P_{1/2}$ level. Due to electric dipole selection rule, Rydberg P states remains unaffected, except for the small repulsive ponderomotive light-shift common to both states [Younge *et al.*, 2010]. Initially suggested by Saffman and Walker [2005], this scheme has been used for the magic trapping of both ground and Rydberg atoms [Li, Dudin, and Kuzmich, 2013].

Implementation A 1006 nm beam, obtained from a tunable cw Ti:sapphire laser, is focused through our aspheric lens on the atomic array and manually aligned on the position of a 850 nm tweezers. We achieved the latter by comparing the fluorescence of atoms trapped at the focus of the 850 nm and 1006 nm beams. The addressing beam has a waist of 3.4 μm (measured by parametric heating, see Section 2.1.3), chosen as a trade-off between adjacent sites cross-talk (1% residual intensity at $R \simeq 5\,\mu$m) and robustness to beam pointing fluctuations. The addressing beam is switched on and off by an electro-optic modulator with a rise time of 10 ns. The laser frequency is locked on a commercial wavemeter (High Finesse, WLM SU10) with a sub-MHz precision.

The 1006 nm transitions used to address the Rydberg nS and nD states are:

- $\left|61D_{3/2}, F = 3, m_F = 3\right\rangle \leftrightarrow \left|6P_{1/2}, F = 2, m_F = 2\right\rangle$ at 298.139450 THz
- $\left|60S_{1/2}, F = 2, m_F = 2\right\rangle \leftrightarrow \left|6P_{1/2}, F = 2, m_F = 2\right\rangle$ at 298.046990 THz

where the stated transition frequencies are the measured one for $B_z \sim 10$ G. The typically achievable Rabi coupling on these transitions is $\Omega_{\text{addr}}/(2\pi) \sim 100$ MHz with a laser power of a few tens of mW. We use this coupling either to apply a light-shift on the Rydberg state, or to split the transition resonance using the Autler-Townes effect.

AC-Stark shift When the addressing beam is detuned by Δ_{addr} from the resonance frequency, it creates an AC-Stark shift on the Rydberg state $|\downarrow\rangle$. As $|\uparrow\rangle$ is unaffected, the microwave transition frequency of $|\downarrow\rangle \leftrightarrow |\uparrow\rangle$ is changed by:

$$\Delta\omega_0 = \frac{\Omega_{\text{addr}}^2}{4\Delta_{\text{addr}}}. \tag{7.5}$$

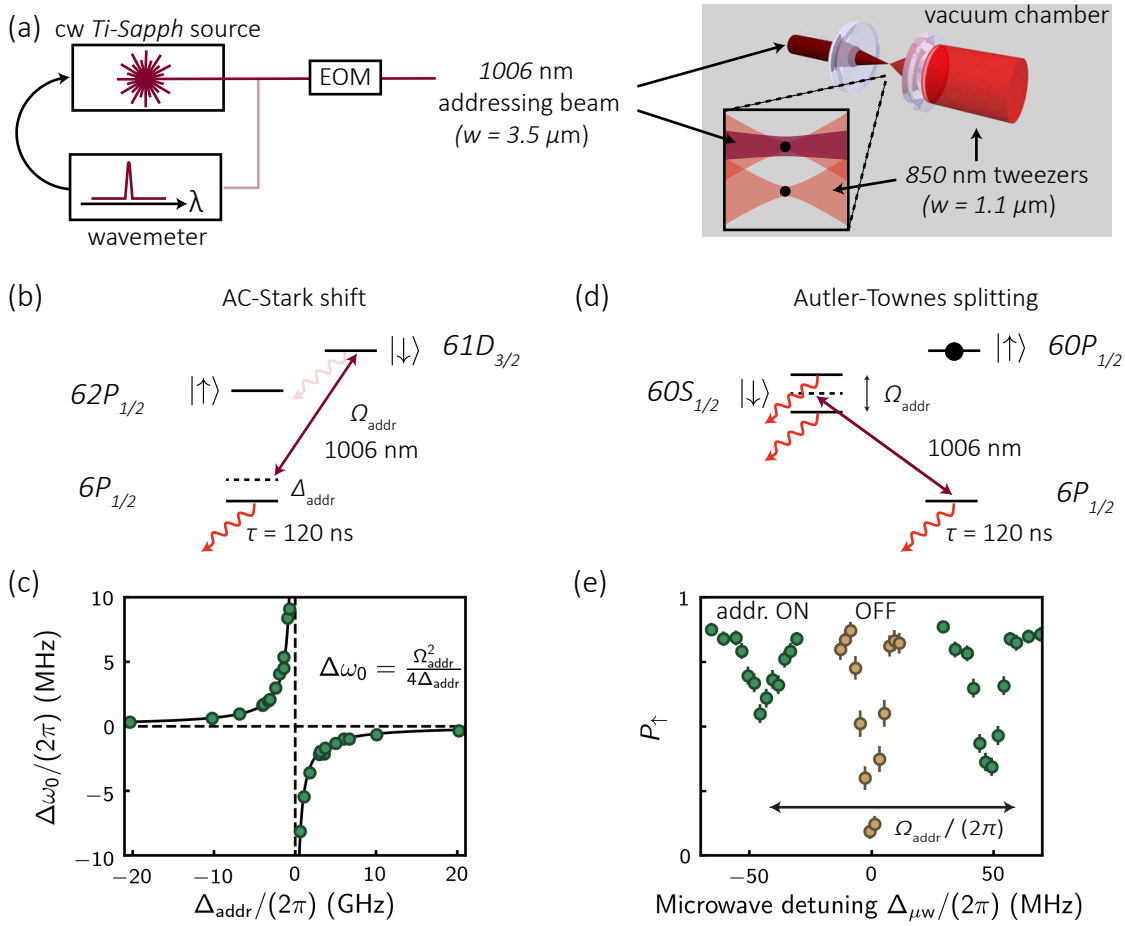

Figure 7.10: AC-Stark shift and Autler-Townes splitting with an addressing laser. (a) Experimental setup for the generation of an addressing laser, locked on a wavelength-meter, focused on a single atom through our aspheric lens. (b) The 1006 nm addressing laser, with Rabi frequency Ω_{addr}, is detuned by Δ_{addr} from the $6P_{1/2} \leftrightarrow 61D_{3/2}$ transition to apply a light-shift $\Delta\omega_0 = \Omega_{\mathrm{addr}}^2/4\Delta_{\mathrm{addr}}$ on the Rydberg state. The shifted state acquires only a small decay rate. (c) The microwave transition frequency between the $62P_{1/2}$ and $61D_{3/2}$ levels is measured for various detunings Δ_{addr} of the addressing beam and shows the expected dispersive dependence. The solid line is the result of a calculation without any adjustable parameters. (d) Tuning the addressing beam on resonance with the $6P_{1/2}$ level ($\Delta_{\mathrm{addr}} = 0$), we realize the Autler-Townes condition where the Rydberg level is split into two short-lived states. (e) The Autler-Townes splitting is observed by preparing the atom in the $60P_{1/2}$ state and then looking for the $60P_{1/2} \leftrightarrow 60S_{1/2}$ transition. With the addressing beam switched on (green circles), the microwave transition is split into two symmetric lines around the reference spectrum (yellow circles), the splitting directly gives the Rabi coupling $\Omega_{\mathrm{addr}}/(2\pi) = 92(1)$ MHz.

Figure 7.10(c) shows the measurement of $\Delta\omega_0$ by microwave spectroscopy for various detuning Δ_{addr} of the addressing beam and a fixed laser power of ~ 30 mW. The experimental data is in perfect agreement with Eq. (7.5) using an ab-initio calculation of the Rabi coupling $\Omega_{\text{addr}}/(2\pi) = 158$ MHz from the dipole matrix element (obtained from the ARC software [Šibalić *et al.*, 2016]) and the independently measured beam waist and incident power. For increasing light-shift, the Rydberg state lifetime τ_r is decreased, due to the mixing with the short-lived $6P_{1/2}$ level, to the value:

$$\tau_r \simeq \left(\frac{\Omega_{\text{addr}}}{\Delta_{\text{addr}}}\right)^2 \tau_{6P}, \tag{7.6}$$

where $\tau_{6P} = 120$ ns is the lifetime of the $6P_{1/2}$ level [Gomez *et al.*, 2004]. For $\Omega_{\text{addr}}/\Delta_{\text{addr}} < 0.1$, we still obtain a considerable light-shift of a few MHz, while the lifetime τ_r remains on the order of several tens of microseconds, comparable to the lifetime of the Rydberg levels, and thus barely affects the system.

Autler-Townes splitting The situation is different when the addressing beam is tuned exactly to the resonance with the $6P_{1/2}$ state and gives rise to an Autler-Townes splitting (see Section 5.1.2). Figure 7.10(e) illustrates the effect with microwave spectra, obtained by coupling an atom initially in $|\uparrow\rangle$ to the addressed state $|\downarrow\rangle$: we observe the splitting of the line when the addressing beam is on, which also gives a direct measurement of the Rabi coupling $\Omega_{\text{addr}}/(2\pi) = 92(1)$ MHz (different than above as we used another Rydberg state and addressing power). Let us note that if the atom is in $|\downarrow\rangle$ when the beam is on, it will quickly decay to the electronic ground state, such that we can only apply this technique when the addressed atom is in $|\uparrow\rangle$.

7.2.3 Preparing a single spin excitation

I now explain how to combine microwave sweeps with the Autler-Townes splitting effect to prepare a single spin excitation in an array of Rydberg atoms. This technique will be used to observe a spin-exchange oscillation between two atoms in the next section, and dynamical properties of an XY magnet in the next chapter. The procedure is shown in Fig. 7.11: After the STIRAP sequence, all atoms are in $|\downarrow\rangle$, and the first step is to transfer them all to $|\uparrow\rangle$ by a first microwave sweep. We then switch on the addressing beam on a selected atom, which will be unaffected by any microwave radiation within $\pm\Omega_{\text{addr}}/2 \sim 2\pi \times 50$ MHz of the resonance. Next, a second microwave sweep transfers all the other atoms back to $|\downarrow\rangle$, leaving a single spin excitation on the

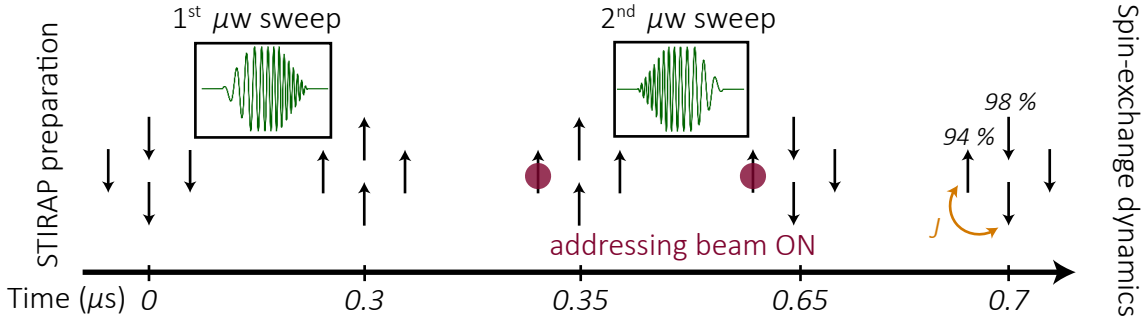

Figure 7.11: Preparation of a single spin excitation. Following the STIRAP initialization, all atoms are in $|\downarrow\rangle$. We then combine microwave sweeps and Autler-Townes effect to flip a single atom in $|\uparrow\rangle$. As the resonant addressing beam can only be applied on an atom in $|\uparrow\rangle$ (when addressed with the Autler-Townes technique, the state $|\downarrow\rangle$ is short-lived), we start by transferring all atoms in $|\uparrow\rangle$ with a first microwave sweep. The addressing beam is then safely shone on a selected atom and a second sweep transfers all the other atoms back to $|\downarrow\rangle$. After switching off the addressing beam, spin-exchange dynamics will start, driven by the resonant dipolar coupling. The quoted efficiencies are corrected for preparation and detection errors.

addressed site. A spin-exchange dynamics will start as soon as the addressing beam is switched off, which tunes back the selected atom in resonance with the other ones.

The efficiency of the procedure is 94 % for the addressed atom and 98 % for the others. We obtain these numbers by measuring the recapture probability of the atoms when shining the read-out pulse directly after the second sweep: 12 % for the addressed atom and 93 % for the others, and by correcting for preparation and detection errors $(\eta, \epsilon, \epsilon') = (0.05, 0.04, 0.05)$. Special care was taken to ensure a complete extinction of the resonant addressing beam when the selected atom A was in $|\downarrow\rangle$. Additionally, even if the 1006 nm laser intensity on another atom B separated by, e.g., $10\,\mu$m from the addressing spot is reduced by a factor $\sim 10^3$, it is still possible that atom B scatters a 1006 nm photon after being transferred back to $|\downarrow\rangle$ by the second sweep. To avoid this, we slightly detune the addressing beam from the resonance by $\Gamma_{6P} \ll \Delta_{\text{addr}} \simeq (2\pi) \times 10\,\text{MHz} \ll \Omega_{\text{addr}}$: we still obtain a quasi-resonant Autler-Townes splitting for the addressed atom A, while the scattering rate of a photon on atom B is reduced by an additional factor $(\Delta_{\text{addr}}/\Gamma_{6P})^2 > 100$.

In our work on a two-atom system [de Léséleuc *et al.*, 2017], we prepared the spin-excitation $|\uparrow\downarrow\rangle$ with a Rabi π-pulse (instead of microwave sweeps) and an AC-Stark shift (instead of the Autler-Townes splitting). However, for strongly interacting systems, the preparation efficiency is maximized with the aforementioned procedure.

7.3 Resonant dipolar interaction between two Rydberg atoms

Having learnt how to manipulate our ensemble of Rydberg atoms with a global microwave field and a local addressing beam, we now explore the effect of the resonant dipolar coupling on an elementary system of two Rydberg atoms. Figure 7.12 shows the situation that we consider: two atoms are separated by a distance R and make an angle θ with the quantization axis. Each atom encodes a spin-1/2 particle using two dipole-coupled Zeeman sublevels. Neglecting other levels, the two-atom system evolves in the Hilbert space spanned by four pair-states: $|\downarrow\downarrow\rangle, |\uparrow\downarrow\rangle, |\downarrow\uparrow\rangle, |\uparrow\uparrow\rangle$. The main effect of the dipole-dipole interaction is to resonantly couple the two degenerate pair-states $|\uparrow\downarrow\rangle$ and $|\downarrow\uparrow\rangle$:

$$\langle\uparrow\downarrow|\,\hat{H}_{dd}\,|\downarrow\uparrow\rangle = \frac{1-3\cos^2\theta}{2} \times \frac{C_3}{R^3} = J(R,\theta), \tag{7.7}$$

where C_3 is proportional to the product of two dipole matrix elements. This expression is readily derived from Eq. (6.2). The angular dependence can be understood with classical permanent dipoles: the interaction energy is of opposite sign for two dipoles side by side ($\theta = \pm 90°$) or head to tail ($\theta = 0°$ or $180°$). The interaction cancels and changes sign at the so-called 'magic' angle $\theta_m = \arccos(1/\sqrt{3}) \simeq 54.7°$.

Other Zeeman sublevels I justify here that we can ignore the other Zeeman sublevels by applying a sufficiently large magnetic field B_z. As can be seen from Fig. 7.12, although the dipole-dipole Hamiltonian couples $|\downarrow\uparrow\rangle$ to $|r''r'\rangle$ (but also $|\uparrow r'\rangle$ and $|r''\downarrow\rangle$), these processes become off-resonant when applying a magnetic field B_z splitting the Zeeman manifolds by $\Delta E_Z = g\mu_B \Delta m B_z$. For example, with $B_z \sim 10$ G, we obtain a splitting $\Delta E_Z \sim 30$ MHz between the two $S_{1/2}$ sublevels, which is much larger than the typical interaction energy J, in the MHz range.

Van der Waals interaction vs dipolar exchange coupling We also need to consider the second-order effect of the dipole-dipole Hamiltonian on the pair-states $|\downarrow\downarrow\rangle$ and $|\uparrow\uparrow\rangle$, which takes the form of a van der Waals shift $V = C_6/R^6$ (see Chapter 6). The C_6 coefficients depend on the pair-states: it is smaller by more than one order of magnitude for P orbitals than for S or D states (remember Fig. 6.4). Here, we want to minimize the van der Waals interaction that gives rise to an Ising coupling between the spins, relatively to the resonant dipole-dipole interaction giving an XY coupling. Due to the different scaling laws $V \propto n^{11}/R^6$ and $J \propto n^4/R^3$, it is possible to tune the relative weight of the two contributions and, in particular, reach the regime $V \ll J$ by

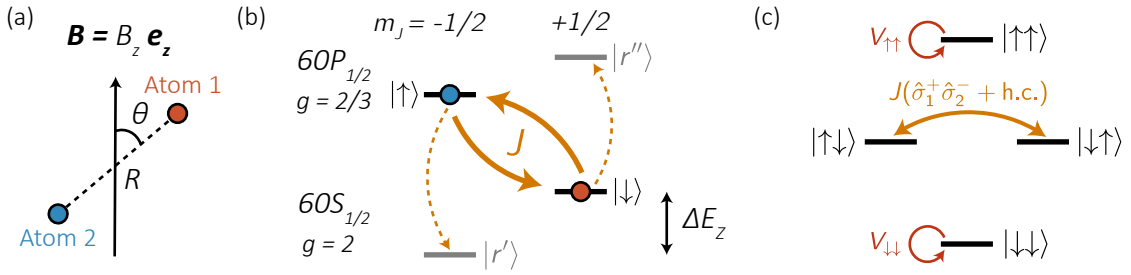

Figure 7.12: Resonant dipole-dipole interaction. (a) Two atoms separated by a distance R and making an angle θ with the quantization axis defined by a magnetic field B_z. (b) Possible dipolar exchange couplings between two atoms in $S_{1/2}$ or $P_{1/2}$ orbitals. Two Zeeman sublevels play the role of pseudo-spin states $|\uparrow\rangle$ and $|\downarrow\rangle$. We are interested in the resonant spin-exchange process $|\downarrow\uparrow\rangle \leftrightarrow |\uparrow\downarrow\rangle$ indicated by the solid orange arrows. The dashed arrows show one of the possible dipolar coupling leading to population of other sublevels (in gray). Such processes are made off-resonant, and thus inhibited, for a sufficiently large Zeeman splitting ΔE_Z. (c) The two-atom system reduces to only four pair-states. The resonant dipole-dipole interaction between the Rydberg atoms translate to an XY coupling between $|\downarrow\uparrow\rangle$ and $|\uparrow\downarrow\rangle$. The van der Waals interactions, $V_{\downarrow\downarrow}$ and $V_{\uparrow\uparrow}$, affecting two atoms in the same Rydberg state are made negligible compared to J for our choice of interatomic separation R and principal quantum number n.

using relatively low n and large interatomic separation R. For the two sets of Rydberg states used in the following experiments, we have:

- $|\uparrow\rangle = |62P_{1/2}, 1/2\rangle$, $|\downarrow\rangle = |61D_{3/2}, 3/2\rangle$: $C_3/h = -7.458$ GHz.μm^3, $C_6^{\uparrow\uparrow,\downarrow\downarrow}/h = (6, -769)$ GHz.μm^6. For $R = 20\,\mu$m, we reach $J/h = 0.93$ MHz and $|V|/h < 0.01$ MHz.

- $|\uparrow\rangle = |60P_{1/2}, -1/2\rangle$, $|\downarrow\rangle = |60S_{1/2}, 1/2\rangle$: $C_3/h = -3.035$ GHz.μm^3, $C_6^{\uparrow\uparrow,\downarrow\downarrow}/h = (4, 137)$ GHz.μm^6. For $R = 12\,\mu$m, we reach $J/h = 1.7$ MHz and $|V|/h < 0.05$ MHz.

For these parameters, we can thus safely neglect the van der Waals shifts V, which are one to two orders of magnitude smaller than the dipolar exchange couplings J. In the future, we could harness the van der Waals interaction to implement an Heisenberg magnet by choosing, e.g., the $90S_{1/2}$ and $90P_{1/2}$ Rydberg states and a typical interatomic separation $R = 10\,\mu$m giving $J \simeq V = h \times 16$ MHz, or tune the relative strength between the XY and Ising couplings to explore different phases of anisotropic XXZ magnets (see Outlook).

Previous studies In an earlier work of the group, Barredo *et al.* [2015] presented the first observation of a spin-exchange process between two single Rydberg atoms, measured the $1/R^3$ dependence of the dipolar coupling J and implemented an elementary XY magnet on a chain of three atoms. At that time, the different tools presented in the previous sections (STIRAP excitation, Rydberg addressing beam) were not yet developed. Using them, I now revisit these previous studies of the dipole-dipole interaction, showing how to extract the interaction energy J either from a spin-exchange oscillation or from a microwave spectrum of the interacting system, and I use it to measure the angular dependence of $J(R, \theta)$.

7.3.1 Microwave spectroscopy of the super-radiant state

The resonant dipole-dipole interaction modifies the spectrum of pair-states as shown in Fig. 7.13(a): the two degenerate pair-states hybridize to form the two eigenstates:

$$|\pm\rangle = \frac{|\uparrow\downarrow\rangle \pm |\downarrow\uparrow\rangle}{\sqrt{2}} \quad \text{with energies} \quad E_\pm = \pm J. \tag{7.8}$$

The anti-symmetric state $|-\rangle$ is not coupled to the microwave field, due to destructive interference between the two pair states, and is sometimes dubbed as a dark or 'subradiant' state. On the contrary, the symmetric state $|+\rangle$ couples to the microwave field with an enhanced Rabi frequency $\sqrt{2}\Omega_{\mu\mathrm{w}}$, and is referred to as the bright or 'superradiant' state. We can thus use the microwave transition $|\downarrow\downarrow\rangle \leftrightarrow |+\rangle$ to measure the coupling strength J.

Starting from $|\downarrow\downarrow\rangle$ prepared by the STIRAP excitation, we shine a microwave field with Rabi frequency $\Omega_{\mu\mathrm{w}}/(2\pi) = 0.3$ MHz during $1\,\mu$s and record the probability $P_{\downarrow\downarrow}$ that the system remains in the initial state for various detuning $\Delta_{\mu\mathrm{w}}$ from the single-atom resonance. The results are shown in Fig. 7.13(b). In the higher panel, where the interaction energy is positive, we observe a single dip at a detuning $\hbar\Delta_{\mu\mathrm{w}} = J$. As expected, there is no signal at $\hbar\Delta_{\mu\mathrm{w}} = -J$ as $|-\rangle$ does not couple to the microwave field. In the middle panel, we changed the orientation θ of the pair of atoms such that the interaction strength is now negative $J/h = -0.8$ MHz. In the lower panel, the interaction is suppressed by choosing the angle $\theta_m = 54.7°$. As a side remark, we also couple to the state $|\uparrow\uparrow\rangle$ through the two-photon resonance $|\downarrow\downarrow\rangle \leftrightarrow |\uparrow\uparrow\rangle$ occurring at $\Delta_{\mu\mathrm{w}} = 0$, which can slightly distort the line shape for $\hbar\Omega_{\mu\mathrm{w}} \sim J$ (but not seen here).

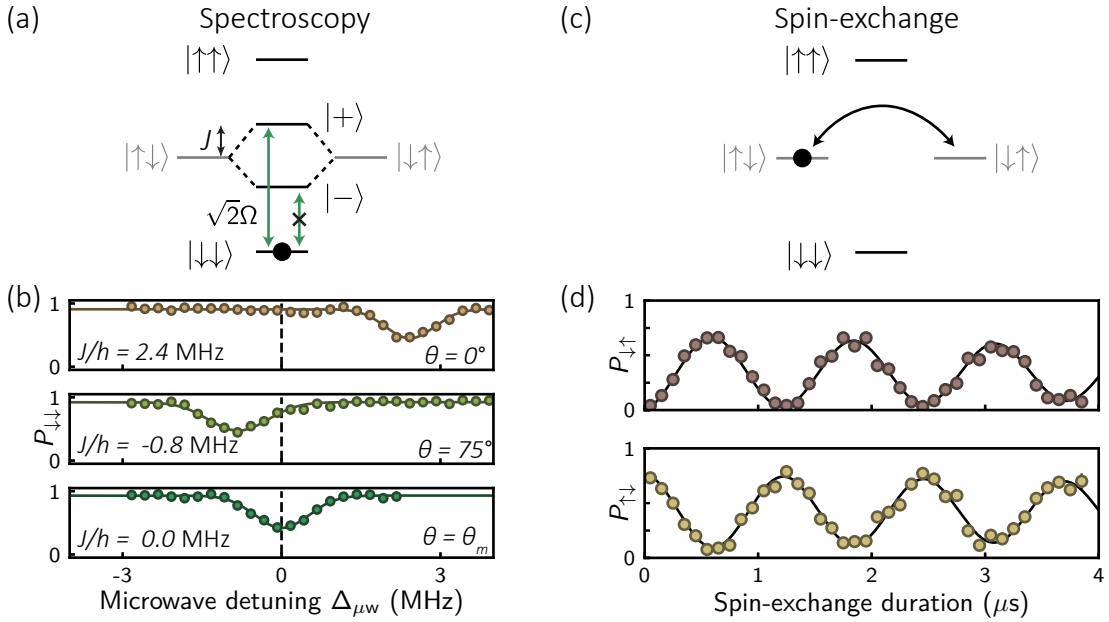

Figure 7.13: Probing the resonant dipolar coupling. (a) The dipole-dipole interaction mixes the two degenerate states $|\uparrow\downarrow\rangle$ and $|\downarrow\uparrow\rangle$ to give symmetric $|+\rangle$ and anti-symmetric $|-\rangle$ eigenstates shifted by an energy $\pm J$. The microwave coupling to the anti-symmetric state vanishes, while it is enhanced by a factor $\sqrt{2}$ for the symmetric state. (b) The interaction energy J is measured by spectroscopy of the $|\downarrow\downarrow\rangle \leftrightarrow |+\rangle$ transition, shown here for three different values $J = 2.4, -0.8, 0.0$ MHz obtained by varying θ. (c) After preparing the two atoms in the state $|\uparrow\downarrow\rangle$, the dipole-dipole interaction gives rise to a spin-exchange dynamics at a frequency $2J$, as observed in (d). Solid lines are fits used to extract the interaction energy.

7.3.2 Spin-exchange oscillation

In addition to probing the stationary eigenstates of the two-atom system, we can also observe directly in the time domain the spin-exchange oscillation $|\uparrow\downarrow\rangle \leftrightarrow |\downarrow\uparrow\rangle$ driven the dipolar coupling J. After preparing the initial state $|\uparrow\downarrow\rangle$ with the procedure described in Section 7.2.3, we let the system evolve freely for a time T before applying the read-out pulse. Figure 7.13(d) shows the population of the two pair-states $P_{\uparrow\downarrow}$ and $P_{\downarrow\uparrow}$, oscillating at a frequency $2J/h = 0.80$ MHz. The finite contrast of the oscillations is caused by preparation and detection errors, while the small damping of the oscillations (discussed in detail in the thesis of Sylvain Ravets [2014]) is due to the finite temperature of the atoms, which gives rise to shot-to-shot fluctuations of the interatomic distance R and thus of the coupling strength $J \propto 1/R^3$ driving the dynamics.

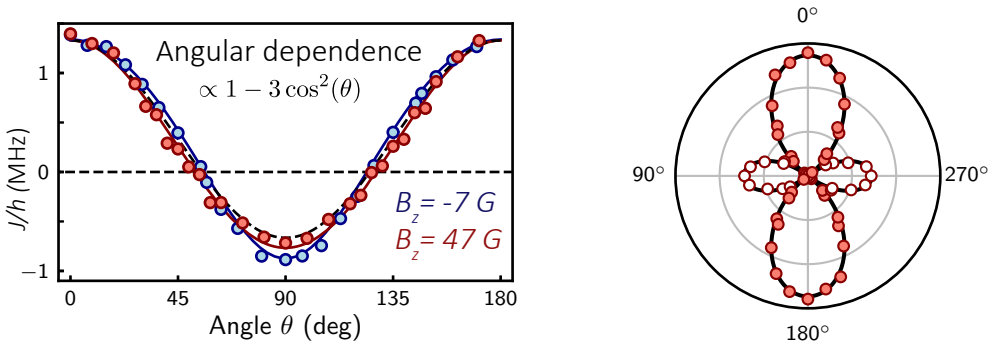

Figure 7.14: Angular dependence. The interaction strength J depends on the angle θ made by the pair of atoms with the quantization axis. The left panel shows measurements of J by spectroscopy for various angles and two values of the magnetic field. The experimental data are in excellent agreement with *ab-initio* calculations (colored solid lines), closely following the $1 - 3\cos^2(\theta)$ scaling (dashed line). Empty circles in the polar plot denote a negative coupling J. Error bars are smaller than the symbol size.

7.3.3 Angular dependence

I now present the measurement of the angular dependence $J(\theta)$ by performing microwave spectroscopy on pairs of atoms with a fixed separation $R = 12\,\mu$m and varying angle θ with the quantization axis. The results are shown on a linear and a polar plot in Fig. 7.14. We observe that $J(\theta)$ slightly differs from the simple $1 - 3\cos^2(\theta)$ dependence (dashed line), in perfect agreement with exact ab-initio calculations of the energy difference between the two pair states $|{\downarrow\downarrow}\rangle$ and $|{+}\rangle$ using the *pairinteraction* solver. The slight difference is caused by residual van der Waals shifts and second-order mixing between Zeeman sublevels, which depend on the Zeeman splitting and thus on the value of B_z, as observed experimentally by performing the measurement for $B_z = -7$ G and 47 G. The interatomic distance used in the calculation is $R_{\mathrm{th}} = 1.045 \times 12\,\mu$m. The correction factor is the same as in Section 6.1.3 and points at a systematic error in our calibration of the inter-atomic distance.

Finally, let us remark that this angular dependence was also observed in a previous work of the group [Ravets *et al.*, 2015], though in a different regime of the dipole-dipole interaction. There, it was between two pair-states $|dd\rangle \leftrightarrow |pf\rangle$, which were tuned at the same energy using an accidental Förster quasi-resonance and an electric field. Here, the coupling is between the two naturally degenerate pair-states $|rr'\rangle$ and $|r'r\rangle$: the system is simpler and more adapted for quantum simulation.

7.4 Control of the dipole-dipole interaction

We have previously studied the effect of the dipole-dipole interaction on two atoms with the same transition frequency. Using the addressing beam, we can tune the transition frequency of atom 1 by $\hbar\Delta\omega_0$, such that the system is now described by:

$$\hat{H} = J(\sigma_1^+\sigma_2^- + \sigma_1^-\sigma_2^+) + \hbar\Delta\omega_0\sigma_1^z, \tag{7.9}$$

By tuning the relative weight of the dipolar coupling J and the energy mismatch $\hbar\Delta\omega_0$, I first demonstrate the transition from the resonant dipole-dipole regime to the van der Waals interaction, and then use it to control a spin-exchange oscillation, freezing it at will, and to create the stationary sub-radiant entangled state $|-\rangle$.

7.4.1 From a resonant coupling to a second-order shift

The pair-state spectrum of Eq. (7.9) is sketched in Fig 7.15(a) for the two extreme regimes. For $J \gg \hbar\Delta\omega_0$, the energy mismatch between the two pair-states is negligible and we retrieve the previously studied resonant dipole-dipole coupling. In turn, for $J \ll \hbar\Delta\omega_0$, the dipole-dipole interaction only affects in second-order the two detuned pair-states and corrects their energy by a van der Waals-like term $\pm J^2/(\hbar\Delta\omega_0)$. Since the pair-states do not mix, they remain equally coupled to the microwave field, which contrasts with the resonant regime where $|-\rangle$ is dark.

Figure 7.15(b) demonstrate the continuous tuning of the dipole-dipole interaction from the resonant to second-order regime, taking the form of an avoided crossing between the dipole-dipole coupled $|\uparrow\downarrow\rangle$ and $|\downarrow\uparrow\rangle$. The energy difference $\hbar\Delta\omega_0$ is obtained by shining the addressing laser on atom 1 to apply a tunable AC Stark shift. Microwave spectra, with a Rabi frequency $\Omega_{\mu w}/(2\pi) = 0.1$ MHz $\ll J/h$ and an excitation time $\tau = \pi/(\sqrt{2}\Omega_{\mathrm{mw}}) = 3.5\,\mu$s, are recorded for different detuning $\Delta\omega_0$ and shown as a 2D color map. The microwave resonances, seen as a drop in the population of the initial state $|\downarrow\downarrow\rangle$, compare well with their predicted positions (right panel).

7.4.2 Freezing a spin-exchange process

We now use the addressing beam as a tool to freeze at will the spin-exchange dynamics between the two states $|\uparrow\downarrow\rangle$ and $|\downarrow\uparrow\rangle$. As a reference, I show again in Fig. 7.16(a) the

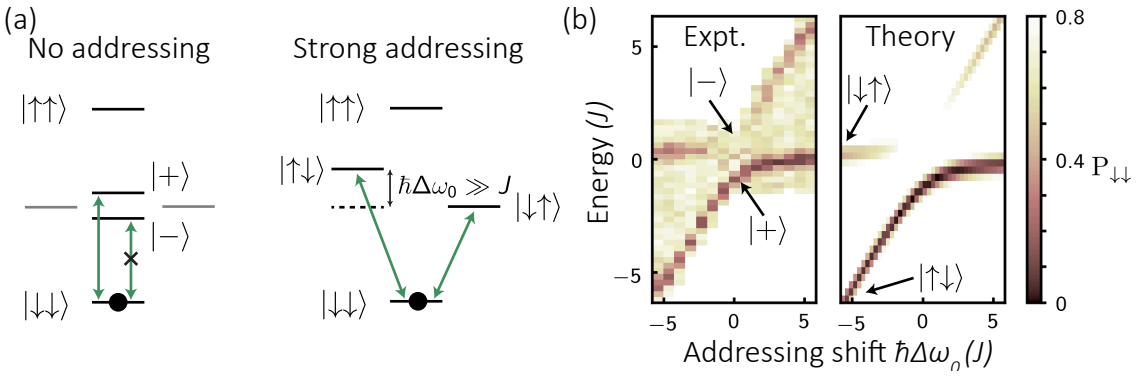

Figure 7.15: From a resonant to second-order interaction. (a) Two-atom spectra in the resonant (left) and off-resonant (right) limit. The addressing beam applies a light-shift $\hbar\Delta\omega_0$ on the state $|\uparrow\rangle$ of atom 1, while all other states are unaffected. Due to the strong energy mismatch between the pair-states $|\uparrow\downarrow\rangle$ and $|\downarrow\uparrow\rangle$, the dipolar coupling takes the form of a second-order van der Waals shift. (b) Microwave spectroscopy for $J/h = 0.40$ MHz and $\Omega_{\text{mw}}/(2\pi) = 0.1$ MHz starting from $|\downarrow\downarrow\rangle$. At resonance, the dark eigenstate $|-\rangle$ is not coupled to by the microwave field.

unperturbed spin-exchange oscillation driven by a dipolar coupling $J/h = 0.4$ MHz. In panel (b), we first let the system evolves to $|\psi\rangle = |\downarrow\uparrow\rangle$, after half a period of spin exchange, and then shine the addressing beam, which detunes atom 1 by $\Delta\omega_0 = 2\pi \times 4.8\,\text{MHz} \gg J$ and froze the spin-exchange dynamics during a controllable time τ. The oscillation then resumes without any noticeable loss of contrast. During the freezing time, the energy-shifted state $|\uparrow\downarrow\rangle$ acquires a dynamical phase $\phi = \Delta\omega_0\tau$, while $|\downarrow\uparrow\rangle$ is unaffected. To observe it, we switch on the addressing beam when the system is in the superposition of states $-\frac{1}{\sqrt{2}}(|\uparrow\downarrow\rangle + i\,|\downarrow\uparrow\rangle)$, which then evolves into $|\psi\rangle = -\frac{1}{\sqrt{2}}(e^{-i\phi}\,|\uparrow\downarrow\rangle + i\,|\downarrow\uparrow\rangle)$. In Fig. 7.16(c), we adjust the addressing time τ such that $\phi = 2\pi$ and the dynamics resumes as before we froze it. For $\phi = 2.5\pi$ (d), we create the stationary eigenstate $|\psi\rangle = i\,|-\rangle$ and the populations do not evolve anymore. Finally in (e), we obtain a π-phase shift of the spin-exchange dynamics when $\phi = 3\pi$.

Bloch sphere representation The previous results can be easily understood on a Bloch sphere, shown in Fig. 7.16(f,g), as the dynamics occurs only in the basis spanned by $|\downarrow\uparrow\rangle$ and $|\uparrow\downarrow\rangle$. The resonant dipolar coupling amounts to a precession of the state vector $|\psi\rangle$ around an horizontal axis at an angular frequency $2J/\hbar$. In turn, when the addressing beam is on, the state vector revolves around the vertical axis at a frequency $\Delta\omega_0$. In Fig. 7.16(c-e), we stopped the exchange when $|\psi\rangle$ was in the equatorial plane, where all the maximally entangled states lie.

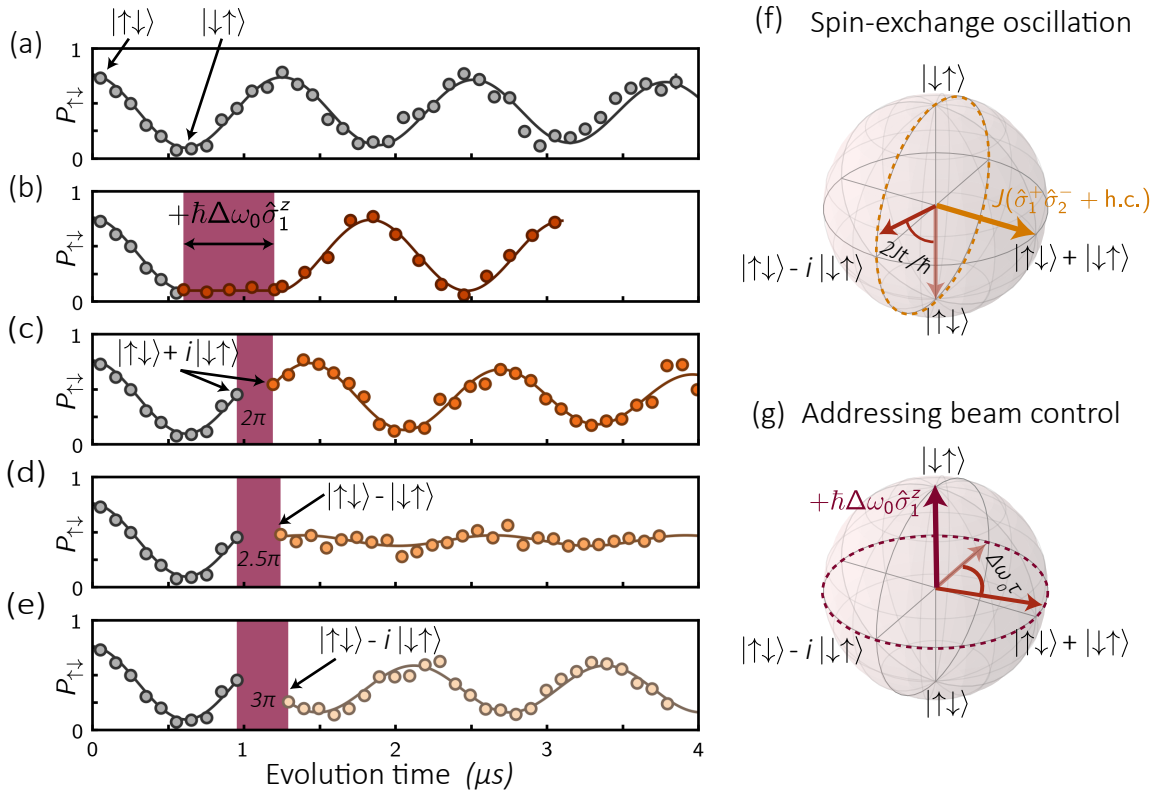

Figure 7.16: Freezing a spin-exchange oscillation. (a) Unperturbed spin-exchange dynamics $|\uparrow\downarrow\rangle \leftrightarrow |\downarrow\uparrow\rangle$. (b) The addressing beam freezes the spin-exchange oscillation during a variable time (purple area). (c-e) The oscillation is now frozen when the system is in the maximally entangled state $|\psi\rangle = -\frac{1}{\sqrt{2}}(|\uparrow\downarrow\rangle + i\,|\downarrow\uparrow\rangle)$. The light-shift on atom 1 modifies the relative phase between the two pair-states by $\Delta\omega_0\tau = 2\pi, 2.5\pi, 3\pi$ (c,d,e), which prepares three different entangled states giving rise to strikingly distinct spin-exchange dynamics. Solid lines are guides to the eyes. (f) Bloch sphere representation of the spin-exchange oscillation: The dipolar coupling makes the state vector (red) rotates around an horizontal axis (orange) at an angular frequency $2J/\hbar$. (g) When $\hbar\Delta\omega_0 \gg J$, the spin-exchange is stopped and the dynamical phase imprinted by the light-shift amounts to a rotation by an angle $\Delta\omega_0\tau$ around the vertical axis.

Creation of entangled states This control gives us two ways to create entangled states of two atoms. A first possibility consists in starting from $|\downarrow\downarrow\rangle$ and in collectively driving the system with microwaves to $|+\rangle$. In contrast to the usual Rydberg blockade protocols, based on optical driving between $|g\rangle$ and $|\downarrow\rangle$, this approach benefits from the high amplitude and phase stability of microwave sources, and the long wavelength of microwave fields compared to the interatomic spacing, making motional phases negligible [Wilk *et al.*, 2010]. A second possibility, demonstrated here, is to start from $|\uparrow\downarrow\rangle$ and to stop the spin-exchange dynamics at the appropriate time, which allows to create any coherent superposition of $|\uparrow\downarrow\rangle$ and $|\downarrow\uparrow\rangle$, in particular the otherwise inaccessible subradiant state $|-\rangle$. In the future, we could map the entanglement back to the long lived hyperfine ground-states.

7.5 Conclusion

In this chapter, I have demonstrated the high level of control that we have reached on XY magnets. The implementation of the STIRAP technique was critical to reach a 95 % efficiency in the preparation of Rydberg atoms and thus the initialization of a magnet with very few holes. The exaggerated response of Rydberg atoms to microwave radiation and the extreme stability of microwave sources give us a highly coherent tool to manipulate the spin-1/2 particles, strikingly better than what is possible on a ground-Rydberg system. The engineering of the addressing beam, combined with microwave sweeps, makes it possible to prepare localized spin excitations. Combining all the aforementioned tools, we performed advanced manipulations of a two-atom system, freezing the dipolar exchange process and preparing entangled Bell states.

The current experimental apparatus could still be improved in future works, for example one could generate several independently-controlled addressing beams using spatial and/or temporal light modulators. This would enlarge our toolbox for the studies of XY magnets, and we could, e.g., initialize a one-dimensional chain in the state $|\uparrow\downarrow\uparrow\downarrow\uparrow\downarrow\cdots\rangle$ and then let it evolve, or apply controlled disorder on the spins for many-body localization studies [Choi *et al.*, 2016; Smith *et al.*, 2016].

In a wider context, the resonant coupling between two-level systems, obtained here with Rydberg atoms whose transition frequencies are by nature all identical, is a more challenging and longed-for goal in solid-state platforms where the bandwidth and resonance frequencies of artificial atoms (e.g., semiconductor quantum dots) are affected by fabrication disparities, which, as we have seen, shifts the coupling from resonant to second-order (see also Shlesinger *et al.* [2018]).

Chapter 8

The Su-Schrieffer-Heeger model with hard-core bosons

Contents

8.1 Introduction to symmetry protected topological phases

A single spin-excitation on an XY magnet behaves as a particle tunneling between lattice sites and can thus be described using the framework of Bloch wavefunctions and bandstructures. In the last decades, there has been a growing interest in materials exhibiting bands with topological properties and a current open question is how there are affected when considering interacting particles. With our experimental platform, where two spin excitations cannot be located on the same lattice site, we naturally

implement hard-core bosons: particles with an infinite on-site interaction energy. In this chapter, I present our study of the simplest model giving rise to a topological phase, — the one-dimensional Su-Schrieffer-Heeger (SSH) model —, both at the single-particle level where its properties are well-known and originate from a chiral symmetry, but also in the many-body regime with a lattice half-filled with hard-core bosons where we will uncover a bosonic topological phase protected by a different symmetry.

Symmetry protected topological phases The most prominent example of a topological phase is the integer quantum Hall (IQH) state with its remarkably robust edge modes giving rise to a quantized Hall conductance [Klitzing, Dorda, and Pepper, 1980], now used as a practical standard for electrical resistance. Triggered by this discovery, a new classification of quantum phases of matter in terms of topological invariants has emerged [Thouless *et al.*, 1982] and led to the prediction [Kane and Mele, 2005a,b] and discovery [König *et al.*, 2007; Hsieh *et al.*, 2008] of topological insulators (see also the review of Hasan and Kane [2010] and Qi and Zhang [2011]). In these materials, in contrast to the original IQH effect, a specific symmetry of the Hamiltonian is required to protect the topological phases, and they are thus nowadays denoted as symmetry protected topological phases (SPT). They appear in systems displaying an excitation gap in the bulk, i.e., bulk insulators, and invariant under a global symmetry operator. The properties of the many-body ground-state, such as the existence of edge-states at the interface between two materials with different topology (one could be the vacuum), are protected from any perturbation that does not close the excitation gap or violates the symmetry.

Non-interacting fermions and the ten-fold way In the specific case of non-interacting fermions, we can use the Fermi sea picture,— stating that the many-body ground-state is obtained by filling the single-particle eigenstates up to a chemical potential—, to classify the SPT phases by considering only the action of the Hamiltonian on a *single* particle, that we call the *single-particle* Hamiltonian. For example, when the particles move on a lattice (as electrons in a material in the tight-binding approximation), the single-particle Hamiltonian is the matrix formed by the hopping amplitude between different sites. Now, there is a remarkable fact, from a mathematical physics origin, that all single-particle Hamiltonians divide in only ten symmetry classes; this classification is known as the ten-fold way and was proposed by Kitaev [2009] and Ryu *et al.* [2010] (see also the recent reviews of Chiu *et al.* [2016] or Ludwig

[2016]). This classification is based on the behavior of the single-particle Hamiltonian under three general operations: the time-reversal (TR), the particle-hole (PH) and the chiral (S) symmetries.

In addition to the search for materials realizing such symmetries, a current hot topic is the realization of SPT phases in artificial systems where Hamiltonians can be designed and the symmetries enforced. Ultracold atoms in optical lattices are a natural platform for this, and there have been, in the last five years, many realizations of topological bandstructures (see the review by Cooper, Dalibard, and Spielman [2018]). Let us remark that, at the *single particle* level, the particle statistics is irrelevant, such that bosons or fermions have been indifferently used in experiments with atomic systems. In addition, it means that topological systems can also be realized with classical objects, such as coupled mechanical oscillators [Süsstrunk and Huber, 2015; Nash *et al.*, 2015; Chaunsali *et al.*, 2017] or radio-frequency circuits [Ningyuan *et al.*, 2015]. Topological properties also find applications in the manipulation of light, leading to the field of topological photonics (reviewed by Ozawa *et al.* [2018]), which could notably lead to the development of lasers harnessing the robustness of edge-modes [St-Jean *et al.*, 2017; Bandres *et al.*, 2018].

Bosonic phases The above discussion started from the description of topological phases for non-interacting fermions. In turn, for bosons we have to consider strong interactions between the particles, as they otherwise accumulate in the lowest single-particle eigenstate to form a Bose-Einstein condensate. Spin models are thus a good place to look at, since a spin excitation can be seen as a hard-core boson, and a primary example of a bosonic SPT phase is the ground state of the anti-ferromagnetic spin-1 chain studied by Haldane [1983a]. Signatures of the Haldane phase have later been observed experimentally in real-world materials [Hagiwara *et al.*, 1990; Glarum *et al.*, 1991; Avenel *et al.*, 1992]. However, there has been no experimental realization of a bosonic topological phase in artificial quantum matter yet.

For the classification of interacting topological phases, the ten-fold way does not apply as the properties of the many-body ground state cannot be derived from the single-particle Hamiltonian. However, for one-dimensional systems, a full classification of bosonic SPT phases has been achieved and expressed in terms of group cohomology [Chen *et al.*, 2012, 2013].

The Su-Schrieffer-Heeger model In this chapter, I report the realization of a symmetry protected topological phase of hard-core bosons using our Rydberg quantum

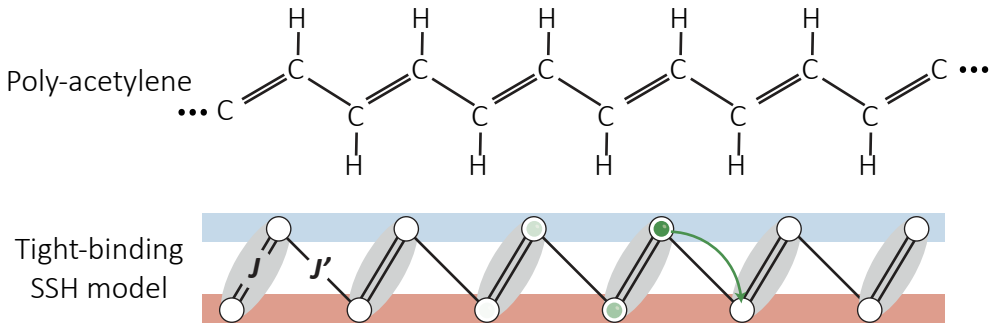

Figure 8.1: The SSH chain. To explain some properties of poly-acetylene (top), Su, Schrieffer, and Heeger [1979] introduced a model Hamiltonian where a particle hops from site to site of a staggered one-dimensional lattice. The hopping amplitude alternates between two values J and J'.

simulator. We implement a coupling matrix between spin-1/2 particle that realizes a modern version of the Su-Schrieffer-Heeger (SSH) model [Su, Schrieffer, and Heeger, 1979, 1980] (see also the review by Heeger *et al.* [1988] or his 2000 Nobel lecture). The model was initially proposed to explain the properties of (trans-)polyacetylene $(\mathrm{CH})_x$, a conjugated polymer, and notably its high conductivity when doped. The most important aspect of this macromolecule is that it takes a dimerized structure with an alternation of single and double chemical bonds between each (CH) group. In a tight-binding approximation, the additional electron brought by the dopant is hopping from one (CH) group to the other with a hopping amplitude alternating between a strong J and weak J' value (see Fig. 8.1). The one-dimensional SSH Hamiltonian thus reads:

$$H_{\mathrm{SSH}} = -J \sum_{\text{odd } i} \left[b_i^\dagger b_{i+1} + \text{h.c.} \right] - J' \sum_{\text{even } i} \left[b_i^\dagger b_{i+1} + \text{h.c.} \right] \tag{8.1}$$

where $b_i^\dagger$ (b_i) are the creation (annihilation) operator of a particle on site i and follows, in the initial formulation of the SSH model, the commutation rules of fermionic operators. In their original paper, Su, Schrieffer and Heeger considered the case where there is a change of dimerization at some position in the chain, called a topological defect, that translates in Eq. 8.1 by interchanging J and J' for sites $i > i_{\mathrm{d}}$, and realized that it gives rise to a zero-energy mode localized at the position of the defect. Similarly, a finite-size system ending with a weak link $J' < J$ also gives rise to a topological defect at the interface between the chain and the vacuum, and thus to localized edge-states. The model has then been recognized as realizing a topological phase for non-interacting fermions protected by the *chiral* symmetry (see details

later), which motivated its experimental realization in artificial systems to observe single-particle properties [Atala *et al.*, 2013; Meier, An, and Gadway, 2016; St-Jean *et al.*, 2017; Chaunsali *et al.*, 2017]. A unique asset of our platform is that we can populate the system with hard-core bosons and study how these strong interaction affects the properties of the many-body phase.

Outline This chapter is organized as follows. I first introduce, in Section 8.2, the defining sub-lattice (chiral) symmetry of the SSH Hamiltonian and describe how to implement it experimentally using the angular dependence of the resonant dipolar interaction between Rydberg atoms. In Section 8.3, I present our experimental studies of the SSH model at the single-particle level demonstrating that we correctly implemented the model. In Section 8.4, we prepare the many-body ground state of the bosonic SSH chain at half-filling using a microwave adiabatic sweep. We then characterize it experimentally to demonstrate that it is a SPT phase, and finally observe a robustness to a perturbation that breaks the chiral symmetry protecting the fermionic phase, indicating the presence of a different symmetry for the bosonic phase. This work was performed in collaboration with a theoretical team composed of Sebastian Weber, Nicolai Lang and Prof. Hans-Peter Büchler, from the University of Stuttgart. A publication is in preparation.

8.2 Implementing the SSH model and its chiral symmetry

Here, I examine the properties of Eq. (8.1) for a single particle in the lattice. This restriction makes sense as the number of particles is conserved in the model. In this limit, the statistics of a particle (bosonic or fermionic) is irrelevant, as we will not have to commute two operators $b^\dagger$. The Hamiltonian eigenstates and their energies are obtained either by using the Bloch theorem for an infinite-size system, or, for a finite one, by exact diagonalization. Below, I describe how we use the zero-energy edge-modes to distinguish a topologically trivial from a non-trivial configuration. Then, I explain the requirements of the chiral symmetry that protects the topological edge-modes. Finally, I show how to implement a long-range version of the SSH model, while enforcing the chiral symmetry, on our Rydberg platform.

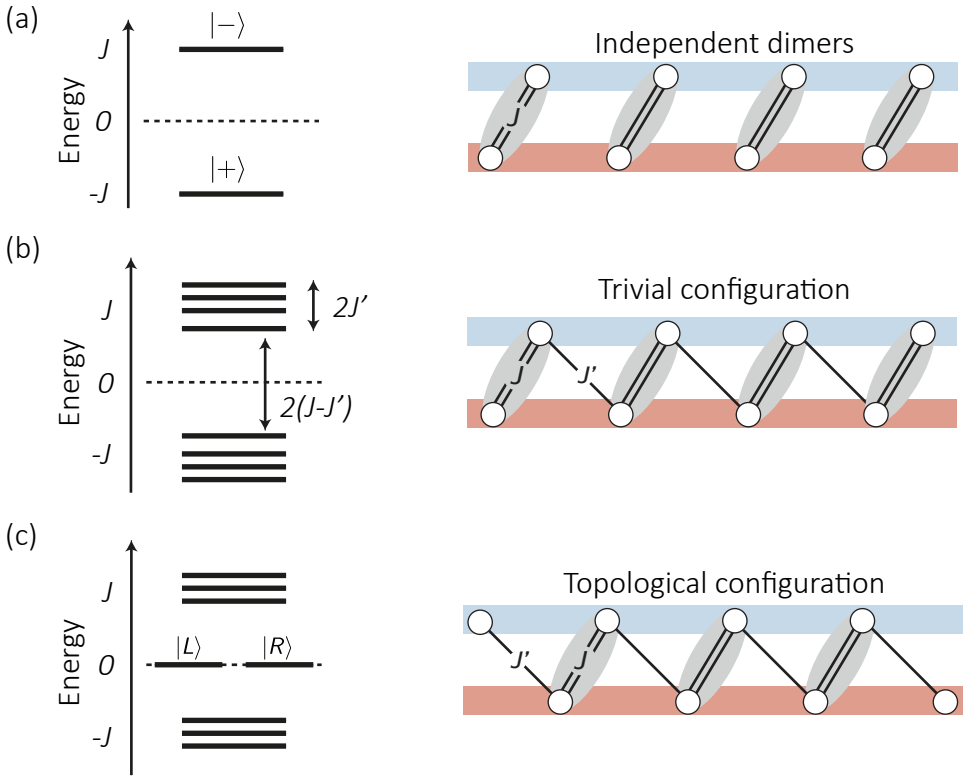

Figure 8.2: Single particle spectra. (a) For $J' = 0$, the SSH chain is a collection of independent dimers. A particle lowers its energy to $-J$ when it is symmetrically delocalized on the two lattice sites. (b) For $J' \neq 0$, the particle delocalizes over the lattice, giving a bandstructure of eigenstates with a width $2J'$. (c) When the chain ends with weak links J', there are two zero-energy modes lying in the gap, corresponding to a particle localized on the left or right side of the chain.

8.2.1 Origin of the zero-energy localized edge-states

We approach the SSH model by first considering the limit $J' = 0$, where the lattice becomes a collection of independent dimers (two sites linked by the hopping amplitude J). On each dimer, a particle delocalizes on the two sites to form either a symmetric eigenstate $|+\rangle$, at energy $-J$ (because of the minus sign in Eq. **??**), or an anti-symmetric one, $|-\rangle$, at an energy $+J$ [see Fig. 8.2(a)]. We have already encountered these eigenstates in the previous chapter, when considering two Rydberg atoms in resonant dipole-dipole interaction. Restoring the inter-dimer hopping J' allows the particle to delocalize over the entire lattice, which leads to an hybridization of the degenerate symmetric and anti-symmetric orbitals of each dimer, and to the formation of two bands of eigenstates centered at $\pm J$ with a width $2J'$, as shown in Fig. 8.2(b). There is a finite gap $2(J - J')$ between the two bands as long as $J' \neq J$.

We now consider edge effects on a finite-size lattice with an even[1] number of sites. If the chain ends with a weak coupling constant J', as shown in Fig. 8.2(c), we readily see that it gives, in the limit $J' = 0$, a zero-energy mode localized on the edge site that is disconnected from the rest of the chain. The interesting fact is that this mode remains at zero-energy even when restoring a finite J', and then reads:

$$|L\rangle \simeq |A_1\rangle - \left(\frac{J'}{J}\right)|A_3\rangle + \left(\frac{J'}{J}\right)^2 |A_5\rangle \dots \tag{8.2}$$

where $|A_i\rangle$ indicates that the particle is on site i. In contrast, there is no such mode when the chain ends with a strong coupling constant J. From the existence of edge modes, we can thus identify two different lattice configurations (ending either with J' or J), which are said to *topologically* distinct. The chain shown in Fig. 8.2(b) is the *trivial* (or topologically trivial) configuration, while the one in Fig. 8.2(c) is the *topological* (or topologically non-trivial) configuration that gives rise to zero-energy modes.

Infinite-size system: winding number I briefly describe how the problem is treated for an infinite-size system, which is not the situation that we will realize experimentally, but is a common approach to the SSH problem. In this limit, the two bands of eigenstates with energies $\pm|J + J'e^{iqa}|$ identified in Fig. 8.2 become continuous and we use the Bloch theorem to label each state with a quasi-momentum $q \in [-\pi/a, \pi/a]$, with a the lattice spacing. There are two eigenstates for each momentum q, because we have to choose a unit cell composed of two lattice sites (a dimer) to restore the translational invariance broken by the staggered hopping. The topology of each band is not revealed in the energy levels, but in the evolution of the wavefunction when going around the Brillouin zone, characterized by a topological invariant,— the winding number or the related Zak phase —, and I refer the reader to the tutorial of Asbóth, Oroszlány, and Pályi [2016] or the review by Cooper, Dalibard, and Spielman [2018], for a more detailed introduction to these concepts.

8.2.2 The chiral symmetry

The zero-energy edge modes of the SSH model are topologically protected from any perturbation of the lattice, that (i) does not close the gap or (ii) breaks the

[1] This condition just makes the situation simpler, as the two edges then have the same properties.

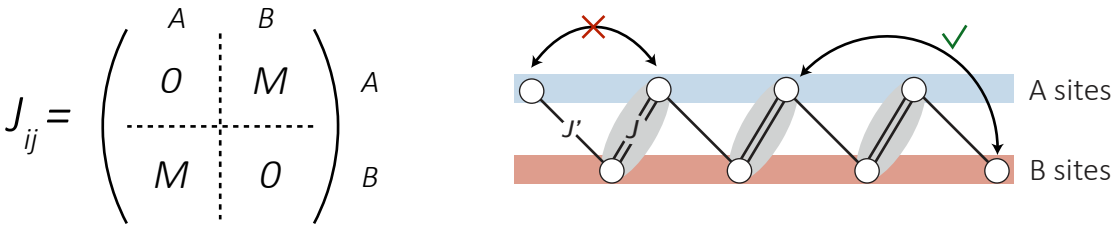

Figure 8.3: Chiral symmetry. We define a more general version of the SSH model where the coupling matrix J_{ij} is not restricted to nearest neighbors. However, we still need to enforce the defining chiral (or sub-lattice) symmetry of the Hamiltonian. This requires that there is no hopping between two sites of the same sub-lattice. Expressed in the basis starting with sites from the A sub-chain, and then all the B sites, the coupling matrix cannot have non-vanishing elements on the two diagonal blocks.

chiral symmetry. We have just seen above why condition (i) is necessary, as the edge states disappear when going from one gapped spectrum $J' < J$ to another $J' > J$, through the gapless situation at $J' = J$. Condition (ii) expresses the fact that the SSH Hamiltonian (8.1) is invariant under a chiral symmetry[2] $\hat{\mathcal{S}}_{\mathrm{F}}$, or in a mathematical language: $[\hat{H}, \hat{\mathcal{S}}_{\mathrm{F}}] = 0$. Now, this statement on the many-body Hamiltonian translates to a property of the single-particle Hamiltonian, which is the matrix J_{ij} containing the hopping amplitudes between the different lattice sites. Following the derivation of Chiu *et al.* [2016] (in particular Section II.C), the chiral symmetry requires that there is a basis in which J_{ij} is block-off-diagonal [see Fig. 8.3(a)]. This basis defines two sets of lattice sites, A and B, and there can only be hopping terms between sites in different sub-lattices. For this reason, the chiral symmetry is often called the sub-lattice symmetry.

Now, we readily see why the SSH model realizes the chiral symmetry, since we can identify two such sub-lattices, as shown in Fig. 8.3(b). In addition, we understand that restricting the hopping terms to nearest neighbors only is not necessary, and we now consider an extended SSH model where long-range hoppings are allowed, as long as they couple two sites of the same sub-chain:

$$H = -\sum_{i\in A, j\in B} J_{ij}\left[b_i^\dagger b_j + b_j^\dagger b_i\right], \tag{8.3}$$

Let us now consider how to break the chiral symmetry. A first possibility is to have non-zero diagonal terms in the coupling matrix. These terms correspond to on-site

[2]The subscript indicates that the symmetry protects the fermionic SPT phase.

potential energies J_{ii} that differ[3] from site to site. A well-studied example is to take $J_{ii} = (-1)^i \Delta$, which realizes the Rice and Mele [1982] model. Another way is to break the symmetry with hopping terms between two sites of the same sub-chain, such as a next-nearest neighbor hopping $J_{i,i+2} = J_2$. We will come back to this idea later in the chapter.

8.2.3 Experimental implementation

I first briefly review implementations of the SSH model in artificial systems, and then describe how we have done it on our experimental platform.

Previous implementations Atala *et al.* [2013] loaded a Bose-Einstein condensate in an optical super-lattice, formed by overlapping two lasers with walevength λ and $2\,\lambda$, leading to staggered tunneling amplitudes. The non-interacting particles are initially in a well-defined quasi-momentum $|q = 0\rangle$ and are then made to perform Bloch oscillations to measure the geometrical Zak phase acquired when moving adiabatically around the Brillouin zone. Meier, An, and Gadway [2016] also used a BEC, but loaded in a finite-size *momentum-space* lattice with staggered couplings engineered with time-dependent (real-space) lattices; they notably reported the adiabatic preparation of the atomic cloud in a localized edge-state in momentum space. Using an array of polariton micropillars, St-Jean *et al.* [2017] demonstrated lasing from the edge-mode that should thus be robust to deformations of the lattice structure. Finally, Chaunsali *et al.* [2017] used mechanical granular chains and observed a vibrational mode localized at the interface between two chains with different dimerizations. These experiments probed the single particle properties of the SSH model, that derive from the chiral symmetry of the coupling matrix J_{ij} and are independent of the particle statistics.

Our implementation with Rydberg atoms In our case, we implement the SSH model on an effective XY magnet (see previous chapter) where the spin excitations are seen as hard-core bosons. We engineer the adequate coupling matrix J_{ij} using the angular dependence of the resonant dipolar interaction between Rydberg atoms.

Our realization of the SSH chain is performed on an artificial structure of 14 Rydberg atoms, assembled atom-by-atom and initialized with our STIRAP procedure in the Rydberg state $|\downarrow\rangle = |60S_{1/2}, m_J = 1/2\rangle$ with an efficiency of 95% (there is thus a 5 % probability that a Rydberg atom is missing). From there, the atom can be coherently

[3] If all $J_{ii} = J_0$, we can just redefine the origin of the energy axis to remove this constant offset.

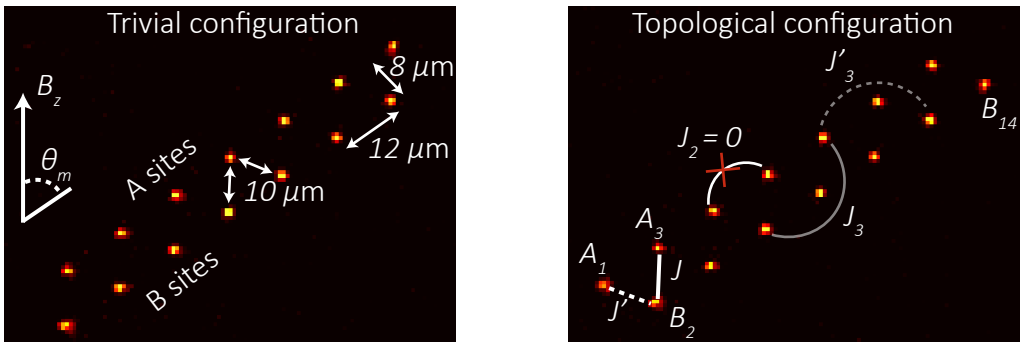

Figure 8.4: The SSH chain with Rydberg atoms A single-shot fluorescence image of the atom assembled in the artificial structure for the trivial (left) and the topological configuration (right). The chain is tilted by the angle θ_m to cancel couplings between sites in the same sub-lattice. The measured couplings are $J/h = 2.42(2)$ MHz, $J'/h = -0.91(2)$ MHz, $|J_2|/h < 0.07$ MHz, $J_3/h = 0.21(1)$ MHz and $J_3'/h = -0.14(1)$ MHz.

transferred to the Rydberg level $|\uparrow\rangle = |60P_{1/2}, m_J = -1/2\rangle$ using microwave radiations at ~ 16.7 GHz. The detuning from the transition is $\Delta_{\mu\mathrm{w}}$, and the Rabi frequency $\Omega_{\mu\mathrm{w}}/(2\pi)$ can range from 0.1 to 20 MHz. We denote the state with all Rydberg atoms in $|\downarrow\rangle$ as the 'vacuum' $|0\rangle$ of the many-body system, while a spin-excitation $|\uparrow\rangle_i$ at site i is described as a bosonic particle $b_i^\dagger|0\rangle$. The creation and annihilation operators satisfy bosonic commutation relations on different sites $i \neq j$, and obey the hard-core constraint $(b_i^\dagger)^2 = 0$, as two particles cannot occupy the same site i.

Then, the resonant dipolar interaction occurring between two Rydberg atoms at site i and j gives rise to hopping of the hard-core bosons, which we use to engineer the hopping matrix J_{ij}. Notably, we need to impose the chiral symmetry requiring that there is no coupling between atoms in the same sub-lattice. Using the angular dependence $J_{ij} \propto 1 - 3\cos^2\theta_{ij}$ of the dipolar coupling, we choose the geometry shown in Fig. 8.4, where the two sub-chains A and B form an angle $\theta_m \simeq 54.7°$ with the quantization axis. The vanishing coupling along this 'magic' angle enforces the required sub-lattice symmetry of the SSH model. The experiment is performed for two different configurations: a topological setup with a weak hopping J' at the boundary, and a trivial setup with a strong hopping J at the boundary.

Hopping amplitudes The couplings up to the third neighbors have been measured experimentally. First, we obtained $J/h = 2.42(2)$ MHz and $J'/h = -0.92(2)$ MHz with an inhomogeneity over the chain smaller than 3 %. For the next-nearest neighbor hopping J_2, forbidden by the chiral symmetry, we estimate a higher bound on the

coupling strength $|J_2|/h < 0.07$ MHz by observing the transfer of a spin-excitation between two atoms at the magic angle. Even though the transfer is in principle suppressed, we observe a slow incoherent transfer, from which we extract the bound, due to the shot-to-shot fluctuation of the atoms position caused by their finite temperature (see Section 2.1.3), resulting in angle $\theta_{i,i+2}$ fluctuating around θ_m by $\pm 0.5°$. Finally, the hopping terms to third neighbors are measured to be $J_3/h = 0.21(1)$ MHz and $J_3'/h = -0.14(1)$ MHz. Couplings between further atoms are not relevant on our experimental time scales. The different signs[4] of J and J' do not modify the physics of the SSH model, but simply change the energy ordering of the single-particle eigenstates compared to the 'usual' situation of identical signs.

8.3 Single-particle regime

In this section, I present four experimental results illustrating the single-particle properties of the SSH model: (i) the presence of zero-energy modes when the SSH chain contains topological defects, (ii) the exponential localization of such modes, (iii) the different dynamics of a particle in a trivial or topological chain, and (iv) the coherent transfer of a particle between two localized modes due to their hybridization.

8.3.1 Microwave spectroscopy of the single-particle eigenstates

Starting with the chain in the vacuum state $|0\rangle$, we shine a weak microwave probe and observe the coherent creation of a particle if the eigenstate energy is matched by the microwave detuning $\Delta_{\mu w}$. The coupling strength $\Omega_{\mu w}/(2\pi) = 0.2$ MHz and the excitation time $t = 0.75\,\mu$s are chosen small enough to limit the creation of multiple particles. Figure 8.5 shows the site-resolved probability to observe a particle on a given site for different SSH chains: the trivial (a) and topological (b) configurations, but also two chains with a topological defect in the bulk (c,d). I first discuss the properties of the *delocalized* modes that are mostly independent on the specific geometry and then the zero-energy ones localized at the position of the defects.

Delocalized modes For all configurations, we observe a clear signal for $\Delta_{\mu w} < |J'| - |J|$ from the lower band modes delocalized along the chain, while there is no

[4] A global change of sign of all coupling constants is equivalent to changing the sign of the microwave detuning (which we do in this chapter as compared to the previous one).

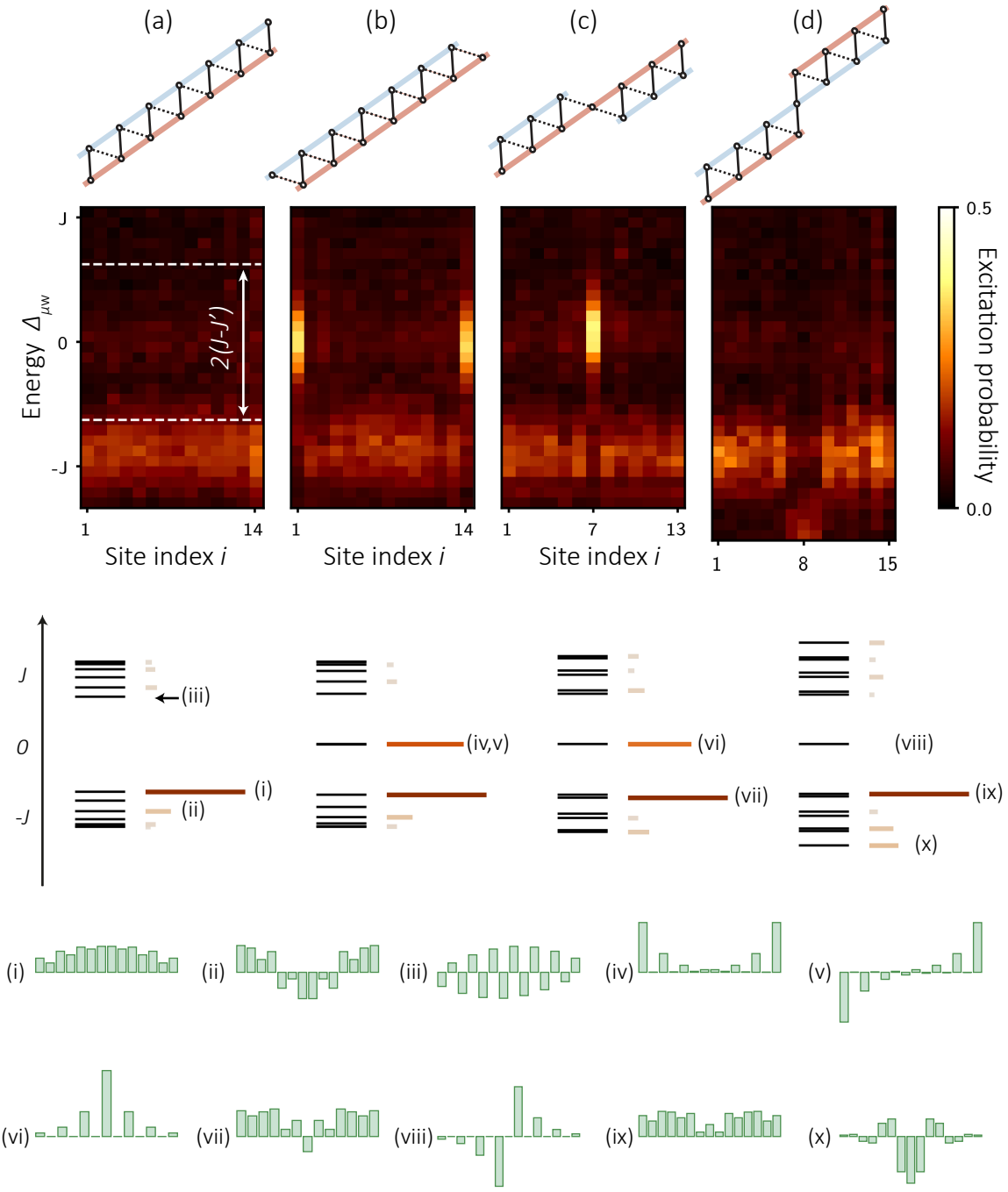

Figure 8.5: Microwave spectroscopy. First row: lattice geometry. Second row: experimental spectra showing the site-resolved probability to find a particle. Third row: calculated spectra and microwave couplings $|\sum_i \alpha_i^k|$ (orange bars). Fourth row: selection of eigenstates. (a) Trivial configuration. The white dashed lines indicates the limit of the spectral gap $\pm(|J| - |J'|)$. (b) Topological configuration. (c) Topological defect of 'type-1' (two consecutive weak links). (d) Topological defect of 'type-2' (two consecutive strong links).

signal from states in the higher band. To explain this, let us consider the microwave transition strength from the vacuum state $|0\rangle$ to the eigenstate $\left|e^k\right\rangle = \sum_i \alpha_i^k b_i^\dagger |0\rangle$:

$$\frac{\hbar\Omega_{\mu\mathrm{w}}}{2} \left\langle e^k \right| \sum_i \left[b_i^\dagger + b_i \right] |0\rangle = \frac{\hbar\Omega_{\mu\mathrm{w}}}{2} \times \sum_i \alpha_i^k. \tag{8.4}$$

I show these couplings on the right of the calculated spectra for each chain configuration, together with a selection of wavefunctions $\{\alpha_i^k\}$. For all chains, a specific delocalized mode (i,vii,ix) has a dominant contribution to the signal: this is the mode where almost all coefficients α_i have the same sign and gives a collectively enhanced coupling to the microwave probe. In contrast, couplings to other modes are either weak (ii) or completely inhibited (iii). The coupling to only a few eigenstates is linked to the use of a coherent probe: for example, St-Jean *et al.* [2017] could observe all the delocalized modes by relying on the incoherent creation of the particles.

For an infinite chain ($N \to \infty$), the mode (i) would correspond to the eigenstate $|q = 0\rangle$ with zero quasi-momentum; no other mode $|q \neq 0\rangle$ can be created by absorbing a microwave photon whose momentum is negligible[5]. On the higher band, the mode (iii) also transforms into an eigenstate with zero quasi-momentum but its Bloch function is anti-symmetric, preventing the coupling to the microwave field. Finally, the mode (i) would have the lowest energy for coupling strengths $J, J' > 0$, it is not the case here as $J' < 0$.

Zero-energy modes I now describe the modes that appear in the gap when topological defects are present in the chain. In the panel (a), the chain is in the trivial configuration and there is no such mode. In panel (b), the chain ends with two weak links that give rise to the left $|L\rangle$ and right $|R\rangle$ edge modes. We couple in fact to the symmetric superposition $|L\rangle + |R\rangle$ of these two modes (iv) and not to the anti-symmetric one $|L\rangle - |R\rangle$ (v). We will see later that (iv) and (v) are not strictly degenerate in finite chains due to their hybridization. In panel (c), there are two consecutive weak links that lead to the localized mode (vi) centered on the topological defect. Finally, in panel (d), two consecutive strong links give rise to an anti-symmetric zero-energy mode (viii) that is thus not observed experimentally, but also to a finite-energy symmetric localized mode (x) observed at the bottom of the spectrum. Let us also note that, in panel (c) and (d), the chiral symmetry is not strictly enforced between the two part of the chains from each side of the defect. The width of the signal comes from the microwave probe Rabi frequency.

[5]Its wavelength exceeds by more than 4 orders of magnitude the spacing between lattice sites.

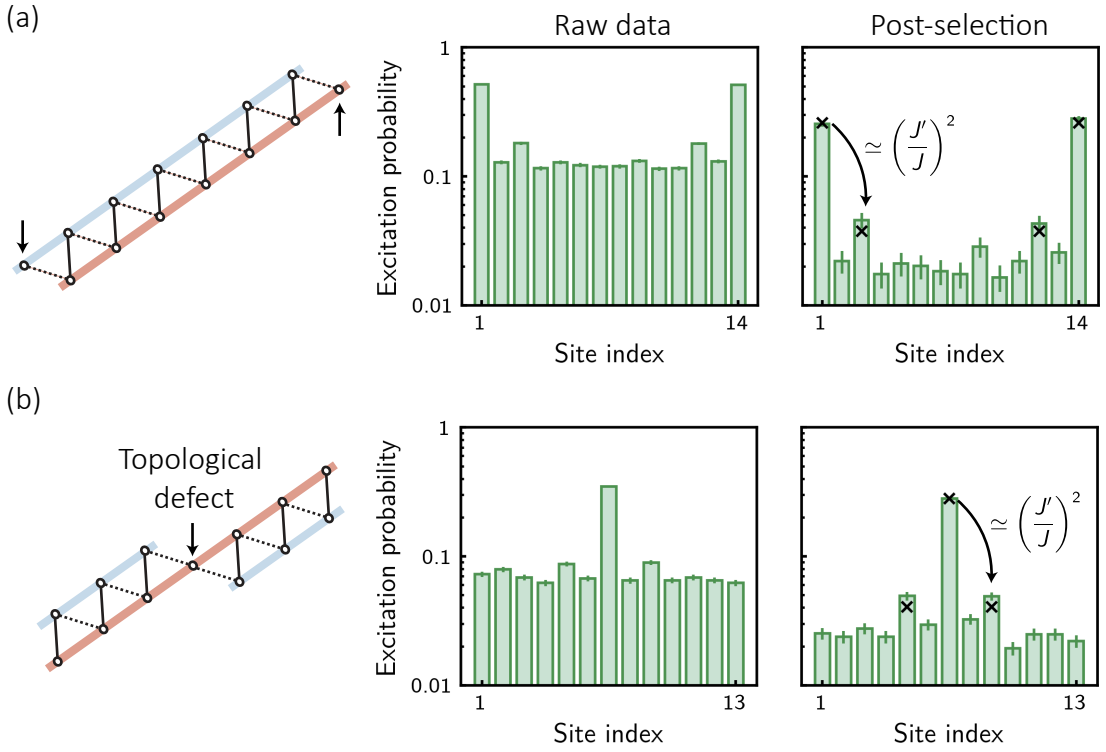

Figure 8.6: Localization of the zero-energy modes. Probability to find a spin-excitation (= a particle) on a given site when shining the microwave field at $\Delta_{\mu w} = 0$ to probe the zero-energy modes on a chain with (a) topological defects at both ends or (b) with a central defect. The microwave probe can also create states with more than 1 particle. To remove the contributions from the $n > 1$ manifolds of eigenstates, we post-select experimental runs where only one particle was observed (right panels). The dark crosses indicate the theoretical probability distribution of the localized mode, rescaled to the measured value at the defect site $i = i_d$. We expect the probability for the particle to be found at site $i_d \pm 2$ to decrease by a factor $(J'/J)^2$, which is indeed observed. For further sites, the expected probability to find a particle is below 1 %.

Edge-state localization Recalling Eq. (8.2), we expect a zero-energy mode to be localized at the position of each topological defect, which is seen in the spectra of Fig. 8.5, but also that the mode extends beyond the defect site. More precisely, having created a particle in the localized mode, there should be a ratio of $\simeq (J'/J)^2$ between the probability to find it at the defect site $i = i_d$ and at the next-nearest neighbor site $i_d \pm 2$. To observe this, I present in Fig. 8.6(a,b) 1d-cuts at $\Delta_{\mu w} = 0$ of Fig. 8.5(b,c), giving us the spatial distribution of the zero-energy edge modes (iv) and (vi) of, respectively, a SSH chain with two topological defects at each end, and an isolated defect in the bulk of the chain (the original situation envisioned by Su, Schrieffer, and

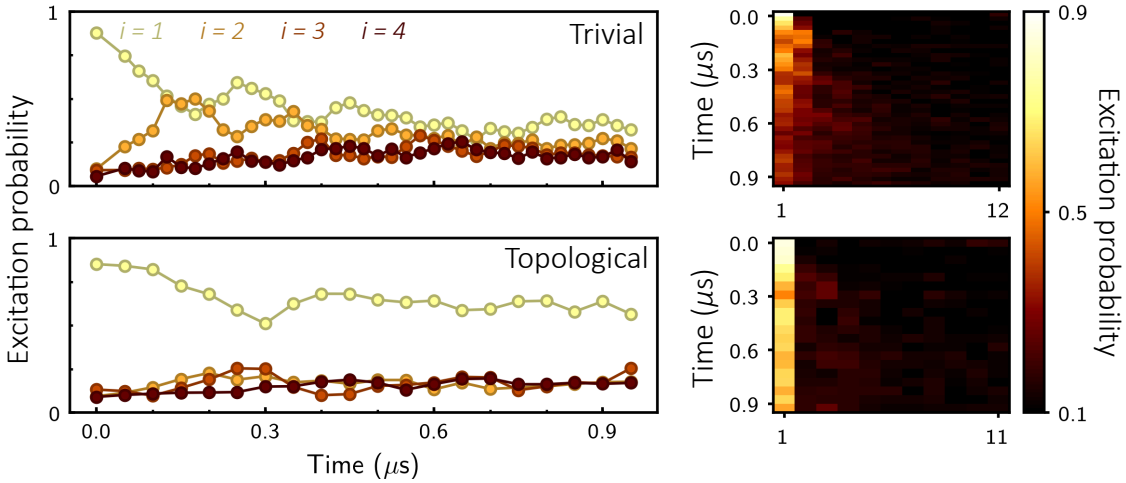

Figure 8.7: Dynamics: trivial vs topological chain. We observe the dynamics of a single particle prepared on the leftmost site of a trivial (top) and topological (bottom) SSH chain. The left curves show the occupancy probability of the first four sites, while the 2d-map on the right shows the dynamics over the entire lattice. In the trivial configuration, the particle delocalizes on the bulk in a coherent manner. In the topological configuration, the initial state has a strong overlap with the left edge modes and only a small fraction of the particle delocalizes.

Heeger [1979]). The left panels show the raw data (as in Fig. 8.5) on a logarithmic scale, while in the right panels we post-select for experimental runs where at most a single particle was observed. This procedure allows us to remove the contributions from delocalized eigenstates with $n = 2$ particles that can also be created at zero detuning[6]. We then clearly observe the expected spatial dependence of the localized mode, that compares well with theory (dark crosses). The effect of longer range couplings J_3 and J_3' was estimated numerically to give a correction of only 10 % to the ratio $(J'/J)^2$, which cannot be resolved experimentally here due to the ~ 2 % background signal caused by preparation and detection errors.

8.3.2 Dynamics of a single particle in a SSH chain

In this section, we now initialize a particle in the leftmost site $|\psi_0\rangle = b_1^\dagger |0\rangle$, using the technique described in Section 7.2.3, and observe its subsequent evolution.

[6] These states can be seen on Fig. 8.9(d).

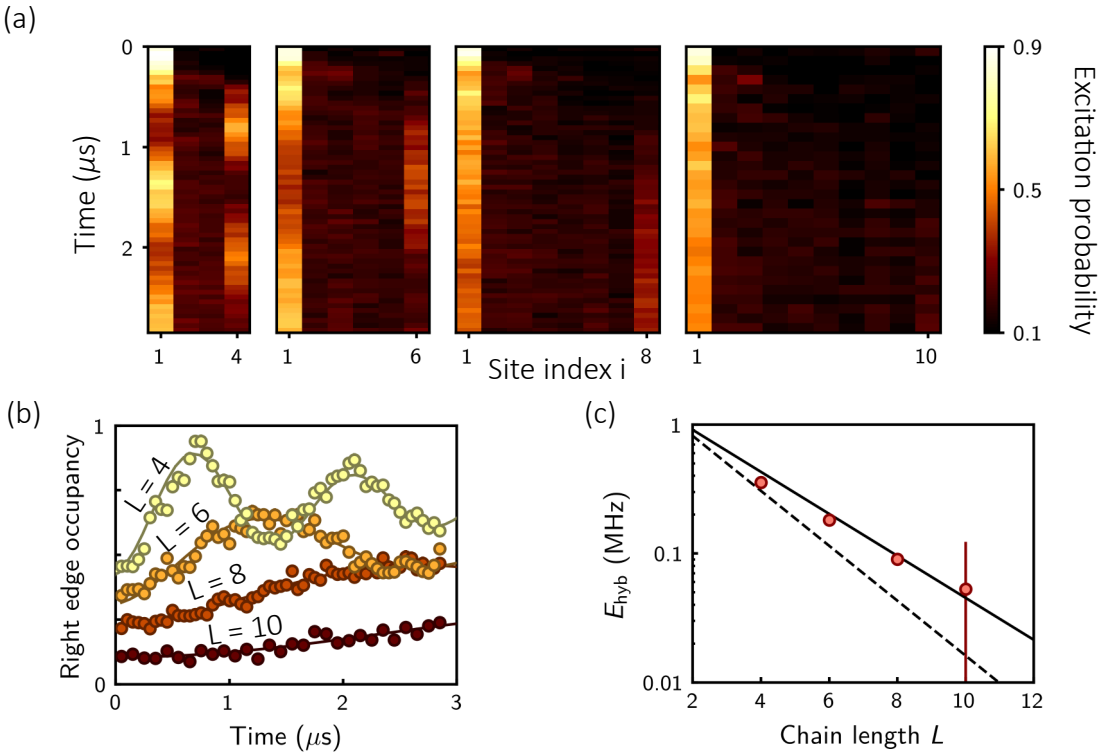

Figure 8.8: Edge-modes hybridization On finite chains, the hybridization between the left and right edge modes allows the coherent transfer of particles between the two extreme sites. (a) Experimental observation for chains of $N = 4$, 6, 8 and 10 sites. (b) Occupancy probability of the rightmost site (with an arbitrary offset between the different curves). The solid lines are sinusoidal fits, with both amplitude and period as free parameters, from which we extract the hybridization energy E_{hyb} shown in (c). We compare it to calculations keeping only nearest-neighbor hoppings (dashed line) or including couplings to the third neighbors (solid line). The error bar on the last point is particularly large as we can only record the very beginning of the transfer.

Trivial vs topological chains Figure 8.7 shows how the dynamics of the particle differs depending if the chain is in a trivial (top) or topological (bottom) configuration. In the former case, the initial state $|\psi_0\rangle$ decomposes into a superposition of delocalized modes leading to a propagation and expansion of the wavepacket in the bulk of the chain. In the topological configuration, the probability to find the particle at its initial location remains high as there is a large overlap $|\langle\psi_0|L\rangle|^2 = 1 - (J'/J)^2 \simeq 0.85$ of the initial state on the left edge-mode. For this specific experiment, we chose a chain with an odd number of sites and there is no edge-mode on the right side.

Hybridization of edge states We now repeat the same experiment as above, but on a topological chain with two edge modes separated by L sites. There is now a finite coupling $E_{\mathrm{hyb}} = \langle L| \hat{H}_{\mathrm{SSH}} |R\rangle$ between the left and right edge-modes that leads to their hybridization into symmetric and anti-symmetric states at energy $\pm E_{\mathrm{hyb}}$. Similarly to the spin-exchange oscillation observed in the previous chapter, we now observe the coherent transfer of a spin-excitation from the leftmost site to the rightmost site. Figure 8.8 shows this effect on chains of length $L = 4$, 6, 8 and 10 sites. We extract the hybridization energy from the transfer frequency between the two extreme sites and compare it, in Fig. 8.8(c), to calculations using only nearest neighbor couplings (dashed line) or including J_3 and J_3' (solid line). The latter gives a much better agreement with our experimental data, and thus demonstrates the influence of the long-range couplings in our version of the SSH model. Finally, let us remark that for a chain of 14 sites, $E_{\mathrm{hyb}}/h = 0.01$ MHz is negligible compared to our experimental energy scale. In the following, we will thus neglect the hybridization between the two edge modes and consider them as degenerate eigenstates.

8.4 Entering the strongly correlated regime: half-filling with hard-core bosons

Having studied the SSH model at the single-particle level, we now turn to the properties of its quantum many-body ground-state. The latter depends on the type of particles that are loaded on the chain, — fermions or bosons, interacting or not —, and I first review the different cases in Section 8.4.1. With our experimental platform, we naturally obtain hard-core bosons that can be coherently created or annihilated with a microwave field. We use this property in Section 8.4.2 to prepare the many-body ground-state of hard-core bosons with a microwave adiabatic sweep. Finally, in Section 8.4.3, I demonstrate that this ground-state is four-fold degenerate, due to the two zero-energy edge-modes, and that this degeneracy remains even when adding a perturbation to the SSH chain that breaks the chiral symmetry of the hopping matrix J_{ij}. The latter fact is explained by the existence of a different symmetry for the bosonic phase, with no equivalent at the single-particle level.

8.4.1 Many-body phases of the SSH model

I describe here the many-body ground-state of the SSH chain when using different types of particles: (i) non-interacting bosons, (ii) non-interacting fermions, (iii) hard-core bosons, and (iv) bosons with a finite interaction energy. The SSH model was originally formulated for non-interacting fermions, while in our experimental platform the particles are hard-core bosons.

Non-interacting bosons The many-body ground-state $|\psi_{\mathrm{B}}\rangle$ is a Bose-Einstein condensation of all bosons in the lowest single-particle eigenstate, as shown in Fig. 8.9(a).

Non-interacting fermions In contrast to bosons, the Pauli principle forbids to have two fermions (considering here spinless or spin-polarized fermions) in the same state. The ground-state $|\psi_{\mathrm{F}}\rangle$ is then obtained using the Fermi sea picture stating that each single-particle eigenstate is occupied by a fermionic particle up to the chemical potential μ. In Eq. (8.3), we have implicitly chosen $\mu = 0$: the chemical potential lies within the spectral gap and only states in the lower band are populated, as shown in Fig. 8.9(b). For a chain in the trivial configuration, one obtains a single insulating ground state, while for the topological case a four-fold degenerate ground state appears due to the two edge modes $|L\rangle$ and $|R\rangle$ at zero energy: each of them can be populated or not without changing the energy of the system.

Hard-core bosons (or spins) We now consider hard-core bosons that obey bosonic commutation rules on different lattice sites, and the constraint $(b_i)^2 = 0$ indicating that there can be at most one particle per site. A direct consequence is that the dimension of the Hilbert space is restricted to 2^N, as in the case of spin-polarized non-interacting fermions (due to the Pauli principle). For a one-dimensional chain with only nearest-neighbor hopping, there is in fact a direct mapping between the two Hilbert spaces, the Jordan-Wigner transformation, that we can use to derive the many-body ground state $|\psi_{\mathrm{HB}}\rangle$ from the fermionic one $|\psi_{\mathrm{F}}\rangle$. The bosonic phase thus inherits the properties of a bulk excitation gap and a four-fold ground state degeneracy for the topological configuration. If we would restrict the coupling matrix J_{ij} to only nearest neighbor, there would be no difference between the fermionic ground-state and our phase of hard-core bosons.

However, in our experiment, the long-range dipolar interaction gives rise to hopping of particles beyond nearest neighbor sites, such that applying the Jordan-Wigner

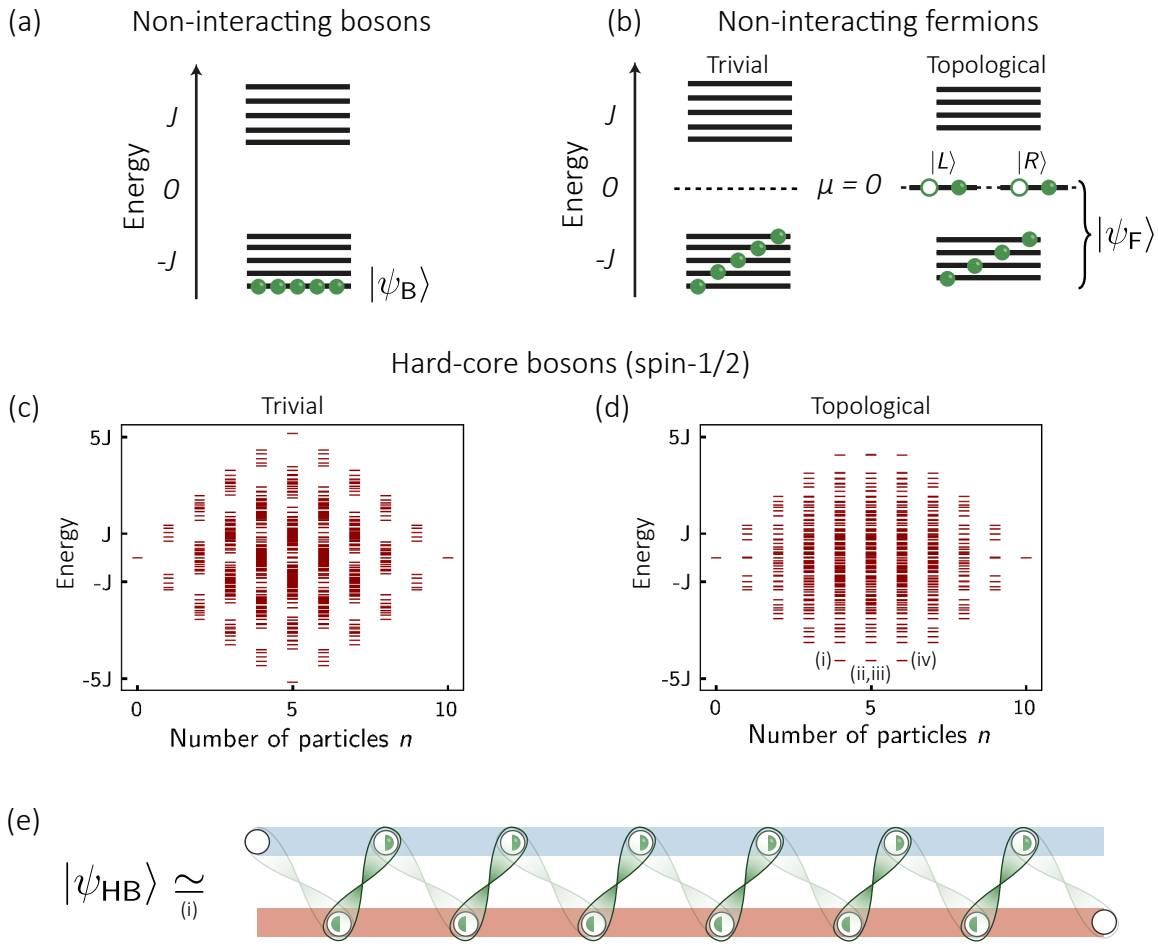

Figure 8.9: Many-body ground-states of the SSH model. We consider different types of particles loaded in the SSH chain: (a) non-interacting bosons forming a Bose-Einstein condensate in the lowest energy single-particle eigenstate, (b) non-interacting fermions forming a Fermi sea with one particle per eigenstate up to the chemical potential (here $\mu = 0$), (c) and (d) hard-core bosons (or spins) for which we represent the full Dicke ladder of 2^N eigenstates arranged by number of particles (= spin-excitations). The spectra are calculated for the couplings J and J' realized in our experiments. sFor the trivial SSH chain, there is a single many-body ground-state with $N/2$ particles, while there are four degenerate states for the topological chain. (e) Pictorial representation of the ground-state with $N/2 - 1$ particles. In the limit $J' = 0$, the edge sites are empty while the bulk of the chain is half-filled with particles, each symmetrically delocalized on the two sites forming a dimer (equivalently each dimer is in a Bell state). For finite J', correlations also appear between dimers.

transformation maps a system of hard-core bosons into interacting fermions. Consequently, $|\psi_{\mathrm{F}}\rangle$ (for free fermions) and $|\psi_{\mathrm{HB}}\rangle$ now have different properties. The most striking difference will be observed upon deforming the SSH chain to allow hoppings between next-nearest neighbor sites that breaks the four-fold degeneracy of $|\psi_{\mathrm{F}}\rangle$, but not of $|\psi_{\mathrm{HB}}\rangle$. The latter thus needs its own representation that does not rely on a Fermi sea picture. Since there are 'only' 2^N eigenstates of the Hamiltonian, we can directly calculate its spectrum which takes the form of a Dicke ladder, shown in Fig. 8.9(c,d) for $N = 10$ sites (to keep the number of states in the figure reasonable). The states are organized by increasing number of particles $n = 0, 1 \ldots, N$. A particle-hole transformation allows to go from the $n = k$ to the $n = N - k$ manifold, which have thus identical properties. For $n = 1$, we recognize the single-particle eigenstates studied in the previous section. For the topological chain, the many-body ground-state $|\psi_{\mathrm{HB}}\rangle$ is given by four degenerate states with $N/2 - 1$ (i), $N/2$ (ii,iii) and $N/2 + 1$ (iv) particles, clearly separated from the first excited states by a spectral gap calculated to be $\Delta_g/(2\pi) \simeq 1.83$ MHz. If there were only nearest neighbor hoppings, this gap would be identical to the single-particle one $\hbar\Delta_g = |J| - |J'|$.

In the limit of vanishing inter-dimer coupling $J' = 0$, an exact formulation of the many-body ground states is readily found. They correspond to exactly one particle per dimer, symmetrically delocalized between the two sites, while the edge sites of the topological chain can be either empty or occupied. In any case, the bulk of the chain is a product of entangled Bell states:

$$\left|\psi_{\mathrm{HB}}^{\mathrm{bulk}}\right\rangle \overset{J'=0}{=} \prod_i \frac{b_{2i}^\dagger - b_{2i+1}^\dagger}{\sqrt{2}} |0\rangle \tag{8.5}$$

A finite coupling J' gives rise to fluctuation of the particle number in each dimer, and to additional correlations between neighboring dimers, pictorially represented in Fig. 8.9(e). We will observe such effects in the following section.

Super-lattice Bose-Hubbard Hamiltonian For completeness, I also present the case where bosons are interacting with an on-site interaction energy U. Hard-core bosons are obtained by taking the limit $U \to \infty$. For finite interaction energies, the problem is more complicated than for hard-core bosons as there can be more than one particle per site, and the Hilbert space is not restricted anymore to 2^N eigenstates. The Hamiltonian now reads:

$$\hat{H} = -\sum_{i\in A,\, j\in B} J_{ij} \left[b_i^\dagger b_j + b_j^\dagger b_i\right] + \frac{U}{2}\sum_i n_i(n_i - 1), \tag{8.6}$$

where $n_i = b_i^\dagger b_i$ counts the number of particles on site i. For uniform couplings $J_{ij} = J$, we obtain the Bose-Hubbard model (BHM), whose quantum phase transitions between a superfluid phase for $U \ll J$ and Mott insulators (MI) for $U \gg J$ have been intensely studied in optical lattice experiments (see, e.g., Bakr *et al.* [2010]). For increasing chemical potential μ, there is a succession of incompressible MI phases with fixed number of particles per site $n/N = 1, 2, 3, \ldots$. By overlapping optical lattices with different periodicity, we obtain the super-lattice Bose-Hubbard model (SL-BHM), with a unit cell containing l lattice sites and MI phases with a fractional number of particles per site [Buonsante and Vezzani, 2004; Grusdt, Höning, and Fleischhauer, 2013]. The specific case $l = 2$ realizes Eq. 8.6 and gives rise to a Mott insulating phase with $n/N = 1/2$ particles per site.

As a first step towards studying many-body phases of interacting particles in topological models, there have been studies of simpler systems with only two particles. In a theoretical analysis of Eq. 8.6, Di Liberto *et al.* [2016] found the existence of repulsive bound pairs. On the experimental side, Tai *et al.* [2017] realized the Harper-Hofstadter Hamiltonian, another topological model, and observed the influence of interaction on the propagation of two particles. However, no study in the many-body regime have been reported so far.

8.4.2 Adiabatic preparation of the ground-state

I now demonstrate the adiabatic preparation of the many-body ground-state of a topological SSH chain of 14 sites. Figure 8.10(a) shows our objective: starting with the system initially in the vacuum state $|0\rangle$, we want to bring it in one of the four degenerate ground states at half-filling. To achieve this, we use an adiabatic microwave sweep. I remind the reader that for a microwave drive $\Omega_{\mu\mathrm{w}}(t)$ with a detuning $\Delta_{\mu\mathrm{w}}(t)$, the Hamiltonian reads:

$$\hat{H} = -\sum_{i\in A, j\in B} J_{ij}\left[b_i^\dagger b_j + b_j^\dagger b_i\right] + \frac{\hbar\Omega_{\mu\mathrm{w}}}{2}\sum_i\left[b_i^\dagger + b_i\right] + \hbar\Delta_{\mu\mathrm{w}}\sum_i b_i^\dagger b_i. \tag{8.7}$$

Recalling that the SSH part can be separated in manifolds of fixed number n of particles, the detuning creates an energy shift $n\hbar\Delta_{\mu\mathrm{w}}$ different for each manifold, while the driving term couples a manifold of n particles to the $n \pm 1$ manifolds through the coherent creation and annihilation of particles by the microwave field. Figure. 8.10(a) shows the microwave amplitude and detuning profiles that we use to prepare the many-body ground state. Starting with a large initial detuning $\hbar\Delta_{\mu\mathrm{w}} \gg |J|, |J'|$, the

vacuum state $|0\rangle$ becomes the many-body ground-state (in the spin language, this is our usual paramagnet for a large longitudinal magnetic field). We then turn on the microwave drive to couple the different manifolds together, and then chirp the microwave frequency until we reach a final detuning $\Delta_{\rm f}$, and finally switch off the coupling strength.

From a theoretical analysis simulating the full time-evolution, discussed just after, we expect that such a ramping procedure prepares the ground-state with high fidelity. In this section, I demonstrate it experimentally by observing (i) the local density of particles as a function of the final detuning $\Delta_{\rm f}$, (ii) the squeezing of the number of particles during the sweep, and (iii) the apparition of strong correlations between sites.

Discussion about adiabaticity A natural question is if we can reach adiabatically the many-body ground state assuming a fully-coherent[7] evolution of the system. In particular, if there is a quantum phase transition between the initial vacuum state (a paramagnet) and the many-body ground state (an ordered state) during the microwave sweep, then there will be a gap closing (for an infinite size system) leading to defect and preparation errors. In fact, in contrast with our studies of Ising antiferromagnets in Chapter 4, there is no such QPT and it is thus possible to prepare almost perfectly the many-body ground state in a finite amount of time.

Using the sweep shown in Fig. 8.10(b) with $\Delta_f/(2\pi) = -1$ MHz and numerically solving a time-dependent Schrödinger equation (for $N = 10$ sites), we find that our ramping procedure prepares the ground state with $N/2 - 1$ particles [marked by an orange star in panel (a)] with a fidelity of 96 %. The efficiency can be increased to 99.7 % by using an optimized sweep, proposed by Sebastian Weber and shown later in Fig. 8.13(b). Let us note that only the half-filled ground states (and the fully filled one) can be adiabatically prepared in the limit $N \to \infty$, since all other states are not separated by a gap from the first excited ones (away from half-filling, the system is a 'metal' without an excitation gap).

Plateaus at half-filling I first present how the local density of particles depends on the final detuning $\Delta_{\rm f}$ and the configuration of the SSH chain. The experimentally observed filling fraction of the bulk sites $i \in [2, 13]$ and the two edge sites are shown in Fig. 8.10 for the trivial (c) and topological SSH chains (d). We find that the bulk sites occupancy (blue curves) presents a characteristic plateau at half-filling when the final detuning lies within the gap $\Delta_g/(2\pi) = 1.83$ MHz.

[7] We have demonstrated in Section **??** that the microwave drive is a perfectly coherent tool.

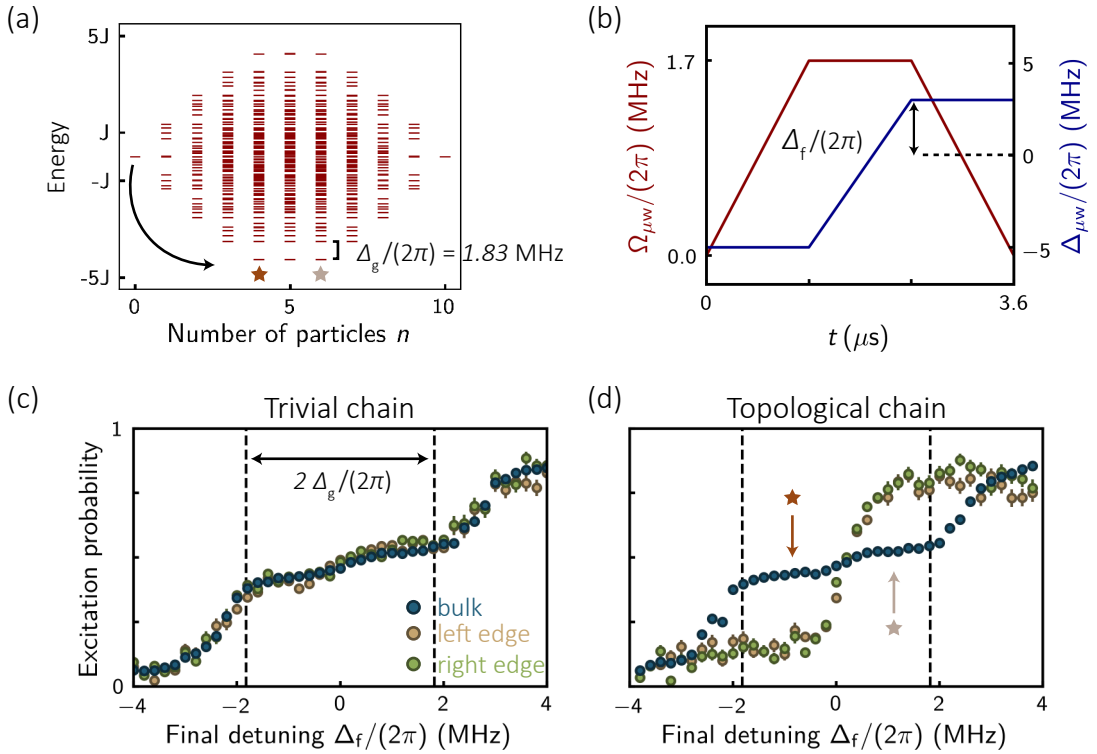

Figure 8.10: Sweeps to half-filling. (a) We aim at preparing one of the four degenerate ground-state of the topological chain with a microwave sweep. (b) Time-dependent microwave coupling strength $\Omega_{\mu\mathrm{w}}(t)$ and detuning $\Delta_{\mu\mathrm{w}}(t)$ ending at Δ_f. (c,d) We scan the final detuning Δ_f and measure the excitation probability of bulk sites (blue) and edge sites (green and brown) for the trivial (c) and topological (d) setup (right). For a sweep ending in the gap (dashed line), the bulk of the chain is half-filled. Bosons are loaded in the edge sites of the topological setup when $\Delta_\mathrm{f} > 0$.

While the local bulk properties are independent of the topology of the setup, it is drastically different for the edge occupancies: in the trivial setup, the edge sites behave as the bulk sites, whereas for the topological setup, the boundaries remain depleted for $\Delta_f < 0$ and exhibits a sharp transition to fully occupied for $\Delta_f > 0$. This is consistent with the ground state degeneracy represented in Fig. 8.10(a) as for $\Delta_f < 0$ (> 0), we create the ground-state of the $n = N/2 - 1$ ($n = N/2 + 1$) manifold where both edge sites are unoccupied (occupied). The small jump of the bulk density around $\Delta_f = 0$ comes from preparation errors of the Rydberg array: this creates holes in the chain and thus topological defects accompanied by zero-energy modes that are filled with a particle for $\Delta_f > 0$.

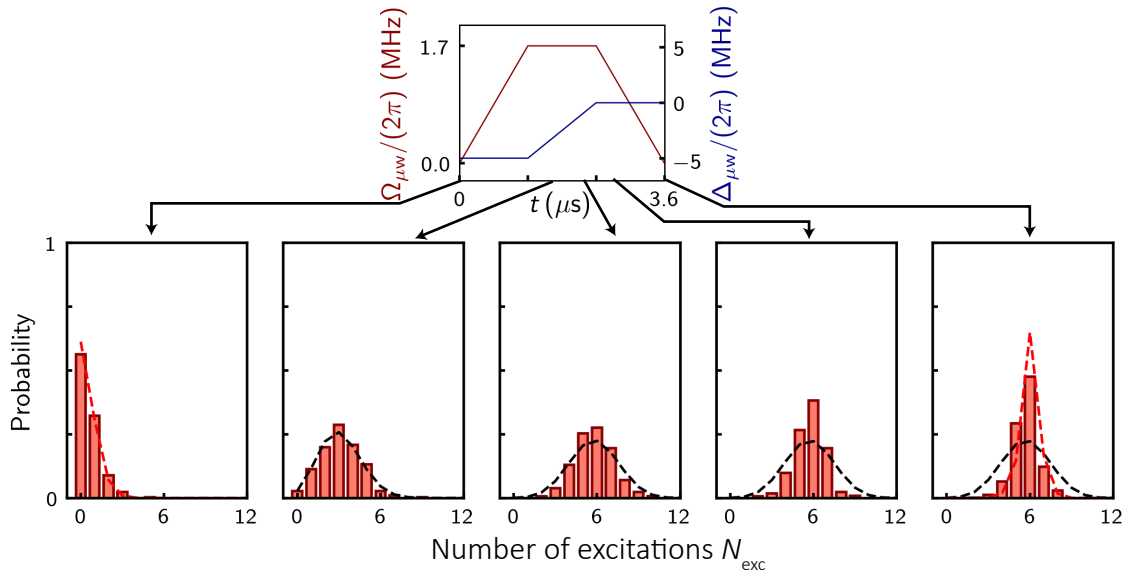

Figure 8.11: Particle number squeezing during the sweep. Measured distributions of the number of spin-excitations in the bulk of the chain, at different times along the microwave sweep. Black curves show binomial distributions (uncorrelated spins) centered at the mean value of the measured ones. Red dashed curves are the results of a Monte-Carlo simulation taking into account detection errors $(\varepsilon, \varepsilon') = (0.04, 0.04)$ for each of the 12 bulk sites, assuming a state with exactly 0 (leftmost panel) and 6 particles (rightmost panel).

Squeezed number of particles In the previous paragraph, we have seen that an adiabatic sweep ending at $\Delta_f = 0$ led to a bulk half-filled with 6 particles on *average*. I now show that we are actually quite close to preparing *exactly* 6 particles in the bulk. Here, I do not consider the edge sites as they give rise to strong fluctuations of the particle number for $\Delta_f = 0$. Figure 8.11 shows the evolution during the sweep of the particle number distribution. Initially, the system is in the vacuum state $|0\rangle$ and the few detected particles come from detection errors. We then observe an increase of particle numbers with a distribution remaining binomial (black dashed curve). In our spin language, we are still in a paramagnetic phase with uncorrelated spins but with a decreasing magnetization. At the end of the sweep, we have reached half-filling (no net magnetization), the particle number distribution is much narrower than a binomial law (the spins are now correlated, see next paragraph) and we obtain a 48 % probability to have *exactly* 6 particles in the bulk. I also show, with the red dashed curve, how an ideal distribution perfectly peaked at $n = 6$ is affected by detection errors $(\varepsilon, \varepsilon') = (0.04, 0.04)$. Due to the accumulation of detection errors over the 12 bulk sites, the probability to observe exactly 6 particles is decreased to 65 %, close to our measured value. The remaining difference originates from preparation errors.

Correlations We expect the many-body ground-state of a half-filled chain, prepared by an adiabatic sweep ending at $\Delta_f = 0$, to show strong correlations between the particles. Especially, from our discussion in Section 8.4.1, and in particular Eq. (8.5), we expect the bulk of the chain to be approximately a product of Bell states on each dimer. A first consequence is that there should be close to only one particle per dimer, giving strong anti-correlations for the excitation probability of two spins in the same dimer. Figure. 8.12(a) shows the correlation map:

$$C_Z(i,j) = \langle \sigma_i^z \sigma_j^z \rangle - \langle \sigma_i^z \rangle \langle \sigma_j^z \rangle, \tag{8.8}$$

which takes the maximal value of $\pm 1/4$ when two lattice sites i and j are always found in the same (opposite) state. As expected, we observe strong 'intra-dimer' correlations $4\,C_Z(2i, 2i+1) = -0.630(6)$ (averaging over all dimers for ∼3000 experimental runs, the error bar is the standard deviation obtained by the bootstrap method). The 'inter-dimer' correlations between two nearest neighbor sites in different dimers are much weaker: $4\,C_Z(2i-1, 2i) = -0.025(9)$.

The above correlations tell us that, on each dimer, only one of the two spins is observed in the excited state, but we do not know if each dimer is in a statistical mixture of $|01\rangle$ and $|10\rangle$ or in a coherent state. To demonstrate the coherence between the two sites, we have to rotate the measurement basis (the method is described below) to measure the correlations:

$$C_X(i,j) = \langle \sigma_i^x \sigma_j^x \rangle - \langle \sigma_i^x \rangle \langle \sigma_j^x \rangle. \tag{8.9}$$

Figure 8.12(b) shows strong intra-dimer correlations $4\,C_X(2i, 2i+1) = +0.454(7)$ demonstrating that a particle is coherently delocalized between the two lattice sites forming a dimer. Additionally, we observe inter-dimer correlations $4\,C_X(2i-1, 2i) = -0.041(8)$ that are stronger than when measuring along the z-axis. The latter fact is a general property of the ground-state of XY magnets: spatial correlations measured along the z-axis decrease faster than along the xy-plane [Giamarchi, 2003].

The rotation of the measurement basis is better explained in the spin language. Our read-out method always projects the state of each spin in the state $|\downarrow\rangle$ or $|\uparrow\rangle$ along Z. However, we can rotate the spins just before the measurement by applying a strong microwave pulse with a Rabi frequency $\Omega_{\mu w}/(2\pi) \simeq 14$ MHz during a time τ. The microwave drive is chosen strong enough, such that interactions are negligible during one period (recall Fig. 7.8). In Fig. 8.12(d), we vary the pulse area $\Omega_{\mu w}\tau$ to measure the spins along any direction in the XZ plane. We obtain an oscillation of the

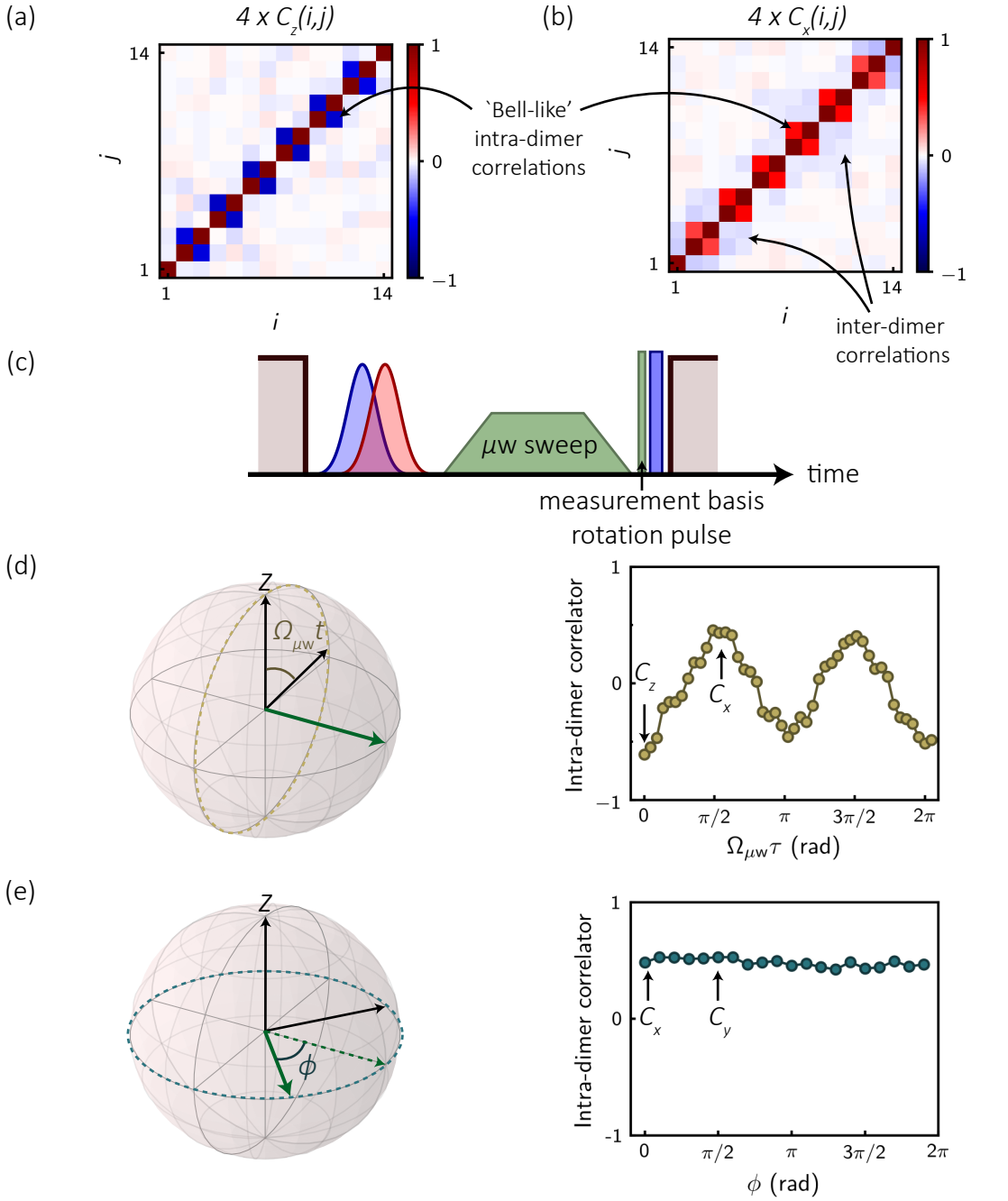

Figure 8.12: Correlations at half-filling. (a) Correlation map $C_Z(i,j)$ and (b) $C_X(i,j)$ showing strong intra-dimer correlations and weaker inter-dimer one. (c) Experimental sequence: after the microwave sweep, and before shining the read-out beam, we apply a strong microwave pulse to rotate the spins. We then show the averaged intra-dimer correlator along different axes of the XZ plane (d) and the XY plane (e).

intra-dimer correlator, alike to parity oscillations used to demonstrate entanglement between two spins (see, e.g., Wilk *et al.* [2010]). Finally, in Fig. 8.12(e), by changing the phase ϕ of the microwave field between the sweep and a $\pi/2$-pulse rotating the measurement basis to the equatorial plane, we project the spins along any directions in the XY plane. As expected for an Hamiltonian with an XY symmetry, the correlations do not depend on the chosen axis in the XY plane.

8.4.3 Ground-state degeneracy and robustness to a perturbation breaking the chiral symmetry

I now turn to the experimental demonstration of the four-fold degeneracy of the many-body ground-state in a topological SSH chain. Figure 8.13(a) shows the four ground-states separated by a spectral gap from the first excited ones. To observe the degeneracy and the finite gap, we use the experimental sequence shown in Fig. 8.13(b): we first initialize the system in the ground-state with $N/2-1$ particles with an adiabatic sweep ending at $\Delta_\mathrm{f}/(2\pi) = -1$ MHz, and then apply a weak microwave probe ($\Omega_{\mu\mathrm{w}}/(2\pi) = 0.3$ MHz, $\tau = 2\,\mu$s) at various detunings Δ_spectro.

The final local density of particles in the bulk and in the edge sites are shown in Fig. 8.13(c). For a detuning $\Delta_\mathrm{spectro}/(2\pi) = \pm 2.1$ MHz, we observe a change in the bulk density resulting from the transitions (i) and (ii) from the ground-state with $N/2-1$ particles to excited states with $N/2-2$ and $N/2$ particles (the microwave field cannot drive a transition to the excited states with the same number of particles). Finally, the fact that the peak (iii) in the excitation probability of the edge sites is exactly at $\Delta_\mathrm{spectro} = 0$ MHz demonstrates that the two other ground-states with $N/2$ particles are degenerate with the one prepared with the adiabatic sweep. From the symmetry of the Hamiltonian, we obtain that the fourth ground-state with $N/2+1$ particles is also at the same energy as the three others. A quantitative simulation of this spectrum is a work in progress at the time of writing this thesis.

Breaking the chiral symmetry We finally explore how the properties of the topological phase are modified upon a perturbation breaking the chiral symmetry $\mathbf{S}_F$:

$$H_\mathrm{pert.} = -J_2 \left[b^\dagger_{N-2} b_N + b^\dagger_N b_{N-2} \right]. \tag{8.10}$$

We engineer it by displacing the rightmost site of the chain out of the magic angle, to give a finite coupling $J_2/h = 0.26$ MHz between the edge site and its second

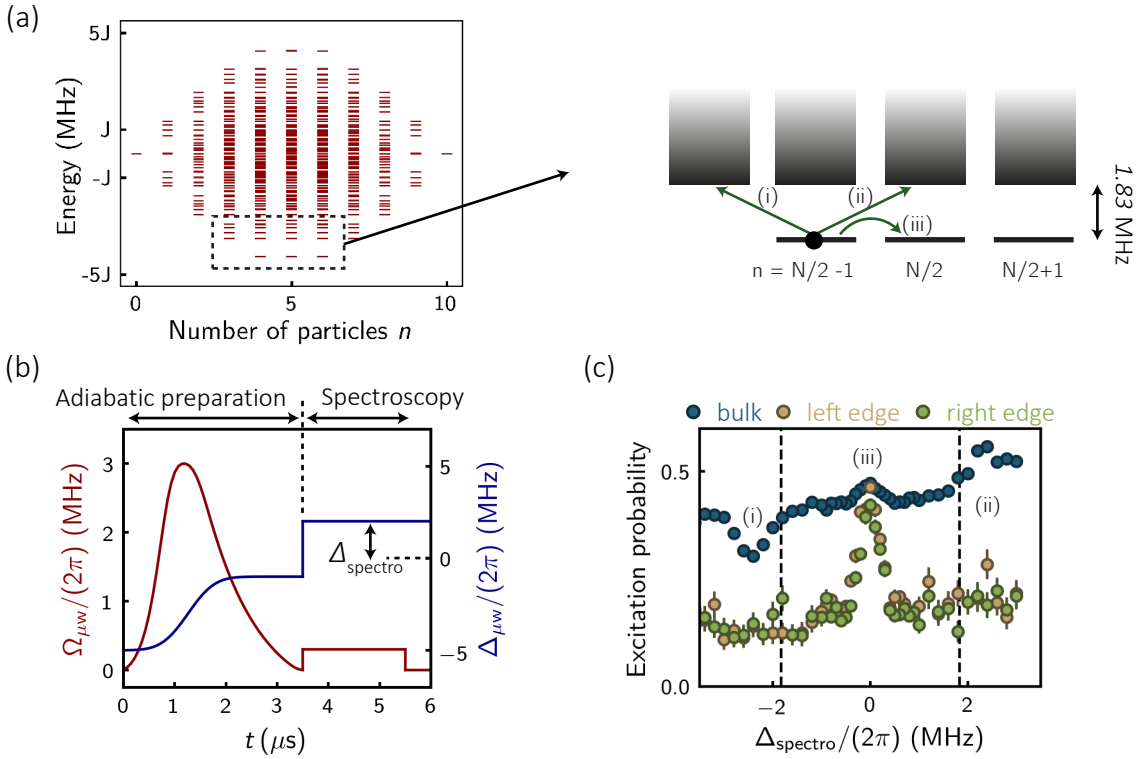

Figure 8.13: Probing the ground-state degeneracy of the topological phase. (a) For an SSH chain in a topological configuration, there are four degenerate states separated by an energy gap of $\Delta_g/(2\pi) = 1.83$ MHz from the first excited states. (b) Microwave sequence starting with an optimized adiabatic preparation of the ground state with $N/2-1$ particles, followed by a spectroscopy experiment where $\Delta_{\mathrm{spectro}}$ is scanned. (c) Density of particles in the bulk and in the edge sites at the end of the experiment. We observe three resonances corresponding to (i) the removal and (ii) the creation of a particle in the bulk for a finite energy cost $> \hbar\Delta_{\mathrm{g}}$ (indicated by the dashed line), and (iii) the addition of a particle in the edge sites at zero-energy.

neighbor [see Fig.8.14(a)]. Recall that the chiral symmetry is protecting the topological phase of the SSH chain when filled with non-interacting fermions, while we have here hard-core bosons. Also, applying the Jordan-Wigner transformation maps our hard-core bosons on interacting fermions due to the long-range character of the perturbation, such that the phases of free fermions and hard-core bosons do not have to share the same properties regarding the perturbation. By deriving the symmetry $\mathcal{S}_{\mathrm{HB}}$ protecting the bosonic phase (described later), our colleagues from the theory team in Stuttgart predicted that the degeneracy of the bosonic ground-state is not broken by the perturbation, whereas numerical calculations of the single-particle eigenstates (that fully describe the fermionic phase) give a finite energy difference

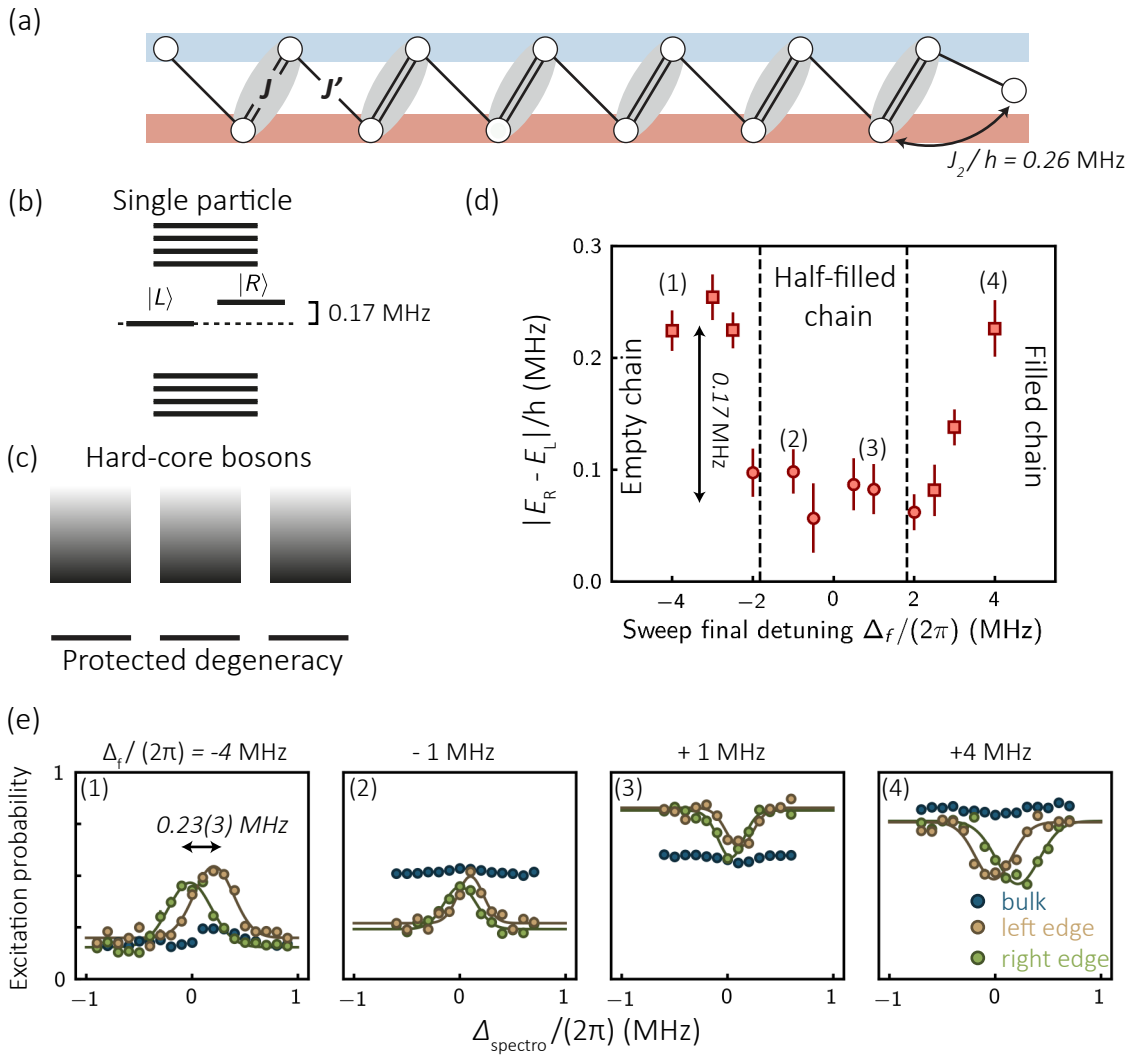

Figure 8.14: Robustness of the bosonic topological phase to a perturbation breaking the chiral symmetry. (a) The rightmost site is shifted upwards to give rise to a finite hopping amplitude J_2 to the second neighbor. (b) The symmetry-breaking perturbation leads to an energy difference $E_\mathrm{R} - E_\mathrm{L} \simeq h \times 0.16$ MHz between the left and right single-particle edge modes. The fermionic ground-state is not degenerate anymore. (c) In contrast, with hard-core bosons, the four many-body ground-states remain degenerate. (d) Energy difference extracted from microwave spectra performed after an adiabatic sweep ending at various Δ_f. When $|\Delta_\mathrm{f}| \gg J, J'$, the chain is either empty or fully filled (the two cases are equivalent), and we are probing the degeneracy of the single-particle edge-modes. For $|\Delta_\mathrm{f}|/(2\pi) < 1.8$ MHz, we have prepared an half-filled chain, and we probe the degeneracy of the many-body states. (e) Examples of spectra from which we extract the energy difference $|E_\mathrm{R} - E_\mathrm{L}|$ using Gaussian fits to the density of particle in the left and right edge sites.

$E_R - E_L = h \times 0.17$ MHz between the left and right edge modes. The difference between the fermionic and bosonic phases is illustrated in Fig. 8.14(b,c).

We probe experimentally the properties described above by microwave spectroscopy performed after a microwave sweep with various final detunings Δ_f. For this experiment (and the one in the previous paragraph), we use an optimized microwave waveform calculated by Sebastian Weber and shown in Fig. 8.13(b), that improves the adiabatic preparation when Δ_f is not deep in the single-particle gap (where the simpler waveform used previously was already giving excellent results). The experiment is identical to the one described in the previous paragraph and we now look more closely at the energy difference $E_R - E_L$ between the peaks corresponding to the population of the leftmost and rightmost edge sites. To improve the spectral resolution, we use a weaker microwave probe $\Omega_{\mu w}/(2\pi) = 0.15$ MHz. The results presented in Fig. 8.14(d) show a striking difference depending if the spectroscopy is performed for a sweep ending in or out of the single-particle gap (dashed line).

For a sweep ending at $\Delta_f/(2\pi) = -4$ MHz, the chain remains in the vacuum state $|0\rangle$, and the spectroscopy experiment probes the energy difference between the two single-particle modes giving $E_R - E_L = h \times 0.23(3)$ MHz [panel (1) of Fig. 8.14(e)]. In contrast, for a sweep ending at $\Delta_f/(2\pi) = -1$ MHz, we have half-filled the bulk with the edge sites remaining empty, and we obtain an energy difference between the many-body ground states of only $h \times 0.08(2)$ MHz [panel (2) of Fig. 8.14(e)]. The two last panels show spectra when the edge-sites are initially filled with a half-filled bulk (3), or when the chain is fully filled with hard-core bosons (4). Recalling that the SSH Hamiltonian is invariant under a change of definition $|\downarrow\rangle \leftrightarrow |\uparrow\rangle$, we understand why the results (3) and (4) are similar to (2) and (1), respectively.

Finally, comparing the energy difference between the single-particle edge-modes and the many-body ground-states, we obtain a value of $0.23(2) - 0.08(2) = 0.15(3)$ MHz in very good agreement with the ab-initio calculation predicting 0.16 MHz. The small energy mismatch of 0.08 MHz between the two many-body ground-states is explained in part by an independently measured difference in microwave transition frequency of $\sim 0.02 - 0.03$ MHz between the two extreme Rydberg atoms (caused by a small gradient of electric field). Another possible contribution is the smaller van der Waals shift between the edge site and its neighbors when moving the rightmost site to engineer the perturbation, and we are currently performing simulation to quantify this effect.

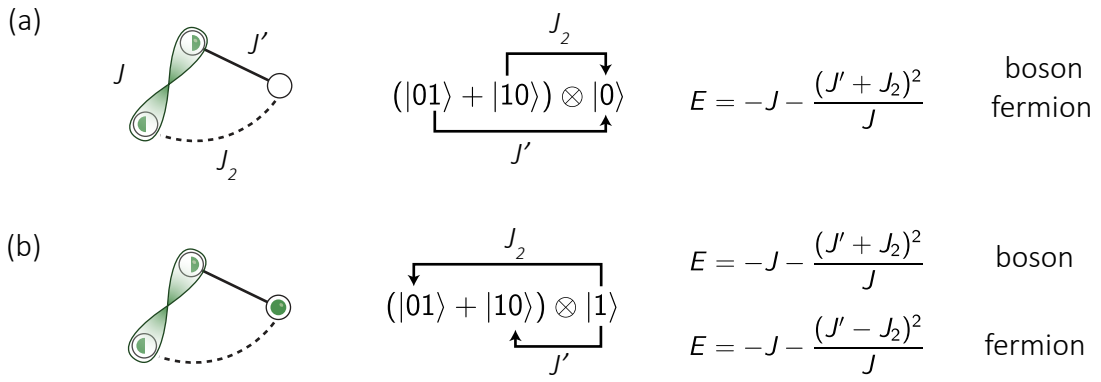

Figure 8.15: A three site model. We restrict to only three sites of the SSH chain with perturbative couplings $J', J_2 \ll J$ and evaluate the energy of the ground-state with (a) one particle and (b) two particles. In both cases and in a zeroth order approximation, the ground state is a particle delocalized on the dimer, thus having an energy $-J$, while the edge site is occupied or not. In a second-order approximation, the energy is lowered as one particle can virtually hop between the dimer and the edge sites. However, in (b), we have to consider the commutation relation between the two particles, such that the energy correction is different for bosons and fermions.

8.5 Conclusion

The remarkable fact that the many-body ground-states of an SSH chain half-filled with hard-core bosons remain degenerate under the perturbation H_{pert} was first indicated by our colleagues in the group of Prof. Hans-Peter Büchler. To understand qualitatively this feature, we consider a simple model of only three sites of the SSH chain: a dimer with a coupling J and an edge site with couplings J' and J_2 to the two first sites, as shown in Fig. 8.15. We use the perturbative limit $J', J_2 \ll J$ to evaluate the energy of the two lowest energy states containing 1 and 2 particles. In the first case of one particle [Fig. 8.15(a)], the ground state is given by a particle delocalized in the dimer at an energy $-J$, the latter is additionally lowered when the particle virtually hops to the edge site at zero energy. In the second case of two particles [Fig. 8.15(b)], the ground state is given by one particle in the dimer and another one in the edge site. Similarly, the second particle lowers its energy by hopping from the edge site to one dimer site. However, the energy correction now depends on the statistics of the particle, because it has to be exchanged with the one located on the dimer. This simplified model captures why the fermionic degeneracy is broken by the J_2 term, while it is not the case for hard-core bosons.

A more general way to come to this conclusion is to derive the bosonic equivalent

to the chiral symmetry $\mathcal{S}_{\mathrm{F}}$ protecting the fermionic topological phase using the Jordan-Wigner transformation:

$$\mathcal{S}_{\mathrm{F}} = \prod_i \left[c_i + (-1)^i c_i^\dagger\right] \circ K \quad \rightarrow \quad \mathcal{S}_{\mathrm{HB}} = \prod_i \left[b_i + b_i^\dagger\right] \circ K, \tag{8.11}$$

where we make a clear distinction between fermionic c_i and (hard-core) bosonic b_i operators, and K denotes the complex conjugation. The perturbation H_{pert} commutes with $\mathcal{S}_{\mathrm{HB}}$:

$$\begin{aligned}
[H_{\mathrm{pert}}, \mathcal{S}_{\mathrm{HB}}] &= \left[(b_N^\dagger b_{N-2} + b_N b_{N-2}^\dagger), \prod (b_i + b_i^\dagger)\right] \\
&= (b_N^\dagger b_{N-2} + b_N b_{N-2}^\dagger)(b_{N-2} + b_{N-2}^\dagger)(b_N + b_N^\dagger) - \dots \\
&= b_N^\dagger b_{N-2} b_N b_{N-2}^\dagger + b_N b_{N-2}^\dagger b_N^\dagger b_{N-2} - \dots \\
&= n_N(n_{N-2}+1) + n_{N-2}(n_N+1) - n_{N-2}(n_N+1) - n_N(n_{N-2}+1) \\
&= 0
\end{aligned}$$

Because the perturbation is invariant by the symmetry $\mathbf{S}_{\mathrm{HB}}$, we indeed expect the ground-state degeneracy to be unaffected by it, which we checked numerically and demonstrated experimentally with the results shown in Fig. 8.14.

Let us note that the derivation of $\mathcal{S}_{\mathrm{HB}}$ from the fermionic one using the Jordan-Wigner transformation does not prove that it gives rise to a symmetry protected topological phase of hard-core bosons. This is in fact a highly non-trivial task that was performed by Nicolaï Lang and that rely on the mathematical concepts of group cohomology used by Chen *et al.* [2012, 2013] to derive a general classification of one-dimensional bosonic SPT phases [Chen *et al.*, 2012, 2013]. In their classification (see Table I of Chen *et al.* [2013]), our bosonic SSH chain is in the symmetry group $U(1) \times Z_2$ inside which Chen and coworkers could construct (with abstract arguments) a trivial and a topological phase. Here, we experimentally realized these two phases by simply populating an SSH chain with hard-core bosons. More generally, the symmetry $\mathcal{S}_{\mathrm{HB}}$ also allows interaction terms of the form $n_i n_j$, that can be used to connect our bosonic SSH model to the Haldane anti-ferromagnetic spin-1 chain [Haldane, 1983b] or to the AKLT model [Affleck *et al.*, 1987].

Chapter 9

Conclusion and Outlook

In this manuscript, I have presented the development of a quantum simulator of spin systems based on assembled arrays of single Rydberg atoms. During the course of this thesis, we have bridged the gap between proof-of-principle experiments with a few Rydberg atoms, and large-scale studies with tens of particles. In 2015, the most critical drawback of our experimental platform, based on arrays of optical tweezers, was the random loading of each trap with zero or one atom. A major progress, described in Chapter 3, has been the engineering of a robust and easy-to-use method to assemble perfectly filled atomic arrays of any shape. The excellent efficiency of this atom-by-atom assembler, with a filling fraction of target arrays higher than 98 %, combined with the fast repetition rate of the experiment (> 3 Hz), offers now a high-performance platform for quantum simulation. The extension of our technique to 3D arrays, by using commercially-available tunable lenses to manipulate atoms in different planes, further improved the flexibility of the platform. Our assembling technique is likely to find many applications in the field of quantum simulation and qunatum information processing [Regal, 2016; Lundblad, 2018].

To obtain sizable interactions between atoms in different optical tweezers separated by a few micrometers, we excite them to Rydberg states. In 2008, our group observed the Rydberg blockade effect, preventing the simultaneous excitation of Rydberg atoms due to strong van der Waals shifts, in the most pristine situation setup of only two atoms. Then, with the new CHADOQ apparatus offering a better control of electric fields, Béguin and coworkers measured the van der Waals shift in 2013. The following year, the team demonstrated that the Rydberg blockade was also efficient in a system of three atoms. When I joined the project, the goal was to realize quantum Ising models on larger arrays of a few tens of traps, where the ground and Rydberg level of each atom encodes a spin-1/2 particle. At that time we did not have yet the assembler and we used large Rydberg blockade volumes to minimize the influence of holes in the randomly loaded arrays. Performing quench experiments, we observed the saturation of the Rydberg fraction (an effective magnetization of the system) and the dynamical emergence of correlations that I presented in Chapter 4. For some choice of array

geometries and Rydberg states, we obtained a perfect agreement with numerical predictions, while for others we observed systematic deviations from the theory.

These results motivated a deeper investigation of the effect of the dipole-dipole interaction between two atoms, presented in Chapter 6, that goes beyond the simple van der Waals approximation to take into account subtle interplays with external magnetic and electric fields. We attributed the observed deviations to complex pair-state properties peculiar to the Rydberg D series, that lead to a mixing of Rydberg levels and thus a failure of the spin-1/2 approximation. We finally found an optimized regime of operation where the spin-1/2 mapping was re-established for D states.

Benefiting from this new insight and the development of the assembling technique, we pursued our studies of Ising models. Tuning the Rydberg blockade volume such that it extends only to nearest neighbor sites, we attempted the adiabatic preparation of antiferromagnetic states in linear, square and triangular lattices. We slowly evolved the laser drive and detuning, respectively mimicking a transverse and longitudinal components of a $\mathbf{B}$-field acting on the spin-1/2 particles, to bring our system from a paramagnetic phase to the ordered one after crossing a quantum phase transition. While we successfully observed the emergence of Néel-like antiferromagnetic correlations, they remained lower than the numerical predictions from a perfectly coherent evolution of our spin-1/2 particles. Our experimental data were well reproduced by an empirical model including a dephasing rate of the Rydberg states. This motivated a detailed characterization of all technical and physical effects that affect, already at the single-particle level, the coherence of the ground-Rydberg laser-drive. Our conclusions, reported in Chapter 5, pointed to the limited coupling strengths achievable with our current setup and, to a lesser extent, to the phase noise of the laser sources. These insights help us in devising the next generation of our Rydberg quantum simulator of Ising models.

The dipole-dipole interaction between Rydberg atoms takes another form when the two atoms are excited in different dipole-coupled orbitals of opposite parities. There, the interaction gives rise to a spin-exchange process allowing the studies of XY spin models, as demonstrated by Barredo and colleagues in elementary setups of two and three atoms in 2015. In Chapter 7, after presenting the STIRAP technique, critical for the initialization of an XY magnet with all atoms in the same Rydberg state, I showed how to manipulate Rydberg-Rydberg spin-1/2 particles using a global microwave field and a local addressing beam. With the latter, we demonstrated our control of the dipole-dipole coupling, stopping at will a spin-exchange processes or creating a sub-radiant entangled state of two atoms.

Finally, in Chapter 8, we implemented a spin (or bosonic) version of the Su-Schrieffer-Heeger model. In its original formulation, an SSH chain is half-filled with non-interacting fermions, which is the simplest setup giving rise to a symmetry-protected topological phase. In our experimental realization, we used spin excitations of an XY magnet to encode bosonic particles with an hard-core constraint, effectively giving infinite on-site interaction energies. Up to this date, realizations of topological phases in artificial quantum systems were limited to the regime of non- or weakly-interacting particles, where the physical properties of the system can be understood at the single particle level. Here, benefiting from the hard-core constraint of spin-excitations, we can explore the interplay between strong interactions and topological phases. Using a microwave adiabatic sweep, we prepared the many-body ground state of an SSH chain half-filled with hard-core bosons, and observed clear signatures of a bosonic symmetry-protected topological phase. Notably, we demonstrated a robustness of the ground-state degeneracy of this phase that cannot be explained at the single-particle level. To the best of our knowledge, this is the first realization of an interacting topological phase in artificial matters.

The above-mentioned experimental studies demonstrate the flexibility of a Rydberg quantum simulator, able to tackle various many-body problems originating from real-world condensed-matter systems. In the immediate future, we will set up new excitation lasers that will give us a much better control on the ground-Rydberg transition, crucial for the studies of Ising models with coherent adiabatic sweeps. In particular, this should allow to explore antiferromagnetism in frustrated geometries. Another direction is to realize these frustrated systems on XY-like magnets, where we benefit from an almost perfect effective magnetic field when driving the Rydberg-Rydberg microwave transition. Until now, we have worked with the quantization axis aligned with the atomic plane such that the resonant dipolar interaction is strongly anisotropic, which we used to implement the SSH model, but this gives ferromagnetic couplings in one direction and anti-ferromagnetic ones in the other. To realize frustrated XY-antiferromagnets, such as the one proposed by [Varney *et al.*, 2011], we ideally need isotropic couplings, that we recently obtained by rotating the orientation of the quantization axis to the normal of the atomic plane. Interestingly, in this configuration, it is also possible to engineer a spin-orbit coupling when the dipolar exchange process is accompanied by a change of total magnetic quantum number ΔM. This process is at the basis of a proposal by Weber *et al.* [2018] to engineer topological flat bands in a honeycomb lattice of Rydberg atoms, adapting ideas originally formulated for polar molecules trapped in optical lattices [Yao *et al.*,

2012; Peter *et al.*, 2015].

So far, only the Ising and XY spin models have been implemented on our Rydberg platform, but it is also possible to combine Ising and XY couplings to realize an anisotropic XXZ model, or, if the two contributions are tuned to be equal, the isotropic Heisenberg model. The properties of these systems are modified by the long-range character of the dipole-dipole interaction, which motivated theoretical studies and proposals for experimental realizations with ions [Hauke *et al.*, 2010] or polar molecules [Peter *et al.*, 2012]. With Rydberg atoms, we could use the same encoding than for the XY magnets, but use higher principal quantum numbers, or closer atoms, to tune the ratio between the van der Waals ($\propto n^{11}/R^6$) and resonant dipolar coupling ($\propto n^4/R^3$). Another possibility is to encode the spin-1/2 particles in two levels of the same Rydberg series, for example the $60S$ and $61S$ states. In this case there is no dipole matrix element between the two states, such that both the Ising and XY terms originate from a second-order perturbation by the dipole-dipole Hamiltonian and thus have the same $1/R^6$ dependence.

We also envision several technical developments of our experimental platform:

- Increasing the available time for Rydberg experiments by cooling the atoms to the motional ground-state of the tweezers [Kaufman, Lester, and Regal, 2012; Thompson *et al.*, 2013b].
- Reaching higher number of atoms in our assembled structure with a more powerful trap laser to create up to a thousand tweezers.
- Suppressing atom loss by working in a cryogenic environment.
- Increasing the experimental cycling rate above 10 Hz by recycling all atoms, which could be achieved by mapping down the Rydberg states to the ground-state hyperfine levels before a state-sensitive fluorescence measurement [Martinez-Dorantes *et al.*, 2017; Kwon *et al.*, 2017].

Additionally, it would be interesting to develop an objective lens with a larger field of view to increase the maximal extent of our atomic structure and a higher NA to reduce the tweezers size and improve the compactness of our 3D structures. This would also enable to bring two Rydberg atoms close enough such that their electronic wavefunction overlap, leading to a delocalization of the electrons, alike in real-materials, and their study using ultrafast coherent probes [Ohmori, 2014; Takei *et al.*, 2016].

Appendix A

Fluorescence signal

Fluorescence signal Up to this work, we have been using an exposure of $\tau = 50$ ms and decreasing it requires to understand what limits our ability to discriminate the presence or absence of an atom. A typical fluorescence signal obtained by taking 8000 images with random loading of a trap is shown in Fig. A.1. The signal is the number of counts from a single pixel where the fluorescence of an atom is focused. The distribution of counts is almost binary: it is low (S_L) if there is no atom in the trap, and high (S_H) if a single atom scatters photons from the cooling beams. Noise, of different sources, contaminates the signal and broadens its low and high parts, giving Gaussian distributions with widths σ_L and σ_H. The signal is re-binarized to give the absence (0) or presence (1) of an atom by setting a threshold S_{thr}; for equal widths $\sigma_L = \sigma_H$ we could simply choose $S_{\text{thr}} = (S_L + S_H)/2$, but more generally the optimal choice is the weighted average:

$$S_{\text{thr}} = \frac{\sigma_H S_L + \sigma_L S_H}{\sigma_L + \sigma_H} \tag{A.1}$$

The probability to make an error is then given by the integral of the Gaussian distribution above (or below) the threshold. In the case shown in Fig. A.1, obtained after noise and signal optimization (see below) and an exposure $\tau = 50$ ms, this probability is ridiculously small ($\sim 10^{-9}$). An error rate of 1 % would be obtained for a reduced exposure $\tau = 20$ ms assuming a constant noise (which is partly wrong, the shot noise contribution will also decrease). As a side remark, we observe that there are 21 counts (0.3 %) in the central region (more than 4σ away from the average low or high part of the signal). They are not caused by the noise (the probability is less than 10^{-5}) but by an atom loss occurring during the exposure time with a probability $\tau/(10\ s) = 0.5\,\%$. I will now present a quantitative analysis of the noise and signal values.

Signal height The number of counts obtained when an atom is present in the tweezers depends on (i) the number of photons emitted by the atom, (ii) their collection on the

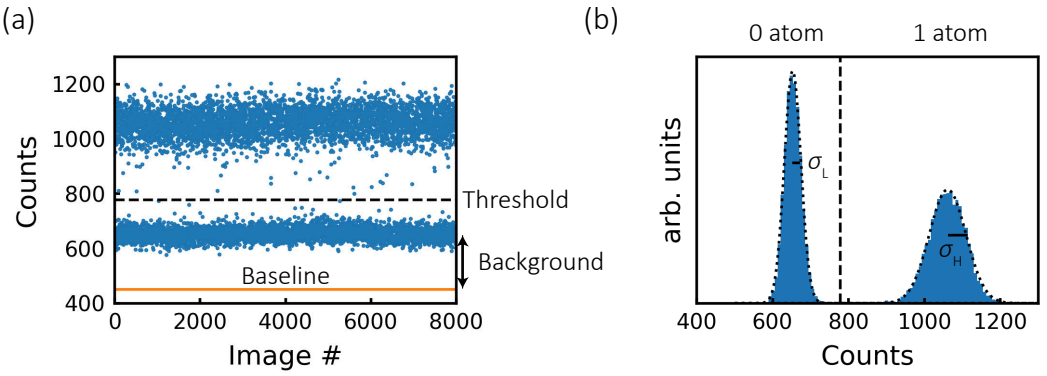

Figure A.1: Fluorescence signal. The exposure is 50 ms, and the EM gain is set to $\times 30$ (the real gain is different though). We measure a signal height of 415 counts and noises $\sigma_L = 22$ counts and $\sigma_R = 48$ counts.

EMCCD chip and (iii) the conversion process from photons to electrons to digital counts in the camera. The number of emitted photons is ultimately limited by the scattering rate of the Rb D_2-line (1 photon every 50 ns), but is usually much less to avoid heating out the atom from the tweezers. It is still unclear how close to the maximal scattering rate we are, and a careful optimization of the cooling beam parameters in view of maximizing the number of emitted photons has yet to be done. Of these fluorescence photons, only a few (typically 1 %) arrive on the camera due to the finite collection efficiency of the aspheric lens ($\sim 7\,\%$) and the large number of optics between the lens and the camera (dichroic mirror, tunable lens, 780 nm interference filter, to cite only the least transparent ones), see Béguin [2013] for a detailed estimate.

The EMCCD conversion process, which can be found in the Andor Hardware Guide, is as follows. Hitting a pixel of the CCD chip, a photon creates a photo-electron with a high probability given by the camera quantum efficiency ($\sim 90\,\%$). After integrating during the exposure time τ, the electron charges are moved towards a readout unit composed of an electronic amplifier and an analog-to-digital converter, which outputs a number of counts. If we use the electron multiplication (EM) technique, the electrons pass through a gain region where they are multiplied by a large factor (10 to 1000) before going to the readout unit.

Depending on the readout rate of the camera (0.08 to 17 MHz) and the amplifier settings, the number of counts per electron given by the readout unit will vary. We always use the fastest readout rate, such that a cropped region of 100×100 pixels (large enough to cover the full extent of typical atomic arrays) is read in ~ 0.5 ms and we can quickly use the image for atom assembly. For our settings, the conversion is

16.87 electrons per counts.

The number of counts lies above a baseline level of 450 counts, simply measured with the camera shutter off (this level changes from camera to camera). On top of this baseline, there is a background signal, caused by the cooling beams. While these beams are not directed towards the camera, it appears that they are clipped, possibly by the aspheric lens holder, and reflected in arbitrary directions. These reflected photons, being at the same wavelength than the fluorescence photons, are not rejected by the interference filter placed in front of the EMCCD.

Noise sources The noise on the number of counts, observed in Fig. A.1, has two main origins: it can already be present in the number of photons incoming on the camera (photon shot-noise), or come from the conversion process in the camera. A detailed modeling of all known sources have been reported by Alberti *et al.* [2016] and I briefly review them here:

- The photon shot noise of the atomic fluorescence signal σ_{SN}, affecting the 'high' signal. It is equal to the square root of the signal height ($\sigma_{\mathrm{SN}} = \sqrt{S_H - S_L} \propto \sqrt{\tau}$). Ultimately, the photon shot noise will limit the minimal exposure time.

- The photon shot noise of the background signal σ_{SNbg}. It affect both the 'low' and 'high' signal.

- The CCD dark current noise, which is reduced to a negligible level (1.3×10^{-4} electrons per second) by cooling the CCD chip to $-80°$ C.

- The clock-induced charge noise due to electrons generated when moving the charges from the CCD chip to the read-out unit. It is quoted at a level of 10^{-3} event per pixel in the camera specifications and should be negligible here.

- The electronic noise σ_{read} of the read-out unit (output amplifier and electron counter), which is the dominating source of noise in cameras. It depends on the readout rate: 220 electrons per pixel at 17 MHz, $14\,\mathrm{e}^-$ at 3 MHz and $4\,\mathrm{e}^-$ at 0.08 MHz (from the camera performance sheet). It can be reduced relatively to the signal by using the electron multiplication (EM) technique, which increases the signal by a large factor before introducing the σ_{read} noise. Nevertheless, the EM technique comes with its own source of noise:

- The EM noise caused by the stochastic nature of the gain process. In practice, it increases by a factor ~ 1.4 all previous source of noises (mainly the photon shot

noise). For this reason, using the EM mode improves the SNR only in low-light applications when $N_{\text{photon}} \ll \sigma^2_{\text{read}}$. We are in this regime as we use the fastest and noisest readout rate, and aim for low exposure time.

We first measure the readout noise when the camera shutter is off and obtain $\sigma_{\text{read}} = 14$ counts (220 electrons according to the ADC sensitivity), as specified in our camera performance sheet. Then, we measure the background level and its associated shot noise by shining only the molasses beam without any atom. By chasing any uncontrolled reflections of these beams, and decreasing their diameter until it destabilizes the MOT operation, we could bring the background to 135 counts (and the associated shot-noise to $\sigma_{\text{SNbg}} = \sqrt{135}$). The total rms deviation of the 'low' signal is measured at $\sigma_L = 21.1$, and is in excellent agreement with our noise budget: $\sigma_L = \sqrt{(1.4\sigma_{\text{SNbg}})^2 + \sigma^2_{\text{read}}} \simeq 21.5$. The same estimation for the 'high' part, taking into account the total shot noise (background and atomic fluorescence) gives $\sigma_H^{\text{th}} = 38$ counts, while the measured noise is slightly higher ($\sigma_H^{\text{exp}} = 48$), which could from additional fluctuations in the fluorescence process.

Conclusion Already, with the previously quoted values, we could decrease the exposure time to 20 ms. It allowed us to minimize the probability to lose an atom during the imaging, to push the cycling rate of 2D experiments (only one plane to image) up to 3 Hz (now mainly limited by the loading time), or to perform 3D experiments with many planes. Further improvements would require a complete cancellation of the background signal to reach the minimal noise floor $\sigma_L = \sigma_{\text{read}}$.

In a previous work in our group, Fuhrmanek *et al.* [2011] imaged an atom using a single laser beam to excite the fluorescence, which could be useful to minimize the background light. Martinez-Dorantes *et al.* [2017] reported similar results in an optical lattice and also performed a detailed experimental and theoretical analysis of the heating-induced losses during the measurement [Martinez-Dorantes *et al.*, 2018]. Finally, I mention here the promising results obtained by Bergschneider *et al.* [2018]. They established an ultra-fast ($20\,\mu$s) *free space* imaging technique of ^{6}Li atoms with a $4\,\mu$m resolution, limited by the atom displacement; despite leading to the loss of the atom, prohibitive for our system where we need to image the atom before doing the experiment (for assembly), this technique shows that enough photons can be collected in far less than 1 ms.

Bibliography

AA Opto Electronics, *"Acousto-optic deflectors DTSXY-400-850,"* [cited in page 47].

Affleck, I., Kennedy, T., Lieb, E. H., and Tasaki, H., *"Rigorous results on valence-bond ground states in antiferromagnets,"* Physical Review Letters **59**, 799 (1987) [cited in page 196].

Akerman, N., Navon, N., Kotler, S., Glickman, Y., and Ozeri, R., *"Universal gate-set for trapped-ion qubits using a narrow linewidth diode laser,"* New Journal of Physics **17**, 113060 (2015) [cited in page 107].

Alberti, A., Robens, C., Alt, W., Brakhane, S., Karski, M., Reimann, R., Widera, A., and Meschede, D., *"Super-resolution microscopy of single atoms in optical lattices,"* New Journal of Physics **18**, 053010 (2016) [cited in page 203].

Anderson, W. R., Veale, J. R., and Gallagher, T. F., *"Resonant dipole-dipole energy transfer in a nearly frozen Rydberg gas,"* Physical Review Letters **80**, 249 (1998) [cited in page 139].

Andor, *"iXon Ultra 897 hardware user guide,"* [cited in pages 21 and 202].

Arduino, *"Arduino Due microcontroller board,"* [cited in page 49].

Asbóth, J. K., Oroszlány, L., and Pályi, A., A Short Course on Topological Insulators (Springer, Cham, 2016) [cited in page 171].

Ashkin, A., Dziedzic, J. M., Bjorkholm, J. E., and Chu, S., *"Observation of a single-beam gradient force optical trap for dielectric particles,"* Optics Letters **11**, 288 (1986) [cited in page 7].

Aspect, A., *"Closing the door on Einstein and Bohr's quantum debate,"* Physics, **8** (2015) [cited in page 7].

Aspect, A., Grangier, P., and Roger, G., *"Experimental realization of Einstein-Podolsky-Rosen-Bohm gedankenexperiment: A new violation of Bell's inequalities,"* Physical Review Letters **49**, 91 (1982) [cited in page 7].

Atala, M., Aidelsburger, M., Barreiro, J. T., Abanin, D., Kitagawa, T., Demler, E., and Bloch, I., *"Direct measurement of the Zak phase in topological Bloch bands,"* Nature Physics **9**, 795 (2013) [cited in pages 169 and 173].

Ates, C. and Lesanovsky, I., *"Entropic enhancement of spatial correlations in a laser-driven Rydberg gas,"* Physical Review A **86**, 013408 (2012) [cited in page 75].

Avenel *et al.*, *"Low-temperature magnetic measurements of an S=1 linear-chain Heisenberg antiferromagnet,"* Physical Review B **46**, 8655 (1992) [cited in page 167].

Bak, P. and Bruinsma, R., *"One-dimensional Ising model and the complete devil's staircase,"* Physical Review Letters **49**, 249 (1982) [cited in page 70].

Bakr, W. S., Peng, A., Tai, M. E., Ma, R., Simon, J., Gillen, J. I., Fölling, S., Pollet, L., and Greiner, M., *"Probing the superfluid–to–Mott insulator transition at the single-atom level,"* Science **329**, 547 (2010) [cited in pages 65 and 185].

Ballance, C. J., Harty, T. P., Linke, N. M., Sepiol, M. A., and Lucas, D. M., *"High-fidelity quantum logic gates using trapped-ion hyperfine qubits,"* Physical Review Letters **117**, 060504 (2016) [cited in page 86].

Bandres, M. A., Wittek, S., Harari, G., Parto, M., Ren, J., Segev, M., Christodoulides, D. N., and Khajavikhan, M., *"Topological insulator laser: Experiments,"* Science (2018), 10.1126/science.aar4005 [cited in page 167].

Barends *et al.*, *"Superconducting quantum circuits at the surface code threshold for fault tolerance,"* Nature **508**, 500 (2014) [cited in page 86].

Barredo, D., Labuhn, H., Ravets, S., Lahaye, T., Browaeys, A., and Adams, C. S., *"Coherent excitation transfer in a spin chain of three Rydberg atoms,"* Physical Review Letters **114**, 113002 (2015) [cited in pages 11, 47, 139, and 158].

Barredo, D., de Léséleuc, S., Lienhard, V., Lahaye, T., and Browaeys, A., *"An atom-by-atom assembler of defect-free arbitrary two-dimensional atomic arrays,"* Science **354**, 1021 (2016) [cited in pages 17, 47, 56, 58, and 62].

Barredo, D., Lienhard, V., de Léséleuc, S., Lahaye, T., and Browaeys, A., *"Synthetic three-dimensional atomic structures assembled atom by atom,"* Nature **561**, 79 (2018) [cited in pages 17, 44, and 47].

Barredo, D., Ravets, S., Labuhn, H., Béguin, L., Vernier, A., Nogrette, F., Lahaye, T., and Browaeys, A., *"Demonstration of a strong Rydberg blockade in three-atom systems with anisotropic interactions,"* Physical Review Letters **112**, 183002 (2014) [cited in pages 10, 114, and 133].

Béguin, L., Measurement of the van der Waals interaction between two Rydberg atoms, Ph.D. thesis, Université Paris-Saclay (2013) [cited in pages 18, 20, 121, and 202].

Béguin, L., Vernier, A., Chicireanu, R., Lahaye, T., and Browaeys, A., *"Direct Measurement of the van der Waals Interaction between Two Rydberg Atoms,"* Physical Review Letters **110**, 263201 (2013) [cited in page 120].

Bergamini, S., Darquié, B., Jones, M., Jacubowiez, L., Browaeys, A., and Grangier, P., *"Holographic generation of microtrap arrays for single atoms by use of a programmable phase modulator,"* J. Opt. Soc. Am. B **21**, 1889 (2004) [cited in pages 20 and 29].

Bergschneider, A., Klinkhamer, V. M., Becher, J. H., Klemt, R., Zürn, G., Preiss, P. M., and Jochim, S., *"Spin-resolved single-atom imaging of* ^{6}Li *in free space,"* Physical Review A **97**, 063613 (2018) [cited in page 204].

Bernien, H., Schwartz, S., Keesling, A., Levine, H., Omran, A., Pichler, H., Choi, S., Zibrov, A. S., Endres, M., Greiner, M., Vuletić, V., and Lukin, M. D., *"Probing many-body dynamics on a 51-atom quantum simulator,"* Nature **551**, 579 (2017) [cited in pages 11, 72, 77, 78, 86, 95, 101, and 110].

Beterov, I. I., Ryabtsev, I. I., Tretyakov, D. B., and Entin, V. M., *"Quasiclassical calculations of blackbody-radiation-induced depopulation rates and effective lifetimes of Rydberg nS, nP, and nD alkali-metal atoms with* $n \leq 80$*,"* Physical Review A **79**, 052504 (2009) [cited in pages 98 and 108].

Beterov, I. I., Saffman, M., Yakshina, E. A., Zhukov, V. P., Tretyakov, D. B., Entin, V. M., Ryabtsev, I. I., Mansell, C. W., MacCormick, C., Bergamini, S., and Fedoruk, M. P., *"Quantum gates in mesoscopic atomic ensembles based on adiabatic passage and Rydberg blockade,"* Physical Review A **88**, 010303 (2013) [cited in page 143].

Beterov, I. I., Tretyakov, D. B., Entin, V. M., Yakshina, E. a., Ryabtsev, I. I., MacCormick, C., and Bergamini, S., *"Deterministic single-atom excitation via*

adiabatic passage and Rydberg blockade," Physical Review A **84**, 1 (2011) [cited in page 143].

Bettelli, S., Maxwell, D., Fernholz, T., Adams, C. S., Lesanovsky, I., and Ates, C., *"Exciton dynamics in emergent Rydberg lattices,"* Physical Review A **88**, 043436 (2013) [cited in page 139].

Beugnon, J. and Navon, N., *"Exploring the Kibble–Zurek mechanism with homogeneous bose gases,"* Journal of Physics B **50**, 022002 (2017) [cited in page 84].

Beugnon, J., Tuchendler, C., Marion, H., Gaetan, A., Miroshnychenko, Y., Sortais, Y., Lance, A., Jones, M., Messin, G., Browaeys, A., and Grangier, P., *"Two-dimensional transport and transfer of a single atomic qubit in optical tweezers,"* Nature Physics **3**, 4 (2007) [cited in page 46].

van Bijnen, R. M. W., Smit, S., van Leeuwen, K. A. H., Vredenbregt, E. J. D., and Kokkelmans, S. J. J. M. F., *"Adiabatic formation of Rydberg crystals with chirped laser pulses,"* Journal of Physics B **44**, 184008 (2011) [cited in page 72].

Blatt, R. and Roos, C., *"Quantum simulations with trapped ions,"* Nature Physics **8**, 277 (2012) [cited in page 9].

Bloch, F., *"The principle of nuclear induction,"* Science **118**, 425 (1953) [cited in page 8].

Blundell, S., Magnetism in Condensed Matter, Oxford Master Series in Condensed Matter Physics (OUP Oxford, 2001) [cited in page 8].

Bohn, J. L., Rey, A. M., and Ye, J., *"Cold molecules: Progress in quantum engineering of chemistry and quantum matter,"* Science **357**, 1002 (2017) [cited in page 138].

Bramwell, S. T. and Gingras, M. J. P., *"Spin ice state in frustrated magnetic pyrochlore materials,"* Science **294**, 1495 (2001) [cited in page 61].

Browaeys, A., Barredo, D., and Lahaye, T., *"Experimental investigations of dipole–dipole interactions between a few Rydberg atoms,"* Journal of Physics B **49**, 152001 (2016) [cited in page 10].

Buonsante, P. and Vezzani, A., *"Phase diagram for ultracold bosons in optical lattices and superlattices,"* Physical Review A **70**, 033608 (2004) [cited in page 185].

Cano, D. and Fortágh, J., *"Nonadditive potentials between three Rydberg atoms,"* Physical Review A **86**, 043422 (2012) [cited in page 114].

Castro Neto, A. H., Guinea, F., Peres, N. M. R., Novoselov, K. S., and Geim, A. K., *"The electronic properties of graphene,"* Review of Modern Physics **81**, 109 (2009) [cited in page 61].

Chaunsali, R., Kim, E., Thakkar, A., Kevrekidis, P. G., and Yang, J., *"Demonstrating an in situ topological band transition in cylindrical granular chains,"* Physical Review Letters **119**, 024301 (2017) [cited in pages 167, 169, and 173].

Chen, X., Gu, Z.-C., Liu, Z.-X., and Wen, X.-G., *"Symmetry-protected topological orders in interacting bosonic systems,"* Science **338**, 1604 (2012) [cited in pages 167 and 196].

Chen, X., Gu, Z.-C., Liu, Z.-X., and Wen, X.-G., *"Symmetry protected topological orders and the group cohomology of their symmetry group,"* Physical Review B **87**, 155114 (2013) [cited in pages 167 and 196].

Cheneau, M., Barmettler, P., Poletti, D., Endres, M., Schauß, P., Fukuhara, T., Gross, C., Bloch, I., Kollath, C., and Kuhr, S., *"Light-cone-like spreading of correlations in a quantum many-body system,"* Nature **484**, 484 (2014) [cited in page 9].

Chiu, C.-K., Teo, J. C. Y., Schnyder, A. P., and Ryu, S., *"Classification of topological quantum matter with symmetries,"* Review of Modern Physics **88**, 035005 (2016) [cited in pages 166 and 172].

Choi, J.-Y., Hild, S., Zeiher, J., Schauss, P., Rubio-Abadal, A., Yefsah, T., Khemani, V., Huse, D. A., Bloch, I., and Gross, C., *"Exploring the many-body localization transition in two dimensions,"* Science **352**, 1547 (2016) [cited in pages 9 and 164].

Chow, J. M., Gambetta, J. M., Córcoles, A. D., Merkel, S. T., Smolin, J. A., Rigetti, C., Poletto, S., Keefe, G. A., Rothwell, M. B., Rozen, J. R., Ketchen, M. B., and Steffen, M., *"Universal quantum gate set approaching fault-tolerant thresholds with superconducting qubits,"* Physical Review Letters **109**, 060501 (2012) [cited in page 86].

Cladé, P., Oscillations de Bloch d'atomes ultrafroids et mesure de la constante de structure fine, Ph.D. thesis, Université Paris 6 (2004) [cited in page 106].

Cooper, N. R., Dalibard, J., and Spielman, I. B., *"Topological bands for ultracold atoms,"* arXiv:1803.00249 (2018) [cited in pages 167 and 171].

Cubel, T., Teo, B. K., Malinovsky, V. S., Guest, J. R., Reinhard, A., Knuffman, B., Berman, P. R., and Raithel, G., *"Coherent population transfer of ground-state atoms into Rydberg states,"* Physical Review A **72**, 023405 (2005) [cited in page 141].

Dalmonte, M., Mirzaei, S. I., Muppalla, P. R., Marcos, D., Zoller, P., and Kirchmair, G., *"Realizing dipolar spin models with arrays of superconducting qubits,"* Physical Review B **92**, 174507 (2015) [cited in page 138].

Dehmelt, H., *"Experiments with an isolated subatomic particle at rest,"* Review of Modern Physics **62**, 525 (1990) [cited in page 7].

Deiglmayr, J., Reetz-Lamour, M., Amthor, T., Westermann, S., de Oliveira, A., and Weidemüller, M., *"Coherent excitation of Rydberg atoms in an ultracold gas,"* Optics Communications **264**, 293 (2006) [cited in pages 86 and 141].

Deng, X. L., Porras, D., and Cirac, J. I., *"Effective spin quantum phases in systems of trapped ions,"* Physical Review A **72**, 1 (2005) [cited in page 138].

Derevianko, A., Kómár, P., Topcu, T., Kroeze, R. M., and Lukin, M. D., *"Effects of molecular resonances on Rydberg blockade,"* Physical Review A **92**, 063419 (2015) [cited in page 114].

Deutsch, J. M., *"Quantum statistical mechanics in a closed system,"* Physical Review A **43**, 2046 (1991) [cited in page 74].

Di Leonardo, R., Ianni, F., and Ruocco, G., *"Computer generation of optimal holograms for optical trap arrays,"* Optics Express **15**, 1913 (2007) [cited in pages 21, 29, and 33].

Di Liberto, M., Recati, A., Carusotto, I., and Menotti, C., *"Two-body physics in the Su-Schrieffer-Heeger model,"* Physical Review A **94**, 062704 (2016) [cited in page 185].

van Ditzhuijzen, C. S. E., Koenderink, A. F., Hernández, J. V., Robicheaux, F., Noordam, L. D., and van den Heuvell, H. B. v. L., *"Spatially resolved observation of dipole-dipole interaction between Rydberg atoms,"* Physical Review Letters **100**, 243201 (2008) [cited in page 139].

Dorner, U., Calarco, T., Zoller, P., Browaeys, A., and Grangier, P., *"Quantum logic via optimal control in holographic dipole traps,"* Journal of Optics B **7**, 341 (2005) [cited in page 46].

Dudin, Y. O., Li, L., Bariani, F., and Kuzmich, A., *"Observation of coherent many-body rabi oscillations,"* Nature Physics **8**, 790 (2012) [cited in page 86].

Dumke, R., Volk, M., Müther, T., Buchkremer, F. B., Birkl, G., and Ertmer, W., *"Micro-optical realization of arrays of selectively addressable dipole traps: A scalable configuration for quantum computation with atomic qubits,"* Physical Review Letters **89**, 3 (2002) [cited in page 29].

Ebert, M., Gill, A., Gibbons, M., Zhang, X., Saffman, M., and Walker, T. G., *"Atomic Fock state preparation using Rydberg blockade,"* Physical Review Letters **112**, 043602 (2014) [cited in page 45].

Ebert, M., Kwon, M., Walker, T. G., and Saffman, M., *"Coherence and Rydberg blockade of atomic ensemble qubits,"* Physical Review Letters **115**, 093601 (2015) [cited in page 86].

Endres, M., Bernien, H., Keesling, A., Levine, H., Anschuetz, E. R., Krajenbrink, A., Senko, C., Vuletic, V., Greiner, M., and Lukin, M. D., *"Atom-by-atom assembly of defect-free one-dimensional cold atom arrays,"* Science **354**, 1024 (2016) [cited in pages 47 and 62].

Fuhrmanek, A., From single to many atoms in a microscopic optical dipole trap, Ph.D. thesis, Université Paris Sud - Parisfleach XI (2011) [cited in page 20].

Fuhrmanek, A., Bourgain, R., Sortais, Y. R. P., and Browaeys, A., *"Free-space lossless state detection of a single trapped atom,"* Physical Review Letters **106**, 133003 (2011) [cited in pages 23 and 204].

Fuhrmanek, A., Bourgain, R., Sortais, Y. R. P., and Browaeys, A., *"Light-assisted collisions between a few cold atoms in a microscopic dipole trap,"* Physical Review A **85**, 1 (2012) [cited in page 19].

Gaëtan, A., Miroshnychenko, Y., Wilk, T., Chotia, A., Viteau, M., Comparat, D., Pillet, P., Browaeys, A., and Grangier, P., *"Observation of collective excitation of two individual atoms in the Rydberg blockade regime,"* Nature Physics **5**, 115 (2009) [cited in pages 10, 120, and 125].

Galitski, V., *"Fermionization transform for certain higher-dimensional quantum spin models,"* Physical Review B **82**, 060411 (2010) [cited in page 138].

Gallagher, T. F., Rydberg Atoms (Cambridge University Press, 1994) [cited in page 98].

Georgescu, I. M., Ashhab, S., and Nori, F., *"Quantum simulation,"* Review of Modern Physics **86**, 153 (2014) [cited in page 7].

Gerchberg, R. W. and Saxton, W. O., *"A practical algorithm for the determination of the phase from image and diffraction plane pictures,"* Optiik **35**, 237 (1972) [cited in page 29].

Giamarchi, T., Quantum Physics in One Dimension (Oxford University Press, 2003) [cited in pages 138 and 189].

Gibbons, M. J., Hamley, C. D., Shih, C.-Y., and Chapman, M. S., *"Nondestructive fluorescent state detection of single neutral atom qubits,"* Physical Review Letters **106**, 133002 (2011) [cited in page 23].

Glarum, S. H., Geschwind, S., Lee, K. M., Kaplan, M. L., and Michel, J., *"Observation of fractional spin S=1/2 on open ends of S=1 linear antiferromagnetic chains: Nonmagnetic doping,"* Physical Review Letters **67**, 1614 (1991) [cited in page 167].

Gomez, E., Aubin, S., Orozco, L. A., and Sprouse, G. D., *"Lifetime and hyperfine splitting measurements on the 7s and 6p levels in rubidium,"* J. Opt. Soc. Am. B **21**, 2058 (2004) [cited in page 154].

Greiner, M., Mandel, O., Esslinger, T., Hänsch, T. W., and Bloch, I., *"Quantum phase transition from a superfluid to a Mott insulator in a gas of ultracold atoms,"* Nature **415**, 39 (2012) [cited in pages 12 and 64].

Grimm, R., Weidemüller, M., and Ovchinnikov, Y. B., *"Optical dipole traps for neutral atoms,"* (Academic Press, 2000) [cited in page 19].

Gross, C. and Bloch, I., *"Quantum simulations with ultracold atoms in optical lattices,"* Science **357**, 995 (2017) [cited in page 9].

Grünzweig, T., Hilliard, a., McGovern, M., and Andersen, M. F., *"Near-deterministic preparation of a single atom in an optical microtrap,"* Nature Physics **6**, 951 (2010) [cited in pages 45 and 57].

Grusdt, F., Höning, M., and Fleischhauer, M., *"Topological edge states in the one-dimensional superlattice Bose-Hubbard model,"* Physical Review Letters **110**, 260405 (2013) [cited in page 185].

Guardado-Sanchez, E., Brown, P. T., Mitra, D., Devakul, T., Huse, D. A., Schauß, P., and Bakr, W. S., *"Probing the quench dynamics of antiferromagnetic correlations in a 2D quantum Ising spin system,"* Physical Review X **8**, 021069 (2018) [cited in pages 72, 78, 83, and 86].

Günter, G., Schempp, H., Robert-de Saint-Vincent, M., Gavryusev, V., Helmrich, S., Hofmann, C. S., Whitlock, S., and Weidemüller, M., *"Observing the dynamics of dipole-mediated energy transport by interaction-enhanced imaging,"* Science **342**, 954 (2013) [cited in page 139].

Hagiwara, M., Katsumata, K., Affleck, I., Halperin, B. I., and Renard, J. P., *"Observation of S=1/2 degrees of freedom in an S=1 linear-chain Heisenberg antiferromagnet,"* Physical Review Letters **65**, 3181 (1990) [cited in page 167].

Hald, J. and Ruseva, V., *"Efficient suppression of diode-laser phase noise by optical filtering,"* J. Opt. Soc. Am. B **22**, 2338 (2005) [cited in page 107].

Haldane, F. D. M., *"Continuum dynamics of the 1-d Heisenberg antiferromagnet: Identification with the O(3) nonlinear sigma model,"* Physics Letters A **93**, 464 (1983a) [cited in page 167].

Haldane, F. D. M., *"Nonlinear field theory of large-spin Heisenberg antiferromagnets: Semiclassically quantized solitons of the one-dimensional easy-axis Néel state,"* Physical Review Letters **50**, 1153 (1983b) [cited in page 196].

Hamamatsu, *"LCOS-SLM X10468-02,"* [cited in page 30].

Han, J., Jamil, Y., Norum, D. V. L., Tanner, P. J., and Gallagher, T. F., *"Rb nf quantum defects from millimeter-wave spectroscopy of cold* ^{85}Rb *Rydberg atoms,"* Physical Review A **74**, 054502 (2006) [cited in page 116].

Hankin, A. M., Jau, Y.-Y., Parazzoli, L. P., Chou, C. W., Armstrong, D. J., Landahl, A. J., and Biedermann, G. W., *"Two-atom Rydberg blockade using direct 6s to np excitation,"* Physical Review A **89**, 033416 (2014) [cited in pages 86 and 103].

Haroche, S., *"Nobel lecture: Controlling photons in a box and exploring the quantum to classical boundary,"* Review of Modern Physics **85**, 1083 (2013) [cited in page 7].

Hasan, M. Z. and Kane, C. L., *"Colloquium: Topological insulators,"* Review of Modern Physics **82**, 3045 (2010) [cited in page 166].

Hauke, P., Cucchietti, F. M., Müller-Hermes, A., Bañuls, M. C., Cirac, J. I., and Lewenstein, M., *"Complete devil's staircase and crystal-superfluid transitions in a dipolar XXZ spin chain: A trapped ion quantum simulation,"* New Journal of Physics **12**, 113037 (2010) [cited in page 200].

Heeger, A. J., Kivelson, S., Schrieffer, J. R., and Su, W. P., *"Solitons in conducting polymers,"* Review of Modern Physics **60**, 781 (1988) [cited in page 168].

Heidemann, R., Raitzsch, U., Bendkowsky, V., Butscher, B., Löw, R., Santos, L., and Pfau, T., *"Evidence for coherent collective Rydberg excitation in the strong blockade regime,"* Physical Review Letters **99**, 163601 (2007) [cited in page 70].

Higgins, G., Pokorny, F., Zhang, C., Bodart, Q., and Hennrich, M., *"Coherent control of a single trapped Rydberg ion,"* Physical Review Letters **119**, 220501 (2017) [cited in page 141].

Hsieh, D., Qian, D., Wray, L., Xia, Y., Hor, Y. S., Cava, R. J., and Hasan, M. Z., *"A topological Dirac insulator in a quantum spin Hall phase,"* Nature **452**, 970 (2008) [cited in page 166].

Imaging Source, *"33 series - USB 3.0 monochrome industrial cameras,"* [cited in page 34].

Isenhower, L., Urban, E., Zhang, X. L., Gill, A. T., Henage, T., Johnson, T. A., Walker, T. G., and Saffman, M., *"Demonstration of a Neutral Atom Controlled-NOT Quantum Gate,"* Physical Review Letters **104**, 010503 (2010) [cited in page 10].

Ising, E., *"Contribution to the Theory of Ferromagnetism,"* Z. Phys. **31**, 253 (1925) [cited in page 8].

Islam, R., Senko, C., Campbell, W. C., Korenblit, S., Smith, J., Lee, A., Edwards, E. E., Wang, C.-C. J., Freericks, J. K., and Monroe, C., *"Emergence and frustration of magnetism with variable-range interactions in a quantum simulator,"* Science **340**, 583 (2013) [cited in page 83].

Jaksch, D., Briegel, H.-J., Cirac, J. I., Gardiner, C. W., and Zoller, P., *"Entanglement of atoms via cold controlled collisions,"* Physical Review Letters **82**, 1975 (1999) [cited in page 65].

Jaksch, D., Cirac, J. I., Zoller, P., Rolston, S. L., Côté, R., and Lukin, M. D., *"Fast Quantum Gates for Neutral Atoms,"* Physical Review Letters **85**, 2208 (2000) [cited in pages 10 and 79].

Jau, Y.-Y., Hankin, A. M., Keating, T., Deutsch, I. H., and Biedermann, G. W., *"Entangling atomic spins with a strong Rydberg-dressed interaction,"* Nature Physics **12**, 71 (2016) [cited in pages 86 and 134].

Johnson, T. A., Urban, E., Henage, T., Isenhower, L., Yavuz, D. D., Walker, T. G., and Saffman, M., *"Rabi Oscillations between Ground and Rydberg States with Dipole-Dipole Atomic Interactions,"* Physical Review Letters **100**, 113003 (2008) [cited in page 86].

Jurcevic, P., Lanyon, B. P., Hauke, P., Hempel, C., Zoller, P., Blatt, R., and Roos, C. F., *"Quasiparticle engineering and entanglement propagation in a quantum many-body system,"* Nature **511**, 202 (2014) [cited in page 9].

Kane, C. L. and Mele, E. J., *"Quantum spin Hall effect in graphene,"* Physical Review Letters **95**, 226801 (2005a) [cited in page 166].

Kane, C. L. and Mele, E. J., *"Z_2 topological order and the quantum spin Hall effect,"* Physical Review Letters **95**, 146802 (2005b) [cited in page 166].

Kaufman, A. M., Lester, B. J., Foss-Feig, M., Wall, M. L., Rey, A. M., and Regal, C. A., *"Entangling two transportable neutral atoms via local spin exchange,"* Nature **527**, 208 (2012) [cited in page 65].

Kaufman, A. M., Lester, B. J., and Regal, C. A., *"Cooling a single atom in an optical tweezer to its quantum ground state,"* Physical Review X **2**, 041014 (2012) [cited in pages 28, 65, 101, and 200].

Kaufman, A. M., Tai, M. E., Lukin, A., Rispoli, M., Schittko, R., Preiss, P. M., and Greiner, M., *"Quantum thermalization through entanglement in an isolated many-body system,"* Science **353**, 794 (2016) [cited in page 9].

Keesling *et al.*, *"Probing quantum critical dynamics on a programmable Rydbreg simulator,"* arXiv:1809.05540 (2018) [cited in pages 72 and 78].

Kim, H., Lee, W., Lee, H., Jo, H., Song, Y., and Ahn, J., *"In situ single-atom array synthesis using dynamic holographic optical tweezers,"* Nature Communications **7**, 13317 (2016) [cited in pages 47 and 63].

Kim, H., Park, Y., Kim, K., Sim, H.-S., and Ahn, J., *"Detailed balance of thermalization dynamics in Rydberg-atom quantum simulators,"* Physical Review Letters **120**, 180502 (2018) [cited in pages 11, 63, 72, 86, and 101].

King, A. *et al.*, *"Observation of topological phenomena in a programmable lattice of 1,800 qubits,"* Nature **560**, 460 (2018) [cited in page 9].

Kitaev, A., *"Periodic table for topological insulators and superconductors,"* AIP Conference Proceedings **1134**, 22 (2009) [cited in page 166].

Klitzing, K. v., Dorda, G., and Pepper, M., *"New method for high-accuracy determination of the fine-structure constant based on quantized Hall resistance,"* Physical Review Letters **45**, 494 (1980) [cited in page 166].

Klöckner, A., Pinto, N., Lee, Y., Catanzaro, B., Ivanov, P., and Fasih, A., *"PyCUDA and PyOpenCL: A scripting-based approach to GPU run-time code generation,"* Parallel Computing **38**, 157 (2012) [cited in page 34].

Kómár, P., Topcu, T., Kessler, E. M., Derevianko, A., Vuletić, V., Ye, J., and Lukin, M. D., *"Quantum network of atom clocks: A possible implementation with neutral atoms,"* Physical Review Letters **117**, 060506 (2016) [cited in page 65].

König, M., Wiedmann, S., Brüne, C., Roth, A., Buhmann, H., Molenkamp, L. W., Qi, X.-L., and Zhang, S.-C., *"Quantum spin Hall insulator state in HgTe quantum wells,"* Science **318**, 766 (2007) [cited in page 166].

Kumar, A., Wu, T.-Y., Mejia, F. G., and Weiss, D. S., *"Sorting ultracold atoms in a three-dimensional optical lattice in a realization of Maxwell's demon,"* Nature **561**, 83 (2018) [cited in pages 47 and 64].

Kwon, M., Ebert, M. F., Walker, T. G., and Saffman, M., *"Parallel low-loss measurement of multiple atomic qubits,"* Physical Review Letters **119**, 180504 (2017) [cited in pages 23 and 200].

Labuhn, H., Rydberg excitation dynamics and correlations in arbitrary 2D arrays of single atoms, Ph.D. thesis, Université Paris-Saclay (2016) [cited in pages 20, 21, 29, 30, 32, 33, 37, 47, and 73].

Labuhn, H., Barredo, D., Ravets, S., de Léséleuc, S., Macrì, T., Lahaye, T., and Browaeys, A., *"Tunable two-dimensional arrays of single Rydberg atoms for realizing*

quantum Ising models," Nature **534**, 667 (2016) [cited in pages 10, 11, 13, 44, 45, 72, 73, 77, 85, 86, 114, 115, 125, 126, 132, and 134].

Labuhn, H., Ravets, S., Barredo, D., Béguin, L., Nogrette, F., Lahaye, T., and Browaeys, A., *"Single-atom addressing in microtraps for quantum-state engineering using Rydberg atoms,"* Physical Review A **90**, 023415 (2014) [cited in pages 46 and 47].

Lacki, M., Pichler, H., Sterdyniak, A., Lyras, A., Lembessis, V. E., Al-Dossary, O., Budich, J. C., and Zoller, P., *"Quantum hall physics with cold atoms in cylindrical optical lattices,"* Physical Review A **93**, 013604 (2016) [cited in page 61].

Leach, J., Sinclair, G., Jordan, P., Courtial, J., Padgett, M., Cooper, J., and J. Laczik, Z., *"3d manipulation of particles into crystal structures using holographic optical tweezers,"* Optics Express **12**, 220 (2004) [cited in page 21].

Lee, W., Kim, H., and Ahn, J., *"Three-dimensional rearrangement of single atoms using actively controlled optical microtraps,"* Optics Express **24**, 9816 (2016) [cited in pages 47 and 63].

Lee, W., Kim, H., and Ahn, J., *"Defect-free atomic array formation using the Hungarian matching algorithm,"* Physical Review A **95**, 053424 (2017) [cited in page 63].

de Léséleuc, S., Barredo, D., Lienhard, V., Browaeys, A., and Lahaye, T., *"Optical control of the resonant dipole-dipole interaction between Rydberg atoms,"* Physical Review Letters **119**, 053202 (2017) [cited in pages 139 and 155].

de Léséleuc, S., Barredo, D., Lienhard, V., Browaeys, A., and Lahaye, T., *"Analysis of imperfections in the coherent optical excitation of single atoms to Rydberg states,"* Physical Review A **97**, 053803 (2018a) [cited in page 87].

de Léséleuc, S., Weber, S., Lienhard, V., Barredo, D., Büchler, H. P., Lahaye, T., and Browaeys, A., *"Accurate mapping of multilevel Rydberg atoms on interacting spin-1/2 particles for the quantum simulation of Ising models,"* Physical Review Letters **120**, 113602 (2018b) [cited in page 116].

Lester, B. J., Luick, N., Kaufman, A. M., Reynolds, C. M., and Regal, C. A., *"Rapid production of uniformly filled arrays of neutral atoms,"* Physical Review Letters **115**, 1 (2015) [cited in pages 45 and 57].

Levine, H., Keesling, A., Omran, A., Bernien, H., Schwartz, S., Zibrov, A. S., Endres, M., Greiner, M., Vuletić, V., and Lukin, M. D., *"High-fidelity control and entanglement of Rydberg-atom qubits,"* Physical Review Letters **121**, 123603 (2018) [cited in pages 86, 103, 105, 108, 110, and 111].

Li, L., Dudin, Y. O., and Kuzmich, A., *"Entanglement between light and an optical atomic excitation,"* Nature **498**, 466 (2013) [cited in page 152].

Li, W., Mourachko, I., Noel, M. W., and Gallagher, T. F., *"Millimeter-wave spectroscopy of cold Rb Rydberg atoms in a magneto-optical trap: Quantum defects of the ns, np, and nd series,"* Physical Review A **67**, 052502 (2003) [cited in pages 116 and 117].

Li, X., Corcovilos, T. A., Wang, Y., and Weiss, D. S., *"3D projection sideband cooling,"* Physical Review Letters **108**, 103001 (2012) [cited in page 64].

Lieb, E. H. and Robinson, D. W., *"The finite group velocity of quantum spin systems,"* Communications in Mathematical Physics **28**, 251 (1972) [cited in page 84].

Lienhard, V., de Léséleuc, S., Barredo, D., Lahaye, T., Browaeys, A., Schuler, M., Henry, L.-P., and Läuchli, A. M., *"Observing the space- and time-dependent growth of correlations in dynamically tuned synthetic Ising models with antiferromagnetic interactions,"* Physical Review X **8**, 021070 (2018) [cited in pages 44, 72, 73, 77, 78, 80, 82, 85, and 86].

Liu, L. R., Hood, J. D., Yu, Y., Zhang, J. T., Hutzler, N. R., Rosenband, T., and Ni, K.-K., *"Building one molecule from a reservoir of two atoms,"* Science **360**, 900 (2018) [cited in page 65].

Löw, R., Weimer, H., Krohn, U., Heidemann, R., Bendkowsky, V., Butscher, B., Büchler, H. P., and Pfau, T., *"Universal scaling in a strongly interacting Rydberg gas,"* Physical Review A **80**, 033422 (2009) [cited in page 71].

Löw, R., Weimer, H., Nipper, J., Balewski, J. B., Butscher, B., Büchler, H. P., and Pfau, T., *"An experimental and theoretical guide to strongly interacting Rydberg gases,"* Journal of Physics B **45**, 113001 (2012) [cited in pages 88, 99, and 111].

Ludlow, A. D., Boyd, M. M., Ye, J., Peik, E., and Schmidt, P. O., *"Optical atomic clocks,"* Review of Modern Physics **87**, 637 (2015) [cited in page 104].

Ludwig, A. W. W., *"Topological phases: classification of topological insulators and superconductors of non-interacting fermions, and beyond,"* Physica Scripta **2016**, 014001 (2016) [cited in page 166].

Lukin, M. D., Fleischhauer, M., Cote, R., Duan, L. M., Jaksch, D., Cirac, J. I., and Zoller, P., *"Dipole blockade and quantum information processing in mesoscopic atomic ensembles,"* Physical Review Letters **87**, 037901 (2001) [cited in pages 10 and 79].

Lundblad, N., *"Designer atom arrays for quantum computing,"* Nature **561**, 43 (2018) [cited in page 197].

Maller, K. M., Lichtman, M. T., Xia, T., Sun, Y., Piotrowicz, M. J., Carr, A. W., Isenhower, L., and Saffman, M., *"Rydberg-blockade controlled-NOT gate and entanglement in a two-dimensional array of neutral-atom qubits,"* Physical Review A **92**, 022336 (2015) [cited in pages 86 and 101].

Marcuzzi, M., Minář, J., Barredo, D., de Léséleuc, S., Labuhn, H., Lahaye, T., Browaeys, A., Levi, E., and Lesanovsky, I., *"Facilitation Dynamics and Localization Phenomena in Rydberg Lattice Gases with Position Disorder,"* Physical Review Letters **118**, 1 (2017) [cited in pages 45 and 47].

Martin, M., Quantum Metrology and Many-Body Physics: Pushing the Frontier of the Optical Lattice Clock, Ph.D. thesis, University of Colorado (2013) [cited in page 106].

Martinez-Dorantes, M., Alt, W., Gallego, J., Ghosh, S., Ratschbacher, L., and Meschede, D., *"State-dependent fluorescence of neutral atoms in optical potentials,"* Physical Review A **97**, 023410 (2018) [cited in page 204].

Martinez-Dorantes, M., Alt, W., Gallego, J., Ghosh, S., Ratschbacher, L., Völzke, Y., and Meschede, D., *"Fast nondestructive parallel readout of neutral atom registers in optical potentials,"* Physical Review Letters **119**, 180503 (2017) [cited in pages 23, 200, and 204].

Matsumoto, N., Inoue, T., Ando, T., Takiguchi, Y., Ohtake, Y., and Toyoda, H., *"High-quality generation of a multispot pattern using a spatial light modulator with adaptive feedback,"* Optics Letters **37**, 3135 (2012) [cited in page 29].

Maxwell, D., Szwer, D. J., Paredes-Barato, D., Busche, H., Pritchard, J. D., Gauguet, A., Weatherill, K. J., Jones, M. P. A., and Adams, C. S., *"Storage and control of*

optical photons using Rydberg polaritons," Physical Review Letters **110**, 103001 (2013) [cited in page 139].

Meier, E. J., An, F. A., and Gadway, B., *"Observation of the topological soliton state in the Su–Schrieffer–Heeger model,"* Nature Communications **7**, 13986 (2016) [cited in pages 169 and 173].

Miroshnychenko, Y., Alt, W., Dotsenko, I., Förster, L., Khudaverdyan, M., Meschede, D., Reick, S., and Rauschenbeutel, A., *"Inserting two atoms into a single optical micropotential,"* Physical Review Letters **97**, 243003 (2006a) [cited in page 57].

Miroshnychenko, Y., Alt, W., Dotsenko, I., Förster, L., Khudaverdyan, M., Meschede, D., Schrader, D., and Rauschenbeutel, A., *"Quantum engineering: an atom-sorting machine."* Nature **442**, 151 (2006b) [cited in page 46].

Miroshnychenko, Y., Gaëtan, A., Evellin, C., Grangier, P., Comparat, D., Pillet, P., Wilk, T., and Browaeys, A., *"Coherent excitation of a single atom to a Rydberg state,"* Physical Review A **82**, 013405 (2010) [cited in pages 86 and 102].

Møller, D., Madsen, L. B., and Mølmer, K., *"Quantum gates and multiparticle entanglement by Rydberg excitation blockade and adiabatic passage,"* Physical Review Letters **100**, 1 (2008) [cited in page 143].

Monroe, C., Meekhof, D. M., King, B. E., Jefferts, S. R., Itano, W. M., Wineland, D. J., and Gould, P., *"Resolved-sideband Raman cooling of a bound atom to the 3d zero-point energy,"* Physical Review Letters **75**, 4011 (1995) [cited in page 27].

Monz, T., Schindler, P., Barreiro, J. T., Chwalla, M., Nigg, D., Coish, W. A., Harlander, M., Hänsel, W., Hennrich, M., and Blatt, R., *"14-qubit entanglement: Creation and coherence,"* Physical Review Letters **106**, 130506 (2011) [cited in page 86].

Mourachko, I., Comparat, D., de Tomasi, F., Fioretti, A., Nosbaum, P., Akulin, V. M., and Pillet, P., *"Many-body effects in a frozen Rydberg gas,"* Physical Review Letters **80**, 253 (1998) [cited in page 139].

Müller, M., Lesanovsky, I., Weimer, H., Büchler, H. P., and Zoller, P., *"Mesoscopic Rydberg gate based on electromagnetically induced transparency,"* Physical Review Letters **102**, 170502 (2009) [cited in page 79].

Nash, L. M., Kleckner, D., Read, A., Vitelli, V., Turner, A. M., and Irvine, W. T. M., *"Topological mechanics of gyroscopic metamaterials,"* Proc. Natl. Acad. Sci. USA **112**, 14495 (2015) [cited in page 167].

Nazarova, T., Lisdat, C., Riehle, F., and Sterr, U., *"Low-frequency-noise diode laser for atom interferometry,"* J. Opt. Soc. Am. B **25**, 1632 (2008) [cited in page 107].

Néel, L., *"Propriétés magnétiques de l'état métallique et énergie d'interaction entre atomes magnétiques,"* Annales de Physique **11**, 232 (1936) [cited in page 8].

Nelson, K. D., Li, X., and Weiss, D. S., *"Imaging single atoms in a three-dimensional array,"* Nature Physics **3**, 556 (2007) [cited in pages 43 and 64].

Ningyuan, J., Owens, C., Sommer, A., Schuster, D., and Simon, J., *"Time- and site-resolved dynamics in a topological circuit,"* Physical Review X **5**, 021031 (2015) [cited in page 167].

Nogrette, F., Labuhn, H., Ravets, S., Barredo, D., Béguin, L., Vernier, A., Lahaye, T., and Browaeys, A., *"Single-atom trapping in holographic 2D arrays of microtraps with arbitrary geometries,"* Physical Review X **4**, 021034 (2014) [cited in pages 10, 20, 21, 29, 32, 33, and 46].

Ohmori, K., *"Optically engineered quantum states in ultrafast and ultracold systems,"* Foundations of Physics **44**, 813 (2014) [cited in page 200].

Optotune, *"Electrically tunable lenses,"* [cited in pages 37 and 48].

Orioli, A., Signoles, A., Wildhagen, H., Günter, G., Berges, J., Whitlock, S., and Weidemüller, M., *"Relaxation of an isolated dipolar-interacting Rydberg quantum spin system,"* Physical Review Letters **120**, 063601 (2018) [cited in page 150].

Ozawa, T., Price, H. M., Amo, A., Goldman, N., Hafezi, M., Lu, L., Rechtsman, M., Schuster, D., Simon, J., Zilberberg, O., and Carusotto, I., *"Topological photonics,"* arXiv:1802.04173 (2018) [cited in page 167].

Paul, W., *"Electromagnetic traps for charged and neutral particles,"* Review of Modern Physics **62**, 531 (1990) [cited in page 7].

Peter, D., Müller, S., Wessel, S., and Büchler, H. P., *"Anomalous behavior of spin systems with dipolar interactions,"* Physical Review Letters **109**, 1 (2012) [cited in pages 65 and 200].

Peter, D., Yao, N. Y., Lang, N., Huber, S. D., Lukin, M. D., and Büchler, H. P., *"Topological bands with a Chern number $c = 2$ by dipolar exchange interactions,"* Physical Review A **91**, 053617 (2015) [cited in page 200].

Petrosyan, D., Höning, M., and Fleischhauer, M., *"Spatial correlations of Rydberg excitations in optically driven atomic ensembles,"* Physical Review A **87**, 053414 (2013) [cited in page 75].

Petrosyan, D., Mølmer, K., and Fleischhauer, M., *"On the adiabatic preparation of spatially-ordered Rydberg excitations of atoms in a one-dimensional optical lattice by laser frequency sweeps,"* Journal of Physics B **49**, 084003 (2016) [cited in page 79].

Petrosyan, D., Motzoi, F., Saffman, M., and Mølmer, K., *"High-fidelity Rydberg quantum gate via a two-atom dark state,"* Physical Review A **96**, 042306 (2017) [cited in page 86].

Petrosyan, D., Rao, D. D. B., and Mølmer, K., *"Filtering single atoms from Rydberg-blockaded mesoscopic ensembles,"* Physical Review A **91**, 1 (2015) [cited in page 143].

Phillips, W. D., *"Nobel lecture: Laser cooling and trapping of neutral atoms,"* Review of Modern Physics **70**, 721 (1998) [cited in page 7].

Picken, C. J., Legaie, R., McDonnell, K., and Pritchard, J. D., *"Entanglement of neutral-atom qubits with long ground-Rydberg coherence times,"* arXiv:1808.04755 (2018) [cited in page 86].

Pohl, T. and Berman, P. R., *"Breaking the Dipole Blockade: Nearly Resonant Dipole Interactions in Few-Atom Systems,"* Physical Review Letters **102**, 013004 (2009) [cited in page 114].

Pohl, T., Demler, E., and Lukin, M. D., *"Dynamical crystallization in the dipole blockade of ultracold atoms,"* Physical Review Letters **104**, 043002 (2010) [cited in page 72].

Popoff, S., *"Wavefront shaping with the wrapper slmpy,"* (2017) [cited in page 34].

Purcell, E. M., *"Research in nuclear magnetism,"* Science **118**, 431 (1953) [cited in page 8].

pyicic, *"Python wrapper for the IC Imaging Control SDK from The Imaging Source (TIS),"* [cited in page 34].

Qi, X.-L. and Zhang, S.-C., *"Topological insulators and superconductors,"* Review of Modern Physics **83**, 1057 (2011) [cited in page 166].

Ravets, S., Development of tools for quantum engineering using individual atoms : optical nanofibers and controlled Rydberg interactions, Ph.D. thesis, Université Paris-Saclay (2014) [cited in pages 20, 90, and 159].

Ravets, S., Labuhn, H., Barredo, D., Beguin, L., Lahaye, T., and Browaeys, A., *"Coherent dipole-dipole coupling between two single Rydberg atoms at an electrically-tuned Förster resonance,"* Nature Physics **10**, 914 (2014) [cited in page 125].

Ravets, S., Labuhn, H., Barredo, D., Lahaye, T., and Browaeys, A., *"Measurement of the angular dependence of the dipole-dipole interaction between two individual Rydberg atoms at a Förster resonance,"* Physical Review A **92**, 020701 (2015) [cited in pages 127 and 160].

Reetz-Lamour, M., Amthor, T., Deiglmayr, J., and Weidemüller, M., *"Rabi oscillations and excitation trapping in the coherent excitation of a mesoscopic frozen Rydberg gas,"* Physical Review Letters **100**, 253001 (2008) [cited in page 86].

Regal, C., *"Bringing order to neutral atom arrays,"* Science **354**, 972 (2016) [cited in pages 62 and 197].

Reinhard, A., Liebisch, T. C., Knuffman, B., and Raithel, G., *"Level shifts of rubidium Rydberg states due to binary interactions,"* Physical Review A **75**, 032712 (2007) [cited in page 119].

Rice, M. J. and Mele, E. J., *"Elementary excitations of a linearly conjugated diatomic polymer,"* Physical Review Letters **49**, 1455 (1982) [cited in page 173].

Richerme, P., Gong, Z.-X., Lee, A., Senko, C., Smith, J., Foss-Feig, M., Michalakis, S., Gorshkov, A. V., and Monroe, C., *"Non-local propagation of correlations in quantum systems with long-range interactions,"* Nature **511**, 198 (2014) [cited in page 9].

Riehle, F., Frequency standards, basics and applications (Wiley-VCH, Weinheim, 2004) [cited in pages 104 and 106].

Robens, C., Zopes, J., Alt, W., Brakhane, S., Meschede, D., and Alberti, A., *"Low-entropy states of neutral atoms in polarization-synthesized optical lattices,"* Physical Review Letters **118**, 065302 (2017) [cited in page 63].

Robicheaux, F. and Hernández, J. V., *"Many-body wave function in a dipole blockade configuration,"* Physical Review A **72**, 063403 (2005) [cited in page 71].

Roushan *et al.*, *"Spectroscopic signatures of localization with interacting photons in superconducting qubits,"* Science **358**, 1175 (2017) [cited in page 9].

Ryabtsev, I. I., Beterov, I. I., Tretyakov, D. B., Entin, V. M., and Yakshina, E. A., *"Doppler- and recoil-free laser excitation of Rydberg states via three-photon transitions,"* Physical Review A **84**, 053409 (2011) [cited in page 101].

Ryu, S., Schnyder, A. P., Furusaki, A., and Ludwig, A. W. W., *"Topological insulators and superconductors: tenfold way and dimensional hierarchy,"* New Journal of Physics **12**, 065010 (2010) [cited in page 166].

Saffman, M., *"Quantum computing with atomic qubits and Rydberg interactions: progress and challenges,"* Journal of Physics B **49**, 202001 (2016) [cited in pages 10, 79, and 86].

Saffman, M. and Walker, T. G., *"Creating single-atom and single-photon sources from entangled atomic ensembles,"* Physical Review A **66**, 065403 (2002) [cited in page 79].

Saffman, M. and Walker, T. G., *"Analysis of a quantum logic device based on dipole-dipole interactions of optically trapped Rydberg atoms,"* Physical Review A **72**, 022347 (2005) [cited in page 152].

Schachenmayer, J., Lesanovsky, I., Micheli, A., and Daley, A. J., *"Dynamical crystal creation with polar molecules or rydberg atoms in optical lattices,"* New Journal of Physics **12**, 103044 (2010) [cited in page 72].

Schauß, P., Cheneau, M., Endres, M., Fukuhara, T., Hild, S., Omran, A., Pohl, T., Gross, C., Kuhr, S., and Bloch, I., *"Observation of mesoscopic crystalline structures in a two-dimensional Rydberg gas,"* Nature **491**, 87 (2012) [cited in pages 11, 72, 75, and 86].

Schauß, P., Zeiher, J., Fukuhara, T., Hild, S., Cheneau, M., Macri, T., Pohl, T., Bloch, I., and Gross, C., *"Crystallization in Ising quantum magnets,"* Science **347**, 1455 (2015) [cited in pages 11, 72, 77, 79, and 86].

Schlosser, N., Etude et réalisation de micro-pièges dipolaires optiques pour atomes neutres, Ph.D. thesis, Université Paris Sud - Paris XI (2001) [cited in pages 18 and 19].

Schlosser, N., Reymond, G., and Grangier, P., *"Collisional blockade in microscopic optical dipole traps,"* Physical Review Letters **89**, 023005 (2002) [cited in page 19].

Schlosser, N., Reymond, G., Protsenko, I., and Grangier, P., *"Sub-poissonian loading of single atoms in a microscopic dipole trap."* Nature **411**, 1024 (2001) [cited in pages 10, 18, 19, and 45].

Schwarzkopf, A., Anderson, D. A., Thaicharoen, N., and Raithel, G., *"Spatial correlations between Rydberg atoms in an optical dipole trap,"* Physical Review A **88**, 061406 (2013) [cited in page 71].

Serwane, F., Zürn, G., Lompe, T., Ottenstein, T. B., Wenz, A. N., and Jochim, S., *"Deterministic preparation of a tunable few-fermion system,"* Science **332**, 336 (2011) [cited in page 57].

Shen, C. and Duan, L.-M., *"Correcting detection errors in quantum state engineering through data processing,"* New Journal of Physics **14**, 053053 (2012) [cited in page 95].

Sherson, J. F., Weitenberg, C., Endres, M., Cheneau, M., Bloch, I., and Kuhr, S., *"Single-atom-resolved fluorescence imaging of an atomic Mott insulator,"* Nature **467**, 68 (2010) [cited in page 64].

Shlesinger, I., Senellart, P., Lanco, L., and Greffet, J.-J., *"Tunable bandwidth and nonlinearities in an atom-photon interface with subradiant states,"* Physical Review A **98**, 013813 (2018) [cited in page 164].

Shull, C. G., Strauser, W. A., and Wollan, E. O., *"Neutron diffraction by paramagnetic and antiferromagnetic substances,"* Physical Review **83**, 333 (1951) [cited in page 8].

Šibalić, N., Pritchard, J. D., Adams, C. S., and Weatherill, K. J., *"ARC: An open-source library for calculating properties of alkali Rydberg atoms,"* Computer Physics Communications **220**, 319 (2016) [cited in pages 115, 134, and 154].

Singer, K., Reetz-Lamour, M., Amthor, T., Marcassa, L. G., and Weidemüller, M., *"Suppression of excitation and spectral broadening induced by interactions in a cold gas of Rydberg atoms,"* Physical Review Letters **93**, 163001 (2004) [cited in page 70].

Smith, J., Lee, A., Richerme, P., Neyenhuis, B., Hess, P. W., Hauke, P., Heyl, M., Huse, D. A., and Monroe, C., *"Many-body localization in a quantum simulator with*

programmable random disorder," Nature Physics **12**, 907 (2016) [cited in pages 9 and 164].

Song *et al.*, *"10-qubit entanglement and parallel logic operations with a superconducting circuit,"* Physical Review Letters **119**, 180511 (2017) [cited in page 86].

Sortais, Y. R. P., Marion, H., Tuchendler, C., Lance, A. M., Lamare, M., Fournet, P., Armellin, C., Mercier, R., Messin, G., Browaeys, A., and Grangier, P., *"Diffraction-limited optics for single-atom manipulation,"* Physical Review A **75**, 8 (2007) [cited in page 20].

St-Jean, P., Goblot, V., Galopin, E., Lemaître, A., Ozawa, T., Le Gratiet, L., Sagnes, I., Bloch, J., and Amo, A., *"Lasing in topological edge states of a one-dimensional lattice,"* Nature Photonics **11**, 651 (2017) [cited in pages 167, 169, 173, and 177].

Steck, D. A., *"Rubidium 87 d line data,"* [cited in page 94].

Su, W. P., Schrieffer, J. R., and Heeger, A. J., *"Solitons in polyacetylene,"* Physical Review Letters **42**, 1698 (1979) [cited in pages 168 and 178].

Su, W. P., Schrieffer, J. R., and Heeger, A. J., *"Soliton excitations in polyacetylene,"* Physical Review B **22**, 2099 (1980) [cited in page 168].

Süsstrunk, R. and Huber, S. D., *"Observation of phononic helical edge states in a mechanical topological insulator,"* Science **349**, 47 (2015) [cited in page 167].

Tai, M. E., Lukin, A., Rispoli, M., Schittko, R., Menke, T., Borgnia, D., Preiss, P. M., Grusdt, F., Kaufman, A. M., and Greiner, M., *"Microscopy of the interacting harper–hofstadter model in the two-body limit,"* Nature **546**, 519 (2017) [cited in page 185].

Takei, N., Sommer, C., Genes, C., Pupillo, G., Goto, H., Koyasu, K., Chiba, H., Weidemüller, M., and Ohmori, K., *"Direct observation of ultrafast many-body electron dynamics in an ultracold Rydberg gas,"* Nature Communications **7**, 13449 (2016) [cited in page 200].

Tarallo, M., Development of a Strontium optical lattice clock, Ph.D. thesis, Università degli studi di Pisa (2009) [cited in page 105].

Thompson, J. D., Tiecke, T. G., de Leon, N. P., Feist, J., Akimov, A. V., Gullans, M., Zibrov, A. S., Vuletic, V., and Lukin, M. D., *"Coupling a single trapped atom to*

a nanoscale optical cavity," Science (2013a), 10.1126/science.1237125 [cited in page 65].

Thompson, J. D., Tiecke, T. G., Zibrov, A. S., Vuletić, V., and Lukin, M. D., *"Coherence and raman sideband cooling of a single atom in an optical tweezer,"* Physical Review Letters **110**, 133001 (2013b) [cited in pages 28, 65, 101, and 200].

Thouless, D. J., Kohmoto, M., Nightingale, M. P., and den Nijs, M., *"Quantized Hall conductance in a two-dimensional periodic potential,"* Physical Review Letters **49**, 405 (1982) [cited in page 166].

Tong, D., Farooqi, S. M., Stanojevic, J., Krishnan, S., Zhang, Y. P., Côté, R., Eyler, E. E., and Gould, P. L., *"Local blockade of Rydberg excitation in an ultracold gas,"* Physical Review Letters **93**, 063001 (2004) [cited in page 70].

Tresp, C., Bienias, P., Weber, S., Gorniaczyk, H., Mirgorodskiy, I., Büchler, H. P., and Hofferberth, S., *"Dipolar dephasing of Rydberg d-state polaritons,"* Physical Review Letters **115**, 083602 (2015) [cited in page 134].

Tuchendler, C., Lance, A. M., Browaeys, A., Sortais, Y. R. P., and Grangier, P., *"Energy distribution and cooling of a single atom in an optical tweezer,"* Physical Review A **78**, 033425 (2008) [cited in page 27].

Urban, E., Johnson, T. A., Henage, T., Isenhower, L., Yavuz, D. D., Walker, T. G., and Saffman, M., *"Observation of Rydberg blockade between two atoms,"* Nature Physics **5**, 110 (2009) [cited in pages 10 and 120].

Varney, C. N., Sun, K., Galitski, V., and Rigol, M., *"Kaleidoscope of exotic quantum phases in a frustrated XY model,"* Physical Review Letters **107**, 077201 (2011) [cited in pages 138 and 199].

Vermersch, B., Glaetzle, A. W., and Zoller, P., *"Magic distances in the blockade mechanism of Rydberg p and d states,"* Physical Review A **91**, 023411 (2015) [cited in pages 114, 128, 129, and 133].

Vigneron, K., Quantum noise of light control and quantum nondemolition measurement using cold trapped atoms., Ph.D. thesis, Université Paris Sud - Paris XI (1998) [cited in page 19].

Vitanov, N. V., Rangelov, A. A., Shore, B. W., and Bergmann, K., *"Stimulated Raman adiabatic passage in physics, chemistry, and beyond,"* Review of Modern Physics **89**, 015006 (2017) [cited in page 141].

Vogt, T., Viteau, M., Zhao, J., Chotia, A., Comparat, D., and Pillet, P., *"Dipole blockade at Förster resonances in high resolution laser excitation of Rydberg states of cesium atoms,"* Physical Review Letters **97**, 083003 (2006) [cited in page 70].

Walker, T. G. and Saffman, M., *"Zeros of Rydberg–Rydberg Föster interactions,"* Journal of Physics B **38**, S309 (2005) [cited in page 114].

Walker, T. G. and Saffman, M., *"Consequences of Zeeman degeneracy for the van der Waals blockade between Rydberg atoms,"* Physical Review A **77**, 032723 (2008) [cited in pages 114, 119, 124, and 128].

Wallis, J. W., Miller, T. R., Lerner, C. A., and Kleerup, E. C., *"Three-dimensional display in nuclear medicine,"* IEEE Trans Med Imaging. **8**, 297 (1989) [cited in page 41].

Wang, Y., Kumar, A., Wu, T.-Y., and Weiss, D. S., *"Single-qubit gates based on targeted phase shifts in a 3d neutral atom array,"* Science **352**, 1562 (2016) [cited in page 64].

Wang, Y., Zhang, X., Corcovilos, T. A., Kumar, A., and Weiss, D. S., *"Coherent addressing of individual neutral atoms in a 3d optical lattice,"* Physical Review Letters **115**, 043003 (2015) [cited in page 64].

Weber, S., de Léséleuc, S., Lienhard, V., Barredo, D., Lahaye, T., Browaeys, A., and Büchler, H. P., *"Topologically protected edge states in small Rydberg systems,"* Quantum Science and Technology **3**, 044001 (2018) [cited in page 199].

Weber, S., Tresp, C., Menke, H., Urvoy, A., Firstenberg, O., Büchler, H. P., and Hofferberth, S., *"Tutorial: Calculation of Rydberg interaction potentials,"* Journal of Physics B **50**, 133001 (2017) [cited in pages 115, 126, and 134].

Weimer, H. and Büchler, H. P., *"Two-stage melting in systems of strongly interacting Rydberg atoms,"* Physical Review Letters **105**, 230403 (2010) [cited in page 78].

Weimer, H., Löw, R., Pfau, T., and Büchler, H. P., *"Quantum critical behavior in strongly interacting Rydberg gases,"* Physical Review Letters **101**, 250601 (2008) [cited in page 71].

Weiss, D. S., Vala, J., Thapliyal, A. V., Myrgren, S., Vazirani, U., and Whaley, K. B., *"Another way to approach zero entropy for a finite system of atoms,"* Physical Review A **70**, 1 (2004) [cited in pages 46, 56, and 63].

van Wijngaarden, W. A., Li, J., and Koh, J., *"Hyperfine-interaction constants of the $8d_{3/2}$ state in ^{85}Rb using quantum-beat spectroscopy,"* Physical Review A **48**, 829 (1993) [cited in pages 88 and 117].

Wilk, T., Gaëtan, A., Evellin, C., Wolters, J., Miroshnychenko, Y., Grangier, P., and Browaeys, A., *"Entanglement of two individual neutral atoms using Rydberg blockade,"* Physical Review Letters **104**, 010502 (2010) [cited in pages 10, 111, 125, 164, and 191].

Xia, T., Zhang, X. L., and Saffman, M., *"Analysis of a controlled phase gate using circular Rydberg states,"* Physical Review A **88**, 062337 (2013) [cited in page 86].

Yao, N. Y., Laumann, C. R., Gorshkov, A. V., Bennett, S. D., Demler, E., Zoller, P., and Lukin, M. D., *"Topological flat bands from dipolar spin systems,"* Physical Review Letters **109**, 266804 (2012) [cited in pages 65 and 199].

Younge, K. C., Knuffman, B., Anderson, S. E., and Raithel, G., *"State-dependent energy shifts of Rydberg atoms in a ponderomotive optical lattice,"* Physical Review Letters **104**, 173001 (2010) [cited in page 152].

Yu, Y., Hutzler, N. R., Zhang, J. T., Liu, L. R., Hood, J. D., Rosenband, T., and Ni, K.-K., *"Motional-ground-state cooling outside the Lamb-Dicke regime,"* Physical Review A **97**, 063423 (2018) [cited in pages 28 and 65].

Zeiher, J., van Bijnen, R., Schauss, P., Hild, S., Choi, J.-Y., Pohl, T., Bloch, I., and Gross, C., *"Many-body interferometry of a Rydberg-dressed spin lattice,"* Nature Physics **12**, 1095 (2016) [cited in page 86].

Zeiher, J., Schauß, P., Hild, S., Macrì, T., Bloch, I., and Gross, C., *"Microscopic characterization of scalable coherent Rydberg superatoms,"* Physical Review X **5**, 031015 (2015) [cited in pages 11 and 86].

Zhang, S., Robicheaux, F., and Saffman, M., *"Magic-wavelength optical traps for Rydberg atoms,"* Physical Review A **84**, 043408 (2011) [cited in page 99].

Zhang, W., Robinson, J. M., Sonderhouse, L., Oelker, E., Benko, C., Hall, J. L., Legero, T., Matei, D. G., Riehle, F., Sterr, U., and Ye, J., *"Ultrastable silicon cavity in a continuously operating closed-cycle cryostat at 4 K,"* Physical Review Letters **119**, 243601 (2017) [cited in page 104].

Zhang, X. L., Gill, A. T., Isenhower, L., Walker, T. G., and Saffman, M., *"Fidelity of a Rydberg-blockade quantum gate from simulated quantum process tomography,"* Physical Review A **85**, 042310 (2012) [cited in page 86].

Zhang, X. L., Isenhower, L., Gill, A. T., Walker, T. G., and Saffman, M., *"Deterministic entanglement of two neutral atoms via Rydberg blockade,"* Physical Review A **82**, 030306 (2010) [cited in page 86].

Zuo, Z., Fukusen, M., Tamaki, Y., Watanabe, T., Nakagawa, Y., and Nakagawa, K., *"Single atom Rydberg excitation in a small dipole trap,"* Optics Express **17**, 22898 (2009) [cited in page 86].

Zupancic, P., Preiss, P. M., Ma, R., Lukin, A., Tai, M. E., Rispoli, M., Islam, R., and Greiner, M., *"Ultra-precise holographic beam shaping for microscopic quantum control,"* Optics Express **24**, 4170 (2016) [cited in page 29].

Zurek, W. H., Dorner, U., and Zoller, P., *"Dynamics of a quantum phase transition,"* Physical Review Letters **95**, 105701 (2005) [cited in page 84].

université PARIS-SACLAY | ÉCOLE DOCTORALE Ondes et Matière (EDOM)

Titre : Simulation quantique de modèles de spins dans des matrices d'atomes de Rydberg

Mots clés : pinces optique, atomes individuels, interaction dipolaire, modèles de spins, simulation quantique

Résumé : Des atomes individuels piégés dans des matrices de pinces optiques et excités vers des états de Rydberg forment une plateforme expérimentale prometteuse pour la simulation quantique de modèles de spins. Lors de cette thèse, nous avons d'abord résolu le problème du chargement aléatoire des pièges, seulement 50 % d'entre eux étant chargés avec un atome. Nous avons développé une technique pour préparer des matrices 2D, puis 3D, d'atomes de ^{87}Rb en les déplaçant un par un avec une pince optique mobile contrôlée par ordinateur. Nous avons ensuite réalisé le modèle d'Ising en excitant de manière cohérente les atomes depuis leur état électronique fondamental vers un niveau de Rydberg. Après avoir trouvé un régime optimal où l'interaction dipolaire entre deux atomes de Rydberg se réduit à une énergie de van der Waals, nous avons tenté de préparer adiabatiquement l'état de Néel qui minimise l'énergie d'interaction. Nous avons montré que l'efficacité de préparation était limitée par la décohérence induite par les lasers d'excitation. Nous avons ensuite utilisé un autre régime d'interaction, le couplage dipolaire résonant, pour étudier des modèles de spins de type XY, dont le modèle Su-Schrieffer-Heeger, connu pour sa phase fermionique topologique protégée par une symétrie chirale. Ici, nous avons remplacé les fermions par des particules effectives de type `boson de cœur dur', ce qui modifie les propriétés de cette phase. Nous avons d'abord retrouvé les propriétés à une particule, comme l'existence d'états de bords à énergie nulle. Nous avons ensuite préparé l'état fondamental à N corps pour un remplissage moitié, et observé sa dégénérescence causée par les états de bords, même en présence d'une perturbation qui lèverait cette dégénérescence dans le cas fermionique. Nous avons expliqué ce résultat par l'existence d'une symétrie plus générale, qui protège la phase bosonique.

Title : Quantum simulation of spin models with assembled arrays of Rydberg atoms

Keywords : optical tweezers, single atoms, dipole-dipole interaction, spin models, quantum simulation

Abstract : Single atoms trapped in arrays of optical tweezers and excited to Rydberg states are a promising experimental platform for the quantum simulation of spin models. In this thesis, we first solved a long-standing challenge to this approach caused by the random loading of the traps, with only 50% of them filled with single atoms. We have engineered a robust and easy-to-use method to assemble perfectly filled two-dimensional arrays of ^{87}Rb atoms by moving them one by one with a moveable optical tweezers controlled by computer, a technique further enhanced to trap, image and assemble three-dimensional arrays. We then implemented the quantum Ising model by coherently coupling ground-state atoms to a Rydberg level. After finding experimental parameters where the dipole-dipole interaction takes the ideal form of a van der Waals shift, we performed adiabatic preparation of the Néel state. We showed that the coherence time of our excitation lasers limited the efficiency of this technique. We then used a different type of interaction, a resonant dipolar coupling, to implement XY spin models and notably the Su-Schrieffer-Heeger model, known for its fermionic topological phase protected by the chiral symmetry. Here, we used effective hard-core bosons, which modify the properties of the topological phase. We first recovered known properties at the single particle level, such as the existence of localized zero-energy edge-states. Then, preparing the many-body ground state at half-filling, we observed a surprising robustness of its four-fold degeneracy upon applying a perturbation. This result was explained by the existence of a more general symmetry protecting the bosonic phase.

Université Paris-Saclay
Espace Technologique / Immeuble Discovery
Route de l'Orme aux Merisiers RD 128 / 91190 Saint-Aubin, France